

UC San Diego

UC San Diego Electronic Theses and Dissertations

Title

Sodium-ion Batteries for Grid Storage: Investigation of Bulk and Interfacial Properties of Electrode Materials

Permalink

<https://escholarship.org/uc/item/4tm8c3xw>

Author

Hirsh, Hayley Sarah

Publication Date

2021

Peer reviewed|Thesis/dissertation

UNIVERSITY OF CALIFORNIA SAN DIEGO

Sodium-ion Batteries for Grid Storage: Investigation of Bulk and Interfacial
Properties of Electrode Materials

A dissertation submitted in partial satisfaction of the requirements for the degree

Doctor of Philosophy

in

Nanoengineering

by

Hayley Sarah Hirsh

Committee in charge:

Professor Ying. Shirley Meng, Chair
Professor David P. Fenning
Professor Ping Liu
Professor Yu Qiao
Professor Michael J. Sailor

2021

Copyright

Hayley Sarah Hirsh, 2021

All rights reserved.

The dissertation of Hayley Sarah Hirsh is approved, and it is acceptable in quality and form for publication on microfilm and electronically.

University of California San Diego

2021

DEDICATION

This work is dedicated to the women in my family who paved the way: my grandmother, Dr.

Gail Schlachter, and my mother, Dr. Sandra Hirsh.

This work is also dedicated to my loving and supporting family.

TABLE OF CONTENTS

DISSERTATION APPROVAL PAGE	iii
DEDICATION	iv
TABLE OF CONTENTS	v
LIST OF FIGURES	vii
LIST OF TABLES	xii
ACKNOWLEDGMENTS	xiv
VITA.....	xvi
ABSTRACT OF THE DISSERTATION.....	xviii
Chapter 1 Introduction and Thesis Outline	1
1.1 Introduction to Sodium-ion Batteries	1
1.2 Characterization Techniques	2
1.3 Thesis Outline.....	8
Chapter 2 Sodium-Ion Batteries Paving the Way for Grid Energy Storage.....	9
2.1 Introduction	9
2.2 Discussion.....	10
2.3 Conclusion.....	21
Chapter 3 Meso-structure Controlled Synthesis of Sodium Iron-Manganese Oxides Cathode for Low-Cost Na-Ion Batteries.....	23
3.1 Introduction	23
3.2 Methods	26
3.3 Results and Discussion	29
3.4 Conclusions	40
Chapter 4 Elucidating the Redox Mechanism of Cathode Materials Made from Earth-Abundant Elements	41
4.1 Introduction	41
4.2 Experimental Section.....	45
4.3 Results and Discussion	47
4.4 Conclusions	57
Chapter 5 The Negative Impact of Transition Metal Migration on Oxygen Redox Activity of Layered Cathode Materials for Na-ion Batteries.....	59

5.1 Introduction	59
5.2 Experimental Methods.....	62
5.3 Results and Discussion	64
5.4 Conclusions	78
Chapter 6 Role of electrolyte in stabilizing hard carbon as an anode for rechargeable sodium-ion batteries with long cycle life.....	80
6.1 Introduction	80
6.2 Methods	84
6.3 Results and Discussion	86
6.4. Conclusions	98
Chapter 7 Conclusions and Future Perspective	100
Appendix A Supporting Information for Chapter 2	103
Appendix B Supporting Information for Chapter 3	110
Appendix C Supporting Information for Chapter 4	117
Appendix D Supporting Information for Chapter 5	121
Appendix E Supporting Information for Chapter 6.....	125
E.1 XPS sample preparation discussion	128
References	132

LIST OF FIGURES

Figure 1.1: Diagram of a sodium-ion battery. The arrows signify the direction of Na ⁺ and e ⁻ migration during charge/discharge.	1
Figure 1.2: A diagram of Bragg's law. The incident X-rays are the black arrows, and the crystal array is in blue.	3
Figure 1.3: Diagram of an XAS spectra with the XANES region in blue and the EXAFS region in green.	4
Figure 1.4: A diagram showing different characterization techniques comparing their field of view with their resolution.	7
Figure 2.1: (a) Current electrochemical storage technologies gravimetric energy density versus volumetric energy density compared. (b) The price trend of sodium carbonate and lithium carbonate from 2005 to 2019. The inset is the percentage of price changes of both materials over the past 10 years. (c) A map of the Li reserves and Soda Ash (Na reserves) in the world reported	12
Figure 2.2: (a) Volumetric energy density (Wh/L) versus the gravimetric energy density (Wh/kg) are compared for differed types of sodium cathode materials. The blue circles are layered oxides, the purple circles are polyanion, and the yellow circles are PBA. (b) Capacity retention of the capacity versus first discharge energy density (Wh/kg) for layered cathode materials	15
Figure 2.3: The root scientific challenges (bottom) of sodium-ion batteries that need to be overcome to support sustainable, safe, large scale energy storage applications (top).....	21
Figure 3.1: Schematic of the modified co-precipitation synthesis process for meso-structure controlled sodium iron manganese oxide.	29
Figure 3.2: XRD and SEM of quenched NFMO (a, b) and slow-cooled NFMO (c, d) show that the two materials have the same crystal structure but different morphology and meso-structures. Selected parameters from XRD refinement, BET, and ICP measurements for the two materials are shown in (e).	30
Figure 3.3: dQ/dV curves of the 1 st , 2 th , and 10 th cycles of slow-cooled (a) and quenched (b) NFMO at a rate of C/50. Bar graphs representing the charge (c) and discharge (d) capacities between 1.5-2.7 V and 2.7-4.3 V at different cycles for slow-cooled and quenched NFMO. Model structures of P2-Na _x Fe _{0.25} Mn _{0.75} O ₂ , where x=3/8, 5/8 and 8/8	31
Figure 3.4: Voltage profiles for quenched and slow-cooled NFMO at a rate of C/50 at (a) cycle 1 and (b) cycle 10. Specific discharge capacity versus cycle number at a rate of (c) C/20 and (d) C/10 and coulombic efficiency as a function of cycle number.	33
Figure 3.5: XPS spectra of (a) Mn 3s, (b) Fe 2p, (c) O 1s, and (d) C 1s regions for slow-cooled (gray background) and quenched (white background) NFMO.	35

Figure 3.6: Nyquist plots of quenched and slow cooled NFMO (a) charged to 4.3 V and (b) discharge to 1.5 V. The fit of the data is based on the circuit shown in (c). The table (d) contains the values for the impedance measurements.	38
Figure 4.1. SEM images and Rietveld refinement of XRD of (a, d) pristine NFMO13, (b, e) NFMO12, and (c, f) NFMO11.	48
Figure 4.2. XPS spectra of (a) Mn 3s & Fe 4s, (b) Fe 2p, (c) C 1s, and (d) O 1s for NFMO13 (top), NFMO12 (middle), and NFMO11 (bottom) surfaces.	49
Figure 4.3. Voltage curves, cycling performance, and coulombic efficiencies of (a,d) NFMO13, (b,e) NFMO12, and (c,f) NFMO11 cycled between 1.5 and 4.3 V at C/10 rate. First charge curve at different rates for (g) NFMO13, (h) NFMO12, and (i) NFMO11.....	51
Figure 4.4: (a) Mn K-edge position and normalized XANES spectra of the Mn K-edge for (b-d) NFMO13, (e-g) NFMO12, and (h-j) NFMO11 at different states of charge during the first cycle and the second charge of operando half cells.	53
Figure 4.5: (a) FE K-edge position and normalized XANES spectra of the Fe K-edge for (b-d) NFMO13, (e-g) NFMO12, and (h-j) NFMO11 at different states of charge during the first cycle and the second charge of operando half cells.	54
Figure 4.6. DOS near the Fermi level for fully desodiated and sodiated NFMO13 (top), NFMO12 (middle), and NFMO11 (bottom). The blue line represents Mn DOS, the red line represents Fe DOS, and the green line represents O DOS. DOS sign refers to spin state. The green arrows guide the eye to the increased intensity of oxygen DOS near the Fermi level with increased Fe content.	56
Figure 5.1: (a) SEM image of NLNMO powder with primary hexagonal particles of 100-500 nm in diameter and secondary spherical particles of 1-3 μm in diameter. (b) A cross section of an NLNMO particle with large pores in its secondary structure. (c) XRD data of NLNMO with superlattice peaks highlighted with an orange square.	65
Figure 5.2: Voltage profiles of NLNMO half cells cycled at rates of (a) C/50, (b) C/10, and (c) C/1. In voltage profile (b) the numbers mark the voltages where <i>ex situ</i> XAS data was recorded.	66
Figure 5.3: The <i>ex situ</i> XANES spectra and respective positions of the (a,d) Ni K-edge, and (b,e) Mn K-edge of NLNMO at different states of charge. (c) <i>ex situ</i> XANES spectra of the O K-edge (FY mode) and the (f) integrated pre-edge intensity of the O K-edge at different states of charge.	67
Figure 5.4: (a) voltage profile of the initial cycle of NLNMO in the operando sXRD data collection; (b) contour plot of the sXRD pattern obtained over cycling; (c) magnified (002) peak and superlattice peak region; (d) lattice <i>a</i> , (e) lattice <i>c</i> and (f) unit cell volume obtained from Rietveld refinement; (g) refinement of PDF pattern of pristine NLNMO powder	70

Figure 5.5: *Ex situ* EXAFS spectra of NLNMO at (a) Ni K-edge and (b) Mn K-edge at different states of charge. (c) A model of the crystal structure of NLNMO with the first two nearest neighbors starting from the atom centered in the circled in dashed red lines. (d) The bond length of Mn/Ni-TM and the (e) bond length of Mn/Ni-O at different states of charge. 74

Figure 6.1: First cycle voltage profiles and their corresponding differential voltage plots of HC with PC (red) or TEGDME electrolyte (blue) at a rate of (a,d) C/20, (b,e) C/10, and (c,f) C/3. The numbers highlighted in the differential voltage plots indicate the plateau voltages during (de)sodiation. 87

Figure 6.2: Sodium stored in the HC at different states of charge with PC (a,b) or TEGDME electrolyte (c,d) measured by TGC (open circles) and electrochemistry (filled circles) with their representative voltage profiles tested at a rate of C/10. (e) Analysis of capacity usage, reversible Na, metallic Na in bulk HC structure, and SEI Na⁺, for HC 89

Figure 6.3: Raman spectra (a) G-band positions and (b) representative voltage curves for HC with PC or TEGDME as the electrolyte tested at a rate of C/10. (c) A schematic showing the sodium pathway (green dotted arrows) through the graphitic region of the HC structure to reach the structural voids. 90

Figure 6.4: Nano-scale structures of (a) pristine HC and HC after 1 cycle at a rate of C/3 in (b) PC and (c) TEGDME electrolyte imaged by cryo-TEM. The thickness of the SEI at various location is measured in the images. 92

Figure 6.5: (a,b) XPS C 1s regions and (c,d) XPS O 1s regions of HC cycled with PC (left) or TEGDME (right) electrolyte samples at different rates. 93

Figure 6.6: (a,b) Voltage profiles and (c,d) specific capacity and CE vs. cycled number for HC in (left) PC or (right) TEGDME electrolyte. 97

Figure 6.7: Cross-sectional schematics of the differences between the SEI on HC in PC vs. TEGDME electrolyte. 98

Figure A.1: (a) Retention of the capacity versus first discharge energy density (Wh/kg), (b) retention of the capacity versus first discharge capacity, and (c) first discharge energy density versus first discharge capacity for layered cathode materials in Na-ion batteries. 103

Figure A.2: Capacity retention of the capacity versus first discharge energy density (Wh/kg) for layered cathode materials in Na-ion batteries with numbers corresponding to the materials in Table A.2 and A.3. 104

Figure A.3: Price of energy (\$/kWh) for selected sodium cathodes that are Li, Ni, Co-free (blue) and contain Li, Ni, and/or Co (red). (Inset) A pie chart that contains the average cost percentage of lithium-ion battery components, with cathodes representing 44% of the total battery cost (CC=current collector). The price of each element is sourced from metalary.com. 107

Figure B.1: Mn(SO₄) (top) and Fe(SO₄) (bottom) aqueous solutions mixed with Na₂CO₃ at different pH values. 110

Figure B.2: (a) XRD spectra of iron manganese precipitates synthesized at different pH and atmospheres with enhanced view (b) of the hydroxide impurity peak at 1.26 Å.	111
Figure B.3: (a) XRD spectra and Rietveld refinement of $\text{Fe}_{1/4}\text{Mn}_{3/4}\text{CO}_3$ synthesized by coprecipitation and with the refined atomic positions and lattice parameters in the table and (b, c) SEM images showing the spherical morphology.	112
Figure B.4: (a) XRD spectra of NFMO calcinated at different temperatures and (b) NFMO with different sodium content.	113
Figure B.5: SEM images of (a) quenched and (b) slow-cooled NFMO.	113
Figure B.6: Partial density of states for $\text{Na}_x\text{Fe}_{0.25}\text{Mn}_{0.75}\text{O}_2$ when $x=3/8, 5/8,$ and $8/8$	114
Figure B.7: Specific discharge capacity versus cycle number at a rate of C/10 and coulombic efficiency as a function of cycle number.	115
Figure B.8: TEM images of (a) quenched and (b) slow cooled NFMO with the surface contamination outlined in orange.	116
Figure C.1: XRD data of the pristine cathode and cathode after 1 cycle for NFMO13, NFMO12, and NFMO11.	117
Figure C.2: The Mn K-edge position as analyzed us the (a) half-height method and (b) edge-crest method.	118
Figure C.3: XANES spectra of the Mn K-edge for (a) MnO, $\text{Mn}_2\text{O}_3,$ and MnO_2 and the Fe K-edge for (b) FeO and Fe_2O_3	118
Figure C.4: FEFF9 simulations of the Fe K-edge for a) NFMO13, b) NFMO12, and c) NFMO11 at different states of charge.	119
Figure C.5: Extracted Fe K-edge edge-crest positions and Mn K-edge inflection points for NaTMO_2 in literature.	119
Figure C.6: Calculated DOS of NFMO13, NFMO12, and NFMO11 at different states of charge ($\text{Na}= 0, 3, 5,$ and 8 out of 8 possible Na atoms) with blue representing Mn DOS, red representing Fe DOS, and green representing O DOS. DOS sign refers to spin state.	120
Figure D.1: Spherical $\text{Ni}_{1/4}\text{Mn}_{3/4}\text{CO}_3$ precursors of NLNMO.	121
Figure D.2: Schematic diagrams of the O K-edge sXAS electronic transitions from the O1s state to empty states in the transition metals of NLNMO. The diagram is simplified to show one electron energy and does not distinguish between spin-up and spin-down states.	123
Figure D.3: Fourier transformed EXAFS of NLNMO at the Mn K-edge and Ni K-edge. The blue lines at a FT magnitude of 2 are guides to compare the backscattering ability.	123

Figure D.4: Calculated DOS for fully charged NLNMO with (a) no Ni migration and (b) with Ni migration with their respective TM layer structures (c, d). Purple represents Mn atoms, silver represents Ni atoms, and red represents oxygen atoms.	124
Figure E.1: Plateau voltages of the first cycle of HC in PC or TEGDME electrolyte at different cycling rates.	125
Table and Figure E.2: TGC results of the potential SEI components of HC in PC or TEGDME electrolyte.	125
Figure E.3: Raman spectra of HC in PC or TEGDME electrolytes at different states of (de)sodiation.	125
Figure E.4: Cryo-TEM images of HC after 1 cycle at a rate of C/3 in (a,c) PC and (b,d) TEGDME electrolyte. The thickness of the SEI at various location is measured and labeled in the images.	126
Figure E.5: SEM images of pristine HC, HC after 1 cycle at a rate of C/3, C/10, and C/20 with PC (top row) or TEGDME (bottom row) as the electrolyte. The scale bar represents 5 μm	126
Figure E.6: EDS mapping of (a) pristine HC, (b,c) HC after 1 cycle at a rate of C/3, (d,e) C/10, and (f,g) C/20 with PC or TEGDME electrolytes.	127
Figure E.7: XPS C 1s regions of washed (left) and unwashed (right) samples of HC at different states of charge with (a,b) PC or (c,d) TEGDME as the electrolyte. XPS O 1s regions of washed (left) and unwashed (right) samples of HC at different states of charge with (e,f) PC or (g,h) TEGDME as the electrolyte.	128
Figure E.8: XPS F 1s regions of washed (left) and unwashed (right) samples of HC at different states of charge with (a,b) PC or (c,d) TEGDME electrolyte.	130
Figure E.9: Nyquist plots of HC in PC (red) or TEGDME (blue) electrolyte after 1 cycle at a rate of C/3. The fit of the data is based on the circuit (inset). The table contains the values from the impedance data fit.	130

LIST OF TABLES

Table 3.1: Synthesis parameters for sodium iron manganese oxide cathode materials reported from literature.....	25
Table 3.2: Co-precipitation synthesis parameters of iron containing sodium TM oxides cathode materials reported from literature.....	25
Table 4.1. Fe redox mechanisms from XAS studies of Fe containing layered NIB cathodes in literature.....	43
Tables 5.1 a & b: <i>Ex situ</i> EXAFS fit results for indicated samples collected at the Mn K-edge (Table 5.1a) and the Ni K-edge (Table 5.1b). The phase-corrected bond length (R) and Debye-Waller factor (σ^2) are shown for each interaction.	76
Table 6.1: Summary of electrolytes and techniques used to characterize the SEI of HC in literature.	83
Table A.1: Comparison of electrochemical energy storage systems.....	103
Table A.2: Layered oxide, polyanion, and PBA type NIB cathode materials properties. Note: Cycle life is Depth of Discharge (DOD) dependent. The numbers we show in the table are only taking into consideration of 80-100% DOD.....	105
Table A.3: Li, Ni, Co- free NIB cathode materials properties.	106
Table A.4: Li, Ni, Co- containing NIB cathode materials properties.....	107
Table A.5: Cost analysis for NIB full cells at 1KWh level constructed with different cathodes. The unit price for the cathode materials are from the calculation in Figure A.3, and the price of other cell components are sourced from prevailing commercial prices.	108
Table B.1: Residual TM in solutions shown in SI Figure 1. The optimized pH values are highlighted for Mn and Fe.	110
Table B.2: XRD Refinement parameters for slow cooled and quenched NFMO.	114
Tables B.3 (a,b): Surface contamination concentration determined by titration of Na ₂ CO ₃ with HCl	115
Table C.1: NIB cathodes with first discharge energy density greater than 450 Wh/kg made from abundant TM from literature.	117
Table C.2: Selected refinement parameters for XRD of NFMO13, NFMO12, and NFMO11...117	117
Table C.3: 1 st cycle CE and % (discharge) capacity retention after 50 cycles for NFMO13, NFMO12, and NFMO11, corresponding to Figure 4.3.....	118

Table D.1: NIB cathodes with oxygen redox. Compounds containing Ni are highlighted in blue.	121
Table D.2: Refinement parameters of NLNMO.....	122
Table D.3: Refinement parameters of powder NLNMO PDF pattern	122
Table E.1: Percent of plateau capacity during the first cycle of HC in PC or TEGDME electrolyte at different cycling rates.	125

ACKNOWLEDGMENTS

I would like to thank my PhD advisor Professor Shirley Meng for her support guidance, mentorship, and financial support. During the past five years she has pushed me to learn and achieve more than I thought was possible. I would also like to express my deepest gratitude to my committee members: Professor David P. Fenning, Professor Ping Liu, Professor Yu Qiao, and Professor Michael J. Sailor.

I am thankful for past and present LESC members who have helped me and supported me through my PhD. I would also like to thank the NanoEngineering admins, Nano3 staff, and the beamlines scientist at Argonne and Brookhaven National Laboratories. Without their work and help, I would not be able to complete my PhD.

Thank you to my supportive family for believing in me and for their unconditional love. They instilled in me the importance of education and inspired my love of science and engineering. They provided opportunities for me to grow and improve as both a scientist and a person. I am thankful to my partner for his continual love and support. I am also thankful for all my friends who have helped and supported me along the way.

I would like to thank all of my funding source: USA National Science Foundation under Award Number DMR1608968.

Chapter 2, in full, is a reprint of the material, “Sodium-Ion Batteries Paving the Way for Grid Energy Storage” as it appears in *Advanced Energy Materials*, H. S. Hirsh, Y. Li, D. H. S, Tan, M. Zhang, E. Zhao, Y. S. Meng, 2020, 10, 2001274. The dissertation author was the co-primary investigator and author of this paper. The author collected and analyzed the data and cowrote the paper.

Chapter 3, in full, is a reprint of the material, “Meso-Structure Controlled Synthesis of Sodium Iron-Manganese Oxides Cathode for Low-Cost Na-Ion Batteries” as it appears in the Journal of The Electrochemical Society, H. Hirsh, M. Olguin, H. Chung, Y. Li, S. Bai, D. Feng, D. Wang, M. Zhang, Y. S. Meng, 2019, 166, A2528–A2535. The dissertation author was the primary investigator and author of this paper. All of the experimental parts were performed by the author except for the DFT, XPS, and TEM.

Chapter 4, in full, is currently being prepared for submission for publication, “Elucidating the Redox Mechanism of Cathode Materials Made from Earth-Abundant Elements” H. S. Hirsh, S. Richardson, M. Olguin, T. A. Wynn, D. Cheng, D. H. S. Tan, M. Zhang, E. Zhao, Y. S. Meng. The dissertation author was the primary investigator and author of this paper. All of the experimental parts were performed by the author except for the DFT and XPS.

Chapter 5, in full, is a reprint of the material, “The Negative Impact of Transition Metal Migration on Oxygen Redox Activity of Layered Cathode Materials for Na-ion Batteries” as it appears in the Journal of The Electrochemical Society, H. S. Hirsh, Y. Li, J. H Cheng, R. Shimizu, M. Zhang, E. Zhao, Y. S. Meng, 2021, 168, 040539. The dissertation author was the co-primary investigator and author of this paper. The author performed the materials synthesis, electrochemical test, SEM, XRD, and data interpretation and analysis.

Chapter 6, in full, is currently being prepared for submission for publication, “Role of electrolyte in stabilizing hard carbon as an anode for sodium-ion batteries” H. S. Hirsh, B. Sayahpour, A. Shen, W. Li, B. Lu, E. Zhao, M. Zhang, Y. S. Meng. The dissertation author was the primary investigator and author of this paper. The author designed all experiments and analyzed all the data collected for this paper.

VITA

- 2012 Bachelor of Science in Materials Science and Engineering, Cornell University
- 2018 Master of Science in NanoEngineering, University of California San Diego
- 2021 Doctor of Philosophy in NanoEngineering, University of California San Diego

PUBLICATIONS

J. Star-Lack, D. Shedlock, D. Swahn, D. Humber, A. Wang, **H. Hirsh**, G. Zentai, D. Sawkey, I. Kruger, M. Sun, E. Abel, G. Virshup, M. Shin, R. Fahrig, “A piecewise-focused high DQE detector for MV imaging”, *Medical Physics*, 42, 5084 (2015).

H. Hirsh, M. Olguin, H. Chung, Y. Li, S. Bai, D. Feng, D. Wang, M. Zhang, Y. S. Meng. “Meso-Structure Controlled Synthesis of Sodium Iron-Manganese Oxides Cathode for Low-Cost Na-Ion Batteries”, *Journal of The Electrochemical Society*, 166, A2528–A2535 (2019).

H. S. Hirsh, Y. Li, D. H. S, Tan, M. Zhang, E. Zhao, Y. S. Meng, “Sodium-Ion Batteries Paving the Way for Grid Energy Storage”, *Advanced Energy Materials*, 10, 2001274. (2020).

H. S. Hirsh, Y. Li, J. H Cheng, R. Shimizu, M. Zhang, E. Zhao, Y. S. Meng, “The Negative Impact of Transition Metal Migration on Oxygen Redox Activity of Layered Cathode Materials for Na-ion Batteries”, *Journal of The Electrochemical Society*, 168, 040539 (2021).

H. S. Hirsh, B. Sayahpour, A. Shen, W. Li, B. Lu, E. Zhao, M. Zhang, Y. S. Meng, “Role of electrolyte in stabilizing hard carbon as an anode for sodium-ion batteries” *Submitted*.

H. S. Hirsh, S. Richardson, T. A. Wynn, M. Olguin, D. Cheng, D. H. S. Tan, M. Zhang, E. Zhao, Y. S. Meng, “Elucidating the Redox Mechanism of Cathode Materials Made from Earth-Abundant Elements” *In preparation*.

O. Y. Gorobtsov, **H. Hirsh**, M. Zhang, D. Sheyfer, S. Matson, D. Weinstock, R. Bouck, Z. Wang, W. Cha, R. Harder, Y. S. Meng, A. Singer, “Imaging operando defect formation in sodium-ion battery cathodes” *In preparation*.

ABSTRACT OF THE DISSERTATION

Sodium-ion Batteries for Grid Storage: Investigation of Interface and Bulk Properties of Electrode Materials

by

Hayley Sarah Hirsh

Doctor of Philosophy in NanoEngineering

University of California San Diego, 2021

Professor Ying Shirley Meng, Chair

Sodium-ion batteries (NIBs) are a promising solution for grid storage because they are inexpensive, sustainable, and have suitable energy densities. Exploration of energy-dense NIB cathode materials that include abundant and inexpensive elements has led to the investigation of sodium iron manganese oxides. However, these materials suffer from poor capacity retention, and their reaction mechanisms remain that presents an obstacle to their optimization.

Herein we optimized a novel co-precipitation method that can be used to synthesize sphere-like meso-structured sodium transition metal (TM) oxide cathode materials. The key parameter for controlling the meso-structure was found to be the synthesis cooling rate and the sphere-like meso-structure improved the capacity and lifetime of the cathodes.

Using this same synthesis route, P2- $\text{Na}_{2/3}\text{Fe}_x\text{Mn}_{1-x}\text{O}_2$ (NFMO) cathodes with three Fe:Mn ratios were prepared. The redox mechanisms dependence on the Fe content were explored with X-ray absorption spectroscopy (XAS) and density functional theory (DFT) calculations. A Fe:Mn ratio less than 1:2 was found to promote capacity retention.

One pathway to improve the energy density of NIB cathodes is to enable oxygen redox activity. Oxygen redox activity was triggered in $\text{Na}_{0.8}\text{Li}_{0.12}\text{Ni}_{0.22}\text{Mn}_{0.66}\text{O}_2$ (NLNMO) by TM layer ordering, however it was irreversible after the first charge. The mechanism of irreversible oxygen activity in NLNMO was observed with XAS, synchrotron X-ray diffraction (sXRD), pair distribution function (PDF), and DFT. Ni migration was found to be detrimental to the reversibility of oxygen redox activity.

In addition to NIB cathodes, the anode performances need to be improved. Specifically, hard carbon (HC), one of the most attractive anode materials for NIB, has a low first cycle coulombic efficiency and poor rate capability. These drawbacks appear to be electrolyte dependent, since ether-based electrolytes can largely improve the HC performance compared to carbonate electrolytes. Using titration gas chromatography (TGC), Raman spectroscopy, cryo-transmission electron microscopy (TEM), and X-ray photoelectron spectroscopy (XPS), we found that the electrolyte controls the quality of the solid electrolyte interphase (SEI), which in turn, controls the first cycle coulombic efficiency and the rate capability. Overall, this work provides

insight on how to improve the design of inexpensive, sustainable, energy-dense NIBs for grid storage.

1.1 Introduction to Sodium-ion Batteries

The demand for grid storage solutions has rapidly increased because of the low cost of renewable energy production. Renewable energy technologies such as wind and solar are inexpensive, but do not have consistent energy production.[1] To fully utilize these sustainable technologies, grid storage is necessary. Grid storage requires a solution that is inexpensive, can work at over a range of charge/discharge rates, and is relative energy-dense. Sodium-ion batteries (NIBs) have the potential to fit these requirements and be an ideal solution for grid storage.

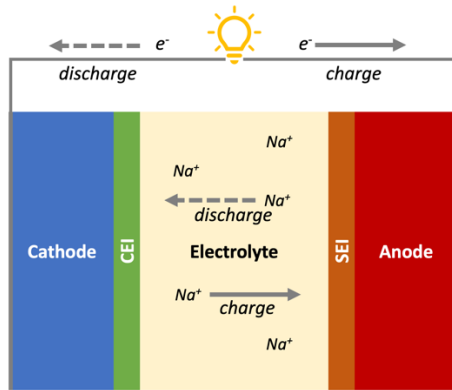


Figure 1.1: Diagram of a sodium-ion battery. The arrows signify the direction of Na^+ and e^- migration during charge/discharge.

Batteries are closed systems where electrical energy is generated by converting chemical energy via redox reactions.[2] Batteries consist of six key components: a cathode, anode, electrolyte, solid electrolyte interphase (SEI), cathode electrolyte interphase (CEI), and current collectors (**Figure 1.1**). **1)** A cathode is the positive electrode of a cell that is associated with reductive chemical reactions upon discharge. NIB cathode materials include intercalation compounds such as transition metal (TM) layered oxides, polyanion, and Prussian blue analogs.[3] **2)** An anode is the negative electrode of a cell that is associated with oxidative chemical reactions upon discharge. NIB anode materials include carbonaceous materials, oxides, sodium metal and

alloys.[4] **3)** An electrolyte's role is to conduct ions between the anode and cathode and to be electronically insulating. Electrolytes contain solvents that can be liquid, solid, or gas, and sodium salts.[5] **4)** An SEI is a film that forms on the surface of the anode material during electrochemical cycling. Ideally it is a thin, passivating layer between the anode and electrolyte that allows Na^+ transport but inhibits further reactions with the electrolyte. The composition of the SEI is dependent on the electrolyte, anode material, binders, and electrochemical cycling conditions. **5)** A CEI is similar to an SEI but it forms on the surface of the cathode material. **6)** A current collector is a conductive material that is the backing of the cathodes and anodes films. For lithium-ion batteries (LIBs) the current collect on the anode side is usually made out of Cu because Li can alloy with Al metal. However, for NIBs both current collectors can be made out of the cheaper and lighter Al metal.[4] The applicability of NIBs for grid storage and issues facing its battery components are discussed in detail in Chapter 2.

While NIBs are promising for grid storage, there are issues that need to be resolved before commercialization. The cathode and anode syntheses, energy-densities, compatibility with electrolytes, and lifetimes must be optimized. However, the mechanisms of sodium storage and capacity loss in these materials are still not fully understood. Using advanced characterization techniques, including the ones described below, these mechanisms can be illuminated to provide insight into improving battery design.

1.2 Characterization Techniques

The following characterization techniques all utilize radiation, either from X-rays or electrons. The techniques discussed are X-ray diffraction (XRD), X-ray absorption spectroscopy (XAS), pair distribution function (PDF), and X-ray photoelectron spectroscopy (XPS), and scanning electron microscopy (SEM).

1.2.1 X-ray Diffraction

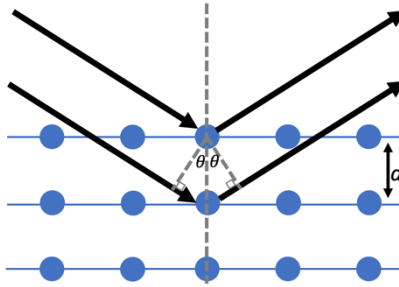


Figure 1.2: A diagram of Bragg's law. The incident X-rays are the black arrows, and the crystal array is in blue.

Powder X-ray diffraction is a fundamental technique in materials science and engineering. XRD is a non-destructive method to identify, quantify, and characterize the crystalline phases of a sample. This technique can be performed in a lab, usually with Cu alpha radiation, or at a synchrotron facility with higher energy X-rays. Higher energy X-rays allows for deeper penetration into sample, which can enable *operando* experiments, higher resolution, and shorter measurement times. However, no matter the X-ray energy, the technique follows the same guiding principles.

In a XRD measurement, a crystalline material's atoms form a regular array where their electrons scatter the incident X-ray waves. Most of the waves cancel each other out through destructive interference, but the ones that add constructively are determined by Bragg's law:

Equation 1.1
$$2d \sin \theta = n\lambda$$

Where d is the spacing between the atomic planes, θ is the incident angle, n is an integer, and λ is the X-ray wavelength. Experimental XRD data can be fit with a calculated profile through Rietveld refinement to quantify the crystalline phase ratios, the phase lattice constants, atomic position, crystallite size, microstrain, textures, and atomic occupancy.[6] This powerful technique is highly utilized in battery cathode research.

In my work, XRD is used bothin *ex situ* and *in situ* to characterize layered oxide cathode materials. *Ex situ* XRD is performed in a lab setting to identify and characterized the phases of synthesized sodium cathode materials. *In situ* XRD was performed at a synchrotron facility during a battery’s electrochemical cycling to observe phase changes. For this experiment, a special *in situ* cell with a X-ray transparent window was used.[7]

1.2.2 X-ray Absorption Spectroscopy

XAS is a nondestructive technique performed at synchrotron facilities to investigate samples electronic states and local atomic structure. High flux and tunable X-ray energy are needed to generate spectra where the percent transmitted X-ray intensity through a sample is measured over a range of X-ray energies.[8] When an X-ray interacts with an atom, one of the core electrons is excited to a higher energy unoccupied state or ejected into the continuum. This forms an absorption edge that is named for the principle quantum number from which the core electron is excited from (examples: 1=K, 2=L, and 3=M). An example diagram of a resulting spectra is shown in **Figure 1.3**.

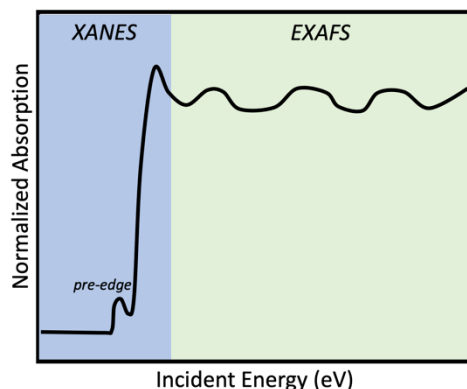


Figure 1.3: Diagram of an XAS spectra with the XANES region in blue and the EXAFS region in green.

There are two main regions of an XAS spectra, the X-ray absorption near edge spectra (XANES), shown in blue in **Figure 1.3**, and the extended X-ray absorption fine structure (EXAFS)

shown in the green region. XANES are element specific and can be used to investigate the electronic states of an element in a sample. As the oxidation state of an atom increases, the XANES absorption edge will increase in energy. A pre-edge structure, in the XANES region, can be seen in the K-edges of first row transition metals arises from the 1s to 3d transition. This feature can also be used to identify the oxidation states of the atoms in a sample. The EXAFS region corresponds to the high energy green region in **Figure 1.3**. This region can provide information on an element's local environment in the sample and can be used to analyze both crystalline and amorphous materials. In XAS, after an electron has been ejected from an atom, an outer electron relaxes into the core shell vacancy. The ejected photoelectron interacts with the surrounding atoms in the sample, producing the oscillations observed in the EXAFS region. The maxima and minima of the oscillations are caused by constructive and destructive interference respectively. The local bonding environment can be deduced by fitting the Fourier transform of the normalized EXAFS region.

XAS can be performed over a range of X-ray energy, the choice of which depends on the elements of interest. The soft X-ray range is used for low Z elements such as oxygen (higher Z elements' L-edges can also be detected in this range), the tender range is used for mid Z elements such as sulfur, and the hard X-ray range is used for high Z elements such as iron. In this thesis, both soft and hard XAS were used to observe the redox reactions of sodium cathode materials, as well as their local atomic ordering.

1.2.3 X-ray Pair Distribution Function

X-ray Pair distribution function (PDF) is an X-ray scattering technique, typically performed at a synchrotron facility, to study the local atomic ordering of a material. The scattering data must be collected at very high scattering angles, in order to probe a wide range of reciprocal

space.[9] The resulting scattering data is processed and a Fourier transformation is applied. A model, fit to the PDF data, can be used to determine the probability of finding a pair of atoms separated by a specific distance. PDF can be measured *ex situ* or *operando* and can be used to analyze amorphous or crystalline materials. PDF measurements can usually be taken in parallel with sXRD. *In situ* PDF was used in Chapter 5 to observe the local ordering of a sodium transition metal layered cathode material.

1.2.4 X-ray Photoelectron Spectroscopy

X-ray photoelectron spectroscopy is a surface sensitive technique that can be used to measure the elemental composition, chemical formula, chemical state, and electronic state of a solid material.[10] The XPS spectra are obtained by irradiating a material's surface with a single wavelength of X-rays and measuring the resulting kinetic energies of the electrons emitted from the materials surface. This material is surface sensitive, with electrons emitted from the top 1-10 nm of the sample material. This phenomenon is called the photoelectric effect and follows the following equation:

Equation 1.2
$$E_{binding} = E_{photon} - (E_{kinetic} + \phi)$$

Where $E_{binding}$ is the binding energy of the measured electron, E_{photon} is the energy of the incident X-rays, $E_{kinetic}$ is the kinetic energy of the ejected electron, and ϕ is the work function which is dependent on the instrument. The resulting spectrum is the number of ejected electrons over a range of kinetic energies. Peaks in the spectra appear at characteristic energies that can be identified and quantified. The peaks can be fit to assign specific chemical species detected on the sample.

In this thesis, XPS was used to characterize the composition on the surface of cathode materials as well as the SEI of anode materials. Extra care was taken in the preparation of XPS

samples for characterizing the SEIs. Air free transfers of the samples were used for SEI analysis to prevent side reactions from occurring.

1.2.5 Scanning Electron Microscopy

Scanning electron microscopy (SEM) is an imaging technique that uses electron radiation to produce images with up to 0.5 nm resolution. The incident electron radiation can interact with a sample in multiple modes and be detected to provide a multitude of information. The two most common detection modes are described here: [11] **1) Secondary electrons:** This mode collects low energy secondary electrons (< 50 eV) ejected from the conduction/valence bands of a sample by inelastic scattering interactions with the incident electron beam. These electrons originate from within a few nanometers of the surface and provides topological information. **2) Backscattered electrons:** This mode collects high energy electrons that originate from the electron beam that are backscattered by the sample due to elastic scattering interactions with the sample's atoms. High atomic number elements backscatter electrons more strongly than low atomic number elements. Therefore, materials containing high atomic number elements appear brighter in the resulting image and can be used to detect regions with different elemental compositions.

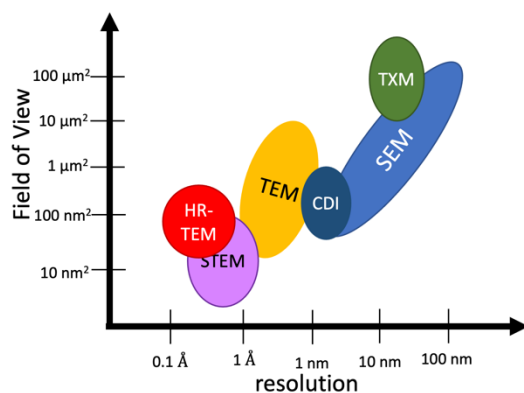


Figure 1.4: A diagram showing different characterization techniques comparing their field of view with their resolution.

SEM has a relatively large field of view compared to other imaging techniques (**Figure 1.4**), has easy sample preparation, and is available at many universities and national laboratories. Combined together, these aspects make SEM a favorable technique used to investigate battery materials. In addition, energy dispersive X-ray spectroscopy (EDS) can be used within and SEM machine. This allows for elemental identification and mapping. SEM was used in my thesis to identify the morphology of sodium cathode materials and the SEIs on the anode materials. EDS was used to observe the elemental distribution and relative amounts of SEIs on hard carbon anodes cycled with different electrolytes.

1.3 Thesis Outline

My PhD thesis consists of seven chapters, including this chapter that provides a general introduction to grid storage, battery components, motivation for NIB materials research, and the characterization tools used. Chapter 2 goes in depth about the applications, promises, and areas of improvement for NIBs. Chapter 3 focuses on a novel method for synthesizing sphere-like meso-structured sodium TM layered oxide cathode materials. The key parameter in controlling the meso-structure was the cooling rate. Chapter 4 evaluates the redox mechanisms of Fe and Mn in sodium TM layer oxide cathode materials using XAS and DFT. Chapter 5 combines advanced synchrotron characterization techniques to observe the redox and structural mechanisms during the first electrochemical cycle of $\text{Na}_{0.8}\text{Li}_{0.12}\text{Ni}_{0.22}\text{Mn}_{0.66}\text{O}_2$. Ni migration within the structure was found to hinder reversible oxygen redox activity. Chapter 6 explores the role of electrolytes on the first cycle coulombic efficiency and rate capability of hard carbon as an anode material for NIBs. This study revealed that the solid electrolyte interphase (SEI) controls both properties and that ether-based electrolytes form superior SEIs. Chapter 8 summarizes the overall work and presents ideas for future research.

2.1 Introduction

The past decade has seen dramatic reductions in levelized cost of energy (LCOE) for renewables such as wind and solar. This has allowed us to achieve grid parity against traditional fossil fuels in the United States (US) and many other parts of the world.[12] However, the widespread adoption of renewables has been consistently plagued by challenges of intermittency in supply and the inability to meet peak demand fluctuations especially when deployed in urban grids. As such, energy storage is vital to bridge the disconnect between renewables generation and distribution for consumption. While stationary storage such as pumped hydroelectric and compressed air exist, their lack of flexible form factors and lower energy efficiencies limit their scalable adoption for urban communities.[13,14] Thus, batteries are believed to be more practical for large scale energy storage capable of deployment in homes, cities, and locations far from the grid where the traditional electrical infrastructure does not reach.

Today's battery technologies are dominated by lithium ion batteries and lead acid batteries. While lithium ion batteries (LIBs) do well to serve emerging markets in electric vehicle and portable electronic devices, its deployment for large scale grid storage is still inhibited by high cost, low safety, and sustainability concerns.[14] Other alternatives that meets the combined properties of low cost, high performance and safety are urgently needed. In addition, methods of handling large volumes of spent batteries at their end-of-life have not been fully developed till date, resulting in the accumulation of battery waste that can potentially undo the environmental benefits it rightfully seeks to achieve. In terms of cost, decades of industrial commercialization have enabled prices of LIBs to tumble by more than an order of magnitude compared to when it

first entered the market. This was achieved through improvements in active (such as better electrode and electrolyte materials) and inactive components of LIBs (such as current collector, separator, packaging, etc.) combined with streamlining of manufacturing protocols to achieve economies of scale. However, production level optimization of LIBs today are approaching its saturation limit, where it is becomes increasingly clear that eliminating use of expensive elements such as Li, Co and Ni are vital to realize further reductions in cost per kWh ($\$/\text{kWh}$).^[15,16] Concerns of energy security and geopolitical considerations in supply chain also drive nations without local access to such materials to seek alternative chemistries to meet energy storage demands. As such, NIBs and its commercialization is slated to serve as one of the alternatives to LIBs for grid energy storage applications.

NIBs offer a host of benefits that include elemental abundance, low costs per kWh, and its environmentally benign nature. While NIBs are commonly perceived to exhibit inferior electrochemical performance compared to conventional LIBs, recent developments in high voltage sodium based cathodes with high capacity and high power capability are starting to challenge such notions. State of the art NIBs today can achieve volumetric energy densities close to conventional LIBs, making them competitive in the grid storage markets. Moreover, environmentally friendly NIBs can alleviate the growing battery waste problems exacerbated by accumulation of spent LIBs retrieved from end-of-life electric vehicles and portable devices, which could only worsen if conventional toxic LIBs are deployed at large scales to serve the grid. In the subsequent sections, we discuss the role of NIBs and how their features of low cost, good performance, and environmental sustainability can overcome obstacles faced in electrochemical grid energy storage and offer perspectives on future directions for research and development.

2.2 Discussion

While it might be intuitive to imagine grid storage as massive deployments of large container-like battery units sprawled across large open areas, current market trends in stationary storage reflect a different reality. Customer demands in stationary storage are starting to skew toward behind-the-meter type installations which typically cover households (kWh) to communal microgrids (MWh), compared with traditional utility scale installations of (GWh).[17,18] This has been driven by international pressure to reduce reliance on traditional energy sources such as nuclear and fossil fuels, incentivizing cities to install standalone renewables generation coupled with storage units within compact urban areas.[19,20] Such configurations allow businesses and consumers to utilize the existing electrical infrastructure for energy redistribution and avoid long range transmission losses from traditional generation plants. As a result, it would be naive to assume that energy density of battery installations is inconsequential when stationary storage in urban environments are considered. In fact, volumetric energy density (Wh L^{-1}) at the system level, is a key evaluation parameter to assess electrochemical grid storage technologies. **Figure 2.1(a)** compares the gravimetric energy density (Wh kg^{-1}) vs volumetric energy density (Wh L^{-1}) of various battery chemistries, with additional details provided in **Table A.1**. [21–29] Comparisons on relative costs and lifetime are also displayed for reference. For the same unit of energy, higher volumetric energy density indicates smaller devices, while higher gravimetric energy density represents lighter systems. Depending on their typical market applications, batteries are divided into four major regions in the figure. The upper right region (light and small batteries) is commonly used in electrical vehicles and personal devices, where portability is essential. On the opposite end, the left bottom region (heavier and larger batteries) is used for power tools or starters that do not require continuous operation. Batteries for drones and flight need to be light, but not necessarily very small; while batteries for stationary storage should take up as little space as possible, with

less regard for its weight. To address safety concerns of batteries that pose fire hazards, electrolyte types used in each system is also included in **Figure 2.1(a)**. [30–32] All-solid-state-batteries that utilize solid-state electrolytes in place of conventional flammable organic liquid electrolytes are believed to be a potential solution to address these safety concerns since they are intrinsically not flammable. [33,34] As such, sodium-ion batteries stand out as a competitive candidate for grid storage applications because of its suitable energy density, relatively low cost, and its potential to offer improved safety and long cycle life especially when solid state electrolytes are used.

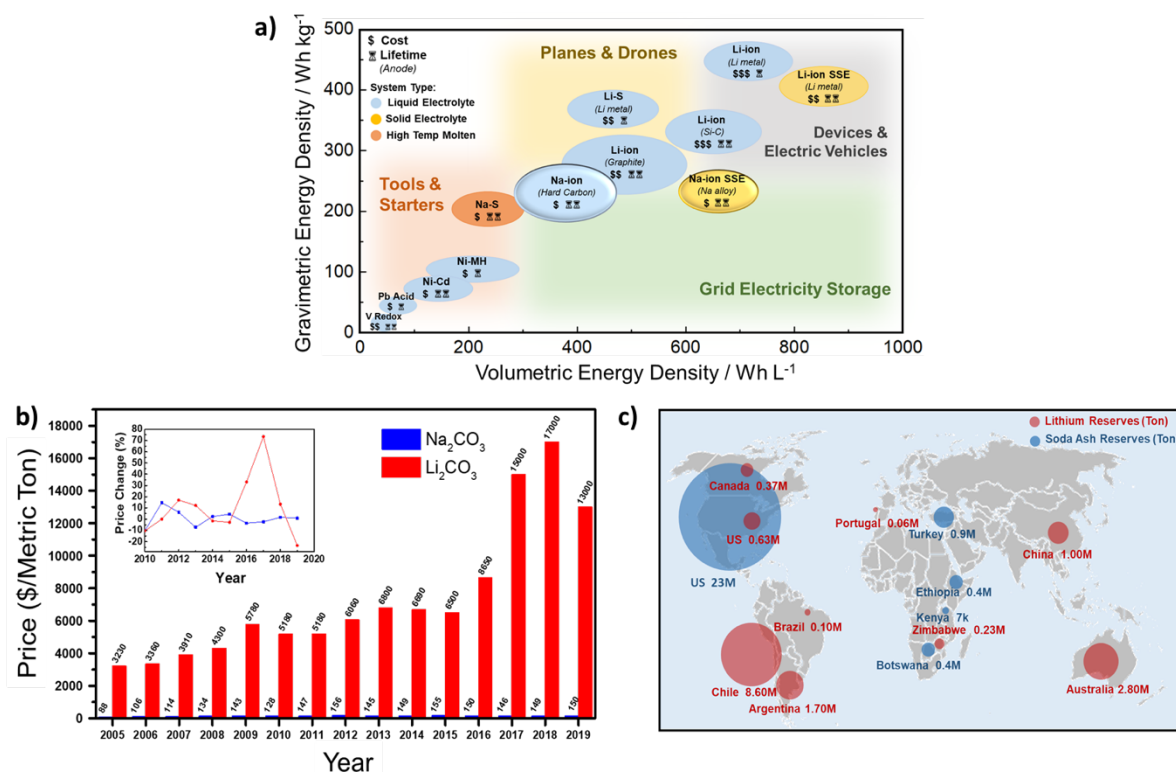


Figure 2.1: (a) Current electrochemical storage technologies gravimetric energy density versus volumetric energy density compared. (b) The price trend of sodium carbonate and lithium carbonate from 2005 to 2019. The inset is the percentage of price changes of both materials over the past 10 years. (c) A map of the Li reserves and Soda Ash (Na reserves) in the world reported in 2020. Li reserves are depicted by red circles and soda ash reserves are depicted by blue circles. The size of the circle represents the amount of reserves in metric tons. Brine is also a source of sodium and this is illustrated by the light blue color of the ocean.

Most battery materials today are synthesized from precursors using lithium carbonate (Li₂CO₃) and sodium carbonate (Na₂CO₃). Thus, price fluctuations in these raw materials can result in significant implications on the cell level costs of batteries per kWh. **Figure 2.1(b)**

compares the price trend of Li_2CO_3 and Na_2CO_3 over the past 15 years.[35–37] It is clearly shown that the prices of Na_2CO_3 are approximately 2 orders of magnitude lower than its lithium counterparts, with Li_2CO_3 at \$13,000 per metric-ton compared to Na_2CO_3 at \$150 per metric-ton in 2019. Additionally, the trend in prices also differ across both materials. Since 2010, the price of lithium carbonate has increased from \$5,180 per metric-ton to \$13,000 per metric-ton (a 151% increase); while the price of sodium carbonate only increased from \$128 per metric-ton to \$150 per metric-ton (a 17% increase). This has been largely attributed to the limited geographical availabilities in lithium mining sources that drive up prices as demand for batteries grow. By contrast, ubiquitous availability of sodium along with the mature soda ash mining industry keeps prices of Na_2CO_3 relatively stable for the foreseeable future. Economically, this makes NIBs a better choice over LIBs for applications in grid storage where market stability is crucial for both manufacturers and customers alike to make long term projections of profitability and utility.

Besides pricing and market considerations, the geopolitical concerns for lithium and sodium material sources should also be analyzed as well. **Figure 2.1(c)** depicts the global reserves of lithium and soda ash (a major sodium source) illustrated as circles (on a square root scale) corresponding to their actual reserve quantities.[35] Chile (8.6 million tons) and Australia (2.8 million tons) represents the top holders of lithium reserves and are the largest exporters by a significant margin. These are followed by Argentina and China, rounding out the top four, with no other countries coming close in lithium reserves around the world. The past century saw the political influence of key natural resources such as fossil fuels around the world, demonstrating the importance of energy security for growing economies. It is natural for lithium and other vital energy resources to play an equivalent or more significant role in future economic and geopolitical considerations. As a result, developing lithium alternatives such as NIBs are of great interest to

certain countries such as the United States, who holds the largest natural soda ash reserves in the world and is a major international supplier of soda ash as well. The current estimated natural soda ash reserve in the US is 23 million tons, allowing the US to benefit from reduced uncertainties in production and supply chain compared to other regions. Moreover, sodium is one of the most abundant elements in the world, making up 2.36% in the continental crust and 2.7% sodium salt salinity in seawater.[38,39] This availability potentially opens up alternative mining sources for sodium raw materials, and provide stable production supply to meet rapidly growing demands for energy storage.

Cathodes for NIBs are generally categorized in the following classifications: layered oxides, polyanion, and Prussian blue analogs (PBAs). The gravimetric and volumetric energy densities for these three types of cathode materials are shown in **Figure 2.1(a)** and **Table A.2**. [40–53] [54–88] [89–97] Polyanion and PBAs inherently have low volumetric energy densities due to low atomic packing density which makes them better suited for application in tools and starters. Layered oxide cathode materials have higher volumetric and gravimetric energy densities, making them more suitable for grid storage applications. Strategies to enhance the energy density of polyanions and PBA type cathodes include incorporating elements such as Ni, Co, and V to increase both the reversible capacities and nominal voltages delivered.[98,99] However, use of such rare elements would inadvertently diminish the cost advantages of NIBs. Additionally, the PBA synthesis process can be difficult to scale due to potential safety hazards involved, such as the release of cyanide containing fumes under heat and generation of toxic waste. [98,99] Amongst these major classes of cathodes, some layered oxides have been shown to exhibit some anionic redox behavior, serving as an additional source of reversible capacity from the same cathode material. During anionic redox, a reversible O^{2-} to O_2^{n-} transformation occurs during

electrochemical charge and discharge.^[13] Such oxygen activity have been reported in a variety of layered oxides such as Li/Mg substituted layered oxides (e.g. $\text{Na}_{0.6}\text{Li}_{0.2}\text{Mn}_{0.8}\text{O}_2$, $\text{Na}_{2/3}\text{Mg}_{0.28}\text{Mn}_{0.72}\text{O}_2$), Na deficient oxides (e.g. $\text{Na}_{4/7}\text{Mn}_{6/7}\text{O}_2$, $\text{Na}_{0.653}\text{Mn}_{0.929}\text{O}_2$), and 4d/5d transition metal containing oxides (e.g. Na_2RuO_3). [40–53] For these reasons, layered oxides are more commonly studied as cathode materials for NIBs and will be further evaluated in the next section.

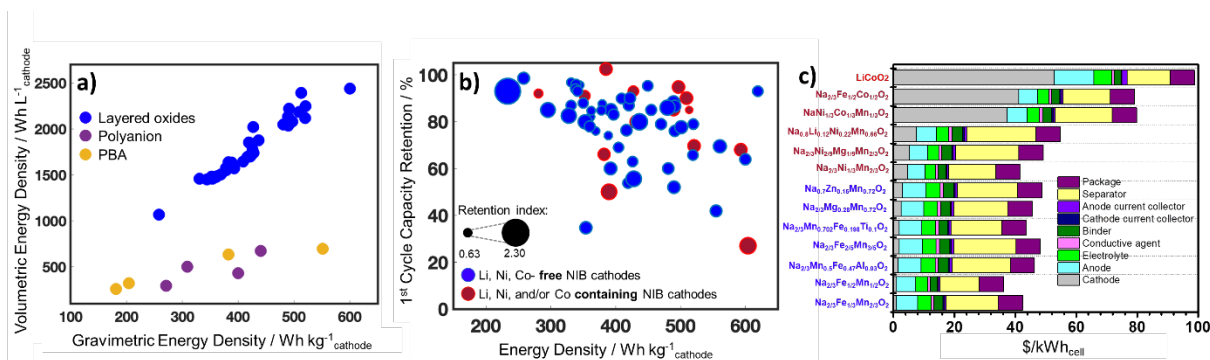


Figure 2.2: (a) Volumetric energy density (Wh/L) versus the gravimetric energy density (Wh/kg) are compared for differed types of sodium cathode materials. The blue circles are layered oxides, the purple circles are polyanion, and the yellow circles are PBA. (b) Capacity retention of the capacity versus first discharge energy density (Wh/kg) for layered cathode materials in Na-ion batteries. Blue circles are Li, Ni, Co-free sodium cathode materials and red circle are Li, Ni, and/or Co containing sodium cathode materials. The size of the circle represents the severity of the testing conditions using the calculated retention index (equation 2.1). (c) Price of energy (\$/kWh) at full cell level for selected sodium cathodes and a representative lithium cathode. The Li, Ni, Co-free sodium cathodes are labelled in blue and the ones that contain Li, Ni, and/or Co are labelled in red.

The costs and performance of layered oxide materials in both LIBs and NIBs are highly sensitive to chemistries chosen that make up its chemical structure. Most battery cathode materials today contain Li, Ni, and Co, collectively making up 44% of total LIB costs.[100] Unfortunately, expensive elements of Ni and Co are unavoidable to increase the performance (energy density and capacity utilization) of the lithium based cathode materials and are difficult to replace. However, this is not necessarily the case for sodium ion batteries. Sodium cathode materials free of these less-abundant earth elements can achieve equal or better performance than those using such elements in the transition metal oxides. These comparisons are shown in **Figure 2.2(b)**. [54–88]

[89–97] Due to the lack of standardized evaluation criterion for NIBs, it is difficult to assess different sodium cathode performances across the literature. Conventionally, cathodes are evaluated by their reported rate capabilities, number of cycles, and voltage ranges. Though equally important, electrolyte excess, cathode mass loading and testing temperatures are seldom reported. To this end, we defined a “retention index” (**Equation (2.1)**) that normalizes the reported number of cycles, voltage range, and C-rate (1C = discharge in 1 hour) in order to evaluate various sodium cathode electrodes reported in the literature thus far.

$$\text{Retention index} = \frac{\# \text{ of cycles}}{500} + \frac{(V_{\text{max}} - V_{\text{min}})}{3.5} + \left(\frac{\text{C rate}}{5} \right)^{0.5} \quad (2.1)$$

In **Figure 2.2(b)**, the retention index is represented by the size of the circles; a larger circle represents more aggressive testing conditions. Using this retention index, cathode capacity retention as a function of percentage (%) is plotted against the first cell discharge energy density for layered sodium cathodes reported in the literature (**Figure A1, Tables A.3 & A.4**). Only layered sodium cathode materials are included in this analysis, conversion or organic based cathodes are excluded from the analysis because there are fewer comparative studies on them.[101–103] Shown by the blue circles, sodium cathode materials free of Li, Co and Ni exhibit performances equal to or even exceeding those that contain Li, Ni, and/or Co with respect to energy density and retention. In terms of cost, Li, Ni, and Co-free sodium cathode materials exhibit significant advantages over other materials. As shown in **Figure A3**, the costs per kWh for $\text{Na}_{2/3}\text{Fe}_{1/3}\text{Mn}_{2/3}\text{O}_2$, a cathode material free of expensive earth elements is reported to be under 1 USD whereas Li and Ni containing cathode cost upwards of \$5/kWh (materials cost only). Prices can reach up to ~\$40/kWh when significant fractions of Co are used. When considering the differences in material performance and their influence in the needed amount of electrolyte/anode and other cell components, a detailed full cell level cost breakdown is presented in **Figure 2.2(c)**

with the supporting information presented in **Table A.5**. In this figure we estimated the cost to construct a full cell at 1 kWh energy level with different cathode materials. The analysis shows that the relative costs from other components carbon, binder, current collector, anode materials, and electrolytes in different cells are not significantly different. By contrast, the cathode price is the main determining factor influencing total cost. This analysis shows that sodium cathodes can achieve good electrochemical performance while keeping costs of materials low by avoiding the use of Li, Ni, and Co.

While layered oxides free of Co and Ni are ideal for grid storage, they still face challenges such as air sensitivity and sodium deficiencies which limit their potential commercialization. Layered oxides containing Fe and Mn tend to form impurities on the surface and risk water intercalation when stored in air, which can irreparably harm its electrochemical performance.[104,105] While moisture sensitivity can be avoided through use of dry environments during production, this would also result in increased manufacturing costs. Alternative strategies include use of protective coatings, TM substitution, and/or ethanol washing can be used to reduce the materials' air sensitivity. [104,105] With regards to sodium deficiency, cathodes with robust electrochemical performances (often layered oxides with P2 phases) tend to be 25-40% sodium deficient in their stoichiometry. This brings about challenges in full cell capacity matching especially under lean electrolyte conditions with a limited sodium reservoir. To mitigate such deficiencies, use of sacrificial salts such as NaN_3 , NaNO_2 , and EDTA-4Na have been studied and found to be promising in compensating sodium deficiencies in the cathode.[106–109] However, improved selection of salt chemistries are still required to mitigate continuous side reaction against the cathodes over cell cycling. [106–109]

Despite the prospects of low cost and high-performance sodium cathode materials, there are still fundamental obstacles to overcome at the cell level before NIBs can be commercialized for the grid. These are summarized as five root challenges in **Figure 2.3**; electrolyte robustness, anode material selection, interfacial stability (between electrodes and electrolytes), safety concerns, and battery recyclability at its end of life. **1)** While organic liquid electrolytes are commonly used in commercialized LIBs, its specific formulations along with optimized solvent, salt, and additives selection still has much room for improvement. As applications in grid storage require NIBs to perform well under a wide range of climatic and intermittent conditions, liquid electrolytes used would require wider operating temperature ranges in order to reduce costly thermal management requirements at the pack and system level. Likewise, cell level engineering and design needs to mitigate the possibility for potential liquid electrolyte leakage and gas evolution over much longer operating lifetimes in stationary storage compared to LIBs used in portable devices. Investigating new systems of electrolytes that have the potential to increase lifetime, such as ionic liquids and solid state electrolyte have led to promising results.[110,111] **2)** As graphite based anode materials in LIBs cannot be used in NIBs, alternative carbon based materials such as hard carbon are often used in NIBs due to its relatively high sodium capacity and chemical potentials close to sodium metal.[112] Moreover, hard carbon is commonly produced from various biomass materials (ex: mangosteen shells[113], sugar[114,115], pomelo peels[116], shaddock peels[117], peanut shells[118], cellulose[119], corn cobs[120], cotton[121], macadamia shells[122], and wood[123]), offering environmental benefits through its secondary usage in NIBs. However, hard carbon still exhibits low first cycle coulombic efficiencies resulting from sodium consumption to form the solid electrolyte interface, keeping reversible capacities low. While the use of sacrificial salts have been shown to mitigate coulombic efficiency losses[108,124] resolving

the performance challenges of hard carbon is still impeded by a poor understanding of its sodium storage and degradation mechanisms.[112,125,126] Alternative anode materials for NIBs can be explored instead, such as the use of metallic sodium or metallic sodium alloys (Sn, Sb) that possess higher storage capacities and chemical potentials compared to hard carbon.[127,128] Although metallic anodes have issues with stability and large volume changes, they also have the potential to drastically increase volumetric energy densities of NIBs due to their dense packing and high mass density. To utilize the benefits of both systems, composites of carbon-based storage together with high capacity metallic anodes may serve as a promising compromise in future NIB anode electrode materials.

3) Designing and optimizing stable interfaces between the electrolyte and anode/cathodes respectively are vital for NIBs to serve grid storage over decades of operation. Interfacial degradation and continuous SEI/CEI growth can result in increased cell impedance overtime which can detrimentally affect the battery's rate capability. Additionally, continuous interface reactions can cause low coulombic efficiencies that will severely limit a battery's lifetime. Strategies to address this include selecting electrolyte formulations with improve thermodynamic stabilities against the anode/cathode or by controlling the kinetics of degradation by incorporating a highly stable coating on the electrodes.[15,129–131]

4) Certain battery safety hazards reported in portable devices can bring about some inconveniences and potential minor injury to individual users. However, the dangers of battery fires and explosions would be more catastrophic at the grid scale, with potential for costly property damage and loss of lives.[132] Safety should be highly considered in battery grid storage design with considerations made for its components and geometry. It is encouraging that some reports on NIBs show that they can be safer than conventional LIBs due to its material's superior thermal

stabilities.[133] Nonetheless, ideal battery systems deployed at the large scale near densely populated urban grids still need to completely eliminate fire and explosions risks. A promising pathway to achieve this is through the adoption of nonflammable solid-state electrolytes to replace the flammable organic liquid electrolytes, forming sodium based all solid-state batteries. All solid-state batteries are also stable and can operate over a wide range of temperatures, potentially enabling their operation under extreme weather conditions without the need for sophisticated thermal management. [110,111] Such configurations also allow the adoption of high voltage cathodes without risk of liquid electrolyte leakage or gas evolution over extended cell cycling.

5) Battery recycling: it would be hypocritical for proponents of NIB adoption to combat climate change, to not consider how to deal with NIBs at its end of life. LIBs today are facing a rapidly growing battery waste problem, with most batteries not designed for recycling. While it might be too late for incumbent LIB manufacturers to change their manufacturing protocols, potential battery recycling strategies for future NIBs manufacturers should be developed to achieve safe and sustainable disposal of large volumes of spent batteries. Fortunately, new recycling processes are currently being researched based on the principles of direct recycling, allowing battery materials to be processed with reduced energy costs and limited waste generation.[134][135][136][137] However, any effective sustainable strategies would require the co-operation of both manufacturers and policy makers alike, and be regulated to include labelling of their chemical classifications that allow ease of sorting based on their core materials for recycling. This is especially crucial in grid storage batteries due to their large variations in battery chemistries compared to LIBs and longer intended lifespans that potentially forces companies to handle decades old battery packs.

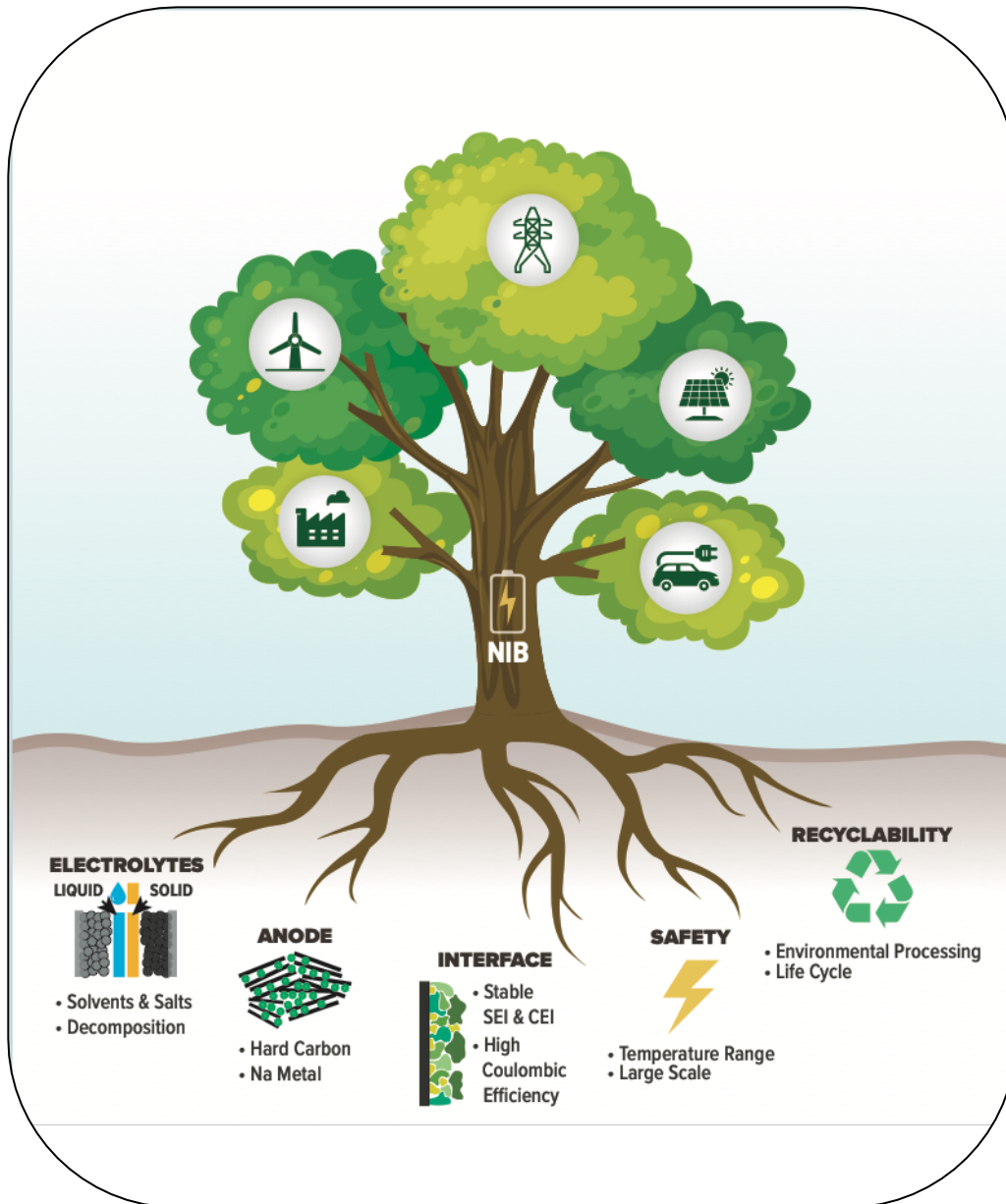


Figure 2.3: The root scientific challenges (bottom) of sodium-ion batteries that need to be overcome to support sustainable, safe, large scale energy storage applications (top).

2.3 Conclusion

Sodium ion batteries (NIBs) and its development shows great promise for grid energy storage applications as an alternative to conventional lithium ion batteries (LIBs). Metrics of energy density, cost, and lifetime are compared across various battery chemistries, where NIBs are surmised as front runners to meet the needs of the grid storage market. Its relative material

abundance and ability to deliver good electrochemical performance without use of expensive earth elements are the main drivers of low costs per kWh. Concerns for supply chain reliability and energy security are also discussed where materials availability are considered. Fundamental obstacles toward commercialization include electrolyte composition, anode performance, electrode-electrolyte interfacial stability, safety hazards, and sustainable recyclability are analyzed, along with discussions for potential solutions to tackle them. However, to truly enable NIBs for grid storage, it would require the scientific community to shift development efforts beyond the academic level toward applied research, supported by investments and inputs from the industry to enable a concerted push toward practical cell/pack level testing and evaluation similar to what LIBs have achieved over the past four decades. Ultimately, today's NIBs may or may not be the *perfect* solution for every challenge faced by grid-scale energy storage, but it will certainly have far-reaching impacts in enabling renewable energy storage and distribution to improve our electrical grid's resilience and reduce humankind's reliance on traditional fossil fuels.

Chapter 2, in full, is a reprint of the material, "Sodium-Ion Batteries Paving the Way for Grid Energy Storage" as it appears in *Advanced Energy Materials*, H. S. Hirsh, Y. Li, D. H. S, Tan, M. Zhang, E. Zhao, Y. S. Meng, 2020, 10, 2001274. The dissertation author was the co-primary investigator and author of this paper. The author collected and analyzed the data and cowrote the paper.

3.1 Introduction

Solar and wind as sustainable and renewable energy sources have attracted considerable attention in recent years. To expand the generation of electrical energy from these highly intermittent energy sources in nature, large-scale inexpensive energy storage has gained great interests from the scientific and community at large.[14] Batteries are considered as the most promising technology for next-generation grid storage due to their high energy density, low operation cost, and long cycle life. Among all the state-of-the-art batteries, Na-ion batteries (NIBs) have a tantalizing possibility for commercial grid storage, by reason of the abundant availability of its sources and the suitable redox potential ($E_{(\text{Na}^+/\text{Na})} = -2.71 \text{ V vs. SHE}$).[100]

Various types of NIB cathode materials have been investigated in the past few decades including layered oxides, poly-anionic frameworks, hexacyanoferrates, and organics[48,138–142] Among these cathode materials, layered oxide materials Na_xTMO_2 (TM=Mn, Co, Fe, Ni, Ti, Cu, Cr or mixtures of the elements) are one of the most favorable candidates due to their large capacities and tunable properties. [138] In the wide range of choices for TM in sodium layered oxides, Li, Ni, and Co are rather expensive elements while Fe and Mn are low-cost and abundant. For NIBs to be viable, the components of the cathode material should include only inexpensive elements in the ideal case. Sodium iron manganese oxides $\text{Na}_x\text{Fe}_{1-y}\text{Mn}_y\text{O}_2$ have already shown promising initial discharge capacities.[143] For example, P2-type layered $\text{Na}_{2/3}\text{Mn}_{1/2}\text{Fe}_{1/2}\text{O}_2$ and $\text{Na}_{2/3}\text{Fe}_{1/3}\text{Mn}_{2/3}\text{O}_2$ are able to deliver first discharge capacities of 200 mAh/g in the voltage range 1.5-4.3 V (vs. Na^+/Na^0).[143] However, the practical and commercial applications of $\text{Na}_x\text{Fe}_{1-y}\text{Mn}_y\text{O}_2$ are hindered because of their poor capacity retention over cycling.[100]

Previous studies have identified several factors contributing to this poor capacity retention, including irreversible phase changes, particle defects and particle pulverization.[143] Correspondingly, modification strategies including TM substitution and surface coating have been put forward to improve the cycling performance.[15,16,144] These two approaches often involve either complex synthesis processes such as atomic layer deposition, or introduce costly elements such as Co and Ni.[15,16,144] Meso-structure control synthesis, on the other hand, can reduce the occurrence of both irreversible phase change and particle pulverization without significant process adaptation.[145,146] As demonstrated in lithium ion batteries, micron sized spherical meso-structures consisting of nanosized primary particles could enable faster Li ion diffusion and at the same time provide enhanced particle strain management, thus mitigating mechanical degradation and improving capacity retention. [145–156]

The synthesis method strongly influences the meso-structure of the layered TM oxides. In reviewing the literature (**Table 3.1**),[55,56,84,85,87,157–163] solid-state synthesis is the most frequently adopted method for $\text{Na}_x\text{Fe}_{1-y}\text{Mn}_y\text{O}_2$. However, the meso-structure is difficult to control in the solid-state synthesis since it entails mixing materials by either ball milling or hand grinding precursors followed by high temperature calcination, producing irregular or plate-like primary particles. Similarly, no meso-structure controlled samples were found in previous work via auto-combustion and sol-gel synthesis methods.[157,162,163] The co-precipitation method, which is commonly used to synthesize spherical secondary particles for lithium TM oxides, was not previously reported to obtain meso-structure controlled $\text{Na}_x\text{Fe}_{1-y}\text{Mn}_y\text{O}_2$ (**Table 3.2**).[56,149,158,164] In the cases where co-precipitation method was applied for sodium iron manganese oxides, the resulting materials were plate-like.

Table 3.1: Synthesis parameters for sodium iron manganese oxide cathode materials reported from literature.

Composition	Phase	Synthesis type	Mn precursor	Fe precursor	Na precursor	Calc. Temp (C)	Calc. time (h)	quenched?	atm?	morphology	citation
Na _{2/3} Fe _{1/2} Mn _{1/2} O ₂	P2	Solid State	Mn ₂ O ₃	Fe ₂ O ₃	Na ₂ O ₂	900	12	Y	air	irregular	[87]
Na _{2/3} Fe _{1/3} Mn _{2/3} O ₂	P2	Solid State	Mn ₂ O ₃	Fe ₂ O ₃	Na ₂ O ₂	900	12	Y	air	irregular	[85]
Na _{2/3} Fe _{1/2} Mn _{1/2} O ₂	P2	Solid State	C ₄ H ₆ MnO ₄ x4H ₂ O	C ₆ H ₅ O ₇ Fe _x H ₂ O	Na ₂ CO ₃	800	8	Y	air	plates	[84]
Na _{0.67} Mn _{0.5} Fe _{0.5} O ₂	P2	Solid State	Mn ₂ O ₃	Fe ₂ O ₃	Na ₂ CO ₃	750, 900	4, 6	N	air	irregular	[55]
Na _{0.67} Mn _{0.5} Fe _{0.5} O ₂	P2	Solid State	Mn ₂ O ₃	Fe ₂ O ₃	Na ₂ CO ₃	900	12	N	air	irregular	[159]
Na _{0.67} Mn _{0.5} Fe _{0.5} O ₂	P2	Solid State	Mn ₂ O ₃	Fe ₂ O ₃	Na ₂ CO ₃	450, 900	6, 15	N	air	Irregular	[160]
Na _{2/3} Fe _{1/2} Mn _{1/2} O ₂	O3	Solid State	Mn ₂ O ₃	Fe ₂ O ₃	Na ₂ O ₂	700	36	Y	air	irregular	[87]
NaFe _{0.5} Mn _{0.5} O ₂	O3	Solid State	Mn ₂ O ₃	Fe ₂ O ₃	Na ₂ CO ₃	900	24	N	air	unknown	[161]
NaFe _{0.5} Mn _{0.5} O ₂	O3	Solid State	Mn ₂ O ₃	Fe ₂ O ₃	Na ₂ CO ₃	700	36	N	air	irregular	[159]
Na _{2/3} Fe _{1/2} Mn _{1/2} O ₂	P2	Autocombustion	Mn(NO ₃) ₂ x4H ₂ O	Fe(NO ₃) ₃ x9H ₂ O	NaNO ₃	1000	6	N	air	plates	[162]
Na _{0.81} Fe _{0.5} Mn _{0.5} O ₂	O3	Autocombustion	Mn(NO ₃) ₂ x4H ₂ O	Fe(NO ₃) ₃ x9H ₂ O	NaNO ₃	700, 1000	20, 5	Y	O ₂	irregular	[163]
Na _{0.77} Fe _{2/3} Mn _{1/3} O ₂	O3	Autocombustion	Mn(NO ₃) ₂ x4H ₂ O	Fe(NO ₃) ₃ x9H ₂ O	NaNO ₃	700, 1000	20, 5	Y	O ₂	irregular	[163]
Na _{0.77} Fe _{2/3} Mn _{1/3} O ₂	P2	Autocombustion	Mn(NO ₃) ₂ x4H ₂ O	Fe(NO ₃) ₃ x9H ₂ O	NaNO ₃	700, 1000	20, 5	Y	O ₂	plates	[163]
Na _{0.67} Mn _{0.5} Fe _{0.5} O ₂	P2	Autocombustion	Mn(NO ₃) ₂ x4H ₂ O	Fe(NO ₃) ₃ x9H ₂ O	NaNO ₃	700, 1000	20, 5	Y	O ₂	plates	[163]
Na _{2/3} Fe _{1/2} Mn _{1/2} O ₂	O3	co-precipitation	Mn(NO ₃) ₂	Fe(NO ₃) ₃	NaOH	700	1	N	air	plates	[56]
Na _{2/3} Fe _{1/2} Mn _{1/2} O ₂	P2	co-precipitation	Mn(NO ₃) ₂	Fe(NO ₃) ₃	NaNO ₃	900	6	N	air	plates	[56]
Na _{2/3} Fe _{1/2} Mn _{1/2} O ₂	P2	Sol-Gel	Mn(CH ₃ COO) ₂	Fe(NO ₃) ₃ x9H ₂ O	NaNO ₃	900	12	N	O ₂	plates	[157]
Na _{0.67} Mn _{0.6} Fe _{0.4} O ₂	P2	acetate decomposition	Mn(Ac) ₂	Fe(Ac) ₂	NaAc	450, 900	7, 12	N	air	plates	[158]

Table 3.2: Co-precipitation synthesis parameters of iron containing sodium TM oxides cathode materials reported from literature.

Composition	Phase	Precursor type	Mn precursor	Fe precursor	Na precursor	Other precursor	Morphology	pH	citation #
Na _{2/3} Fe _{1/2} Mn _{1/2} O ₂	P2	-	Mn(NO ₃) ₂	Fe(NO ₃) ₃	NaNO ₃	-	plates	10	[56]
Na _{2/3} Fe _{1/2} Mn _{1/2} O ₂	O3	-	Mn(NO ₃) ₂	Fe(NO ₃) ₃	NaOH	-	plates	10	[56]
NaNi _{0.2} Fe _{0.55} Mn _{0.25} O ₂	O3	oxalate	MnSO ₄ ·H ₂ O	FeSO ₄ ·7H ₂ O	Na ₂ CO ₃	(NH ₄) ₂ C ₂ O ₄ , NiSO ₄ ·6H ₂ O, NH ₄ OH	irregular	7	[164]
NaNi _{1/3} Fe _{1/3} Mn _{1/3} O ₂	O3	oxalate	MnSO ₄ ·H ₂ O	FeSO ₄ ·7H ₂ O	Na ₂ CO ₃	NiSO ₄ ·6H ₂ O, Na ₂ C ₂ O ₄	unknown	-	[165]
NaNi _{1/3} Fe _{1/3} Mn _{1/3} O ₂	O3	hydroxide	MnSO ₄ ·H ₂ O	FeSO ₄ ·7H ₂ O	Na ₂ CO ₃	NaOH, NH ₃ , NiSO ₄ ·6H ₂ O	plates	10.5	[149]

In this study, pure phase P2-type Na_{0.67}Fe_{1/4}Mn_{3/4}O₂ with a spherical meso-structure was synthesized through modified co-precipitation method for the first time. To enable the formation of the desired meso-structure Na_{0.67}Fe_{1/4}Mn_{3/4}O₂, spherical precursors Fe_{1/4}Mn_{3/4}CO₃ were synthesized under optimized conditions such as suitable pH value and N₂ atmosphere. It is found that cooling rate played an important role in controlling the meso-structures of the final product.

A pure phase P2-type $\text{Na}_{0.67}\text{Fe}_{1/4}\text{Mn}_{3/4}\text{O}_2$ was made into hexagonal plates with no secondary structure by quenching or into a spherical meso-structure by slow-cooling. The formation of meso-structure enables fast Na diffusion as well as a reduced surface concentration of sodium carbonate which lowers resistance during cycling. Both features can effectively minimize capacity loss of sodium layered oxides during long-term cycling. This comparison of different morphologically controlled samples will determine a future direction of designing improved NIB cathode materials.

3.2 Methods

Materials preparation

The synthesis set-up for pure phase P2- $\text{Na}_{0.67}\text{Fe}_{1/4}\text{Mn}_{3/4}\text{O}_2$ (NFMO) is shown in **Figure 3.1**. Stoichiometric amounts of the precursors, $\text{Fe}(\text{SO}_4)\cdot 7\text{H}_2\text{O}$ and $\text{Mn}(\text{SO}_4)\cdot \text{H}_2\text{O}$ (Fe:Mn = 1:3 in molar ratio) were dissolved in deionized water for a total concentration of 3 M. TM sulfate solution and an aqueous solution of 0.2 M Na_2CO_3 were separately pumped into a reaction vessel to maintain the pH value at 8.8. The reaction was stirred continuously with N_2 bubbled through the reaction vessel. The obtained mixture was aged at 80°C for 12 hours. The resulting $\text{Fe}_{1/4}\text{Mn}_{3/4}\text{CO}_3$ was washed with deionized water to remove residual Na^+ and dried at 80°C overnight. $\text{Fe}_{1/4}\text{Mn}_{3/4}\text{CO}_3$ powder was then mixed with a 5% excess stoichiometric ratio of Na_2CO_3 and the mixture was calcinated at 900°C for 15 hours in air. For quenched samples, the crucible was taken out of the furnace directly after the 15 hours calcination and cooled in air on a metal plate. For the slow-cooled samples, after the 15 hours calcination time the furnace was set to cool down to room temperature over 12 hours.

Materials Characterization

The crystal structures were characterized by X-ray diffraction (XRD) using a Bruker D8

advance diffractometer with copper $K\alpha$ source or Mo $K\alpha$ source. Rietveld refinement was applied to the obtained diffraction pattern using FullProf software. The morphology and meso-structure of the particles were identified by using a Zeiss Sigma 500 scanning electron microscope (SEM) with an accelerating voltage of 1 kV for the carbonate precursors and 3 kV for the TM oxides. Surface area of the particles was determined using nitrogen physisorption by the Brunauer–Emmett–Teller (BET) method. ICP-OES was performed using a Perkin Elmer 3000 DV optical emission plasma spectrometer. X-ray photoelectron spectroscopy (XPS) was performed using an AXIS Supra by Kratos Analytica. The XPS was operated using an Al anode source at 15 kV, scanning with step size of 0.1 eV and 200 ms dwell time. Fits of the XPS spectra were performed with CasaXPS software to estimate the oxidation states of the TMs. Sodium carbonate titration was performed by washing 1 g of cathode material with 10 mL of DI water. The resulting solution was separated from the powder by filtration. The surface contamination content was determined using a titration method with 0.05 M HCl. The titration was monitored with a pH probe to an end pH of 8.0. Electron microscopy work was carried out on a JEOL-2800 TEM/SEM microscope. TEM images were acquired at 200 kV.

Electrochemical Characterization

Composite cathode electrodes were prepared by mixing a slurry of active material, acetylene carbon black, and polyvinylidene fluoride (PVDF) in a weight ratio of 8:1:1, with *n*-methyl-2-pyrrolidone. The slurry was cast onto aluminum foil and dried under vacuum at 80°C overnight. Na metal was used as the counter electrode with 1 M NaPF₆ in PC as the electrolyte and glass fiber GF/D (Whatman) as the separator. The electrodes were assembled in 2032 coin cells in an argon filled glove box ($H_2O < 0.1$ ppm) and tested on an Arbin battery cycler. Coin cells were allowed to rest 8 h before electrochemical tests were performed. The voltage range was maintained

between 1.5-4.3 V and C-rates were calculated by assuming a theoretical specific capacity of 120 mAh/g. Additionally, electrochemical spectroscopy (EIS) measurements were carried out with 10 mV perturbation and AC frequencies from 0.01 to 1×10^6 Hz on galvanostatic cycled electrodes charge to 3 V, 4.3 V and discharged to 3 V, and 1.5 V during the first cycle. A Solartron 1287 Potentiostat was used to measure impedance at different states of charge. An equivalent circuit model was used to fit the data and analyze the reactions using Zview software (v. 3.4a, Scribner Associates, Inc.).

Computational Study

Electronic structure calculations were performed within the framework of periodic planewave density functional theory (DFT) using the Vienna ab initio Simulation Package (VASP.5.4.4) for three different Na/Fe/Mn/O based model cathode systems. Both GGA+U and hybrid density functionals were employed for Density of States (DOS) calculations. The GGA+U calculations employed the spin-polarized Perdew-Burke-Ernzerhof (PBE) exchange-correlation functional with the projector-augmented wave (PAW) scheme to treat core electrons. For the +U augmented treatment of Fe and Mn 3d orbitals, we chose U_{eff} values given on the Materials Project of 5.3 eV for Fe and 3.9 eV for Mn. The corresponding U_{eff} values for Fe and Mn capture the $\text{Fe}^{2+}/\text{Fe}^{3+}$ and $\text{Mn}^{2+}/\text{Mn}^{4+}$ redox couple, respectively, in transition metal oxides. The PAW pseudopotentials employed for the transition metal atoms Fe and Mn (denoted as Fe_pv and Mn_pv, respectively) treat p semi-core states as valence states. The Na_sv pseudopotential used for Na treats the 2s shell as valence states. The standard pseudopotential was used for oxygen. Anti-ferromagnetic coupling between magnetic Fe and Mn cations was assumed. A planewave energy cutoff of 600 eV was employed in all calculations. Cell relaxation calculations (ISIF=3) at the PBE+U level plus Grimme's D3 dispersion correction on the Na/Fe/Mn/O bulk structures were

performed using a 10^{-4} eV energy convergence criterion with a $5 \times 5 \times 3$ k-point grid. In order to obtain a high-accuracy electronic DOS, the Heyd–Scuseria–Ernzerhof (HSE06) hybrid functional with 25% exact exchange was used for single-point energy calculations on PBE+U-D3 optimized structures. The single-point energy DOS calculations were performed using a 10^{-5} eV energy convergence criterion with a $12 \times 12 \times 6$ k-point grid for PBE+U calculations and a $4 \times 4 \times 2$ k-point grid for HSE06 calculations. To obtain a high-resolution DOS within an energy window bracketing the Fermi level, we set the energy range for evaluation of the DOS to -10 eV to $+10$ eV with 2001 grid points (EMIN=-10; EMAX=10; NEDOS=2001).

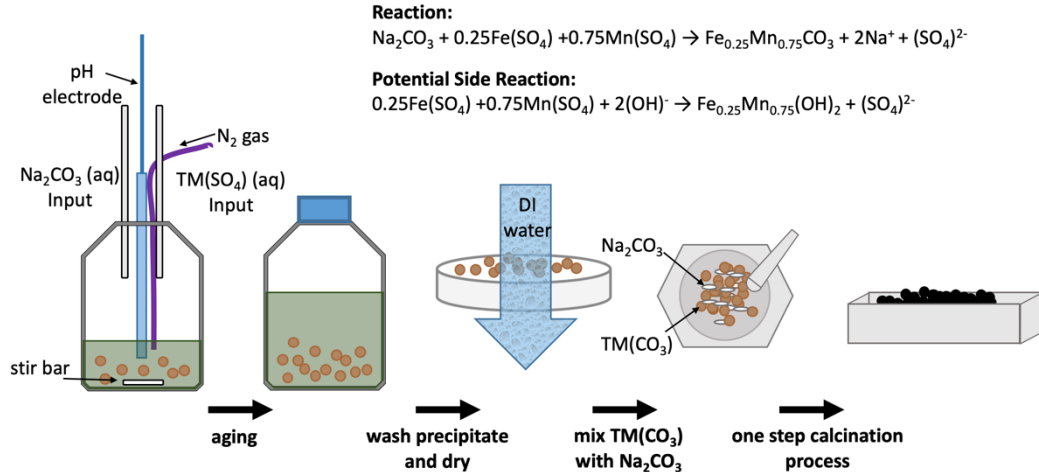


Figure 3.1: Schematic of the modified co-precipitation synthesis process for meso-structure controlled sodium iron manganese oxide.

3.3 Results and Discussion

The co-precipitation method for pure phase meso-structure controlled NFMO begins with obtaining a spherical TM carbonate precursor without hydroxide or other impurities. Two factors, pH value and nitrogen bubbling, are critical to synthesize pure phase carbonate precursor with desired TM ratio (see **Appendix B** for details). In short, residual TM ions will be found if the solution is too acidic, and hydroxide impurities will form if the co-precipitation occurs without nitrogen bubbling. A pure carbonate precursor was finally obtained with pH controlled at 8.8 and

continuous N₂ bubbling through the reaction vessel. After high temperature calcination, NFMO samples were either quenched or slow-cooled to obtain the final product. **Figure 3.2** shows a comparison between the quenched and slow-cooled NFMO including XRD data, SEM images, and a table of parameters including XRD refinement results, BET surface area, and ICP-OES measurements. In both samples, all the diffraction peaks can be well indexed to space group *P6₃/mmc*. The Rietveld refinement results confirm that both samples are pure phase P2 layered material with similar lattice parameters. According to a classification by Delmas et al., P2-type layered structure has ABBA oxygen stacking sequence where Na ions are located in trigonal prismatic (P) sites.[166] The ICP-OES results show that both samples have the same designed stoichiometric ratio. These results quantitatively reveal that NFMO samples synthesized by different cooling rate are similar in terms of bulk structure and chemical composition.

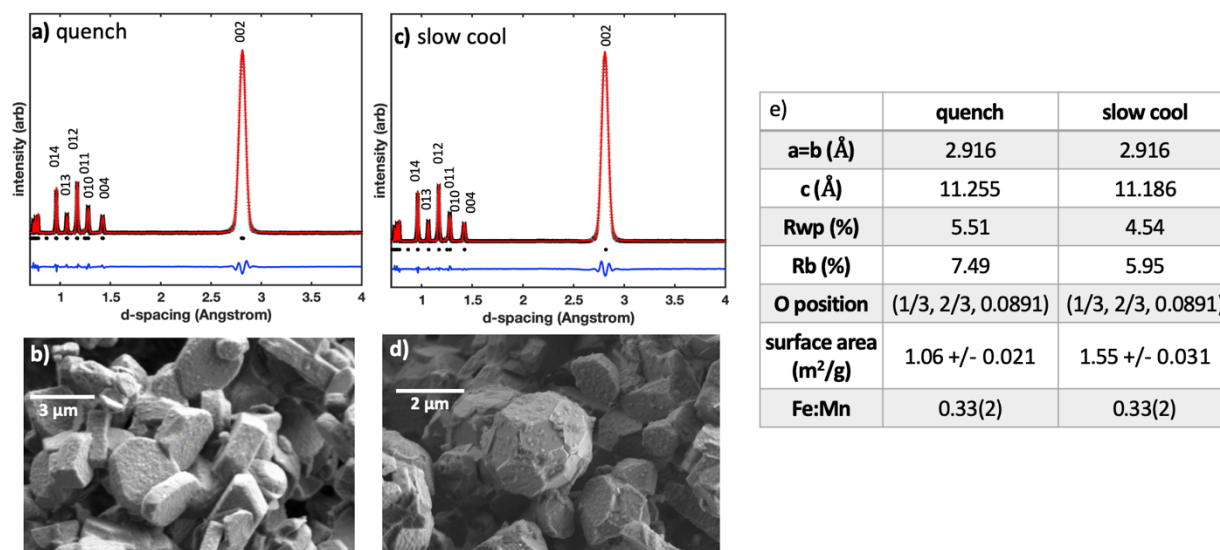


Figure 3.2: XRD and SEM of quenched NFMO (a, b) and slow-cooled NFMO (c, d) show that the two materials have the same crystal structure but different morphology and meso-structures. Selected parameters from XRD refinement, BET, and ICP measurements for the two materials are shown in (e).

The main differences between the two samples are the different meso-structures and specific surface areas. As shown in **Figure 3.2 (b)** and **(d)**, the quenched NFMO contains

hexagonal plate-like particles that are 1-5 μm in diameter and less than a micron thick. While the slow-cooled NFMO has a well-controlled meso-structure containing ~ 500 nm hexagonal plate-like primary particles and 2-3 μm secondary sphere-like particles (**Figure B.5**). It is hypothesized that the quenched material retained too much stress which leads to breakdown of the spherical particles, although we cannot exclude other possibilities. Further experiments are in progress to explore the relationship between cooling rate and meso-structure formation in NFMO. The specific surface area of both samples was also determined by BET adsorption measurements. Plate-like NFMO sample has a specific surface area of 1.06 ± 0.021 m^2/g , while meso-structure controlled NFMO has a higher number of 1.55 ± 0.031 m^2/g . The higher surface area of slow cooled NFMO can be attributed to smaller primary particle size and porosity between primary particles.

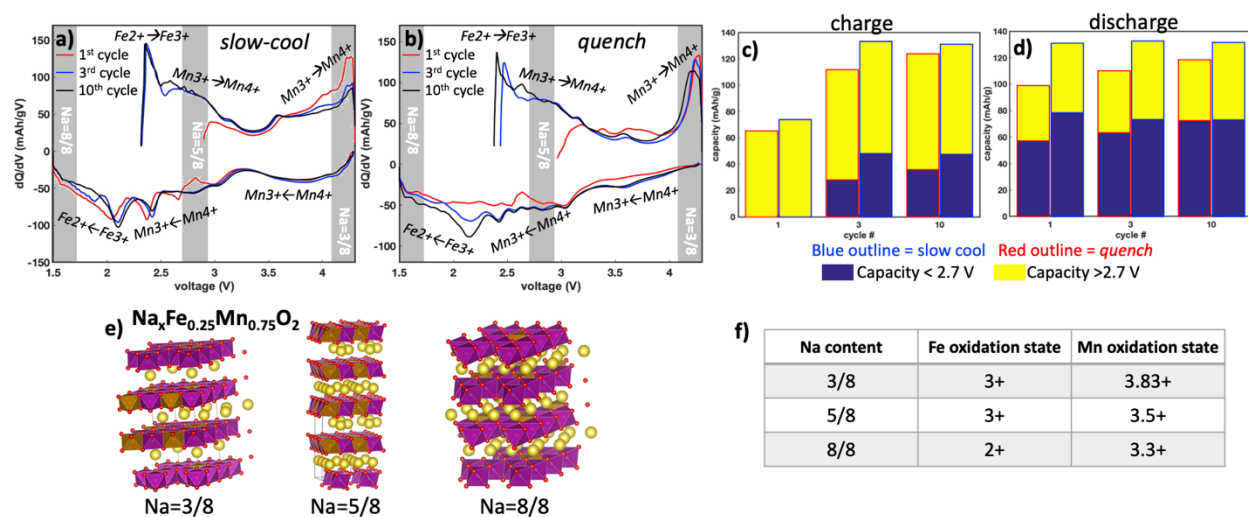


Figure 3.3: dQ/dV curves of the 1st, 2nd, and 10th cycles of slow-cooled (a) and quenched (b) NFMO at a rate of $C/50$. Bar graphs representing the charge (c) and discharge (d) capacities between 1.5-2.7 V and 2.7-4.3 V at different cycles for slow-cooled and quenched NFMO. Model structures of $\text{P2-Na}_x\text{Fe}_{0.25}\text{Mn}_{0.75}\text{O}_2$, where $x=3/8$, $5/8$ and $8/8$ (e) were used to calculate average Fe and Mn oxidation states of their respective structures (f).

To probe the mechanisms of sodium intercalation/deintercalation from NFMO, dQ/dV studies were coupled with DFT calculations of the TM oxidation states in NFMO at different states of charge (see **Figure 3.3**). In pristine NFMO ($\text{Na}=5/8$), DFT predicts the average oxidation states for Fe and Mn are 3+ and 3.5+ respectively, determined by the magnetization output. When 2/8

Na are removed from the pristine structure, representing the first charge state, the calculated capacity is 65 mAh/g. This value for the first charge matches well with the experimental value for both quenched and slow-cooled NFMO (**Figure 3.3 (c)**). The Fe oxidation state does not change during this first charge while the average Mn oxidation state changes from 3.5+ to 3.83+, which indicates that solely Mn is redox active. When discharging NFMO from fully charged state (Na=3/8) to the fully discharged state (Na=8/8), the total calculated discharge capacity is 163 mAh/g. This calculated discharge capacity is larger than the experimental capacity for quenched and slow-cooled NFMO shown in **Figure 3.3 (d)**. During the discharge to Na=8/8, Fe is calculated to reduce from 3+ to 2+ and Mn is calculated to reduce from 3.5+ to 3.3+. In the model when Na=8/8 (**Figure 3.3 (e)**), 4/18 Mn 3+ atoms are calculated to be in the high spin state, signifying they are Jahn-Teller active. If these four Mn atoms do not reduce to the 3+ state, the discharge capacity is reduced by 32.5 mAh/g, resulting in the calculated discharge capacity to be 131 mAh/g. This discharge capacity matches the experimental 10th discharge capacity of slow-cooled NFMO, suggesting that this model is a valid representation of the NFMO system. Additionally, the good cycling retention for NFMO (**Figure 3.4 (c, d)**) can be attributed to the fact that all the Mn 3+ in this system are not Jahn-Teller active.

From DFT calculations of NFMO at different states of charge, the TM redox can be attributed to different regions of the dQ/dV curve. In the high voltage region (Na=5/8 to Na=3/8) only the Mn 3+/4+ redox couple is active while in the low voltage region (Na=5/8 to Na=8/8) both the Fe 2+/3+ and Mn 3+/4+ redox couples are active (see pDOS in **Figure B.6**). The low voltage peaks in the slow-cooled NFMO dQ/dV (**Figure 3.3 (a, b)**) are initially larger than the peaks in the quenched NFMO dQ/dV. This indicates that the Fe redox couple is initially more active for slow-cooled NFMO than for quenched NFMO and is corroborated by the larger capacity in the

low voltage region (1.5-2.7 V) for slow-cooled NFMO (**Figure 3.3 (c, d)**). Additionally, for the quenched NFMO, the low voltage peaks in the dQ/dV curve increase in size and the capacity from the low voltage region increases from the 1st cycle (discharge capacity = 57.4 mAh/g) to the 10th cycle (discharge capacity = 72.58 mAh/g). At the 10th cycle, the discharge capacity in the 1.5-2.7 V region are almost equivalent for quenched NFMO (72.58 mAh/g) and slow-cooled NFMO (73.2 mAh/g), signifying that the Fe redox couple is kinetically limited for quenched NFMO. The same trend is observed during charging in the low voltage region for quenched NFMO, although the capacity is still less than that of the slow-cooled NFMO. These observations indicate Fe redox couple has sluggish kinetics and has limited activity for quenched NFMO.

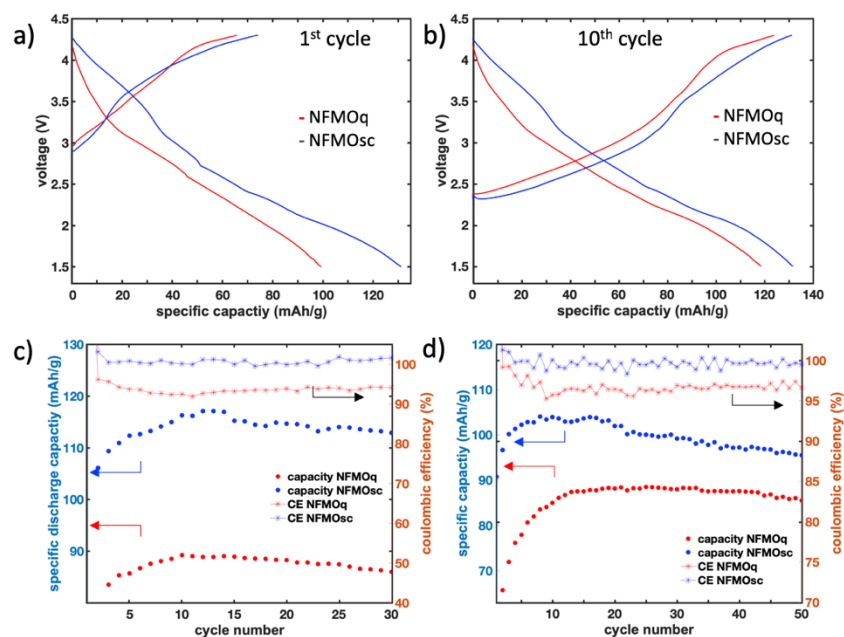


Figure 3.4: Voltage profiles for quenched and slow-cooled NFMO at a rate of C/50 at (a) cycle 1 and (b) cycle 10. Specific discharge capacity versus cycle number at a rate of (c) C/20 and (d) C/10 and coulombic efficiency as a function of cycle number.

To further compare the electrochemical performance of quenched and slow-cooled NFMO, half cells with sodium metal as the anode were assembled and cycled in galvanostatic mode.

Figure 3.4 (a) shows the first cycle voltage profile of both NFMO samples. Both samples have

larger discharge capacity than charge capacity, which implies more Na ions intercalate back to the cathode materials compared to the original state. The quenched sample delivers a first discharge capacity of 100 mAhg^{-1} in the voltage range of 1.5-4.3 V at a rate of C/50 compared to slow-cooled NFMO which delivers a first discharge capacity of 131 mAh/g. After 10 cycles, slow-cooled NFMO still delivers higher discharge capacity of 132 mAh/g compared to 119 mAh/g of quenched NFMO, as shown in **Figure 3.4 (b)**. This large difference in discharge capacity can be explained by bulk and surface difference in the quenched and slow-cooled NFMO materials: (1) Fe has redox couple has sluggish kinetics for quenched NFMO, (2) there are disparities in the surface area and surface contamination of sodium carbonate. Based on BET data in **Figure 3.2 (e)**, it is determined that slow-cooled NFMO material has a 46% larger surface area than quenched NFMO material. This increase in surface area allows for more pathways for Na ion diffusion to the bulk of material, and thus improves discharge capacity. The small capacity fade observed for both materials could be caused by the formation of stacking faults during cycling, as reported by Yabuuchi.[87] The capacity fade of NFMO is one of the lowest of $\text{Na}_x\text{Fe}_y\text{Mn}_{1-y}\text{O}_2$ cathode materials reported in literature.[55,56,84,85,87,157–163] The low capacity fade of the materials reported here can be attributed to the low Fe content and potentially lower sodium carbonate surface contamination. Fe in the TM layer has been reported to increase the sodium carbonate contamination on Na TM layered oxides,[55] however quantification of the sodium carbonate contamination is not commonly reported in cathode literature.

Additionally, in cycling tests, slow-cooled NFMO also shows higher coulombic efficiency at rates of C/20 and C/10 (**Figure 3.4 (c), (d) and Figure B.7**). The difference in coulombic efficiency manifests that slow-cooled NFMO has better capacity retention over cycling. The low coulombic efficiency of quenched NFMO could be caused by continual decomposition of

electrolyte near the surface of quenched NFMO during charging, triggered by excess sodium carbonate surface contamination.[55] Slow-cooled NFMO has significantly higher coulombic efficiency that fluctuates around 100% (fluctuations likely caused by temperature changes in the laboratory) after the first cycle. The significant difference in the coulombic efficiency between quenched and slow-cooled NFMO can be attributed to the differences in their surface chemistry.

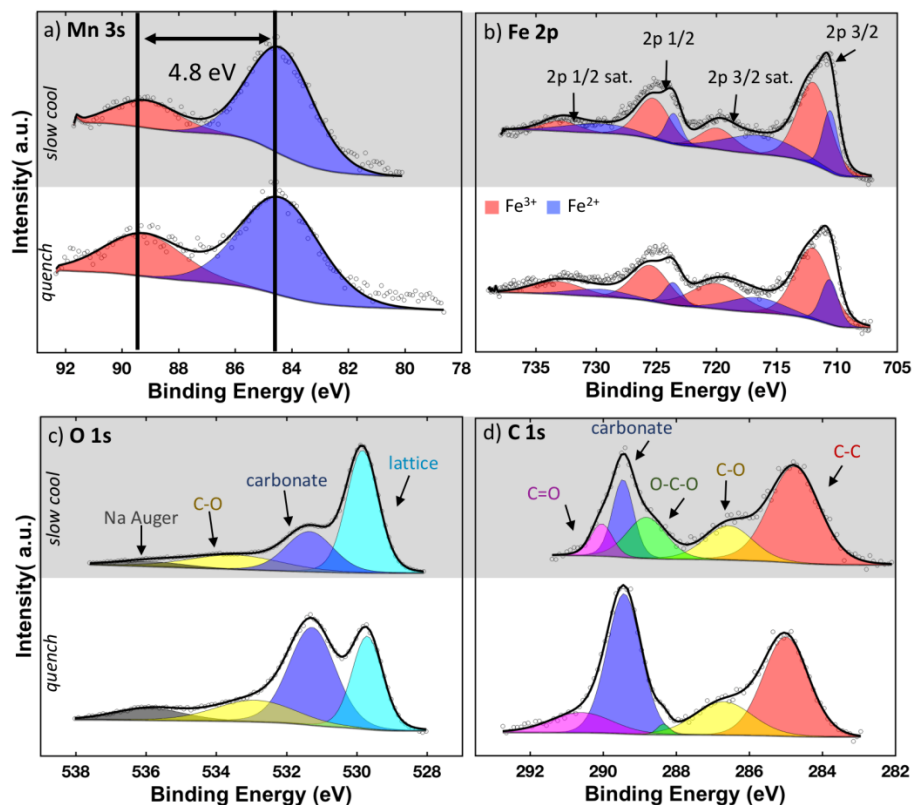


Figure 3.5: XPS spectra of (a) Mn 3s, (b) Fe 2p, (c) O 1s, and (d) C 1s regions for slow-cooled (gray background) and quenched (white background) NFMO.

XPS was applied to investigate differences in the surface chemistry between the slow-cooled and quenched NFMO samples (see **Figure 3.5**). **Figure 3.5 (a)** shows each material's Mn 3s regions. Previous work has demonstrated that splitting between the main Mn 3s peak and its satellite is highly sensitive to the Mn valence state.[165] The larger the splitting, the lower its oxidation state. From the Mn 3s spectra, oxidation state of Mn is 4+ for both samples as indicated by the 4.8 eV peak separation.[167] **Figure 3.5 (b)** show the Fe 2p region for each material. The

binding energy of Fe 2p peaks and their satellites shift to higher binding energy for increased oxidation state.[168,169] A combination of peaks for Fe²⁺ and Fe³⁺ were fit to the experimental data to determine the percentage of the oxidation states in the sample. Iron is a mix of two oxidation states, 2+ and 3+, with slow-cooled sample containing 36% Fe²⁺ and quenched sample containing 30% Fe²⁺. [170] The discrepancies in these values from the DFT results can be attributed to surface modifications or reactions. Based on these results, TM oxidation states on the surface are essentially identical for slow-cooled and quenched NFMO sample. Other surface factors, such as sodium carbonate surface contamination can contribute to the differences in performance between slow-cooled and quenched NFMO.

Sodium carbonate is a common surface contaminant on sodium TM oxide cathodes and can form on the surface of the cathode particles through sodium's reaction with air during synthesis.[105,170] It is hypothesized that sodium carbonate forms preferentially on the edges of the TM layers ((1 0 0) plane) instead of the hexagonal surfaces ((0 0 1) plane). The sodium diffusion channels are perpendicular to the (1 0 0) plane, which could promote the formation of sodium carbonate during synthesis. Additionally, the (1 0 0) planes of slow-cooled NFMO primary particles are less exposed than the quenched NFMO particles, given slow-cooled NFMO sphere-like meso-structure (**Figure 3.2 (d)**). The minimization of the (1 0 0) plane exposure of slow-cooled NFMO may explain the lower concentration of sodium carbonate on the surface. The mechanism of sodium carbonate formation on the surface of sodium layered oxide cathodes is currently under investigation by DFT surface calculations. Sodium carbonate was identified on the surface of both materials based on the O 1s (531.3 eV) and C 1s (289.4 eV) XPS spectra. Interestingly, quenched NFMO has twice the sodium carbonate on its surface as compared to slow-cooled NFMO. This was verified through titration of the surface species and TEM imaging shown

in **Tables B.3 & B.4** and **Figure B.8**. Titration of the surface species for sodium layered cathode materials was used only as a qualitative measurement for two reasons: (1) The initial pH value of the washed cathode solution was higher than the pH of pure concentrated Na_2CO_3 (pH of 11.56 for 10 M). This higher pH value is likely caused by other surface contaminants such as NaOH which can increase the pH beyond 11.56. (2) It has been reported that some sodium layered cathode materials can react with water, causing sodium ions to de-intercalate.[105] This method is considered to adequately compare the surface contamination of materials with the same composition. The XPS, and titration results confirm the quenched NFMO having around twice the surface contamination than that of slow-cooled NFMO. The increase of surface sodium carbonate on the quenched material could be ascribed to the quenched surface having a higher surface energy. In literature, annealing has been used to decrease the surface energy of cathode material due to increased ordering of the TMs.[171] Further research is being conducted to determine the surface energy and TM ordering in NFMO. Sodium carbonate on the surface of the cathode material could lead to higher resistance during electrochemical reaction, thus lowering the capacity of the cathode. The increase of resistance in quenched NFMO can be evidenced by the average voltage vs. cycle number shown in **Figure B.9**. The average voltage during the 10th charge is 3.21 V and 3.13 V for the quenched and slow-cooled NFMO respectively. During the 10th discharge, the average voltage is 2.56 V and 2.70 V for quenched and slow-cooled NFMO respectively. The higher voltage during charging and lower voltage during discharge, known as polarization, is indicative of higher resistance.

The above characterization results demonstrate that both NFMO samples have similar crystallinity and composition, but significantly different morphologies, specific surface area, and surface sodium carbonate concentration. Slow cooling is the key to form spherical meso-structures

which could have the following advantages: (1) the robust meso-structures could release particle strain generated during electrochemical cycling; (2) the high specific area could provide more Na ion diffusion pathways; (3) the low surface carbonate concentration could reduce the surface charge transfer resistance. These factors together can contribute to an improved electrochemistry performance of NFMO cathode material.[87,172,173]

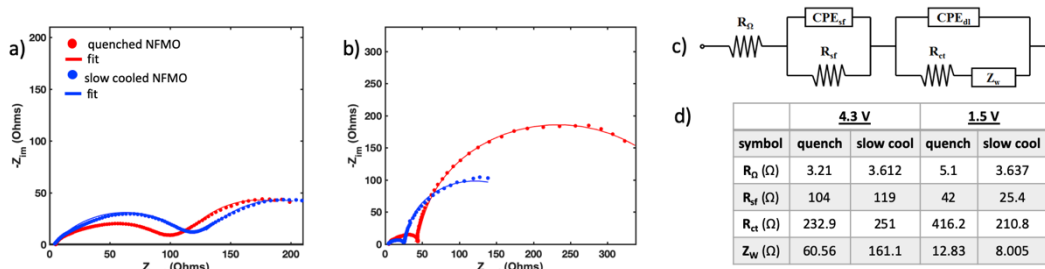


Figure 3.6: Nyquist plots of quenched and slow cooled NFMO (a) charged to 4.3 V and (b) discharge to 1.5 V. The fit of the data is based on the circuit shown in (c). The table (d) contains the values for the impedance measurements.

In order to investigate the electrochemical resistance of both samples, EIS was conducted during the first charging and discharging cycle. The Nyquist plots in **Figure 3.6 (a)** and **(b)** show the real versus imaginary impedance over a range of AC frequencies of both materials as they are charged to 4.3 V and discharged to 1.5 V. The impedance spectra can be quantitatively analyzed using a model circuit shown in **Figure 3.6 (c)**. This model accounts for the ohmic resistance of the set-up (R_{Ω}), the double layer capacitance of the electrode/electrolyte interface (CPE_{st}), the resistance due to Na ion diffusion through the surface of the cathode (R_{sf}), the double layer capacitance (CPE_{dl}) the charge transfer resistance (R_{ct}) and the impedance of the solid state diffusion of Na ions through the bulk of the active material known as the Warburg impedance (Z_w). From **Figure 3.6 (a)** and **(b)**, the impedance at 4.3 V is comparable for quenched and slow-cooled NFMO. A similar observation was found by G. Zhuang et. al. where a cathode heavily contaminated with lithium carbonate had a comparably high resistance to a minimally

contaminated cathode.[174] They also observed that after the first charge, the resistance for both materials decreased. For quenched and slow-cooled NFMO there is a decrease in R_{sf} in both materials at 1.5 V. This decrease in resistance could reflect sodium carbonate decomposition at high voltage or dissolution and penetration of the carbonate coating caused by particle volume change. Because of the higher concentration of sodium carbonate on the surface of quenched NFMO, after sodium carbonate decomposition or dissolution, the impedance of quenched NFMO is higher at 1.5 V than the impedance of slow-cooled NFMO. The resulting cathode electrolyte interphase (CEI) caused by excess sodium carbonate on the quenched NFMO surface results in a higher R_{ct} across the CEI. A thick and resistive CEI could impede Na intercalation into the center of the larger primary particles of the quenched NFMO.[175] This mass transport resistance eventually increases cathode overpotential that leads to inferior electrochemical performance during cell cycling.

A key parameter that affects the capacity of NIB cathode materials is the level of surface contamination. Surface contamination can increase resistance and reduce capacity. In literature, besides storing the material in an inert environment, which only stops further contamination, no effective and simple methods are known to reduce surface contamination of NIB cathode materials. Here, we show that through controlling the meso-structure of NFMO, the extent of surface contamination can be minimized. The mechanism of surface contamination for layered NIB cathode materials has not been thoroughly discussed in literature. If surface contamination preferentially forms on certain facets of the cathode crystal structure, then a secondary meso-structure could reduce the exposure of these facets to react with the atmosphere. If the surface contamination forms more readily on unrelaxed surfaces, then the secondary meso-structure

obtained by slow cooling could have a more relaxed surface which effectively reduces the surface contamination.

3.4 Conclusions

Meso-structure controlled P2-type $\text{Na}_{0.67}\text{Fe}_{1/4}\text{Mn}_{3/4}\text{O}_2$ is synthesized as a high-performance low-cost cathode material for NIBs. Cooling rate after high temperature calcination is the key to synthesizing meso-structure controlled particles for NFMO material. It is found that quenching will produce hexagonal particles with no secondary structure while slowly cooling will produce sphere-like meso-structure controlled particles. The meso-structure of NFMO provides larger surface area, lower surface concentration of sodium carbonate, and higher Fe electrochemical activity, which together improve the electrochemical performance. Through this work we demonstrated that cooling rate is a vital parameter in synthesizing meso-structure controlled sodium ion cathode material and is an often overlooked avenue for controlling electrochemical performance. NFMO with spherical meso-structure and only with inexpensive elements represents a promising direction for the future development of cathode materials for NIBs.

Chapter 3, in full, is a reprint of the material, “Meso-Structure Controlled Synthesis of Sodium Iron-Manganese Oxides Cathode for Low-Cost Na-Ion Batteries” as it appears in the Journal of The Electrochemical Society, H. Hirsh, M. Olguin, H. Chung, Y. Li, S. Bai, D. Feng, D. Wang, M. Zhang, Y. S. Meng, 2019, 166, A2528–A2535. The dissertation author was the primary investigator and author of this paper. All of the experimental parts were performed by the author except for the DFT, XPS, and TEM.

4.1 Introduction

Grid storage is an essential component of a modernized electrical grid to effectively employ solar and wind energy generation. The cost of energy storage and its energy-density are key considerations of the power industry in the deployment of large-scale energy storage. Meeting these requirements at such a large scale is not practical with today's commercialized lithium-ion batteries (LIBs) due to the high cost of lithium and transition metals (TMs) in their cathode components.[102,176,177] The projected cost of energy storage for sodium-ion batteries (NIBs), made with abundant TMs, is significantly less than current LIBs. This positions NIBs, with cathodes containing only inexpensive elements, to be some of the most promising options for grid storage if their energy densities and lifetimes can be improved.[178] However, the mechanisms of poor lifetimes in these cathode materials have remained unclear, which impedes the design of suitable cathode materials for grid storage. Herein, we investigate and report the mechanism of capacity loss for energy dense NIB cathode materials by exploring the redox mechanisms of cathode materials containing only earth abundant elements.

Cathodes containing the abundant and inexpensive elements Fe and Mn are especially promising for solving the need for low energy cost and high energy-density grid storage batteries because they have materials-level energy-densities above 450 Wh/kg. In the category of energy-dense abundant TM layered-oxide cathode materials, the majority of studied materials contain Fe and Mn (**Table C.1**).[54,55,58,60,67,72,76,77,81,84,85,87,158,179] For efforts focused on NIB development, this makes $\text{Na}_{2/3}\text{Fe}_x\text{Mn}_{1-x}\text{O}_2$ compounds attractive to investigate. However, these compounds have poor capacity retention, especially under rigorous testing conditions such as high

electrochemical charge/discharge rates and many cycles. To understand the cause of the poor capacity retention, the mechanisms of irreversibly capacity must be understood. In the simplest cases of Fe-Mn compounds, the irreversibility of Na_xMnO_2 and Na_xFeO_2 have been studied in literature.[180–184] Both materials have poor capacity retention because of large structural changes during electrochemical cycling, but this can be mitigated by TM substitution. Even in cases where TM substitution alleviated structural changes, large irreversible capacities were still observed when the Fe:Mn ratio is greater than one, but the mechanism of irreversible capacity remains unclear.[67] While there is less irreversible capacity for compounds where the Fe:Mn ratio is less than one, there has been no systematic study of the mechanism of irreversible capacity for the $\text{Na}_{2/3}\text{Fe}_x\text{Mn}_{1-x}\text{O}_2$ system. While separate studies have been conducted on $\text{Na}_{2/3}\text{Fe}_x\text{Mn}_{1-x}\text{O}_2$ cathode materials, they are difficult to compare and draw conclusions from because the electrochemical properties are highly dependent on the Fe content, synthesis methods, and testing conditions. [65,70,82,85–87,185]

While conclusions on the $\text{Na}_{2/3}\text{Fe}_x\text{Mn}_{1-x}\text{O}_2$ system cannot be drawn from comparing the cathodes in literature, it is still important to understand the current theories for the Mn and Fe redox mechanisms. Throughout literature, there is a clear understanding for the redox mechanism of Mn but not for Fe. For single transition metal compounds (NaTMO_2), the redox mechanism for $\text{TM}=\text{Mn}$ has clearly been shown to be $\text{Mn}^{3+}/4+$.[180–184] However, for the redox mechanism of $\text{TM}=\text{Fe}$ there is no consensus. For example, L. Chen et. al. used X-ray absorption spectroscopy (XAS) and X-ray photoelectron spectroscopy (XPS) to show that the redox mechanism is solely oxygen redox with no Fe redox.[186] K. Y. Chung et. al. has also used XAS and EELS to show that the redox mechanism for Na_xFeO_2 is oxygen redox.[187] However, O. Yamamoto et. al. and C. S. Johnson et. al. used Mössbauer spectroscopy to show the redox mechanism for Na_xFeO_2 is

Fe 3+/4+.[183,188] In addition, minimal information for the redox mechanism of Na_xFeO_2 can be gleaned from LIBs because of the analogous compound, Li_xFeO_2 , is electrochemically inactive unless nanosized and the first delithiation process triggers oxygen release.[189][190] Meanwhile, the interpretation of redox mechanisms becomes more difficult when there are potentially multiple active redox mechanisms. This is especially true for $\text{P2-Na}_{2/3}\text{Fe}_x\text{Mn}_{1-x}\text{O}_2$ where Fe, Mn, and O all have the potential redox activity.

Table 4.1. Fe redox mechanisms from XAS studies of Fe containing layered NIB cathodes in literature.

Compound	Type	Fe redox	Year	Reference #
$\text{Na}_{2/3}\text{Fe}_{1/2}\text{Mn}_{1/2}\text{O}_2$	<i>ex situ</i>	3+/4+	2012	[87]
$\text{Na}_{2/3}\text{Fe}_{1/3}\text{Mn}_{2/3}\text{O}_2$	<i>ex situ</i>	3+/4+	2014	[85]
$\text{Na}_{2/3}\text{Fe}_{1/2}\text{Mn}_{1/2}\text{O}_2$	<i>ex situ</i>	3+/4+	2020	[191]
$\text{Na}_x\text{Mn}_{0.66}\text{Fe}_{0.20}\text{Cu}_{0.14}\text{O}_2$	<i>operando</i>	anionic redox	2017	[77]
$\text{NaCr}_{1/3}\text{Fe}_{1/3}\text{Mn}_{1/3}\text{O}_2$	<i>ex situ</i>	2+/3+	2017	[86]
$\text{Na}_{2/3}\text{Ni}_{1/4}\text{Mn}_{7/12}\text{Fe}_{1/6}\text{O}_2$ $\text{Na}_{2/3}\text{Ni}_{1/6}\text{Mn}_{1/2}\text{Fe}_{1/3}\text{O}_2$	<i>ex situ</i>	3+/4+	2018	[192]
$\text{Na}_{0.7}\text{Cu}_{0.15}\text{Fe}_{0.3}\text{Mn}_{0.55}\text{O}_2$ $\text{Na}_{0.7}\text{Cu}_{0.2}\text{Fe}_{0.2}\text{Mn}_{0.6}\text{O}_2$	<i>in situ</i>	3+/4+	2018	[193]
$\text{Na}_{0.67}\text{Li}_{0.2}\text{Fe}_{0.4}\text{Mn}_{0.4}\text{O}_{1.6}$ $\text{Na}_{0.67}\text{Li}_{0.2}\text{Fe}_{0.6}\text{Mn}_{0.2}\text{O}_{1.6}$	<i>ex situ</i>	reversible	2018	[185]
$\text{NaMn}_{0.48}\text{Ni}_{0.2}\text{Fe}_{0.3}\text{Mg}_{0.02}\text{O}_2$	<i>ex situ</i>	3+/4+	2018	[194]
$\text{Na}_{0.67}\text{Mn}_{0.6}\text{Fe}_{0.25}\text{Al}_{0.15}\text{O}_2$	<i>ex situ</i>	3+/4+	2018	[71]
$\text{Na}_{0.83}\text{Cr}_{1/3}\text{Fe}_{1/3}\text{Mn}_{1/6}\text{Ti}_{1/6}\text{O}_2$	<i>ex situ</i>	3+/4+	2019	[70]
$\text{Na}_{0.66}\text{Li}_{0.18}\text{Fe}_{0.12}\text{Mn}_{0.7}\text{O}_2$	<i>ex situ</i>	3+/4+	2019	[195]
$\text{Na}_x\text{Mn}_{0.5}\text{Ni}_{0.3}\text{Fe}_{0.1}\text{Mg}_{0.1}\text{O}_2$	<i>in situ</i>	3+/4+	2019	[196]
NaFeO_2	<i>in situ</i>	oxygen redox	2019	[187]

One reason for conflicting findings for the redox mechanisms could be due to the interpretations and limitations of characterization techniques. Common bulk sensitive techniques used to analyze the redox mechanism of $\text{P2-Na}_{2/3}\text{Fe}_x\text{Mn}_{1-x}\text{O}_2$ include Mössbauer spectroscopy and X-ray absorption spectroscopy (XAS). Mössbauer spectroscopy is used to detect the oxidation state of Fe in the bulk but cannot be used concurrently to detect the oxidation state of Mn in these compounds. Additionally, Mössbauer spectroscopy is difficult to analyze, which can lead to

multiple interpretations of the spectra. Alternatively, XAS has been used to detect multiple element oxidation states in the bulk but has never been used in *operando* for P2-Na_{2/3}Fe_xMn_{1-x}O₂ compounds.[85,87,191] A summary of XAS experimental conditions and results for the Fe/O redox mechanisms in literature are shown in in **Table 4.1**. *Operando* XAS has been used for layered cathodes but has never been used for the Na_{2/3}Fe_xMn_{1-x}O₂, and extra TM substitutions can influence the Fe redox mechanism. *Operando* is essential for XAS because *ex situ* experiments have limited data points, potential redox relaxation, and because the *ex situ* samples are washed, which can cause reactions that affect the TM oxidation state. In addition, none of these studies (shown in **Table 4.1**) collected data during the second electrochemical charge of these cathode materials even though the first charge tends to diverge in the locations of the voltage plateaus and capacities from subsequent cycles. These deviations could be caused by cathode electrolyte interface (CEI) formation and/or TM redox activation. Investigations into the redox mechanisms of the second charge are essential to understand the full picture of the redox mechanisms and irreversible reactions.

To determine how the redox mechanisms are dependent on Fe content, three compounds of P2-Na_{2/3}Fe_xMn_{1-x}O₂ ($x=1, 4, 1/3, 1/2$) with different atomic ratio of Fe and Mn were used in this work. In order to achieve a direct comparison of their redox mechanisms, each compound was synthesized using the same method and has the same phase, morphology, and surface species. To the best of our knowledge, the redox mechanisms of these compounds were observed using *operando* XAS for the first time, and the hybridization of Mn-O and Fe-O were explored using computation to explain the irreversibility of certain redox mechanisms. The in-depth understanding of the redox mechanisms will inform the design of sustainable and inexpensive energy-dense NIB cathodes for grid storage.

4.2 Experimental Section

4.2.1 Materials Preparation

A co-precipitation synthesis set-up for pure phase P2- $\text{Na}_{2/3}\text{Fe}_x\text{Mn}_{1-x}\text{O}_2$ ($x=1/4, 1/3, 1/2$) was used as previously reported.[82] Stoichiometric amounts of the precursors, $\text{Fe}(\text{SO}_4)\cdot 7\text{H}_2\text{O}$ and $\text{Mn}(\text{SO}_4)\cdot \text{H}_2\text{O}$ ($\text{Fe}:\text{Mn} = 1:3, 1:2, 1:1$ for $x= 1/4, 1/3, 1/2$ in molar ratio respectively) were dissolved in deionized water for a total concentration of 1 M. The TM sulfate solution and an aqueous solution of 0.2 M Na_2CO_3 were separately pumped into a reaction vessel to maintain the pH value at 8.8. The reaction was stirred continuously with N_2 bubbled through the reaction vessel. The obtained mixture was aged at 80°C for 12 hours. The resulting $\text{Fe}_{1/4}\text{Mn}_{3/4}\text{CO}_3$, $\text{Fe}_{1/3}\text{Mn}_{2/3}\text{CO}_3$, or $\text{Fe}_{1/2}\text{Mn}_{1/2}\text{CO}_3$ was washed with deionized water to remove residual Na^+ and dried at 80°C overnight. The iron manganese carbonate powder was then mixed with a 5% excess stoichiometric ratio of Na_2CO_3 and the mixture was calcinated at 900°C for 15 hours in air. After the 15 hours calcination time the furnace was set to cool down to room temperature over 15 hours.

4.2.2 Materials Characterization

The crystal structures were characterized by X-ray diffraction (XRD) using a Rigaku Smartlab XRD with copper $K\alpha$ source. Rietveld refinement was applied to the obtained diffraction pattern using GSAS-II software.[197] The morphology and meso-structure of the particles were identified by using a FEI Apreo scanning electron microscope (SEM) with an accelerating voltage of 2 kV. X-ray photoelectron spectroscopy (XPS) was performed using an AXIS Supra by Kratos Analytica. The XPS was operated using an Al anode source at 15 kV, scanning with step size of 0.1 eV and 200 ms dwell time. Fits of the XPS spectra were performed with CasaXPS software to estimate the oxidation states of the TMs.

X-ray absorption spectroscopy measurements were performed on the 10-ID-B beamline at the Applied Photon Source (APS) at Argonne National Laboratory. Measurements were performed at the Fe and Mn K-edge under transmission mode using a gas ionization chamber to monitor the incident and transmitted X-ray intensities. A third ionization chamber was used in conjunction with Fe and Mn foil standards to provide internal calibration for the alignment of the edge positions. The incident beam was monochromatized using a Si (111) double-crystal fixed exit monochromator. The XAS spectra were aligned, merged and normalized using the Athena software from the IFEFFIT package.[198] Ampix cells were assembled with sodium metal as the anode and cycled on a Maccor cycler.[7]

4.2.3 Electrochemical Characterization

Composite cathode electrodes were prepared by mixing a slurry of active material, acetylene carbon black, and polyvinylidene fluoride (PVDF) in a weight ratio of 8:1:1, with *n*-methyl-2-pyrrolidone as the solvent. The slurry was cast onto aluminum foil and dried under vacuum at 80°C overnight. Na metal was used as the counter electrode with 50 μ L of 1 M NaPF₆ in propylene carbonate (PC) as the electrolyte and glass fiber GF/F (Whatman) as the separator. Electrodes 14 mm in diameter with an active mass of 2-3.3 mg/cm² were assembled in 2032 coin cells in an argon filled glove box (H₂O < 0.1 ppm) and tested on an Arbin battery cycler. Coin cells were allowed to rest 8 h before electrochemical tests were performed. The voltage range was maintained between 1.5–4.3 V and C-rates were calculated by assuming a theoretical specific capacity of 100 mAh/g, 120 mAh/g and 150 mAh/g for $x = 1/4$, $1/3$, and $1/2$ respectively.

4.2.4 Computational Study

A spin-polarized GGA+U approximation to density functional theory (DFT) was employed, to account for electron correlations in transition metals.⁴⁶ Projector augmented-wave

method (PAW)[199] pseudopotentials were used as implemented in the Vienna Ab initio Simulation Package (VASP).[200,201] The Perdew–Burke–Ernzerhof exchange correlation and a plane wave representation for the wavefunction with a cut-off energy of 450 eV were applied. Effective U values of 3.9 and 5.3 used for Mn and Fe, respectively, applying the rotationally invariant approach.[202] The Brillouin zone was sampled with a k-point mesh of 8x8x4 by Gamma packing for a bulk supercell with a stoichiometry of $\text{Na}_x\text{Mn}_{(4+y)}\text{Fe}_{(4-y)}\text{O}_{16}$, where $0 \leq x \leq 8$ and $0 \leq y \leq 2$. Atomic coordinates and lattice vectors were fully relaxed for each structure.

XANES spectra simulations of NFMO were conducted using FEFF9 software.[203] The crystal structures used for simulations were achieved via DFT relaxations. The simulation parameters for FEFF9 included xkmax value of 4 and xkstep value of 0.001. The atomic coordinates were multiplied by the value 0.95 to reduce the interatomic distances, which means that the cluster shrinks to 95% of its original size.[204] Hedin-Lundqvist self-energy was used for the exchange correlation potential and Final State Rule (FSR) approximation was used for the core hole interaction.

4.3 Results and Discussion

To enable the direct comparison of redox mechanisms between different Fe:Mn ratios for P2- $\text{Na}_{2/3}\text{Fe}_x\text{Mn}_{1-x}\text{O}_2$ cathode materials, the compounds must be synthesized using the same method and have the same phase, similar meso-structure, and consistent surface species. To accomplish this, we use a co-precipitated method to synthesize the P2- $\text{Na}_{2/3}\text{Fe}_x\text{Mn}_{1-x}\text{O}_2$ ($x=1/4, 1/3, 1/2$) compounds and then used XRD to determine the phase, SEM to compare the meso-structures, and XPS to detect the surface species.

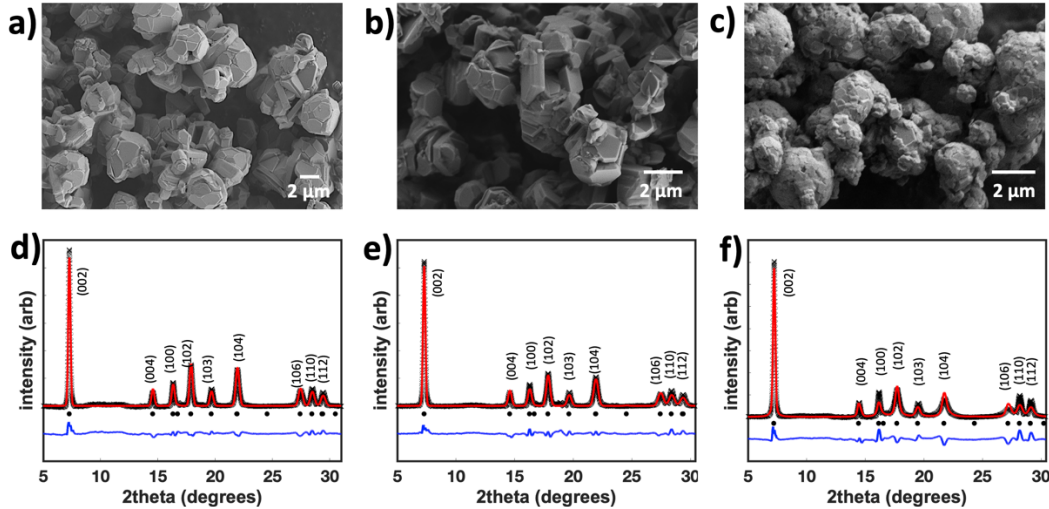


Figure 4.1. SEM images and Rietveld refinement of XRD of (a, d) pristine NFMO13, (b, e) NFMO12, and (c, f) NFMO11.

Pure-phase $P2\text{-Na}_{2/3}\text{Fe}_x\text{Mn}_{1-x}\text{O}_2$ ($x=1/4, 1/3, 1/2$) cathode materials were synthesized and will be referred to as NFMO13, NFMO12, and NFMO11, where the final digits represent the molar ratio of Fe:Mn in the compound of 1:3, 1:2 and 1:1 respectively. Rietveld refinement of XRD data and scanning electron microscopy (SEM) images of these three compounds are shown in **Figure 4.1**. The lattice parameters and oxygen z-position are listed in **Table A.2**. All samples are pure P2 phase and have primary hexagonal particles and sphere-like meso-structures. The main variations in the phases between compounds are the lattice parameters. The a lattice parameter increases ($2.889 \rightarrow 2.910 \text{ \AA}$) with increasing Fe content because Fe has a larger ion radius than Mn.[205] The primary particles of these compounds are hexagonal particles with secondary sphere like meso-structures. All the compounds are the same phase and have similar meso-structure which eliminates these variables as the origins of electrochemical performance and redox mechanism differences. The cathode structure was observed after one cycle (**Figure A.1**) and minimal phase changes were observed. This is consistent with previous studies that show NFMO has minimal and highly reversible structural changes during cycling and is not the primary mechanism of irreversible capacity.[87,191,206]

Surface species have been shown to have large effects on the electrochemical performance for NIB cathode materials.[82] Using XPS, the surface TM oxidation states and surface species were investigated as shown in **Figure 4.2**. Previous studies have shown that the splitting of the Mn 3s peak from its satellite is correlated to the Mn oxidation state, where increased splitting is caused by a lowered oxidation state.[167] Additionally, the binding energy of Fe 2p peaks and their satellites shift to higher energy with increasing oxidation state.[168,169] Using this analysis, the transition metal surface oxidation states for all materials is determined to primarily be Fe 2+/3+ and Mn 4+. The exception is for NFMO11, where there is an extra peak in the Fe 4s region that may belong to Fe 4+. It is difficult to identify because there is little information on XPS of Fe 4+ due to its instability in nature. Furthermore, the oxidation states on the surface may not match the bulk oxidation states because of the surface's reactions with air and their potential relaxation. The other surface species, such as carbonate, as shown in the C1s and O1s regions, are essentially the same for each compound, suggesting that the changes in electrochemical properties are not caused by surface reactions. Because the phase, meso-structure, and surface species of these compounds are the same, the electrochemical performance differences like originate from the differences Fe:Mn ratio.

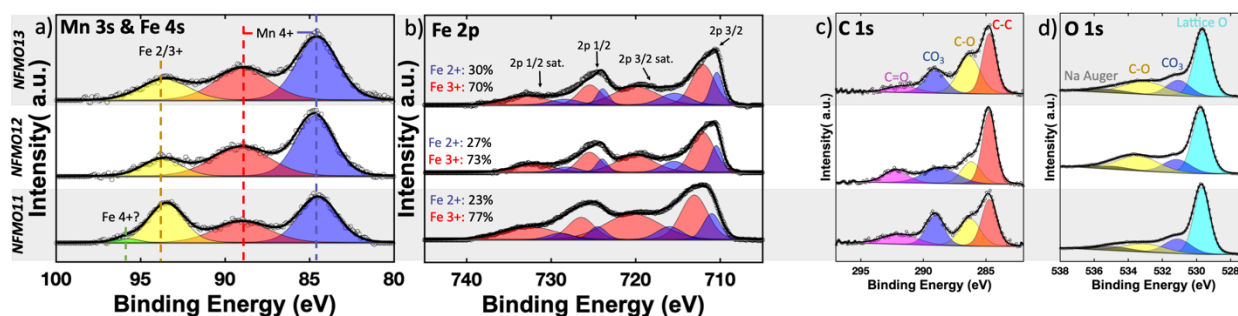


Figure 4.2. XPS spectra of (a) Mn 3s & Fe 4s, (b) Fe 2p, (c) C 1s, and (d) O 1s for NFMO13 (top), NFMO12 (middle), and NFMO11 (bottom) surfaces.

To determine how the Fe:Mn ratio affects the electrochemical performances of P2- $\text{Na}_{2/3}\text{Fe}_x\text{Mn}_{1-x}\text{O}_2$, sodium half cells were assembled and cycled at a rate of C/10 (1C = 100 mAh/g for NFMO13, 120 mAh/g for NFMO12, and 150 mAh/g for NFMO11) and are shown in **Figure 4.3**. As the Fe:Mn ratio increases, the initial capacity increases but the capacity retention over 50 cycles decreases. This is especially apparent when comparing NFMO13 and NFMO11 where the first discharge capacities and capacity retentions after 50 cycles are 91 mAh/g and 105% vs. 163 mAh/g and 75% respectively (1st cycle CE and retention shown in **Table C.3**). Additionally, the shape and capacities of the first charge curves for NFMO13, NFM12, and NFMO11 are distinctive with increasing capacity with increasing Fe:Mn ratio. The first charge is likely solely due to the redox of Fe, as the capacity of the first charge at C/50 is equal to the theoretical capacity of Fe giving up one electron for each compound and the first voltage curve starts at 2.7 V which is above the region where Mn redox is likely active. The first charge shape for NFMO13 and NFMO12 consists of a slope up to about 4V and then another slope above 4V. Alternatively, the shape of the first charge for NFMO11 consists of a slope below 4V and a plateau above 4V. This suggest that the redox mechanisms for the first charge are Fe 3+/4+ for NFMO13, NFMO12, and NFMO11, with larger Fe-O hybridization for NFMO11.

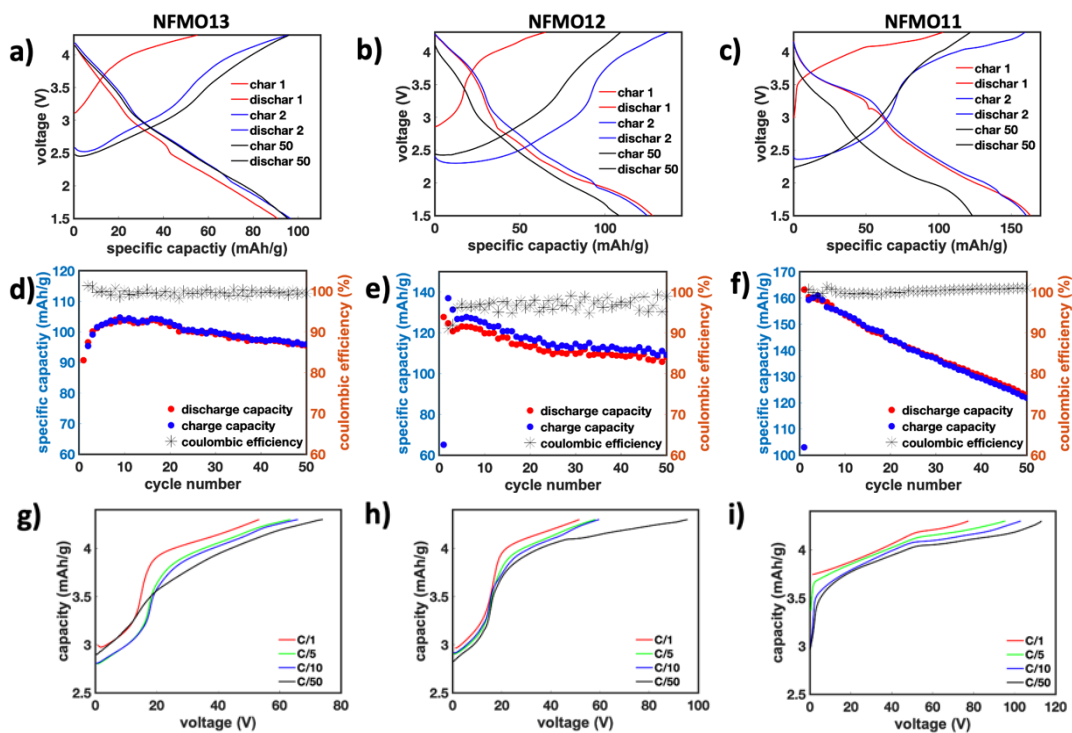


Figure 4.3. Voltage curves, cycling performance, and coulombic efficiencies of (a,d) NFMO13, (b,e) NFMO12, and (c,f) NFMO11 cycled between 1.5 and 4.3 V at C/10 rate. First charge curve at different rates for (g) NFMO13, (h) NFMO12, and (i) NFMO11.

In order to explore the bulk redox mechanisms, *operando* XAS measurements for the Mn K-edge and Fe K-edge were performed during the first cycle and the second charge of NFMO13, NFMO12, and NFMO11 as shown in **Figure 4.4** and **Figure 4.5** respectively. The second charge was monitored, in addition to the first cycle, because the redox reactions are not fully activated for the first charge of the NFMO system. Past studies have not quantified the shifts of the K-edges during cycling which prevents the quantification of the TM oxidation states. In this study the inflection point of the edge and the peak of the edge-crest were monitored for oxidation state changes of the Mn K-edge and Fe K-edge spectra respectively (**Figure 4.4(a)** & **4.5(a)**) in order to observe the TM oxidation states. The inflection point for the Mn K-edge was chosen to monitor the oxidation state of Mn because the edge position has been shown to reflect the oxidation state of Mn and is commonly used in understanding the Mn redox mechanism in battery materials.[67] The half-height and edge-crest were also calculated for the Mn K-edge and follow the same trend

(**Figure C.2**). In contrast, the Fe K-edge is more complicated because the Fe K-edge is very sensitive to its bonding environment, so traditional oxide standards, FeO and Fe₂O₃, are not accurate for layered TM oxides (standards shown in **Figure C.3**).^[207–209] In addition, there are no Fe 4+ standards because Fe 4+ is not stable in nature (stable iron oxides FeO, Fe₃O₄, Fe₂O₃). However, the edge-crest (peak) of the Fe K-edge can be used to monitor the Fe oxidation state in compounds with similar Fe environments. Simulations of the Fe K-edge for NFM013, NFM012, and NFM011 at different states of charge are shown in **Figure C.4** to compare with the experimental data. These simulations show comparable shapes, and the edge-crest follows the same trend as the *operando* XAS data for these compounds. The same trend was also found in literature for extracted XAS data of Fe and Mn containing NaTMO₂. Although the exact values of the Fe K-edge edge-crest vary slightly, it is clear that with the edge-crest shifts to higher energy with higher oxidation state and vice versa. The same trend is seen for the edge position of the Mn K-edge, and the shift is limited during the first charge showing Mn redox activation during the first discharge. Extracted edge inflection points of Mn K-edges and edge crest positions of Fe K-edges from literature XAS data are shown **Figure C.5**.^[65,70,85,180,181,186] The XAS simulations and extracted XAS data from literature implies that the position of the Mn K-edge inflection points and the Fe K-edge edge crests can be used to determine the oxidation states of Mn and Fe respectively. In addition, computation was compared with the XAS results and found to be consistent.

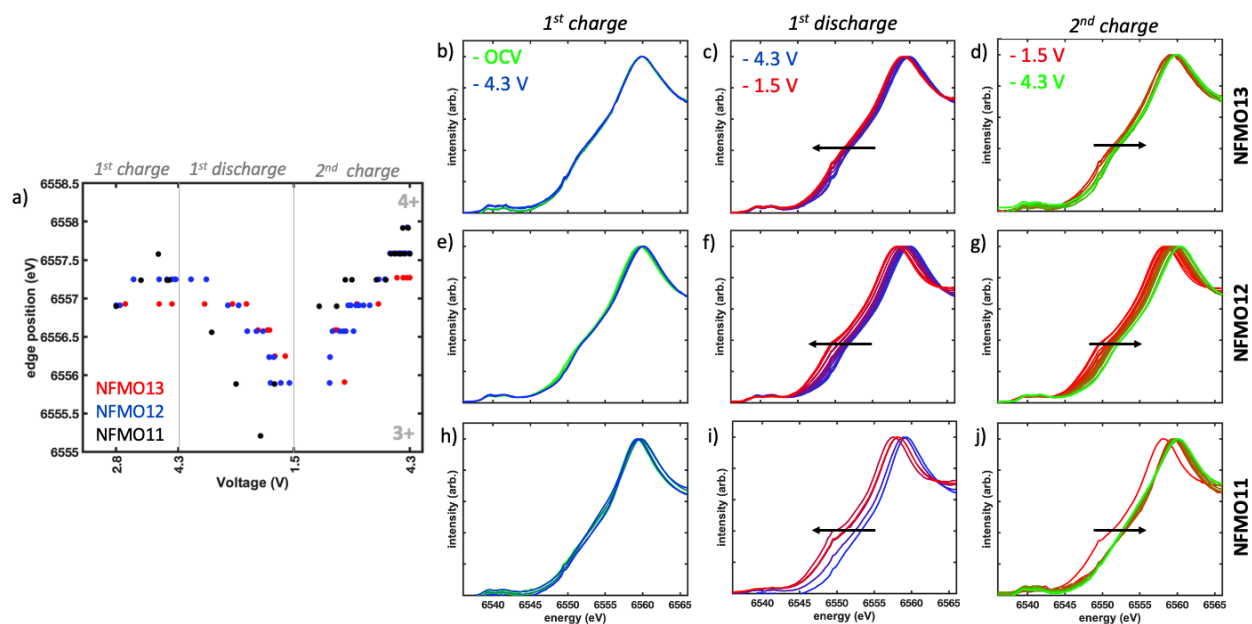


Figure 4.4: (a) Mn K-edge position and normalized XANES spectra of the Mn K-edge for (b-d) NFM013, (e-g) NFM012, and (h-j) NFM011 at different states of charge during the first cycle and the second charge of operando half cells.

Because data was collected for both the Mn K-edge and Fe K-edge at multiple states of charge during the electrochemical cycling, the voltage regions where each element becomes redox active can be determined. For the first charge, there is minimal edge shift for the Mn K-edge for all the compounds, whereas there is a shift in the Fe K-edge edge-crest for all compounds. This is consistent with the findings from electrochemical testing that show the first charge compensation is mainly provided by the oxidation of Fe during the first charge. This occurs because the OCV of the assembled battery is 2.7 V which is higher than the voltage region where Mn redox is active and because the initial amount of Na in the compound is less than one, limiting the TM redox. During the first discharge, both Fe and Mn redox are active with Fe redox primarily occurring in the higher voltage regime and Mn primarily occurring in the low voltage regime. The second charge is distinct from the first because both the Mn and Fe redox mechanism are active. Again, Mn redox primary occurs in the low voltage regime and Fe redox primarily occurs in the high

voltage regime. This is consistent with our computation results that indicate the Mn 3+/4+ redox occurs at a lower voltage than Fe 3+/4+ for the NFMO compounds.

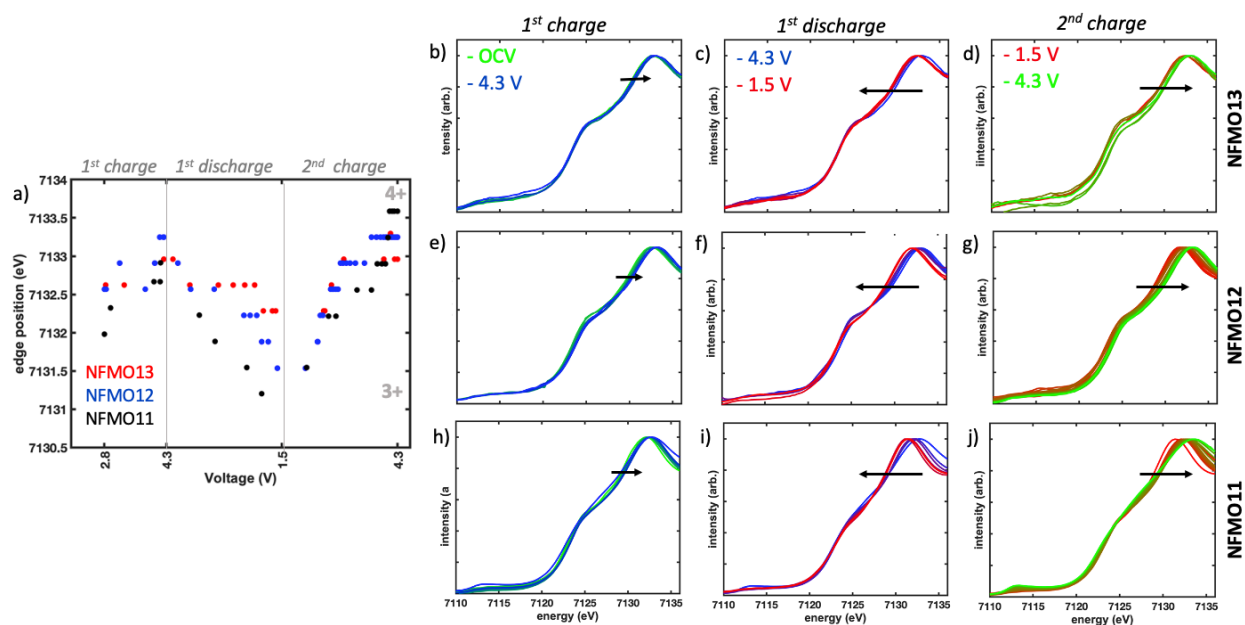


Figure 4.5: (a) FE K-edge position and normalized XANES spectra of the Fe K-edge for (b-d) NFMO13, (e-g) NFMO12, and (h-j) NFMO11 at different states of charge during the first cycle and the second charge of operando half cells.

The initial Mn oxidation state is likely similar for NFMO13, NFMO12, and NFMO11 because their initial Mn K-edge positions are comparable (**Figure 4.4**). In contrast, initial Fe oxidation state is likely lower for compounds with larger Fe content (**Figure 4.5**). This suggests that the initial Mn oxidation state is less than +3.3 because the larger Fe:Mn ratios must have lower oxidation states to maintain charge neutrality within the cathode. During the first charge, the Mn edge-position changes minimally for all compounds which suggests no or only slight increase in oxidation state. The Fe edge-position increases by ~ 0.5 eV for NFMO13 and by ~ 1 eV for NFMO11 during the first charge, which indicates that Fe is oxidized towards a 4+ state. During the first discharge, the Mn K-edge position decreased by ~ 1 eV for NFMO13 and ~ 2 eV for NFMO11. This indicates that Mn is reduced toward the 3+ state for all the compounds but is

reduced further for larger Fe:Mn ratios. The same trend follows for the Fe K-edge during the first discharge with Fe being reduced further toward the 3+ state for larger Fe:Mn ratios. The second charge is distinct from the first because 1) both Mn and Fe are redox active and 2) the K-edge shifts are larger in magnitude than the first cycle. These two trends suggest that more of the 3+/4+ redox reactions are activated during the second charge. This is especially true for the compounds with larger Fe:Mn ratios and more evident in the Fe K-edge. The Fe K-edge position increase in the second charge is only ~ 1 eV for NFM013 and is ~ 2.5 eV for NFM011. This suggests that more of the Fe 3+/4+ redox can be activated for compounds with larger Fe content. The higher activation of the Fe 3+/4+ redox could also be the reason that larger Fe content is correlated with inferior capacity retention. To explore the Fe 3+/4+ redox instabilities, computation was used to model each of the compounds to explore their electronic structure.

Computational studies using density function theory (DFT) were conducted on the $\text{P2-Na}_x\text{Fe}_y\text{Mn}_{1-y}\text{O}_2$ ($y=1/4, 1/3, 1/2$) system to explore electronic structures of the charge compensation mechanisms. Density of states (DOS) were calculated for different states of charge ($x=0, 3/8, 5/8, 1$) where $x=0$ is the fully desodiated state and $x=1$ is the fully sodiated state. DOS for these states of charge and compositions are shown in **Figure C.6**, and DOS near the Fermi level for the fully desodiated and sodiated compounds are shown in **Figure C.6**. It is clear that at higher levels of sodiation ($x= 5/8$ and $x=1$), Mn has the most states near the Fermi level which indicates that it is the element participating in redox.[210] This matches our electrochemical and XAS data, that show that Mn redox primarily occurs in the lower voltage regime.

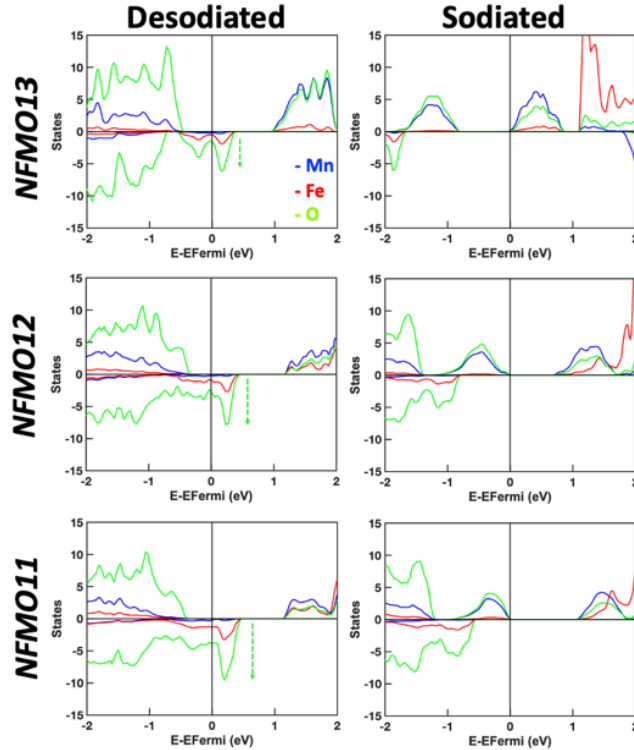


Figure 4.6. DOS near the Fermi level for fully desodiated and sodiated NFM013 (top), NFM012 (middle), and NFM011 (bottom). The blue line represents Mn DOS, the red line represents Fe DOS, and the green line represents O DOS. DOS sign refers to spin state. The green arrows guide the eye to the increased intensity of oxygen DOS near the Fermi level with increased Fe content.

It is also clear that at high levels of desodiation ($x=0$ and $x= 3/8$) Fe, not Mn, has more states near the Fermi level. This suggests that Fe is participating in redox in high voltage regime, in agreement with the electrochemical and XAS data. However, there are also a significant amount of oxygen states near the Fermi level. The shapes of the Fe and O DOS match which implies that the Fe and O are highly hybridized and share electrons.[211] Additionally, the amount of oxygen states near the Fermi level increases with increasing Fe content, as denoted by the green arrows in **Figure 4.6**. The ratio of the number of O state vs. the number of Fe states (and normalized with respect of Fe content) from $-0.5 - 0$ eV increases with Fe content from 0.78 for NFM013 to 1.72 for NFM011. This shows an increase in hybridization for increasing Fe content in NFM0 which suggests that the redox of Fe $3+/4+$ closely share electrons with oxygen atoms. The increased

hybridization of Fe and O in NFMO11 could be the reason the Fe 3+/4+ redox is more irreversible than Fe 2+/3+ redox. The electronic structure for NFMO11 is more characteristic of a charge-transfer system than a Mott-Hubbard system because there are empty metallic bands above filled oxygen-iron orbitals.[212] The charge-transfer system can have unstable oxygen dimer formation that lead to irreversible reactions. These irreversible reactions include surface reactions with the electrolyte, formation of oxygen dimers, and/or cation migration.[213][214] It is clear from **Figure 4.2** that the NFMO11 high voltage region, where Fe redox occurs, shows more severe deteriorations in discharge capacity and voltage when compared to NFMO12 and NFMO13, which demonstrates the instability of the highly hybridized Fe-O.

From electrochemical and *operando* XAS data, it is clear that the Mn redox and Fe redox mechanisms are the same (3+/4+) for all Fe:Mn ratios. In addition, computational modeling of these compounds shows large Fe-O hybridization for the larger Fe:Mn ratios which can cause irreversible reactions in the surface and bulk of the cathode. Using this knowledge to design energy-dense, long lifetime cathode materials containing only abundant elements, the maximum Fe:Mn ratio should be 1:2 to minimize irreversible capacity while maximizing energy density. Another technique to increase the cathode lifetime could be to substitute abundant elements such as Ti or Al into the cathode material to limit the hybridization of Fe-O, but this could also reduce the overall energy density. Overall, these observations and analysis of the redox mechanisms for the P2-Na_{2/3}Fe_xMn_{1-x}O₂ system will inform the design of inexpensive energy-dense NIB cathode materials for grid storage.

4.4 Conclusions

In this work, the dependence of the redox mechanisms of P2-Na_{2/3}Fe_xMn_{1-x}O₂ (x=1/4, 1/3, 1/2) on the Fe:Mn ratio was clarified for the first time using a combination of *operando* XAS and

computation. To ensure differences observed were only from the redox mechanism, the cathodes were all synthesized using the same method, had the same phase, and contained the same surface species. From analyzing the large data set collected from *operando* XAS, and comparing it to computation results, we found that the Mn redox primary occurs in the low voltage regime whereas Fe redox primary occurs in the high voltage regime. The redox mechanism for all NFMO compounds utilize the Mn $3+/4+$ and Fe $3+/4+$ redox pairs. However, with larger Fe:Mn ratios, Fe is highly hybridized with O causing irreversible reactions. These results indicate that improved reversibility of sodium iron manganese oxides can be obtained by limiting Fe-O hybridization by constraining the Fe:Mn ratio to a maximum of 1:2. Alternatively, electrode coatings and/or electrolyte optimization could be tested to reduce irreversible reactions caused by Fe-O hybridizations. This understanding of the Fe redox mechanisms will contribute to the rational design of long lifetime cathode materials made from earth-abundant elements.

Chapter 4, in full, is currently being prepared for submission for publication, “Elucidating the Redox Mechanism of Cathode Materials Made from Earth-Abundant Elements” H. S. Hirsh, S. Richardson, M. Olguin, T. A. Wynn, D. Cheng, D. H. S. Tan, M. Zhang, E. Zhao, Y. S. Meng. The dissertation author was the primary investigator and author of this paper. All of the experimental parts were performed by the author except for the DFT and XPS.

Chapter 5 The Negative Impact of Transition Metal Migration on Oxygen Redox Activity of Layered Cathode Materials for Na-ion Batteries

5.1 Introduction

Sodium ion batteries (NIBs) are emerging as a promising grid storage technology due to its low cost of energy.[21] Various types of cathode materials have been investigated for NIBs, including layered oxides, poly-anionic frameworks, hexacyanoferrates, and organics.[48,138–142] Among the sodium cathode materials, layered sodium transition metal oxides, Na_xTMO_2 (TM=Mn, Fe, Ni, Cu, Ti, Co, Cr or mixture of elements), are strong contenders due to their high volumetric energy densities.[178,215] Specifically, P2-type Na_xTMO_2 have enhanced electrochemical performance due to minimal structural changes during cycling.[56,163,216] In these structures, P2 refers to the stacking sequence of the layered oxide, as introduced by Delmas et al.[166] In this notation, the letter indicates the coordination environment of the sodium ion (P for prismatic, O for octahedral, or T for tetragonal) and the number indicates the quantity of sheets within a unit cell (1, 2, or 3). Even with the relatively high capacity of P2 cathodes compared to other sodium cathode materials, there is still a need to further increase the capacity at high voltage to optimize their energy density for use in grid storage.

In conventional cathode materials, cationic redox ($\text{Mn}^{3+}/\text{Mn}^{4+}$, $\text{Ni}^{2+}/\text{Ni}^{4+}$, $\text{Co}^{3+}/\text{Co}^{4+}$, etc.) is utilized to maintain a charge balance as Li^+/Na^+ ions leave the compound.[217,218] The capacity of these cathode materials is limited by the cationic redox. Recently, oxygen redox has been accessed for cathodes in LIBs to increase their capacity beyond the “theoretical” capacities based on cationic redox.[219–222] This is observed in lithium rich layered oxide (LRLO) cathode materials with the composition, $x\text{Li}_2\text{TMO}_3 \bullet (1-x)\text{LiTMO}_2$ (TM=3d, 4d, and 5d transition metals) as a nano composite. During charge and discharge, LRLO materials experience the redox of TMs

with simultaneous extraction/insertion of Li ions similar to classical layered NMC materials. However, above 4.3 V, LRLO materials also experience redox activity of oxygen, which contributes significantly to the large capacities of LRLO.[223,224] In these materials, the excess lithium, which has a similar radius to TMs, sits in the TM layers. This creates an environment where the Li-O-Li bond has a lone-pair of oxygen electrons that are oxidized for charge compensation during Li-extraction.[225] In the voltage curve, this mechanism has a characteristic plateau at high voltage. Within lithium rich cathodes, ordering of the atoms in the TM layer is commonly seen and contributes to the activation of oxygen activity. [211] For oxygen redox to be activated in layered cathode materials, pure oxygen O (2p) states are required to be slightly below the Fermi level.[221] This condition can be triggered by the O-TM stoichiometry and bonding environment.[74,223,226,227]

In sodium 3d TM layered cathode materials, oxygen activity has been observed in two cases. In the first case, sodium cathode materials are substituted with Li, such as $\text{Na}_{0.6}\text{Li}_{0.2}\text{Mn}_{0.8}\text{O}_2$ and $\text{Na}_{0.72}\text{Li}_{0.24}\text{Mn}_{0.76}\text{O}_2$. [53,228] The oxygen redox mechanism for these Li-rich Na-ion layered compounds is proposed to be identical to the one for Li_2MnO_3 and Li-rich Li-ion layered compounds, where the lone-pair oxygen electrons in the Na (Li)-O-Li bond are oxidized for charge compensation during Na (Li)-extraction. However, the substitution of Li is not necessary to create such O 2p nonbonding orbitals.[229] In fact, similar oxygen redox behavior has also been reported in Mg-substituted samples such as $\text{Na}_{2/3}\text{Mg}_{0.28}\text{Mn}_{0.72}\text{O}_2$. [42] In the second case, using a similar concept, under coordinated oxygen caused by vacancies in the TM layer, can trigger oxygen redox in the following compounds: $\text{Na}_{4/7}\text{Mn}_{6/7}\text{O}_2$, $\text{Na}_{0.78}\text{Ni}_{0.23}\text{Mn}_{0.69}\text{O}_2$, and $\text{Na}_{0.653}\text{Mn}_{0.929}\text{O}_2$. [43,72,230] A table of NIB cathodes that are reported to have oxygen redox are shown in **Table D.1**. It is notable that most of the compounds containing Ni do not have reversible oxygen redox.

Specifically, the high voltage plateaus in these compounds lack reversibility even if the cation redox processes remain reversible. This leads to the question: does Ni play a role in irreversible oxygen redox, and if so, what is the mechanism of irreversibility?

While Ni has not been identified as the origin of irreversible oxygen redox in NIBs, Ni has been reported as a problematic component of Li-rich disordered rock salt cathodes.[231] In these compounds, Ni, in contrast with Mn, induces irreversible oxygen redox through oxygen gas release. Ni migration, in these disorder rock salt cathodes, could play a role in the irreversible oxygen redox processes, where Ni migration within the structure could alter the bonding environment of oxygen. This makes oxygen reduction unfavorable during discharge, therefore inhibiting the oxygen redox reversibility. Additionally, the negative impacts of TM migration were previously reported for Li-rich layered TM oxide cathode materials.[232] There are several unfavorable electrochemical properties in Li-rich layered oxides, such as the open-circuit voltage hysteresis, that arise from the drastic change in the local oxygen coordination environments induced by TM migration. Furthermore, in oxygen redox active compounds that rely on TM layer ordering for suitable oxygen bonding environments, TM migration could disrupt the ordered structure and inhibit further oxygen redox. There are examples of such phenomena in both Li-ion layered cathode and Na-ion layered compounds.[232,233]

In this work, we explore a pure phase spherical meso-structure controlled P2-type $\text{Na}_{0.8}\text{Li}_{0.12}\text{Ni}_{0.22}\text{Mn}_{0.66}\text{O}_2$ (NLNMO) with TM layer ordering that was synthesized using a carbonate co-precipitation method. In NLNMO, a plateau region is observed at high voltages during the first charge. Superlattice peaks are seen in the X-ray diffraction pattern, which indicate TM metal layer ordering. This ordering can potentially alter the environment of the oxygen atoms and this allows oxygen redox to become favorable. After the first electrochemical cycle, the TM

ordering disappears along with the oxygen plateau. Ni migration is identified as the cause of the irreversible oxygen redox by disrupting the TM honeycomb ordering and inhibiting oxygen reduction during sodiation. These mechanisms could have a profound impact on the future design of sodium cathode materials. By controlling the reversibility of oxygen activity, the energy density of sodium cathode materials can be dramatically increased.

5.2 Experimental Methods

5.2.1 Materials Preparation

Stoichiometric amounts of the precursor, $\text{Ni}(\text{NO}_3)_2 \cdot 6\text{H}_2\text{O}$ and $\text{Mn}(\text{NO}_3)_2 \cdot 4\text{H}_2\text{O}$ (Ni:Mn = 1:3 in molar ratio), were dissolved in DI water for a total concentration of 1 M. The TM nitrate solution and an aqueous solution of 0.2 M Na_2CO_3 were separately pumped into a reaction vessel to maintain the pH value at 7.8. The obtained mixture was aged at 80°C for 12 hours in a sealed vessel. The resulting spherical $\text{Ni}_{1/4}\text{Mn}_{3/4}\text{CO}_3$ was washed with deionized water to remove residual Na^+ and NO_3^{2-} and then dried at 80°C overnight. The obtained $\text{Ni}_{1/4}\text{Mn}_{3/4}\text{CO}_3$ powder was mixed with a 5% excess stoichiometric ratio of Na_2CO_3 and Li_2CO_3 . The mixture was calcinated at 900°C for 15h in air.

5.2.2 Materials Characterization

The crystal structures were characterized by X-ray diffraction (XRD) using a Rigaku Smartlab XRD with a copper $K\alpha$ source. Rietveld refinement was applied to the obtained diffraction pattern using FullProf Software. The morphology and meso-structure of the particles were identified using a Ziess Sigma 500 scanning electron microscope (SEM) with an accelerating voltage of 1 keV. Cross-section of the particles was acquired and imaged using a FEI Scios DualBeam focused ion beam (FIB)/SEM. Inductively coupled plasma optical emission

spectroscopy (ICP-OES) was performed using a Perkin Elmer 3000 optical emission plasma spectrometer.

X-ray absorption spectroscopy (XAS) spectra were performed at National Synchrotron Radiation Research Center (NSRRC) in Taiwan. Ni and Mn K-edges hard X-ray absorption spectra were collected at the beamline BL17C by using the transmission mode. Ni and Mn reference foils were measured simultaneously to calibrate energy for each scan. Spectra were analyzed using the Demeter XAS software package. O K-edge spectra were performed at soft XAS beamline (BL20A) with a fluorescence yield (FY) mode in an ultrahigh-vacuum (UHV) chamber. *Ex situ* XAS samples were prepared by charging/discharging 2032 cells at a rate of C/10 as described in the electrochemical characterization section and then disassembled. The electrodes were rinsed with propylene carbonate (PC) and dried in an Ar-filled glovebox.

Operando synchrotron XRD (sXRD) and pair distribution function (PDF) data were collected at 11-ID-B in Advanced Photon Source (APS) at Argonne National Laboratory with a wavelength of 0.2115 Å. An AMPIX cell was assembled with a NLNMO cathode and Na metal anode and cycled at a rate of C/15 (1C = 118 mA/g) between 2.0 V to 4.4 V. GSAS-2[6] was used to extract the XRD pattern as well as to perform Rietveld refinement to the collected data. PDF data was analyzed through PDF suite and PDF gui.[234] The Q-max used for the Fourier transfer is 20.5 Å⁻². In the PDF refinement, the instrumental parameters Qdamp and Qbroad were set to be 0.0251 Å⁻² and 0.0199 Å⁻² separately.

5.2.3 Electrochemical Characterization

Composite cathode electrodes were prepared by mixing a slurry of NLNMO, acetylene carbon black, and polyvinylidene fluoride (PVDF) in a weight ratio of 8:1:1, with n-methyl-2-pyrrolidone as the solvent. The slurry was cast on aluminum foil and dried under vacuum at 80°C

overnight. The electrodes were assembled in 2032 coin cells in an argon filled glove box ($\text{H}_2\text{O} < 0.1$ ppm) with Na metal as the counter electrode, glass fiber GF/D (Whatman) as the separator, and $70\mu\text{L}$ of 1 M NaPF_6 in PC as the electrolyte. The coin cells were allowed to rest 8 h before electrochemical testing on an Arbin battery cycler. The C-rates were calculated with a theoretical specific capacity of 118 mAh/g and the voltage range was maintained between $2-4.4\text{ V}$.

5.2.4 Computation Study

The electronic structure of NLNMO was investigated in the spin polarized GGA+U approximation to Density Functional Theory (DFT). Projector augmented-wave method (PAW) pseudopotentials were employed, as implemented, in the Vienna Ab initio Simulation Package (VASP).[199] The Perdew-Bruke-Ernzerhof (PBE) exchange correlation and a plane-wave representation for the wavefunction[235] were used, where a cut-off energy was set at 450 eV . The Brillouin zone was sampled with a k-points mesh of $5\times 4\times 4$ for structural relaxations and $10\times 8\times 8$ for density of states (DOS) calculations. Effective U values used through all the calculations were 3.9 for Mn and 6.2 for Ni, which are adopted from recent studies in the Materials Project.[236] $\text{Na}_{14}\text{Mn}_8\text{Ni}_4\text{Li}_2\text{O}_{28}$ was used as a starting structure and density of states were calculated at the structure of $\text{Na}_{3/14}$ with Li vacancy.

5.3 Results and Discussion

Pristine $\text{P2-Na}_{0.8}\text{Li}_{0.12}\text{Ni}_{0.22}\text{Mn}_{0.66}\text{O}_2$ (NLNMO) was prepared by a modified meso-structure controlled co-precipitation method. Unlike previously reported methods which result in a hexagonal particle morphology, this modified co-precipitation yields spherical secondary particles $2-3\ \mu\text{m}$ in diameter comprised of hexagonal primary particles $100-500\text{ nm}$ in diameter (**Figure 5.1 (a)**). [89,237] A cross section of a secondary particle is shown in **Figure 5.1(b)**. The secondary particle contains pores that are beneficial for electrolyte penetration into the bulk of this

material. Electrolyte penetration into the bulk of the material enables all of the primary particles in the meso-structure to be electrochemically active. The spherical shape of the carbonate precursors (**Figure D.1**) is retained in the final product of NLNMO.

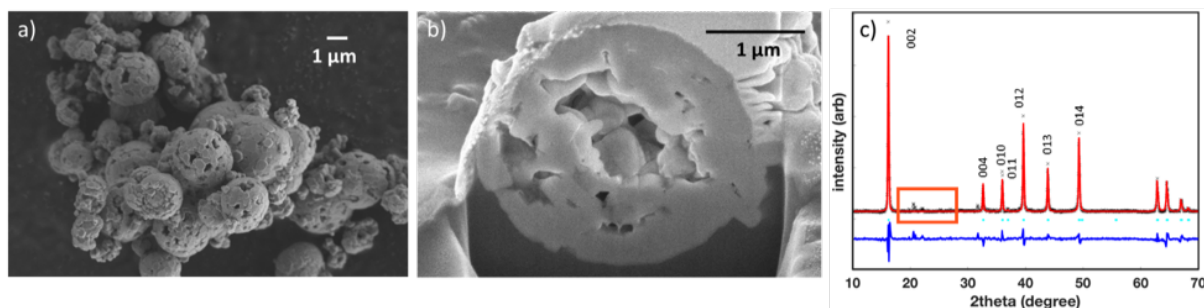


Figure 5.1: (a) SEM image of NLNMO powder with primary hexagonal particles of 100-500 nm in diameter and secondary spherical particles of 1-3 μm in diameter. (b) A cross section of an NLNMO particle with large pores in its secondary structure. (c) XRD data of NLNMO with superlattice peaks highlighted with an orange square.

The composition of NLNMO was confirmed with ICP-OES (**Table D.2**). NLNMO diffraction peaks can be well indexed to space group $P6_3/mmc$ (**Figure 5.1** (c)) with Rietveld refinement results (**Table D.2**) confirming that the material is a pure phase P2 layered material. A P2-type layered structure, as defined by Delmas et. al., has ABBA oxygen stacking sequence where Na ions are located in the trigonal prismatic sites.[166] Additionally, the XRD data of NLNMO have small but noticeable peaks between 19-28 degrees that do not correspond to the otherwise pure P2 phase. These peaks indicate superlattice ordering in the TM layer. A. R. Armstrong et. al. reported that these peaks correspond to ordering of Li/Mn/Ni in the TM layer.[238] When the radii of the ions in the TM have a difference of 15% or larger, TM layer ordering is favorable.[239] The ionic radii of the ions in the TM layer fit this criterion Li^+ (0.76 Å), Ni^{2+} (0.69 Å), and Mn^{4+} (0.53 Å).[205] Although such TM ordering is thermodynamically favorable, it may be dependent on the synthesis method. This may explain why some previous reported sodium layered cathode materials containing Li/Ni/Mn do not have TM layer ordering.[240]

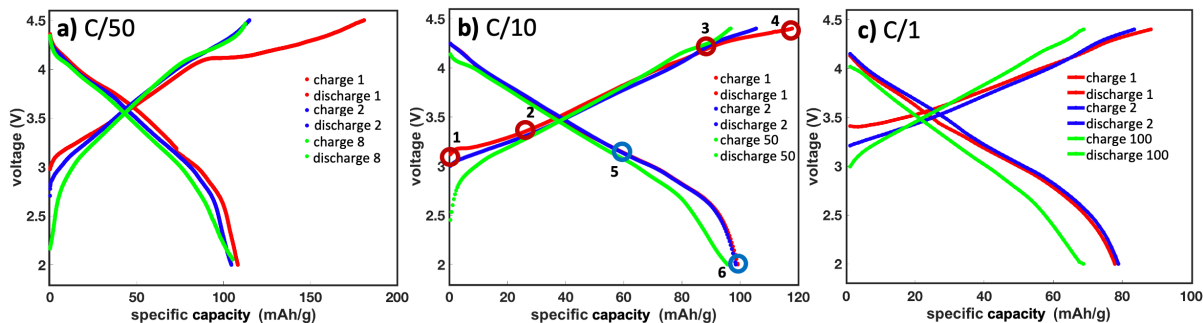


Figure 5.2: Voltage profiles of NLNMO half cells cycled at rates of (a) C/50, (b) C/10, and (c) C/1. In voltage profile (b) the numbers mark the voltages where *ex situ* XAS data was recorded.

To explore the electrochemical properties of NLNMO, half cells, with sodium metal as the anode, were prepared and cycled in galvanostatic mode at various rates, C/1, C/10, and C/50 where the theoretical capacity is 118 mAh/g based on the $\text{Ni}^{2+}/\text{Ni}^{4+}$ redox (**Figure 5.2**). At a rate of C/50, there is a prominent voltage plateau in the first charge voltage curve between 4.2-4.4V (**Figure 5.2(a)**). This plateau increases the first charge capacity from 118 mAh/g to 180 mAh/g. The extent of the high voltage plateau during the first charge is rate dependent. At a faster rate of C/10 (**Figure 5.2(b)**), the high voltage plateau is reduced but still contributes ~ 20 mAh/g to the first charge capacity. For a fast rate of C/1 (**Figure 5.2(c)**) no plateau is observed in first charge. Given the capacity limitations of the Ni redox, high charge capacity at slow rates cannot solely be the result of the $\text{Ni}^{2+}/\text{Ni}^{4+}$ redox. Because the high voltage plateau is rate dependent and does not contribute to the discharge capacity or subsequent cycles, irreversible oxygen redox could be the origin. Furthermore, in previous literature of NLNMO, neither a high voltage plateau during the first charge nor superlattice ordering in the XRD data were reported.[89] The TM ordering in NLNMO of this study may alter the oxygen bonding environment and this triggers oxygen redox. The extra capacity disappears for subsequent cycles at all rates. This suggests that the environment of the oxygen atoms likely changes after the first charge, which inhibits further oxygen redox. The

environment and oxidation states of NLNMO are thus explored to determine the source of the high voltage plateau.

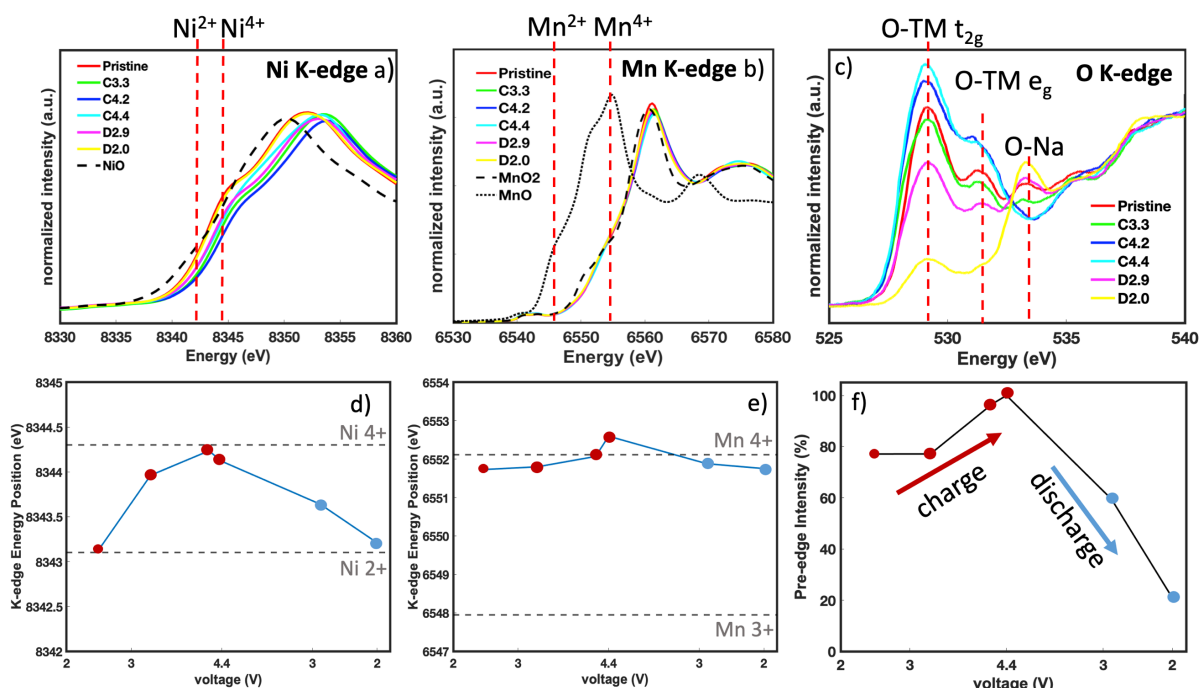


Figure 5.3: The *ex situ* XANES spectra and respective positions of the (a,d) Ni K-edge, and (b,e) Mn K-edge of NLNMO at different states of charge. (c) *ex situ* XANES spectra of the O K-edge (FY mode) and the (f) integrated pre-edge intensity of the O K-edge at different states of charge.

To investigate the high-capacity origin in the meso-structure controlled NLNMO, the evolution of the oxidation state and local environment of Mn, Ni, and O were probed by XAS. *Ex situ* samples of NLNMO were prepared at six different states of charge and discharge as shown in **Figure 5.2(b)**, including pristine, charging to 3.2V, 4.2V and 4.4V (red circles and prefixed as “C”), and then discharging to 2.9V and 2.0V (blue circles and prefixed as “D”). X-ray absorption near edge spectroscopy (XANES) spectra at Ni K-edge and Mn K-edge are shown in **Figure 5.3(a)** and (b). Based on comparison with standard references (NiO, MnO, Mn₂O₃, and MnO₂), the pristine NLNMO is suggested to predominantly consist of Mn⁴⁺ and Ni²⁺. The Mn K-edge shifts negligibly during the first cycle (**Figure 5.3(e)**), signifying that Mn does not participate in the electrochemical charge transfer reaction. On the other hand, Ni K-edge shifts to higher energy

when charged to 4.2 V, indicating that Ni^{2+} has been oxidized to Ni^{4+} (**Figure 5.3(d)**). The Ni K-edge at 4.4 V is shifted to lower energy than the edge at 4.2 V. This implies that between 4.2 V and 4.4 V, Ni is slightly reduced even though that region of the voltage curve delivers 30 mAh/g of capacity. Given that $\text{Ni}^{2+}/\text{Ni}^{4+}$ redox occurs below 4.2 V, a different charge transfer mechanism must contribute to the capacity in the high voltage plateau between 4.2-4.4 V. This high voltage mechanism is not Mn redox because, based on the XANES Mn K-edge observations, Mn^{4+} is redox inactive. Therefore, it is likely that oxygen participates in the high voltage charge compensation process, similar to other layered sodium cathode materials with oxygen redox activities.[42,230] To further explore this charge compensation process in NLNMO at high voltage, the O K-edge was used to investigate oxygen's participation in the redox mechanism.

The pre-edge peak position and intensities of the O K-edge XANES spectra can provide structural and chemical bond information between the oxygen and transition metal species, as shown in **Figure 5.3(c)**. The O K-edge can be divided into two regions: the pre-edge peaks below 535 eV, which correspond to electronic transitions from the O 1s state to the O 2p-TM 3d hybridized state, and the broad peaks above 535 eV, which correspond to transitions to O 2p-TM 4sp hybridization states.[241] For the lower energy peaks, the possible O K-edge sXAS transitions anticipated for these states are shown in **Figure D.2**. The dominant TM ions in NLNMO at 4.2 V are Mn^{4+} ($3d^3$) and Ni^{4+} ($3d^6$).[219] There are seven possible sXAS transitions associated with Mn^{4+} : three spin-down t_{2g} , two spin-up e_g , and two spin-down e_g . For Ni^{4+} , there are four possible sXAS transitions: two spin-up e_g and two spin-down e_g transitions. Given that per unit formula $\text{Mn}^{4+}=0.66$ and $\text{Ni}^{4+}=0.22$, Mn^{4+} accounts for 84% of the expected sXAS transitions to the unoccupied states and thus dominates the spectrum. The peaks around 529 eV and 532 eV can be assigned to the unoccupied hybridized orbitals of O 2p-TM t_{2g} and O 2p-TM e_g respectively.[240]

The O K-edge spectrum of pristine NLNMO shows a peak at 534 eV, which is ascribed to the unoccupied hybridization orbital of O 2p-Na 3p, and its intensity reflects the amount of Na in the lattice.[242] As the NLNMO is charged, the O 2p-Na 3p signal diminishes, in agreement with desodiation. The peak intensity of O 2p-TM t_{2g} and e_g increase upon charging, which indicates hole generation in the O 2p-TM orbital. Hole generation in the O 2p-TM orbital could be created to compensate the positive charge of the Na^+ ion leaving the cathode structure. Although O K-edge alone cannot prove the electron holes in oxygen are present due to strong hybridization of O 2p-TM, it is highly likely given the observations that Mn remains in the 4+ state and Ni becomes slightly reduced at the fully charged state.[237]

On discharge, the peaks due to O 2p-TM t_{2g} and O 2p-TM e_g decrease and the O 2p-Na 3p peak increases upon sodiation. At the fully discharged state (2.0 V), the O-TM t_{2g} and O-TM e_g signals are minimized, with lower intensity than the pristine state. This may indicate an irreversible change in the TM-O bond, which may inhibit further oxygen redox. Oxygen loss from the lattice during the first charge is common in oxygen redox cathode materials and may contribute to the irreversible capacity loss seen in NLNMO.[179] The Ni K-edge is shifted to lower energy upon discharge and at the fully discharged state, the Ni ions are reduced back to their divalent state. This demonstrates that the Ni redox reaction is completely reversible, unlike the case of irreversible oxygen redox. Mn K-edge shifts negligibly during discharge, implying that it stays electrochemically inactive.

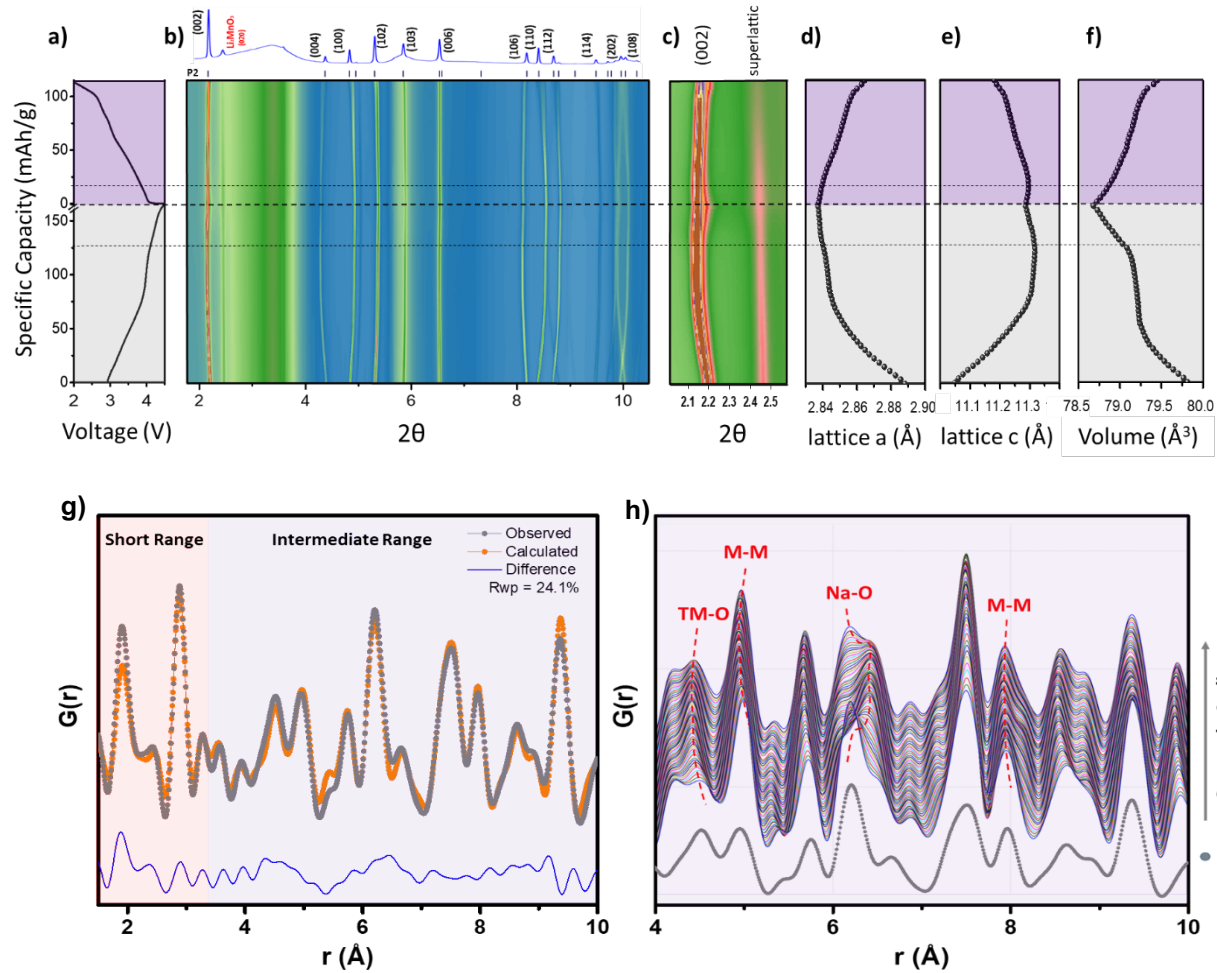


Figure 5.4: (a) voltage profile of the initial cycle of NLNMO in the operando sXRD data collection; (b) contour plot of the sXRD pattern obtained over cycling; (c) magnified (002) peak and superlattice peak region; (d) lattice a , (e) lattice c and (f) unit cell volume obtained from Rietveld refinement; (g) refinement of PDF pattern of pristine NLNMO powder, detailed refinement results are listed in SI table 3; (h) operando PDF of NLNMO during first cycle between 2.0 – 4.4 V.

The structure changes of NLNMO during the first electrochemical cycle were explored with operando sXRD shown in **Figure 5.4**. The operando cell has a specific charge capacity of 165 mAh/g and a specific discharge capacity of 113 mAh/g. The collected sXRD patterns over cycling were plotted into a contour plot and shown in **Figure 5.4(b)**. All the peaks in the data can be well indexed to $P6_3/mmc$ space group, except for the peak at $2\theta = 2.46^\circ$. This peak is at the position of Li_2MnO_3 (0 2 0) peak and is known as a superlattice peak in layered structures and

corresponds to a honeycomb superstructure within the TM layer. [243,244] After the initial cycle, the XRD patterns indicate that the P2 structure remains with slight peak position shifts, which will be quantified with lattice parameter changes later. A magnified region of the (002) peak and the superlattice peak is presented in **Figure 5.4(c)**, where a decrease of the superlattice peak intensity can be observed during the first cycle. As a comparison, the (002) peak maintains the same intensity level during the whole cycle, with the peak shifting in both charge and discharge process. The decrease of superlattice peak after cycling indicates severe degradation of the TM ordering in the TM layer in NLNMO. Such degradation corresponds to the loss of the honeycomb superstructure within the TM layer that may be caused by migration of TM ions in the structure.[233,238]

The changes in the overall crystal structure are characterized with a/c lattice parameters change through Rietveld refinement (**Figure 5.4(d,e)**). The pristine material has a lattice a parameter of 2.89 Å that shrinks to 2.83 Å at the end of the first charge. The reduction in the a lattice parameter corresponds to shortening TM-TM bonds due to oxidation of the TM upon charging.[89] During the discharge, the a lattice parameter increases due to reduction of the TMs and returns to 2.86 Å at the end of the discharge. Lattice parameter a cannot fully return to its initial state due to decreased ordering of the TM layer which inhibits bond lengths from returning to their original state.

The changes in the c lattice parameter over cycling are more complex than the changes in lattice a . The c lattice parameter is 11.05 Å in the pristine state and it increases to a maximum of 11.32 Å around 4.05 V in the charging, and then decreases to 11.29 Å at the end of charge. The initial increase in the c lattice parameter is due to the increased electrostatic repulsion between the negatively charged oxygen layers along with the removal of the positively charged sodium ions.

The following decrease of the c lattice parameter from 4.05 V to 4.4 V could be due to the oxidation of oxygen which reduces the magnitude of repulsion between the oxygen layers. The magnitude of repulsion is decreased due to charge of oxygen reducing from -2 to a value closer to -1. During the discharge, the c lattice parameter increases first to 11.30 Å around 3.80 V and decreases to 11.18 Å at the end of discharge. Similar to the charge process, the oxidized lattice oxygen could initially be reduced, which increases the repulsion between the layers until 3.80 V and where the reduction of electrostatic repulsion by the addition of sodium ions reduces the c lattice parameter. And similar to a lattice parameter, the c lattice parameter cannot fully return to its initial state due to irreversible changes in TM layer ordering. The volume of NLNMO unit cell was calculated from refined a and c lattice parameters. The initial unit cell volume is 79.81 Å³ and decreases to 78.68 Å³ at the end of charge. It recovers in the discharge process and increases back to 79.45 Å³ in the end of discharge. Similar to lattice a and lattice c , the shrinking of the total volume cannot fully recover even at the end of discharge, indicating the loss of honeycomb ordering within the TM layer. The initial lattice parameters are essentially identical to the parameters of previously reported structures but have larger changes during the charging and do not return to their initial states, indicating a different mechanism of redox reactions in the material reported here.[245]

The overall structure of NLNMO was explored with sXRD and the loss of TM ordering within the TM layer is observed with the severe decrease of superlattice peak. The local environment of NLNMO was probed with pair distribution function (PDF) shown in **Figure 5.4(g,h)**. PDF results of pristine NLNMO powder were refined through small box (unit-cell based) refinements. The observed PDF pattern matches the calculated pattern from $P6_3/mmc$ space group. The a and c lattice parameters obtained from PDF refinement ($a = 2.88$ Å, $c = 11.00$ Å) are consistent with the Rietveld refined values from sXRD. The anisotropic thermal displacement

parameter was modeled as U12 in the PDF refinement and shows an increase in the refinement liability, which indicates anisotropic behavior of this material.

The changes of local environment in NLNMO over cycling was studied with operando PDF (**Figure 5.4(h)**). A series of PDF patterns were collected while an NLNMO AMPIX cell was charged to 4.4 V and discharged to 2.0 V. The peak positions of different local bonding species evolve distinctly during cycling. The bond length of M-M bonds (M = Na, Li, Ni, Mn) decreases during charge and increases during discharge, which is in good agreement with the decreased lattice parameter a observed in sXRD. The decrease of M-M bond length during charge is primarily caused by the oxidation of TM ions, and this bond length increases during discharge as the TM ions are reduced. Similarly, the TM-O bond length is observed to decrease during charging and the bond length increases during discharging (TM = Ni, Mn, Li as here Li are within the TM layer). The potential contribution of oxygen redox was also investigated with the changes of Na-O bond length in operando PDF. In the charge process, an increase of Na-O bond length was initially observed, followed by a slight decrease at the end of the charge. The initial increase of Na-O bond length is caused by the reduced electrostatic attraction between oxygen and sodium ions with the removal of positively charged sodium ions. At high voltage, the decrease of the Na-O bond length can be explained by the oxidation of the oxygen ions, as this increases the electrostatic attraction between oxygen and sodium ions. During discharge, the Na-O bond length slightly increases in the beginning, followed by a continual decrease until the end of discharge. The oxidized lattice oxygen could initially be reduced, which leads to a decrease of electrostatic attraction between oxygen and sodium ions, until enough sodium ions intercalate back into the structure to provide increased attraction. It is noticeable that the changes of Na-O bond length in PDF are remarkably similar to the changes of the c lattice in sXRD. The changes in the Na-O bond length in PDF

matches well with our analysis of the pre-edge intensity changes of O K-edge in XAS and with the proposed oxygen redox activity at high voltage.

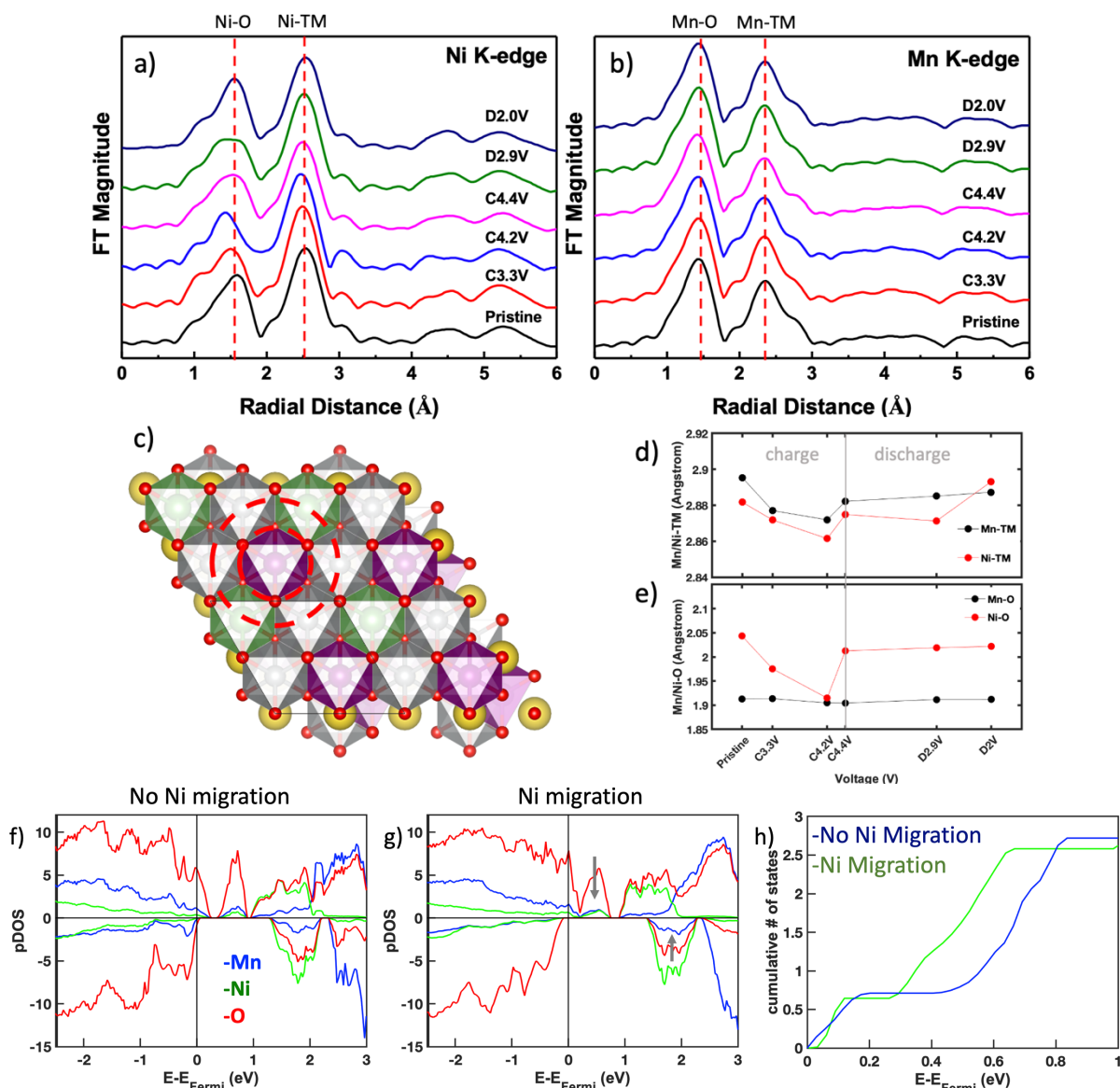


Figure 5.5: *Ex situ* EXAFS spectra of NLNMO at (a) Ni K-edge and (b) Mn K-edge at different states of charge. (c) A model of the crystal structure of NLNMO with the first two nearest neighbors starting from the atom centered in the circled in dashed red lines. (d) The bond length of Mn/Ni-TM and the (e) bond length of Mn/Ni-O at different states of charge. The black points represent the Mn- bonds while the red points represent the Ni-bonds. DOS near the Fermi level for fully charged NLNMO with (f) no Ni migration and (g) with Ni migration. (h) The cumulative number of unoccupied oxygen states above the Fermi level.

The higher energy region of XAS, known as extended x-ray absorption fine structures (EXAFS), can provide information about both the local structure and oxidation states of the

irradiated material. Herein, the Fourier transformed EXAFS spectra for NLNMO (**Figure 5.5(a,b)**) at Mn and Ni K-edges are studied to quantify the changes of Ni and Mn local ordering. EXAFS analysis is a powerful method to determine the local interatomic distances in TM oxides, and the best-fit values of the structure parameters used for NLNMO are listed in **Tables 5.1**. In Mn and Ni K-edge EXAFS spectra, the first intense peak corresponds to the TM-O distance in the first coordination sphere and the second intense peak correspond to the TM-TM distance (**Figure 5.5 (c,d,e)**). The magnitudes of the TM-O and TM-TM bonds for both Mn K-edge and Ni K-edge are compared and shown in **Figure D.3** with blue lines as guides. The Mn-O peak has a larger magnitude than the Mn-TM peak whereas the Ni-O peak has a smaller magnitude than the Ni-TM peak. Ni and Mn have higher electron backscattering ability than Li because they have higher atomic numbers. Since the Mn-TM peak has a smaller magnitude than Ni-TM peak, it is inferred that Mn atoms typically surround Li atoms in the TM layer. Ni atoms may be mostly surrounded by other Ni atoms and Mn atoms, which increases the magnitude of the Ni-TM peak. The preferred transition metal positioning observed in the EXAFS data is corroborated by the findings in the sXRD data. The Mn atoms surrounding Li atoms can together form the partially ordered LiMn_6 honeycomb structures,[246] which lead to the superlattice peak observed in sXRD. TM layer ordering in 4d TM sodium cathodes has been shown to alter the oxygen bonding to trigger oxygen redox.[240] This same phenomenon can be seen for the NLNMO reported here for 3d TM sodium cathodes, enabling a new route for oxygen redox.

Tables 5.1 a & b: *Ex situ* EXAFS fit results for indicated samples collected at the Mn K-edge (Table 5.1a) and the Ni K-edge (Table 5.1b). The phase-corrected bond length (R) and Debye-Waller factor (σ^2) are shown for each interaction.

a) EXAFS fit results for Mn K-edge.

Sample	Pristine	c3.3 V	c4.2 V	c4.4 V	d2.9 V	d2.0 V
R_{Mn-O} (\AA)	1.913	1.913	1.904	1.904	1.912	1.912
R_{Mn-TM} (\AA)	2.895	2.877	2.872	2.882	2.885	2.887
$\sigma_{Mn-O} \times 10^{-3}$	3.5	3.8	4.1	4.5	3.5	3.6
$\sigma_{Mn-TM} \times 10^{-3}$	4.4	4.6	5.1	5.6	4.5	4.6

k-range: 2.566 - 13.167, R-range: 0.873 - 3.085

b) EXAFS fit results for Ni K-edge.

Sample	Pristine	c3.3 V	c4.2 V	c4.4 V	d2.9 V	d2.0 V
R_{Ni-O1} (\AA)	2.043	1.975	1.9148	2.0127	2.019	2.022
R_{Ni-TM} (\AA)	2.882	2.872	2.861	2.875	2.871	2.893
R_{Ni-O2} (\AA)	3.361	3.356	3.414	3.378	3.343	3.358
$\sigma_{Ni-O1} \times 10^{-3}$	6.3	10.3	11.0	10.2	11.0	6.7
$\sigma_{Ni-TM} \times 10^{-3}$	5.6	5.0	5.3	6.2	5.3	5.7
$\sigma_{Ni-O2} \times 10^{-3}$	4.8	3.9	5.0	6.5	5.1	4.9

k-range: 2.566 - 13.167, R-range: 1.169 - 3.420

In the charge process, as sodium is extracted from the crystal lattice, the first coordination Ni-O interatomic distance changes clearly whereas the Mn-O distance has negligible changes. The Ni-O interatomic distance decreases during charge to 4.2 V, representing the Ni oxidation during charge. From 4.2 V to 4.4 V, the Ni-O interatomic spacing increases, which implies a slight reduction of Ni oxidation state at high voltage, thus indicating a different reaction pathway related to oxygen activity. After discharge to 2.0 V, the Ni-O interatomic distance exhibits little change compared to the pristine state, showing that the Ni oxidation is mostly reversible. This is in good agreement with the data from the XANES spectrum that Ni redox reaction is reversible whereas Mn remains inactive during charge and discharge. The TM ordering within the TM layer can be evaluated by the Debye-Waller factor (σ) as well as the peak intensity of Ni-O and Mn-O peaks in EXAFS. The Debye-Waller factor (σ) reflects the random thermal and static vibrations of the absorbing atoms around their equilibrium atomic positions. Larger values of the Debye-Waller factor are a result of structure distortions that deviate from the ideal model.[70] As displayed in **Tables 5.1**, the Debye-Waller factor increases for TM-O during charging, which indicates

structure distortion of the TM-O bond. Specifically, the Ni-O Debye-Waller factor increases significantly during charging, indicating that the NiO₆ octahedron distorts more than the MnO₆ bond during cycling. This increased distortion during charging may signify a change in Ni-O covalency through the creation of unsymmetrical oxygen bonds. This distortion could also be caused by the migration of Ni from its pristine state. The peak intensity of Ni-O and Mn-O peak in EXAFS are also compared in **Figure D.3**, where a drop of peak intensity in TM-O bond is seen at high voltage, especially for the Ni-O case. The peak height is highly dependent on the system ordering; thus, the large drop of Ni-O peak intensity indicates severe disruption of the local TM-O honeycomb ordering, which can result from the TM migration.

To further explore the local TM migration and the effect of the loss of TM ordering, density of states (DOS) were calculated for NLNMO at fully charged state with and without Ni migration (**Figure 5.5** (f,g) and **Figure D.4**). At high voltage, undercoordinated oxygen can lead to a slight reduction of TM. This can induce electron transfer from the O to the TM, causing O₂ gas release along with the reduction of TM.[231] Oxygen gas release has been reported during the high voltage region in other Ni containing oxygen redox active cathodes.[247] TM reduction is also observed in our Ni XAS results where Ni is reduced from 4.2 to 4.4V. After Ni migration, there is a reduction of the number of unoccupied oxygen states above the Fermi level (**Figure 5.5** (f,g), **Figure D.4**). This can inhibit oxygen reduction upon cell discharge, resulting in irreversibility during the first cycle. The combination of oxygen loss and Ni migration can result in irreversible oxygen redox activity that will lead to reduced capacity in the following discharge.[212]

This experimental study of the origin of the irreversible oxygen redox activity combined with information gleaned through literature review, reveals that the inclusion of Ni is detrimental to the reversibility of oxygen redox at high voltage in NIBs. The inclusion of Ni may enable

irreversible O₂ gas release, and Ni migration within the structure can alter the bonding environment of oxygen so that it is not favorable for further oxygen redox activity. To mitigate O₂ gas release, other TMs, such as Fe, should be included to enhance TM-O hybridization.[247] Unlike LIB cathode materials, the inclusion of Ni in sodium cathodes that exhibit oxygen redox due to TM ordering should be carefully managed to optimize the reversibility of oxygen redox activity at high voltage.

5.4 Conclusions

Meso-structured controlled P2-type Na_{0.8}Li_{0.12}Ni_{0.22}Mn_{0.66}O₂ (NLNMO) was synthesized by meso-structure controlled carbonate co-precipitation with transition metal layer ordering in the pristine structure as confirmed by sXRD and EXAFS. NLNMO, synthesized in this study, has a rate dependent plateau during the first charge, which likely indicates oxygen redox activity. To evaluate the redox activities of NLNMO at high voltage, *ex situ* XAS was used to observe the O K-edge, Ni K-edge, and Mn K-edge during the first electrochemical cycle. An increase in the O pre-edge integrated intensity was observed from 4.2 V- 4.4 V whereas the Mn K-edge shifted negligibly, and Ni was reduced in this voltage range. This indicates that oxygen redox activity is responsible for the plateau at high voltage during the first charge. After the first charge, the plateau disappears and will not appear in the following cycles: the superlattice peak observed in sXRD also diminish after first cycle, indicating loss of ordering in the TM layer. Ni migration was studied through EXAFS and DOS and is considered to be responsible for the loss of TM layer ordering and the decrease of available states in oxygen above Fermi level. This change of oxygen environment, along with O₂ gas production, is likely the cause of the irreversibility of oxygen redox. Through this work we demonstrated that the inclusion of Ni in sodium cathodes is detrimental to the reversibility of oxygen redox at high voltage. This work emphasizes the

importance of TM layer ordering on inducing oxygen redox activity and reveals the unfavorable effect that Ni has on its reversibility. As such, future compositional design of sodium cathodes should avoid adoption of high Ni content in order to enhance reversible oxygen redox and achieve energy-dense and long-lasting sodium cathodes.

Chapter 5, in full, is a reprint of the material, “The Negative Impact of Transition Metal Migration on Oxygen Redox Activity of Layered Cathode Materials for Na-ion Batteries” as it appears in the Journal of The Electrochemical Society, H. S. Hirsh, Y. Li, J. H Cheng, R. Shimizu, M. Zhang, E. Zhao, Y. S. Meng, 2021, 168, 040539. The dissertation author was the co-primary investigator and author of this paper. The author performed the materials synthesis, electrochemical test, SEM, XRD, and data interpretation and analysis.

6.1 Introduction

Low-cost and reliable energy storage is essential for a safe, stable, and sustainable electrical grid. [21,177] Sodium-ion batteries (NIBs) with Co and Ni free cathodes are one of the promising solutions for grid energy storage, considering elemental abundance and their environmentally benign nature.[101,178] While the energy density of NIB cathodes has increased over the years, the commercialization of NIBs for grid energy storage is hindered by the inferior electrochemical performance of sodium anode materials.[178] Graphite, a common anode material for conventional lithium-ion batteries (LIBs), is not applicable for NIBs due to its negligible reversible capacity in carbonate-based electrolytes.[248] Though glyme-based electrolytes enable reversible capacity of sodium in graphite through solvent co-intercalation, the capacity is limited to ~100 mAh/g, and the reaction potential increases to about 0.75 V vs. Na metal.[249] Alternative anode materials for NIBs include sodium metal which has the highest theoretical capacity (1166 mAh/g) and lowest reaction potential, but it has severe safety hazards and a short lifetime.[250] Alloy and conversion types of anodes, such as Sn and SnO₂, also have high capacity, yet poor lifetimes caused by large volumetric changes during electrochemical cycling.[127,251] Insertion compounds, such as NiCoO₂O₄ and TiO₂, have relatively high average voltages (>0.5 V vs Na⁺/Na⁰), which reduce the energy density of a full cell. [153,252] Other anode materials like soft carbon and reduced graphene oxide also have high average voltages and shortened lifetimes due to low first cycle Coulombic efficiencies (CEs) (less than 60%).[253,254] A promising exception is hard carbon (HC), which has been widely investigated as an anode material for NIBs because it is relatively safe, has a high capacity (> 200 mAh/g), and has a low reaction potential near 0 V vs. Na⁺/Na⁰.

By definition, HC, also known as non-graphitizing carbon, cannot be converted into graphite through heat treatment. It contains regions of parallel groups of graphite-like layers with no long-range order that form voids between the groups of layers. An additional advantage is that HC can be sustainably synthesized from biomass precursors such as banana peels, corn husks, peanut shells, as well as polymer/plastic derivatives.[118,120,255–257] The HC bulk structure, governed by the synthesis conditions, determines its electrochemical properties and performance.[258,259] Previous research has discovered ways to optimize the HC bulk structure (defects, surface area, graphitic like regions, and voids) for maximum capacity, CE, lifetime, and lowest average voltage.[258]

Even with an optimized bulk structure, the low first cycle CE and poor rate capability of HC have hindered its use in NIB full cells. The first cycle CE of HC in high performing carbonate electrolyte is between 60-80% at a rate of C/20, and only ~30% of the capacity is retained at a higher rate.[260] A low first cycle CE limits the lifetime of a battery because it reduces the total amount of sodium available in the system. This is especially problematic for commercialized cells where the only sources of sodium are from the cathode material and the lean amount of electrolyte. In literature, it has been proposed that the low first cycle CE is a result of trapped sodium in the bulk structure.[124,258,261] In addition, a battery that has excellent rate capability is essential for grid storage applications. Solutions for grid storage handle power fluctuations, which would be severely impaired by a poor rate performing battery.[262] The origin of the poor rate capability is proposed to be dictated by the poor kinetics of sodium filling the HC structural voids during the plateau region of the voltage curve.[258,263]

However, recent research suggests the first cycle CE and rate performance is not solely determined by the HC bulk structure but is also highly dependent on the choice of electrolyte.[264]

For example, an HC anode with an ether-based electrolyte (1M NaBF₄ in TEGDME) has shown a first cycle CE of 87% and a retention of 84% of its C/20 capacity at 2C.[264] Electrolyte is known to have a major role in the formation of the solid electrolyte interphase (SEI). An ideal SEI that inhibits parasitic reactions between the HC surface and the electrolyte should be thin, ionically conductive, conformal, and robust. These aspects can affect both the first cycle CE, through consumption of sodium-ions, and rate performance, through impedance at the interface. This raises the question that if the first cycle CE and rate capability are controlled by the HC bulk structure or by the SEI formation.

Properties of the SEI can vary with different electrolytes and electrochemical testing conditions. However, minimal research has been conducted on the formation of the SEI on HC, with most of the focus on carbonate-based electrolytes (summary in **Table 6.1**). Moreover, in the few studies that used non-carbonate electrolytes (TMP, DEGDME), the exact chemical composition and SEI morphology were not examined.[265,266] Previously, quantifying the consumption of Na⁺ due to the SEI formation and observing the SEI's morphology at the nanoscale (HC is a beam-sensitive material) were very challenging. Due to the recently developed techniques such as titration gas chromatography (TGC) and cryogenic transmission electron microscopy (cryo-TEM), the SEI can now be better characterized. [267]

Table 6.1: Summary of electrolytes and techniques used to characterize the SEI of HC in literature.

Electrolyte	Technique	Washed?	SOC	Rate	Citation
1M NaClO ₄ in PC 1M NaClO ₄ in EC:PC 1:1 1M NaClO ₄ in EC:PC 1:1 w/ 10% DMC 1M NaPF ₆ in EC:PC 1:1 w/ 10% DME	XPS peak fitting	DMC	sodiated	C/20	[268]
0.5M NaBOB in TMP 1M NaPF ₆ in TMP	XPS peak positions	TMP	1 cycle	C/10	[265]
0.8 M NaPF ₆ in DEGDME 0.8 M NaPF ₆ in EC:DEC 1:1	XPS elemental content, SEM	DMC	15 cycles	C/6	[266]
1M NaPF ₆ in EC:DEC 1:1 1M NaClO ₄ in EC:DEC 1:1 1M NaTFSI in EC:DEC 1:1 1M NaFTFSI in EC:DEC 1:1 1M NaFSI in EC:DEC 1:1	XPS peak fitting & elemental content	DMC	sodiated	C/20	[269]
3M NaFSI in PC 3M NaFSI in PC:EC	XPS peak fitting, TEM	PC	5 cycles	C/10	[270]
1M NaClO ₄ in PC 1M NaClO ₄ in PC w/ 0.5% FEC 1M NaClO ₄ in PC w/ 2% FEC 1M NaClO ₄ in PC w/ 10% FEC	XPS peak positions, SEM	Not listed	1 cycle	C/10	[271]
1M NaClO ₄ in PC:EC 1:1	XPS peak positions, SEM	Not listed	sodiated, desodiated	C/6	[116]
1M NaClO ₄ in PC	XPS peak positions, TOF-SIMS, TEM	Not listed	1 cycle	C/10	[129]
1M NaPF₆ in PC 1M NaBF₄ in TEGDME	XPS peak fitting & elemental content, SEM, EDS, Cryo-TEM	Washed with PC or TEGDME and Unwashed	sodiated, desodiated	C/3, C/10, C/20	This paper

In this study, we explored the origin of the first cycle CE and rate capability of HC in two electrolytes: conventional carbonate electrolyte and ether electrolyte. Electrochemical testing, TGC, and *ex-situ* Raman spectroscopy were applied to observe the (de)sodiation processes and the reversibility of metallic sodium in the HC bulk structure. Cryo-TEM, scanning electron microscopy (SEM), energy dispersive X-ray spectroscopy (EDS), and X-ray photoelectron spectroscopy (XPS) were used to characterize both the morphological and composition changes of the SEI for carbonate- and ether- based electrolytes at three different cycling rates. A long-term electrochemical study of HC in these two electrolytes was used to determine how the SEI formation affects the lifetime of the anode material. These techniques demonstrate that SEI is the dominant influence on both the first cycle CE and rate capability of HC.

6.2 Methods

6.2.1 Electrochemical Characterization

Composite anodes were prepared by mixing a slurry of 90.4 wt. % HC (Xiamen Tmax Battery Equipments Limited) and 9.06 wt. % carboxy methyl cellulose sodium salt (CMC) 250,00 MW with DI water as the solvent. The slurry was cast onto aluminum foil and dried under vacuum at 80°C overnight. Na metal was used as the counter electrode. 1M NaPF₆ in PC was used for the conventional carbonate electrolyte cells, and 1M NaBF₄ in TEGDME was used for the ether-based electrolyte cells. For all cells, except those used for TGC measurements, 50 μL of electrolyte and one layer of glass fiber GF/F (Whatman) was used as the separator. Cells used for TGC measurements had 70 μL of electrolyte and two layers of glass fiber GF/F (Whatman) as the separator. Electrodes 14 mm in diameter with an active mass loading of 3.2-4.0 mg/cm² were assembled in 2032 coin cells in an argon-filled glove box (H₂O < 0.1 ppm) and tested on an Arbin battery cycler. Coin cells were allowed to rest 8 h before electrochemical tests were performed. The voltage range was maintained between 0.005V-2 V and the C-rates were calculated, assuming a theoretical specific capacity of 150 mAh/g. Electrochemical impedance spectroscopy (EIS) was carried out with 10 mV perturbation and AC frequencies from 100 kHz to 1 mHz. A SP-150 Biologic Potentiostat was used to measure impedance after 1 cycle at a rate of C/3. An equivalent circuit model was used to fit and analyze the data using Zview software (v. 3.4a, Scribner Associates, Inc.)

6.2.2 Materials Characterization

TGC was performed using a Shimadzu GC instrument equipped with a BID detector and using an ultra-high purity Helium (99.999%) as the carrier gas. The samples were prepared in an argon-filled glovebox (H₂O < 0.1 ppm). Each sample was immediately transferred to a glass flask

after disassembling and sealed using a septum under Argon. Then, 0.5mL of ethanol was injected into the container to fully react with ionic and metallic sodium. After the reaction is completed, a 30 μ L gas sample was taken from the container using a gastight Hamilton syringe and immediately injected into the GC. The amount of ionic and metallic sodium was quantified based on the amount of detected H₂ gas by the GC.

Raman spectroscopy was performed using Renishaw inVia Raman Microscope. The samples were sealed between two very thin transparent glass slides in an argon-filled glovebox (H₂O < 0.1 ppm). The measurements were run using a 532-nm laser source, 1800 1/mm grating, and x20 magnification.

The morphology of the electrodes was identified using an FEI Apreo SEM equipped with EDS operating at 3 kV. For the cryo-TEM sample preparation, a TEM grid was directly dropped into the pristine HC powders to pick up the particles. For the cycled HC particles, the sample particles were first dispersed in the corresponding electrolyte solvents (PC or TEGDME), then the particle suspension was dropped onto the TEM grid. The TEM grids with particle suspension were dried under vacuum overnight. Once dried, the sample grids were sealed in airtight bags before being transferred to the TEM facility. The grids were mounted onto a TEM cryo-holder (Gatan) via a cryo-transfer station. TEM characterizations were carried out on JEM-2100F at 200 kV.

XPS was performed using an AXIS Supra by Kratos Analytica. XPS electrode samples were disassembled and removed from their cells. Washed samples were washed with either PC or TEGDME and then dried under vacuum. Unwashed samples were directly dried under vacuum. The XPS was operated using an Al anode source at 15 kV, scanning with a step size of 0.1 eV and 200 ms dwell time. Fits of the XPS spectra were performed with CasaXPS software to identify the chemical composition of the surface of the electrodes.

6.3 Results and Discussion

6.3.1 Electrochemical performance comparison with different electrolytes

Electrochemical measurements provide insight into the origin of the first cycle CE and rate capability of HC in PC electrolyte in comparison to that in TEGDME electrolyte. To investigate cycling rate dependence, HC was electrochemically tested at three different rates ($C/20$, $C/10$, and $C/3$). The results are shown in **Figure 6.1**: 1) The HC cycled in the PC electrolyte has a lower first cycle CE than that in the TEGDME electrolyte at all rates (68.7% vs. 84.8% at $C/3$). This indicates that more sodium is trapped in the HC bulk structure or in the HC-SEI when cycled in PC electrolyte. 2) Overpotential increases significantly at faster rates for the PC electrolyte whereas the increase is less evident for the TEGDME electrolyte. This is exemplified by the differences of the plateau voltages, extracted from the low voltage peaks of the dQ/dV curves, for sodiation vs. desodiation as shown in **Figure E.1**. Larger overpotentials imply either slower reaction kinetics of the bulk (de)sodiation mechanism or an increase of interface resistance in the PC electrolyte system. 3) Reversible capacity for the PC electrolyte decreases rapidly, from 247.5 mAh/g at $C/20$ to 112.4 mAh/g at $C/3$, whereas the reversible capacity for the TEGDME electrolyte only slightly decreases, from 268.1 mAh/g at $C/20$ to 259.0 mAh/g at $C/3$. The section of the HC-PC voltage curve most effected by the current rate is the plateau region (**Table E.1**), corresponding to the void filling mechanism. The bulk structure and/or SEI formation phenomena are potentially responsible for the differences in the electrochemical performances of HC in the PC and the TEGDME electrolytes.

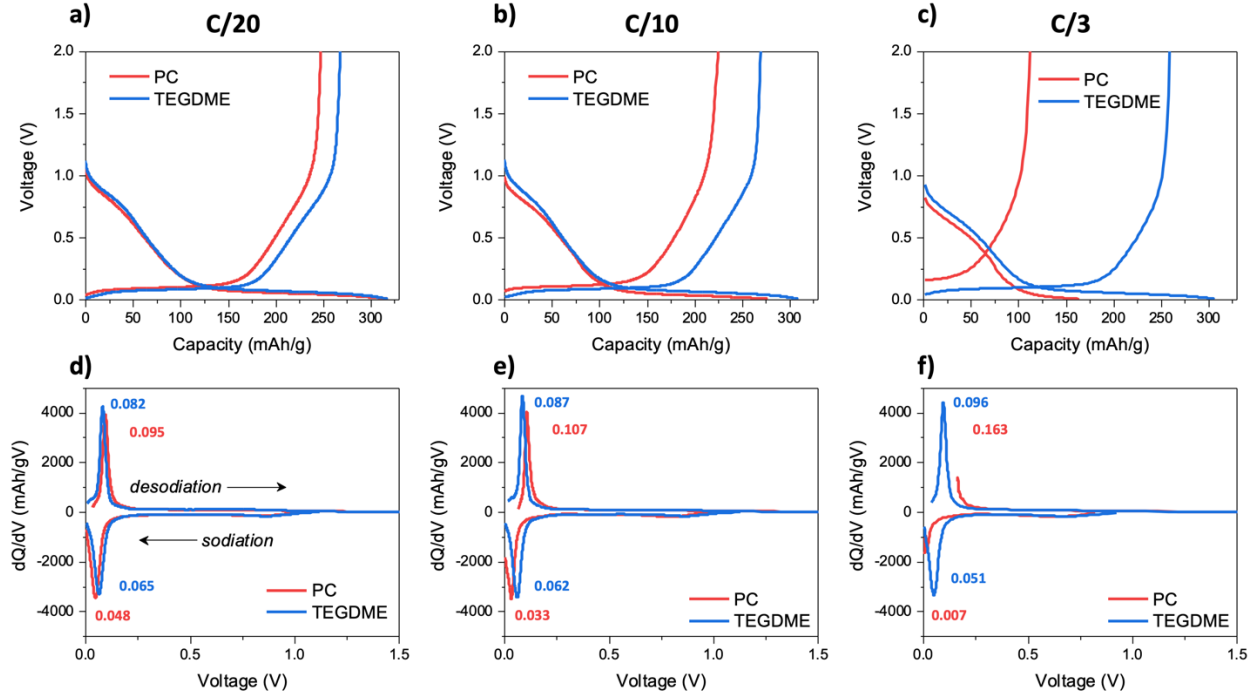
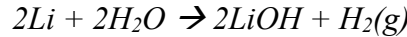


Figure 6.1: First cycle voltage profiles and their corresponding differential voltage plots of HC with PC (red) or TEGDME electrolyte (blue) at a rate of (a,d) C/20, (b,e) C/10, and (c,f) C/3. The numbers highlighted in the differential voltage plots indicate the plateau voltages during (de)sodiation.

6.3.2 Sodiation/desodiation processes of HC

To investigate the irreversible sodium that controls the first cycle CE of HC, TGC was used to separate the contribution of metallic sodium trapped in the HC bulk structure and the sodium in the SEI. This method was inspired by the Li metal TGC technique, first used to detect the mechanism of irreversible capacity for lithium plating/stripping.[267] The following reaction:

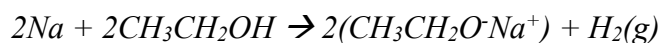


was applied to quantify the amount of residual metallic Li versus Li-containing compounds in the SEI on a stripped Li electrode. The TGC technique was also used to quantify the amount of metallic Li inserted into a graphite anode[272]:



This method works by measuring the amount of H_2 gas formed to calculate the amount of irreversible metallic Li in the electrode. The irreversible capacity, not accounted for by irreversible

metallic Li, is ascribed to the SEI formation. These two types of irreversible lithium can be separated because the SEI components do not react with water to form H₂ gas. In this study, ethanol was used as the titration solvent, because water could react with a possible SEI component, NaF, thereby forming HF. The potential reaction between HF and the aluminum current collector could then lead to the further generation of H₂. [273] Possible components of the SEI, along with the pristine HC electrode, were tested with the TGC method and none reacted with ethanol to form H₂ (**Table** and **Figure E.2**). It confirms that the H₂ gas was only produced by reacting ethanol with metallic sodium (Na⁰ and NaC_x) based on the following reactions:



The results of TGC tests are shown in **Figure 6.2**, where the calculated amounts of metallic Na at different states of charge for HC in PC and TEGDME electrolytes are compared. Both the PC and the TEGDME electrolytes show a volcano-like shape where the amount of sodium calculated from the electrochemical capacity is always larger than the amount of metallic sodium detected by TGC. This indicates that Na is involved in SEI formation throughout the first cycle. The amount of metallic sodium that can be stored in the HC bulk structure, is NaC₁₁ (theoretically NaC_{8.0} for a capacity of 280 mAh/g) for PC and NaC₉ for TEGDME. Assuming the SEI formation process is highly irreversible, the increase in the amount of metallic sodium stored in the HC bulk structure partially explains why TEGDME has a larger reversible capacity than PC. Additionally, there is negligible trapped metallic sodium detected in the HC bulk structure after one cycle for both electrolytes. Unlike the Li metal deposition and stripping, residual metallic sodium in the HC bulk structure is not the reason for the low first cycle CE. Instead, the first cycle CE of HC is more likely determined by the SEI formation process with Na inventory lost. The slight reduction of

sodium utilized in the SEI upon desodiation could be due to partially reversible SEI species. This conclusion is also in agreement with the observation reported in literature that HCs with larger surface areas have lower first cycle CEs due to more interphase reactions.[120,122,255,274,275]

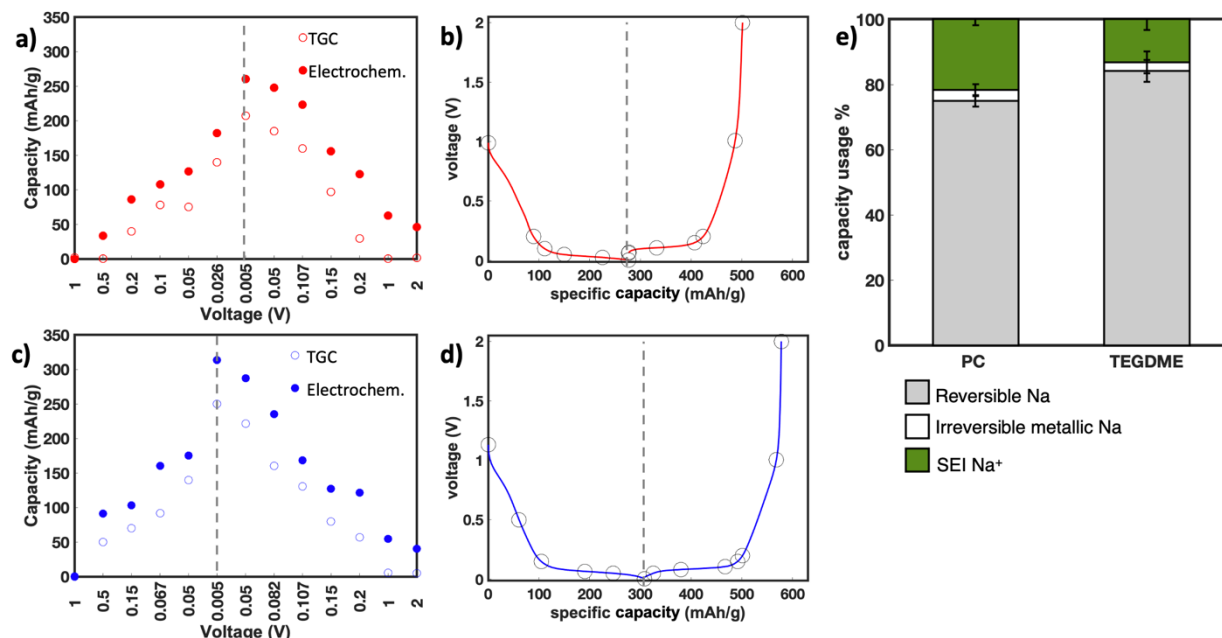


Figure 6.2: Sodium stored in the HC at different states of charge with PC (a,b) or TEGDME electrolyte (c,d) measured by TGC (open circles) and electrochemistry (filled circles) with their representative voltage profiles tested at a rate of C/10. (e) Analysis of capacity usage, reversible Na, metallic Na in bulk HC structure, and SEI Na⁺, for HC with PC and TEGDME electrolyte using the TGC method. The error bars represent the standard deviation from the average values of the measured metallic Na vs. SEI Na⁺.

The rate capability of HC has been proposed to be controlled by the kinetics of the sodium void filling mechanism, which occurs during the low voltage plateau.[258,263] If HC has similar (de)sodiation processes in the PC and TEGDME electrolytes, then it is unlikely that the kinetics of these processes control the rate capability of HC. Raman spectroscopy was used to study the (de)sodiation processes. As shown in **Figure 6.3**, the Raman spectra of pristine HC contain two characteristic peaks termed the G and D bands. The G band ($\sim 1580\text{ cm}^{-1}$) is characteristic of graphitic carbon and is related to the in-plane motion of the carbon atoms in graphene planes.[276] The D band ($\sim 1360\text{ cm}^{-1}$) is related to the presence of disorder or defects in the graphene planes.[277] The shift of these bands and/or the presence of a new peak can be induced by the

(de)sodiation processes. An initial inspection of the TEGDME and PC samples (**Figure E.3**) reveals that the two characteristic peaks remain visible for both systems throughout the first cycle and that no other peaks manifest. This implies that: 1) the HC structure remains intact and 2) there is no intercalation staging since there is no splitting of the G band.[278,279] These observations are in agreement with the current understanding of the sodium storage mechanism in HC and indicate that both electrolytes elicit similar (de)sodiation processes.

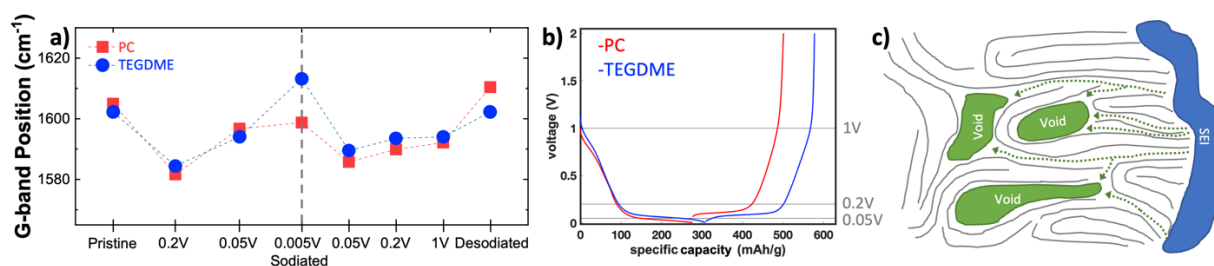


Figure 6.3: Raman spectra (a) G-band positions and (b) representative voltage curves for HC with PC or TEGDME as the electrolyte tested at a rate of C/10. (c) A schematic showing the sodium pathway (green dotted arrows) through the graphitic region of the HC structure to reach the structural voids.

In addition to the presence of the D and G bands, the position of the G band can reveal more information about the (de)sodiation processes (**Figure 6.3**). The G band position is controlled by both charge transfer and lattice parameter changes in the graphitic regions.[280] For both samples, the G band position initially has a red shift for the slope region and then a blue shift for the voltage plateau region during sodiation. Upon desodiation, the reverse trend occurs. The initial red shift in the G band during the sloping region of sodiation indicates sodium intercalation in the graphitic regions.[279] The G band position reaches a minimum at the beginning of the voltage plateau region and a blue shift occurs as sodium fills the voids in the HC bulk structure (**Figure 6.3(c)**).[281] Given that there is a more significant blue shift of the G band for TEGDME sample upon maximum sodiation and that the plateau region has a larger capacity than the PC sample, ether-based electrolytes could enable an increase in HC void filling. This could be due to an increase in overpotential for the PC electrolyte, where less sodium can be stored in the voids at

equivalent voltages. Given this information on the similar (de)sodiation processes for both PC and TEGDME electrolytes, the rate performance of HC should not be solely controlled by the kinetics of the bulk structure. The formation of the SEI, as influenced by the choice of electrolyte and electrochemical conditions will thus be the focus of this study.

6.3.3 Morphology and composition of SEI with different electrolyte

The sodium consumption, resistance, and stability of an SEI are related to its morphology and chemical composition. The SEI morphology and elemental composition of HC with PC and TEGDME electrolytes were first explored by cryo-TEM, SEM, and EDS (**Figure 6.4 and Figure E.4, E.5, and E.6**). In order to observe the nano-scale structure of the SEI by TEM, while preserving the intrinsic morphology of the SEI, cryogenic protection is required to minimize the beam damage. Clear differences in the SEI morphology on the irregularly shaped HC particles are observed for PC and TEGDME. The SEI formed in the PC electrolyte consists of a dense outer layer and a porous inner layer, whereas the SEI formed in the TEGDME electrolyte is uniformly dense around the whole HC particle. The SEI formed in the PC electrolyte morphology is also rate dependent, while the SEI formed in the TEGDME electrolyte is not (**Figure E.5**). At a rate of $C/3$, the SEI formed in the PC electrolyte is irregular, thick, and contains cracks, while at a rate of $C/20$ the SEI is thinner and more conformal. From cryo-TEM measurements, the thickness of formed SEI in the PC electrolyte at $C/3$ rate ranges from 10-20 nm whereas the SEI formed in the TEGDME is only 3-8 nm thick at the same C-rate. Additionally, EDS confirms that the SEI formed in the PC electrolyte contains significantly more sodium, oxygen, and fluorine than the SEI formed in the TEGDME electrolyte (**Figure E.6**). This, along with the cryo-TEM measurements, indicates that the SEI formed in the PC electrolyte could be the origin of sodium inventory lost that leads to the low first cycle CE.

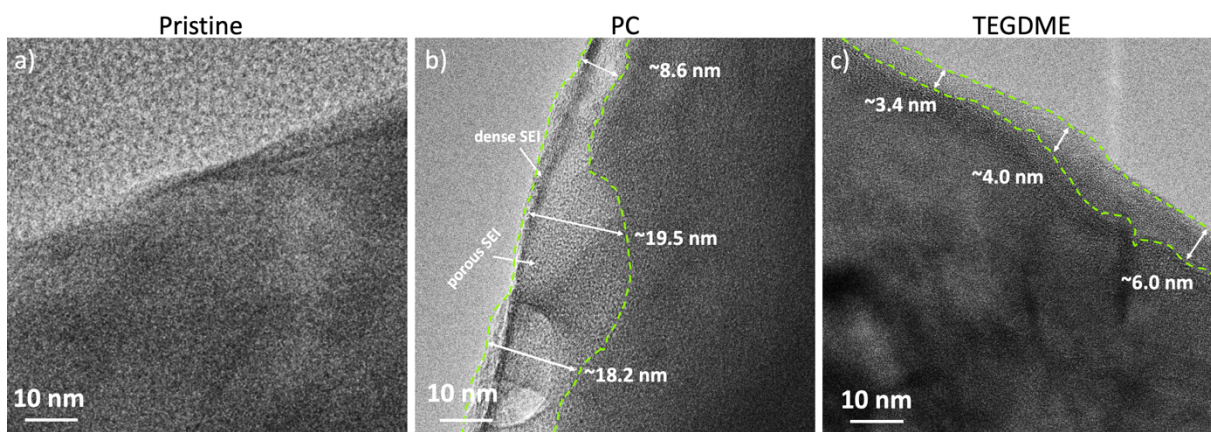


Figure 6.4: Nano-scale structures of (a) pristine HC and HC after 1 cycle at a rate of C/3 in (b) PC and (c) TEGDME electrolyte imaged by cryo-TEM. The thickness of the SEI at various location is measured in the images.

The actual chemical bonding environment that comprises the SEI has a critical effect on the sodium consumption and rate capability. XPS is one of the most common and useful tools for identifying the chemical bonding for elements that are contained in the SEI. It is essential that XPS samples are carefully prepared because the technique is surface sensitive and the SEI can be quite reactive. Past XPS studies prepared the SEI sample by washing it with a solvent, the intention of which was to remove the residue electrolyte salt. This preparation step can potentially disturb or damage the SEI prior to XPS measurements. As part of this study, we compared washed HC samples with unwashed samples and found that the act of washing actually removes fragile and/or reactive SEI components such as C-H, C-OH, CO₃, and Na₂O. This limits the observations of the SEI to the compounds remaining on the surface after washing, which obscures the changes between the sodiated and desodiated states of the HC SEI (**Figure E.7**). It is also important to note that the salt species do not overwhelm the signals for the unwashed samples (**Figure E.8**) which repudiates the arguments for washing XPS samples. We recommend that future XPS work on the characterization of HC and other anode SEIs should be performed on unwashed samples.

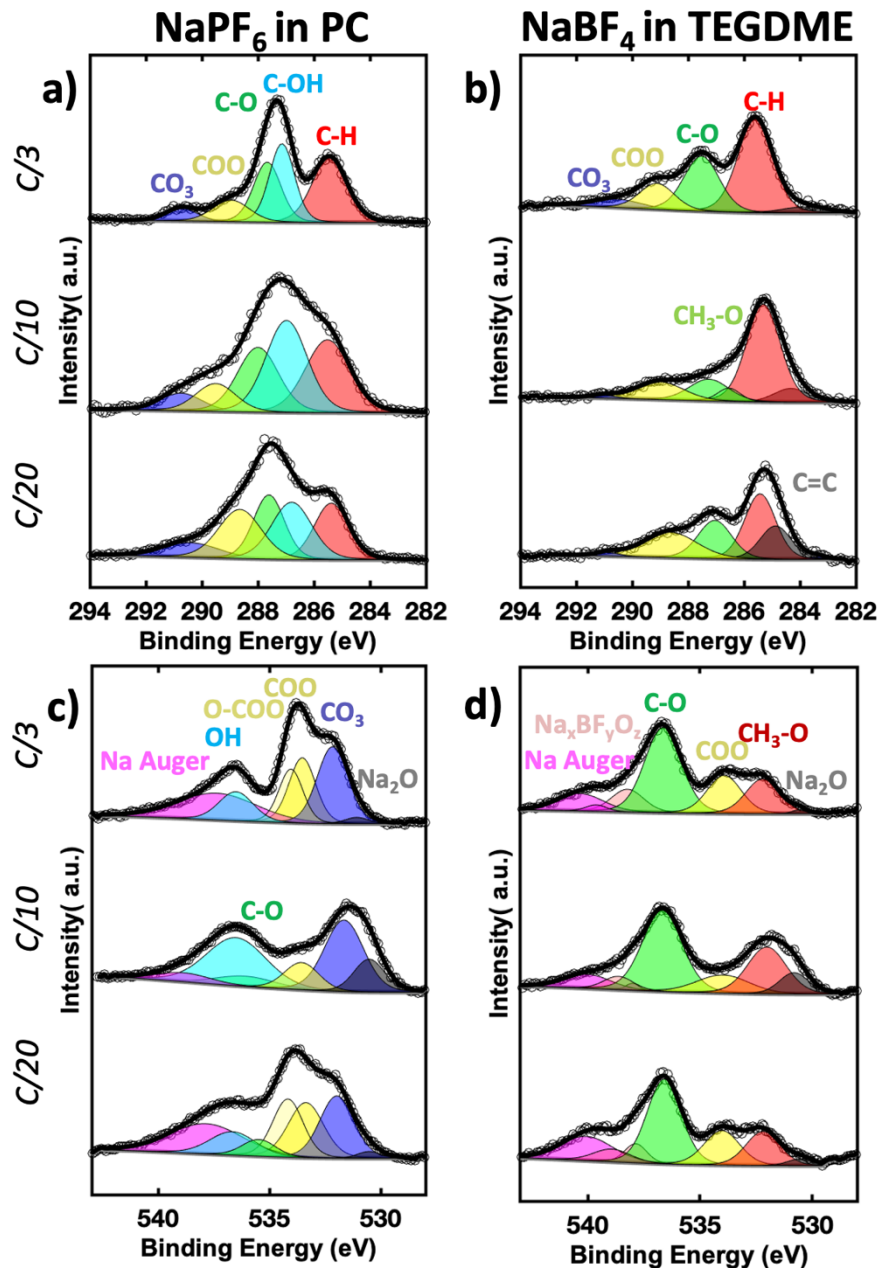


Figure 6.5: (a,b) XPS C 1s regions and (c,d) XPS O 1s regions of HC cycled with PC (left) or TEGDME (right) electrolyte samples at different rates.

It is clear from comparing the sodiated and desodiated XPS spectra (Figure E.7) that for both PC and TEGDME electrolytes, the majority of the SEI is formed during the first sodiation process. Almost all the new chemical species, in comparison to the pristine electrode, appear in the sodiated spectra with minimal changes upon desodiation. The main difference between the

sodiated and desodiated SEI is the relative amount of C-H bonding compared with other carbon bonds. Specifically, upon desodiation, the C-H bond increases for both electrolytes. This suggests that the ester and ether species polymerized or that hydrocarbons are formed on the SEI during desodiation. The overall minimal changes for the SEIs upon desodiation support the hypothesis that the low first cycle CE, i.e., irreversible capacity, is mainly caused by SEI formation. Although SEI formed in the PC and TEGDME electrolytes are alike in primarily being formed during sodiation, their chemical species and relative amounts diverge.

The SEI formed in the PC electrolyte is mainly composed of alkyl/sodium carbonates (C-H, CO₃), polyesters (COO, O-COO, C-H), hydroxides (-OH), sodium fluoride (NaF), sodium oxide (Na₂O), and salt decomposition (Na_xPF_y). The SEI formed in the TEGDME electrolyte is composed of sodium alkoxides (CH₃-O, C-H), polyethers (C-O, C-H), sodium fluoride (NaF), sodium oxide (Na₂O), and salt decomposition (Na_xBF_yO_z). Solvent and salt (from the electrolyte) decomposition are the origin of these chemical species. PC can decompose through a ring opening reaction by single electron nucleophilic attack pathway to form a linear alkyl carbonate.[282] This molecule can then decompose into oxygen and propylene, which react with PC to produce polyesters. Sodium alkoxides and polyether are derived from the decomposition of TEGDME molecules.

The components of the SEI influence its stability and through studying these components we can better understand why the SEI formed in the PC electrolyte is more unstable than the SEI formed in the TEGDME electrolyte. The reaction pathway for the decomposition of PC, that eventually forms polyesters, can lead to continuous decomposition of PC molecules and does not form a compact and conformal morphology, as seen in the cryo-TEM images.[282] In addition, hydroxide groups are partially soluble in PC, which means they likely cause continual parasitic

reactions. NaPF_6 has also been shown to react with an SEI component, sodium carbonate, to form CO_2 .^[269] Gas formation from the PC and NaPF_6 decomposition can damage the SEI, especially one that contains brittle components, like sodium carbonate.^[283] In addition, carbonate and polyester species are considered unfavorable for ion transport which can lead to larger overpotentials and poor electrochemical performance. In contrast, TEGDME decomposition products, sodium alkoxides and polyethers, are already known to form superior, compact, thin, and stable SEIs on tin, bismuth, and rGO anodes.^[284–286] This compact and elastic nature of alkoxides and polyethers can enable fast ion transport through the SEI.^[284–286] The influence of the electrolyte on cell impedance was further evaluated by EIS (**Figure E.9**). The PC electrolyte resulted in both higher charge transfer resistance and resistance due to Na^+ diffusion through the SEI than the TEGDME electrolyte. The high resistance of the PC cell is likely caused by the thick SEI composed of chemical species with poor ionic transport properties, such as sodium carbonate and polyesters. In contrast, the stability and fast ionic transport of SEI components formed in the TEGDME electrolyte can enable superior battery lifetime and rate capability.

SEI formation and stability is controlled not only by the electrolyte, but also the rate of electrochemical cycling. This factor is especially important in investigating the HC system where the PC and TEGDME electrolytes have significantly different rate capabilities. The XPS spectra for the SEI formed in the PC and TEGDME electrolytes for three rates are shown in **Figure 6.5**. Over the different rates, the SEI formed in the TEGDME electrolyte components have minimal changes whereas the SEI formed in the PC electrolyte composition varies. At a rate of C/3, the SEI formed in the PC electrolyte contains a larger amount of hydroxide groups (-OH) relative to ester (COO) and ether (CO) groups. Since hydroxide groups are partially soluble in PC, they are likely to cause continual parasitic reactions, which limits the lifetime of a battery at fast rates. As the rate

slows, the composition of the SEI formed in the PC electrolyte becomes more similar to the composition of the SEI formed in the TEGDME electrolyte with a decrease of hydroxide groups and an increase in ether groups (CO). Ether groups are not soluble in PC and can form a more compact and therefore stable SEI. Other peaks, such as carbonate and C-H relative amounts, remain rate independent for the PC electrolyte. The SEI formed in the TEGDME electrolyte components and relative amounts appear to be rate independent. The one exception is a small carbonate peak, only identified in the C/3 SEI. The carbonate peak could be a result of an altered reaction at the faster rate or the detection of carbonate on the surface of HC due to a very thin SEI. The other consistent SEI components reveal that they are stable at slow and fast rates for TEGDME electrolyte. The compact and elastic nature of alkoxides and polyethers that compose the SEI formed in the TEGDME electrolyte enables fast ion transport at all rates.[284–286]

6.3.4 Long-term cycling stability of HC

Long-term electrochemical HC studies were performed for the PC and TEGDME electrolytes where the first three cycles were run at a rate of C/10 and the following cycles were operated at a rate of C/3 (**Figure 6.6**). This mirrors how full cells are tested with the initial cycles run at a slower rate, known as formation cycles. The HC cell with PC electrolyte performs poorly, with a capacity of 74.9 mAh/g, CE of 98.7%, and a capacity retention of 31.6% after 150 cycles. The capacity of the cell with PC electrolyte rapidly declines during the first 50 cycles and then stabilizes. This, along with the relatively low average CE, shows that even the SEI formed with PC at a slower rate is unstable and leads to a poor lifetime at faster rates. In contrast, the HC cell with TEGDME electrolyte performs well, with a capacity of 222.9 mAh/g, average CE of 100.0%, and a capacity retention of 90.4% after 150 cycles. This shows that SEI formed in the TEGDME electrolyte is extremely stable at a faster rate and enables a long lifetime. The variations of the CE

around 100% could be a result of temperature fluctuations during testing and/or potential SEI component reversibility.

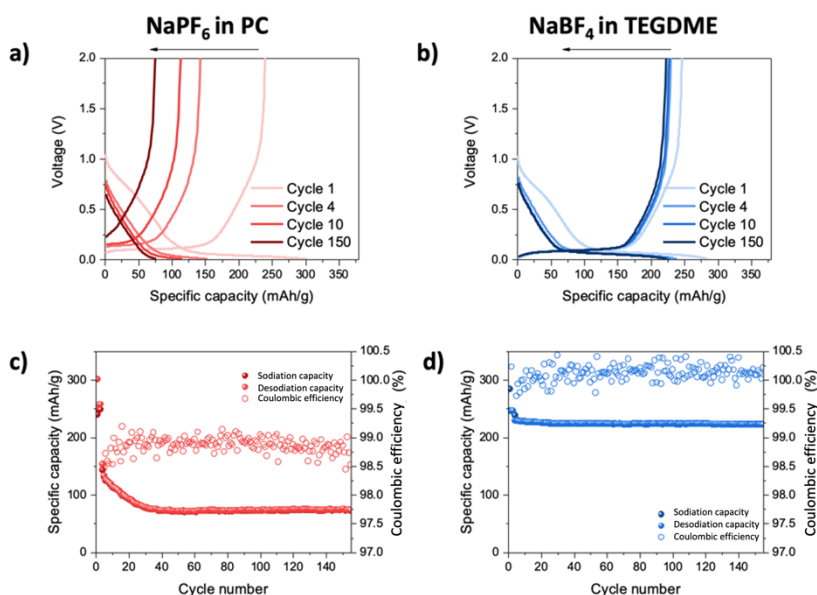


Figure 6.6: (a,b) Voltage profiles and (c,d) specific capacity and CE vs. cycled number for HC in (left) PC or (right) TEGDME electrolyte.

6.3.5 Schematics for SEI with different electrolytes

The results from this study were combined into a schematic for the SEI formation on HC with PC and TEGDME electrolytes as shown in **Figure 6.7**. This schematic illustrates the main chemical components, characteristics, and morphologies of the SEIs formed in PC and TEGDME electrolytes. The PC-based SEI is mainly composed of alkyl carbonates, polyesters, sodium fluoride, sodium oxide, and NaPF₆ decomposition products. This SEI appears thick, with nonuniform density and coverage, qualities which can promote continuous reactions that shorten the battery lifetime. In addition, this type of SEI inhibits sodium transport and becomes more unstable at high rates, limiting the HC rate capability. The TEGDME-based SEI is composed of sodium alkoxides, polyethers, sodium fluoride, sodium oxide, and NaBF₄ decomposition products. This thin, conformal, and uniform SEI enables cycling stability and fast sodium ion transport. This model is in contrast with the hypothesis proposed in literature in which trapped metallic sodium

and slow kinetics of the voltage plateau (de)sodiation processes are considered as the causes for the low first cycle CE and poor rate capability, respectively. Adopting this model suggests shifting the research direction away from presodiating HC, in an effort to reduce the amount of trapped metallic sodium in the HC structure, toward improving the SEI properties.[124,261]

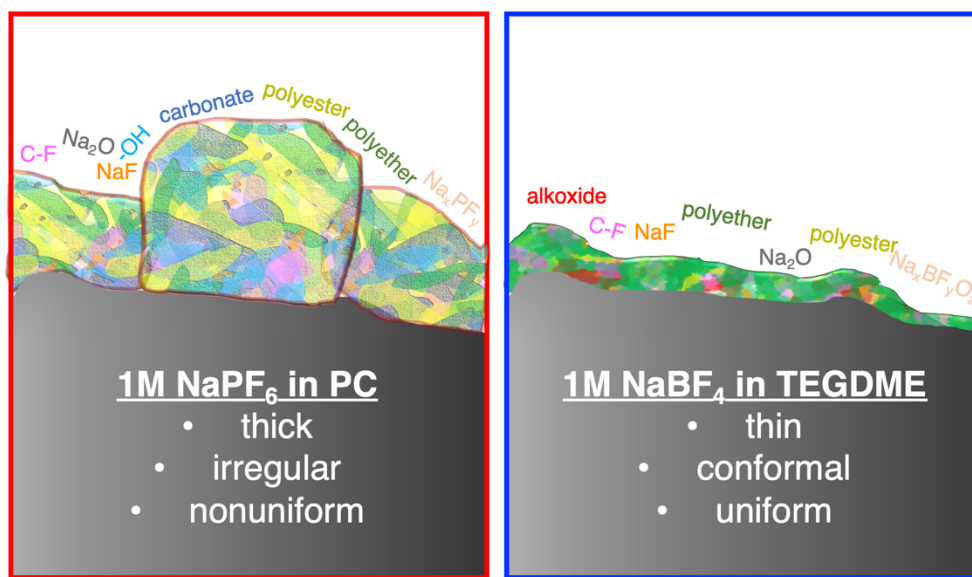


Figure 6.7: Cross-sectional schematics of the differences between the SEI on HC in PC vs. TEGDME electrolyte.

6.4. Conclusions

In this study, the performance and mechanistic differences of HC in a conventional carbonate electrolyte (1M NaPF₆ in PC) and a high performing ether electrolyte (1M NaBF₄ in TEGDME) are explored. The TEGDME electrolyte enables a higher first cycle CE, better rate performance, and improved lifetime of HC. The trapped metallic sodium, (de)sodiation processes, and SEI formation were examined to study the origin of these performance differences. It is found that the same (de)sodiation processes occur in PC and TEGDME system. In addition, there is no trapped metallic sodium found in the HC structure after the first cycle, which indicates that the first cycle CE and rate capability are not controlled by the sodium storage processes in bulk structure. Thereafter, the SEI formation was explored during the first cycle at three rates using

cryo-TEM, SEM, EDS, and XPS. The results are combined to form a model for SEI formation on HC with PC and TEGDME electrolytes. The growth of a thin, conformal, and uniform SEI in TEGDME electrolyte enables stable cycling behavior of HC under different current densities. This model for the HC SEI can be potentially generalized to other carbonate- and ether-based electrolytes. HC with ether-based electrolytes has superior electrochemical performances but its compatibility with sodium cathodes should be further explored to enable a high-energy, long-life full cell. These findings demonstrate a new pathway through electrolyte design and interfacial engineering to further improve the electrochemical performances of the HC anode for grid-storage level long cycle life NIBs.

Chapter 6, in full, is currently being prepared for submission for publication, “Role of electrolyte in stabilizing hard carbon as an anode for sodium-ion batteries” H. S. Hirsh, B. Sayahpour, A. Shen, W. Li, B. Lu, E. Zhao, M. Zhang, Y. S. Meng. The dissertation author was the primary investigator and author of this paper. The author designed all experiments and analyzed all the data collected for this paper.

Chapter 7 Conclusions and Future Perspective

Sodium-ion batteries (NIBs) are poised to become an essential technology for grid storage because they can be made from abundant and inexpensive elements, are sustainable, and are relatively energy-dense. However, before NIBs can be commercialized for grid storage there are key issues that need to be resolved. Specifically, the lifetime of energy-dense electrode materials needs to be improved. For cathode materials, this can be achieved by controlling its morphology and composition. For anode materials, such as hard carbon (HC), the first cycle Coulombic efficiency and rate capability need to be improved. The focus of my thesis is to investigate the mechanisms of morphological and compositional control on NIB cathode materials as well as determine the effect of electrolyte on the HC anode performance. The physical and chemical properties were studied using both lab and synchrotron based advanced characterization tools.

In Chapter 2, NIB battery development and its suitability for grid storage were explored. The worldwide prices and availabilities of NIB and lithium-ion battery (LIB) precursors were compared. With this in mind, the energy density, cost, and lifetime of cathode materials were evaluated across chemistries. We found that NIBs without expensive element such as Ni, Li, and Co provide the lowest cost of energy. In addition, scientific challenges facing NIBs including electrolytes, anode, interface, safety, and recyclability were introduced.

In Chapter 3, a new co-precipitation method was introduced to synthesize NIB cathode material, $\text{P2-Na}_{2/3}\text{Fe}_{1/4}\text{Mn}_{3/4}\text{O}_2$, with a sphere-like meso-structure. The cooling rate during synthesis was found to be the key parameter to control the meso-structure of this material. The sphere-like meso-structure enabled larger capacities and improved cyclability. This enhanced performance is attributed to the sphere-like material having a larger surface area, reduced surface contamination, and higher TM redox activity.

In Chapter 4, the redox mechanisms of NFMO ($x=1/4, 1/3, 1/3$) were investigated using operando XAS and computation to explore the Fe:Mn ratio effects on the redox mechanisms and the materials capacity retention. The redox mechanism of NFMO is $Mn^{3+/4+}$ and $Fe^{3+/4+}$ with more redox utilization at higher Fe:Mn ratios.

In Chapter 5, the irreversibility of oxygen redox activity in TM layer ordered P2-NLNMO was explored using XAS, sXRD, PDF, and computation. The irreversible oxygen redox activity was correlated with Ni migration at high voltage that resulted in the loss of TM ordering in the structure. Ni migration changes the oxygen environment, which inhibits the reduction of oxygen during sodiation.

In Chapter 6, the effect of electrolyte on the first cycle CE and rate performance of HC were explored using TGC, Raman spectroscopy, cryo-TEM, and XPS. The SEI formed on HC was found to be the key difference between ether- and carbonate-based electrolytes because it determines the extent of parasitic reactions and charge kinetics. Both electrolytes showed negligible residual metallic sodium in the HC bulk structure however the ether-based SEI had superior chemical components, uniformity, and morphology.

Given the abovementioned work, there is still room for improving the understanding and performance of NIBs: 1) The mechanism of NIB cathode meso-structure formation during the high temperature synthesis and cooling should be investigated. Why is the spherical shape maintained as the oxide is slowly cooled but not when quenched? This question is difficult to answer because both imaging and XRD measurements must be taken *in situ*. In addition, synchrotron radiation must be used for both imaging and diffraction measurements to have suitable time and spatial resolution. This information can be useful for designing the synthesis of cathodes with different compositions and scales.

2) When moving to a full cell (where the opposite electrode is not excessive sodium metal), the total amount of sodium in the system must be carefully considered. If P2-TM oxides, most of which contain $\text{Na}=2/3$, is paired with an anode, such as HC, which contains no sodium, then the system is sodium deficient. There are two methods to overcome this sodium deficiency. The first method is to use add a sacrificial salt. This is a sodium containing salt that decomposes irreversibly to add sodium-ions to the system. This method can decrease a cells energy density and potentially cause unwanted side reactions. The second method is to use a cathode with $\text{Na}=1$. Oxides with $\text{Na}=1$ tend to be in the O3 phase and have inferior capacity retention due to phase changes.

3) Electrolytes have not been fully optimized for the NIB system. Improved stability of the electrolyte against both the cathode and anode is required to minimize parasitic reactions and extend the lifetime of NIBs. Electrolyte stability can be improved through optimizing additives, salts, and solvents. Nonliquid electrolytes such as liquified gas and solid-state electrolytes could provide new avenues to improve the safety and stability of NIBs. Cost, safety, and lifetime should be carefully considered when designing NIBs for grid storage.

Appendix A Supporting Information for Chapter 2

Table A.1: Comparison of electrochemical energy storage systems.

Systems	Volumetric	Gravimetric	Electrolyte Type	Voltage Range [V]	Cycle Life
	Energy density [WhL ⁻¹]	Energy Density [Whkg ⁻¹]			
Li-ion (graphite)	320-600	220-330	organic liquid	3.0-4.2	1000-3000
Li-ion (Si-C)	580-780	300-370	organic liquid	2.9-4.1	100-500
Li-ion (Li metal)	620-800	420-480	organic liquid	3.1-4.3	100-500
Li-ion all solid state	760-940	370-440	solid	3.1-4.3	1000-5000
Na-ion all solid state	600-750	200-280	solid	2.6-3.3	1000-5000
Na-ion (hard carbon)	190-480	180-280	organic liquid	2.6-3.3	800-1000
Na-S (high T)	140-300	150-240	molten salt	1.8-2.1	~4000
Li-S	390-550	340-410	organic liquid	1.8-2.0	100-500
NiMH	80-300	70-100	aqueous liquid	0.9-1.3	~1000
NiCd	80-200	40-60	aqueous liquid	0.8-1.3	~2000
Pb Acid	40-100	25-45	aqueous liquid	1.8-2.1	100-500
V Redox	40-60	10-30	aqueous liquid	1.1-1.6	5000-10000

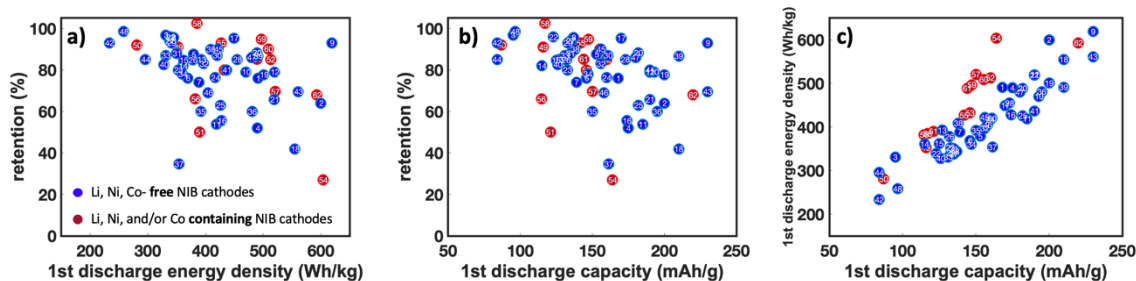


Figure A.1: (a) Retention of the capacity versus first discharge energy density (Wh/kg), (b) retention of the capacity versus first discharge capacity, and (c) first discharge energy density versus first discharge capacity for layered cathode materials in Na-ion batteries. Blue circles are Li, Ni, and Co-free sodium cathode materials and red circle are Li, Ni, and/or Co containing sodium cathode materials. The numbers refer to the data in Tables A.3 and A.4.

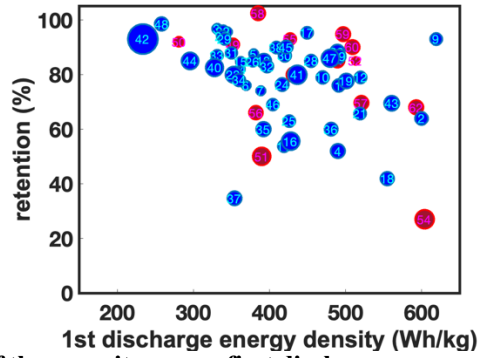


Figure A.2: Capacity retention of the capacity versus first discharge energy density (Wh/kg) for layered cathode materials in Na-ion batteries with numbers corresponding to the materials in Table A.2 and A.3. Blue circles are Li, Ni, Co-free sodium cathode materials and red circle are Li, Ni, and/or Co containing sodium cathode materials. The size of the circle represents the severity of the testing conditions using the calculated retention index (equation 2.1).

Table A.2: Layered oxide, polyanion, and PBA type NIB cathode materials properties. Note: Cycle life is Depth of Discharge (DOD) dependent. The numbers we show in the table are only taking into consideration of 80-100% DOD.

Compound	Type	1 st dis. cap. [mAh/g]	1 st dis. Grav. energy density [Wh/kg]	1 st dis. Vol. energy density [Wh/L]	C-rate	# cycles	retention [%]	low V	high V	phase	DOI
Na _{0.67} [Fe _{0.5} Mn _{0.5}]O ₂	Layered	168	491	2219	0.1	20	76	1.5	4.3	P2	10.1038/ncomms10308
Na _{0.67} [Fe _{0.5} Mn _{0.5}]O ₂	Layered	200	600	2441	0.05	50	64	1.5	4.3	P2	10.1021/acs.chemmater.5b00097
Na _{0.9} [Cu _{0.22} Fe _{0.30} Mn _{0.48}]O ₂	Layered	95	331	1458	0.1	100	96.8	2.5	4.05	O3	10.1002/adma.201502449
Na _{0.67} [Mn _{0.66} Fe _{0.20} Cu _{0.14}]O ₂	Layered	175	490	2037	0.05	100	52	1.5	4.3	P2	10.1021/acs.chemmater.7b01146
Na _{0.67} Mn _{2/3} Fe _{1/3} O ₂	Layered	153	379	1552	0.01	10	87.5	1.5	3.8	P2	10.1149/2.032304jes
Na _{0.67} Mn _{1/2} Fe _{1/2} O ₂	Layered	146	369	1506	0.01	10	76	1.5	3.8	P2	10.1149/2.032304jes
Na _{0.82} Mn _{1/3} Fe _{2/3} O ₂	Layered	139	388.5	1634	0.01	10	74.1	1.5	3.8	O3	10.1149/2.032304jes
Na _{0.8} Mn _{1/2} Fe _{1/2} O ₂	Layered	137	344.4	1452	0.01	10	95.6	1.5	3.8	O3	10.1149/2.032304jes
NaCr _{1/3} Fe _{1/3} Mn _{1/3} O ₂	Layered	185	419	1852	0.05	35	53.75	1.5	4.2	O3	10.1039/C6TA10818K
Na _{2/3} [Fe _{1/2} Mn _{1/2}]O ₂	Layered	190	520	2121	0.05	30	79	1.5	4.2	P2	10.1038/NMAT3309
Na _{0.7} Mn _{1/3} Fe _{1/3} Cu _{1/6} Mg _{1/6} O ₂	Layered	127	392.7	1570	0.1	100	85.04	1.5	4.2	O3	10.1021/acsami.7b15590
Na _{0.67} [Fe _{0.5} Mn _{0.5}]O ₂	Layered	115	361	1476	0.1	25	82	2	4	P2	10.1016/j.electacta.2015.10.003
Na _{0.67} [Fe _{0.5} Mn _{0.5}]O ₂	Layered	125	362.1	1486	0.1	25	84.7	2	4	O3	10.1016/j.electacta.2015.10.003
Na _{0.64} Mg _{0.11} Mn _{0.89} O ₂	Layered	174	427.8	1740	0.1	200	55.6	1.5	4.4	P2	10.1016/j.jpowsour.2015.02.069
Na _{0.67} Mn _{0.5} Fe _{0.47} Al _{0.03} O ₂	Layered	160	416.8	1697	0.1	50	76.3	1.5	4.2	P2	10.1021/acs.inorgchem.8b00284
Na _{0.67} Mn _{0.95} Mg _{0.05} O ₂	Layered	182	425.8	1773	0.08	25	63	1.5	4.1	P2	10.1039/C4EE00465E
Na _{0.77} Mn _{1/3} Fe _{2/3} O ₂ +2	Layered	132	378	1574	0.02	50	84.8	1.5	3.8	O3	10.1039/c4ta06688j
Na _{2/3} Mn _{7/9} Zn _{2/9} O ₂	Layered	195	481	2049	0.1	50	60	1.5	4.2	P2	10.1002/aenm.201802379
Na _{0.83} Cr _{1/3} Fe _{1/3} Mn _{1/6} Ti _{1/6} O ₂	Layered	161.4	354	1458	0.1	100	34.7	1.5	4.1	O3	10.1016/j.electacta.2018.11.137
Na _{0.67} Mn _{0.6} Fe _{0.25} Al _{0.15} O ₂	Layered	138	408.8	1647	0.1	50	89.9	2.1	4.5	P2	10.1021/acsacem.8b01015
Na _{2/3} [Mn _{0.7} Zn _{0.3}]O ₂	Layered	190	436.7	1878	0.1	200	80	1.5	4.6	P2	10.1016/j.nanoem.2019.02.042
Na _{2/3} Mn _{0.8} Fe _{0.1} Mg _{0.1} O ₂	Layered	156	422	1700	0.1	50	90	1.5	4.2	P2	10.1007/s11581-019-03208-w
Na _{0.67} Fe _{0.25} Mn _{0.75} O ₂	Layered	96.6	258.3	1068.	0.1	50	98.5	1.5	4.3	P2	10.1149/2.0701912jes
Na _{0.8} [Li _{0.12} Ni _{0.22} Mn _{0.66}]O ₂	Layered	116	352.3	1481	0.1	50	91	2	4.4	P2	10.1021/cm403855t
NaFe _{0.5} Co _{0.5} O ₂	Layered	160	513	2393	0.05	50	85	2.5	4	O3	10.1016/j.elecom.2013.05.012
NaNi _{1/3} Co _{1/3} Mn _{1/3} O ₂	Layered	142	427	2022	0.1	50	93	2	4.4	O3	10.1002/adfm.201701870
Na _{0.67} Ni _{0.1} Cu _{0.2} Mn _{0.7} O ₂	Layered	114.7	382.4	1638	0.1	100	66	2	4.5	P2	10.1039/c7ta00880e
Na _{2/3} Ni _{1/3} Mn _{2/3} O ₂	Layered	150.1	520.7	2247	0.5	30	69.6	2	4.5	P2	10.1016/j.matlet.2014.07.153
Na _{2/3} Ni _{2/9} Mg _{1/9} Mn _{2/3} O ₂	Layered	117.1	385	1596	0.5	30	102.4	2	4.5	P2	10.1016/j.matlet.2014.07.153
Na _{2/3} Ni _{2/9} Al _{1/9} Mn _{2/3} O ₂	Layered	147.2	496.8	2081	0.5	30	94.8	2	4.5	P2	10.1016/j.matlet.2014.07.153
Na _{2/3} Ni _{2/9} Fe _{1/9} Mn _{2/3} O ₂	Layered	155.3	509	2184	0.5	30	90.1	2	4.5	P2	10.1016/j.matlet.2014.07.153
Na _{2/3} Ni _{2/9} Co _{1/9} Mn _{2/3} O ₂	Layered	144.1	489	2133	0.5	30	85.2	2	4.5	P2	10.1016/j.matlet.2014.07.153
Na ₄ Fe ₃ (PO ₄) ₂ (P ₂ O ₇)	Polyanion	105.7	308.6	499	0.2	250	85	2	4	Pn2a	10.1038/s41467-019-09170-5
Na ₃ V ₂ (PO ₄) ₃	Polyanion	113	400	430	1	1000	86.7	2.3	3.9	Pn2a	10.1002/aenm.201200803
Na ₄ NiV(PO ₄) ₃	Polyanion	80	271	292	1	500	83	2.5	4.1	R-3c	10.1021/acs.nanolett.6b04044
Na ₂ MnSiO ₄	Polyanion	155	440.4	671	1	500	89.5	2	4.3	Pn	10.1016/j.jpowsour.2017.05.069
Na _{0.61} Fe[Fe(CN) ₆] _{0.94}	PBA	179	551.5	694	0.125	150	100	2	4.2	FCC	10.1039/c3ee44004d
Na _{1.87} Ni _{0.02} Mn _{0.95} [Fe(CN) ₆] _{0.98} ·4.06H ₂ O	PBA	117	382.5	635	0.833	500	94	2	4	FCC	10.1021/acsami.6b10884
Na _{0.84} Ni[Fe(CN) ₆] _{0.71} ·6H ₂ O	PBA	66	204.3	318	0.285	200	99.7	2	4.1	FCC	10.1039/c3ta13223d
Na ₂ Zn ₃ [Fe(CN) ₆] ₂ ·9H ₂ O	PBA	56.4	181.2	259	0.15	50	85.2	2	4	R-3c	10.1039/c2cc33771a

Table A.3: Li, Ni, Co- free NIB cathode materials properties.

#	Compound	1st dis. cap. [mAh/g]	1st dis. energy density [Wh/kg]	C-rate	# cycles	retention [%]	low V	high V	phase	retention index	year	DOI
1	Na _{0.67} Fe _{0.5} Mn _{0.5} O ₂	168	491	0.1	20	76	1.5	4.3	P2	0.981	2015	10.1038/ncomms10308
2	Na _{0.67} Mn _{0.3} Fe _{0.3} O ₂	200	600	0.05	50	64	1.5	4.3	P2	1	2015	10.1021/acs.chemmater.5b00097
3	Na _{0.9} Cu _{0.22} Fe _{0.30} Mn _{0.48} O ₂	95	331	0.1	100	96.8	2.5	4.05	O3	0.784	2015	10.1002/adma.201502449
4	Na _{0.67} Mn _{0.66} Fe _{0.20} Cu _{0.14} O ₂	175	490	0.05	100	52	1.5	4.3	P2	1.1	2017	10.1021/acs.chemmater.7b01146
5	Na _{0.67} Mn _{0.23} Fe _{0.13} O ₂	153	379	0.01	10	87.58	1.5	3.8	P2	0.721	2013	10.1149/2.032304jes
6	Na _{0.67} Mn _{0.12} Fe _{0.12} O ₂	146	369	0.01	10	76.02	1.5	3.8	P2	0.721	2013	10.1149/2.032304jes
7	Na _{0.82} Mn _{0.13} Fe _{0.23} O ₂	139	388.5	0.01	10	74.10	1.5	3.8	O3	0.721	2013	10.1149/2.032304jes
8	Na _{0.8} Mn _{0.12} Fe _{0.12} O ₂	137	344.4	0.01	10	95.62	1.5	3.8	O3	0.721	2013	10.1149/2.032304jes
9	Na ₂₃ Fe ₁₂ Mn ₁₂ O ₂	230	619	0.1	10	93	1.5	4.2	P2	0.932	2017	10.1016/j.matlet.2017.05.084
10	Na ₂₃ Fe ₁₃ Mn ₂₅ O ₂	193	470	0.05	40	79	1.5	4.3	P2	0.98	2014	10.1016/j.jpowsour.2014.04.048
11	NaCr _{1/3} Fe _{1/3} Mn _{1/3} O ₂	185	419	0.05	35	53.75	1.5	4.2	O3	0.941	2017	10.1039/C6TA10818K
12	Na ₂₃ Fe ₁₂ Mn ₁₂ O ₂	190	520	0.05	30	79	1.5	4.2	P2	0.931	2012	10.1038/NMAT3309
13	Na _{0.7} Mn _{1/3} Fe _{1/3} Cu _{1/6} Mg _{1/6} O ₂	127	392.7	0.1	100	85.04	1.5	4.2	O3	1.112	2018	10.1021/acsami.7b15590
14	Na _{0.67} Fe _{0.5} Mn _{0.5} O ₂	115	361	0.1	25	82	2	4	P2	0.762	2015	10.1016/j.electacta.2015.10.003
15	Na _{0.67} Fe _{0.5} Mn _{0.5} O ₂	125	362.1	0.1	25	84.7	2	4	O3	0.762	2015	10.1016/j.electacta.2015.10.003
16	Na _{0.64} Mg _{0.11} Mn _{0.89} O ₂	174	427.8	0.1	200	55.6	1.5	4.4	P2	1.369	2015	10.1016/j.jpowsour.2015.02.069
17	Na ₂₃ Mg _{0.28} Mn _{0.72} O ₂	170	449.2	0.058	50	95.3	2	4.5	P2	0.922	2018	10.1038/nchem.2923
18	Na ₂₃ Fe ₁₂ Mn ₁₂ O ₂	210	555	0.1	50	41.9	1.5	4.3	P2	1.041	2018	10.1149/2.0911802jes
19	Na _{0.67} Mn _{0.6} Fe _{0.4} O ₂	200	501	0.1	100	77.7	1.5	4.3	P2	1.141	2018	10.1007/s11581-018-2442-5
20	Na _{0.67} Mn _{0.6} Fe _{0.3} Zn _{0.1} O ₂	182	489	0.1	100	88.3	1.5	4.3	P2	1.141	2018	10.1007/s11581-018-2442-5
21	NaMnO ₂	190	519.2	0.05	100	65.8	2	4.2	Pmmm	0.928	2014	10.1021/ja509704t
22	NaMnO ₂	123	339	0.1	20	95.93	1.25	3.75	C2/m	0.895	2011	10.1149/2.035112jes
23	Na _{0.6} Mn _{0.9} Cu _{0.1} O ₂	132.8	352.7	1	100	80	2	4.1	P2/Tunnels	1.247	2018	10.1021/acsami.8b00614
24	Na _{0.67} Mn _{0.5} Fe _{0.47} Al _{0.03} O ₂	160	416.8	0.1	50	76.3	1.5	4.2	P2	1.012	2018	10.1021/acs.inorgchem.8b00284
25	Na _{0.67} Mn _{0.95} Mg _{0.05} O ₂	182	425.8	0.08	25	63	1.5	4.1	P2	0.919	2014	10.1039/C4EE00465E
26	Na _{0.77} Mn _{0.13} Fe _{0.23} O ₂	132	378	0.02	50	84.8	1.5	3.8	O3	0.820	2015	10.1039/c4ta06688j
27	Na _{0.5} Fe _{0.5} Mn _{0.5} O ₂	135	338	0.1	20	94	1.5	4	O3	0.895	2012	10.1149/2.058302jes
28	Na _{0.5} Fe _{0.5} Mn _{0.5} O ₂	173	455	0.1	20	85	1.5	4.25	O3	0.967	2012	10.1149/2.058302jes
29	Na _{0.55} Fe _{0.55} Mn _{0.45} O ₂	133	341	0.1	20	93	1.5	4	O3	0.895	2012	10.1149/2.058302jes
30	Na _{0.55} Fe _{0.55} Mn _{0.45} O ₂	161	420	0.1	20	87	1.5	4.25	O3	0.967	2012	10.1149/2.058302jes
31	Na _{0.6} Fe _{0.6} Mn _{0.4} O ₂	135	350	0.1	20	88	1.5	4	O3	0.895	2012	10.1149/2.058302jes
32	Na _{0.6} Fe _{0.6} Mn _{0.4} O ₂	156	397	0.1	20	83	1.5	4.25	O3	0.967	2012	10.1149/2.058302jes
33	Na _{0.65} Fe _{0.65} Mn _{0.35} O ₂	131	331	0.1	20	87	1.5	4	O3	0.895	2012	10.1149/2.058302jes
34	Na _{0.65} Fe _{0.65} Mn _{0.35} O ₂	147	360	0.1	20	78	1.5	4.25	O3	0.967	2012	10.1149/2.058302jes
35	Na ₂₃ Mn ₃₅ Fe ₂₅ O ₂	150	392	0.1	100	60	1.5	4.2	P2	1.112	2018	10.1002/batt.201800034
36	Na ₂₃ Mn ₇₉ Zn ₂₉ O ₂	195	481	0.1	50	60	1.5	4.2	P2	1.012	2018	10.1002/aenm.201802379
37	Na _{0.83} Cr _{1/3} Fe _{1/3} Mn _{1/6} Ti _{1/6} O ₂	161.4	354	0.1	100	34.7	1.5	4.1	O3	1.084	2019	10.1016/j.electacta.2018.11.137
38	Na _{0.67} Mn _{0.6} Fe _{0.25} Al _{0.15} O ₂	138	408.8	0.1	50	89.9	2.1	4.5	P2	0.927	2018	10.1021/acsami.8b01015
39	Na _{0.653} Mn _{0.929} O ₂	210	491.1	0.1	60	86.7	1.5	4.3	O3	1.061	2018	10.1016/j.ensm.2018.10.025
40	Na _{0.8} Fe _{0.5} Mn _{0.5} O ₂	126	327.8	1	60	82.6	1.5	4.2	O3	1.338	2019	10.1007/s10853-018-03277-8
41	Na ₂₃ Mn _{0.7} Zn _{0.3} O ₂	190	436.7	0.1	200	80	1.5	4.6	P2	1.427	2019	10.1016/j.nanoen.2019.02.042
42	Na _{0.67} Mn _{0.8} Cu _{0.1} Mg _{0.1} O ₂	84	233.3	2	500	93	2	4.2	P2	2.261	2019	10.1016/j.jpowsour.2019.01.086
43	Na ₂₃ Mg _{1/3} Ti _{1/6} Mn _{1/2} O ₂	230	561	0.2	50	69.5	1.5	4.5	P2	1.157	2019	10.1016/j.chempr.2019.08.003
44	Na _{0.78} Cu _{0.27} Zn _{0.06} Mn _{0.67} O ₂	84	295.6	1	200	85	2.5	4.1	P2/P3	1.304	2019	10.1002/anie.201811882
45	Na ₂₃ Mn _{0.8} Fe _{0.1} Mg _{0.1} O ₂	156	422	0.1	50	90	1.5	4.2	P2	1.012	2019	10.1007/s11581-019-03208-w
46	Na _{0.7} Zn _{0.15} Mn _{0.75} O ₂	158	404.6	0.1	40	69	2	4.4	P2	0.9071	2018	10.1007/s11581-018-2681-5
47	Na _{0.67} [(Mn _{0.78} Fe _{0.22}) _{0.9} Ti _{0.1}]O ₂	180	479.8	0.1	200	86	1.5	4.3	P2	1.341	2019	10.1002/adfm.201901912
48	Na _{0.67} Fe _{0.25} Mn _{0.75} O ₂	96.6	258.3	0.1	50	98.5	1.5	4.3	P2	1.041	2019	10.1149/2.0701912jes

Table A.4: Li, Ni, Co- containing NIB cathode materials properties.

#	Compound	1st dis cap. [mAh/g]	1st dis energy density [Wh/kg]	C-rate	# cycles	retention [%]	low V	high V	phase	retention index	year	DOI
49	Na _{0.8} Li _{0.12} Ni _{0.22} Mn _{0.66} O ₂	116	352.3	0.1	50	91	2	4.4	P2	0.927	2014	10.1021/cm403855t
50	Na _{0.78} Ni _{0.2} Fe _{0.38} Mn _{0.42} O ₂	87	280.95	0.1	100	92	2.5	4	P2-O3	0.769	2017	10.1021/acsami.7b11282
51	Na _{0.66} Mn _{0.54} Co _{0.13} Ni _{0.13} O ₂	121	390	1	100	50	2	4.5	P2	1.361	2017	10.1002/adfm.201701870
52	NaFe _{0.5} Co _{0.5} O ₂	160	513	0.05	50	85	2.5	4	O3	0.628	2013	10.1016/j.elecom.2013.05.012
53	NaNi _{0.6} Co _{0.2} Mn _{0.2} O ₂	146	432.6	0.5	50	80	1.5	4.2	O3	1.187	2017	10.1039/c7ta08443a
54	Na _{2/3} Ni _{1/3} Mn _{2/3} O ₂	164	604	0.5	300	27	2.5	4.3	P2	1.430	2016	10.1016/j.nanoen.2016.06.026
55	NaNi _{1/3} Co _{1/3} Mn _{1/3} O ₂	142	427	0.1	50	93	2	4.4	O3	0.927	2017	10.1002/adfm.201701870
56	Na _{0.67} Ni _{0.1} Cu _{0.2} Mn _{0.7} O ₂	114.7	382.4	0.1	100	66	2	4.5	P2	1.055	2017	10.1039/c7ta00880e
57	Na _{2/3} Ni _{1/3} Mn _{2/3} O ₂	150.1	520.7	0.5	30	69.6	2	4.5	P2	1.090	2014	10.1016/j.matlet.2014.07.153
58	Na _{2/3} Ni _{2/9} Mg _{1/9} Mn _{2/3} O ₂	117.1	385	0.5	30	102.4	2	4.5	P2	1.090	2014	10.1016/j.matlet.2014.07.153
59	Na _{2/3} Ni _{2/9} Al _{1/9} Mn _{2/3} O ₂	147.2	496.8	0.5	30	94.8	2	4.5	P2	1.090	2014	10.1016/j.matlet.2014.07.153
60	Na _{2/3} Ni _{2/9} Fe _{1/9} Mn _{2/3} O ₂	155.3	509	0.5	30	90.1	2	4.5	P2	1.090	2014	10.1016/j.matlet.2014.07.153
61	Na _{2/3} Ni _{2/9} Co _{1/9} Mn _{2/3} O ₂	144.1	489	0.5	30	85.2	2	4.5	P2	1.090	2014	10.1016/j.matlet.2014.07.153
62	Na _{0.6} Li _{0.2} Mn _{0.8} O ₂	220	593	0.1	50	68	1.5	4.5	P2	1.090	2018	10.1016/j.jpowsour.2017.12.072

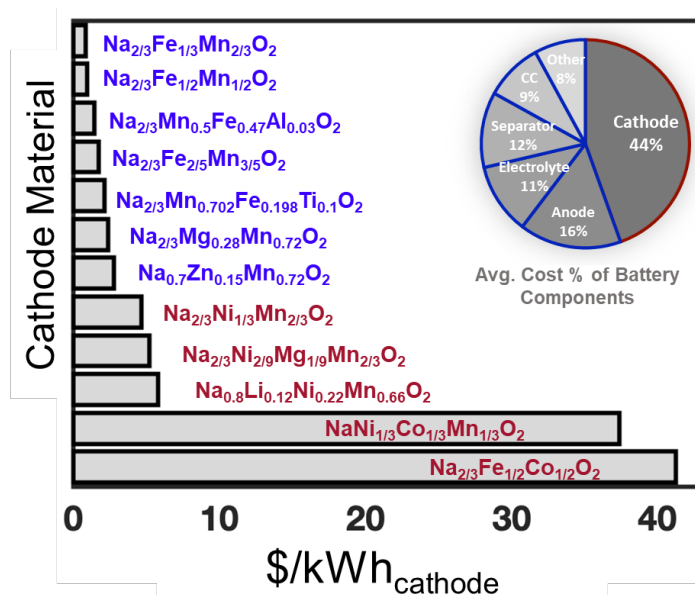


Figure A.3: Price of energy (\$/kWh) for selected sodium cathodes that are Li, Ni, Co-free (blue) and contain Li, Ni, and/or Co (red). (Inset) A pie chart that contains the average cost percentage of lithium-ion battery components, with cathodes representing 44% of the total battery cost (CC=current collector). The price of each element is sourced from metalary.com.

Table A.5: Cost analysis for NIB full cells at 1KWh level constructed with different cathodes. The unit price for the cathode materials are from the calculation in Figure A.3, and the price of other cell components are sourced from prevailing commercial prices.

Materials	$\text{Na}_{2.0}\text{Fe}_{1.0}\text{Mn}_{2.0}\text{O}_2$	$\text{Na}_{2.2}\text{Fe}_{1.2}\text{Mn}_{1.2}\text{O}_2$	$\text{Na}_{0.67}\text{Mn}_{0.5}\text{Fe}_{0.47}\text{Al}_{0.03}\text{O}_2$	$\text{Na}_{2.0}[\text{Mn}_{0.5}\text{Fe}_{2.5}\text{O}_2]$	$\text{Na}_{0.67}[(\text{Mn}_{0.78}\text{Fe}_{0.22})_{0.9}\text{Ti}_{0.1}]\text{O}_2$	$\text{Na}_{2.2}[\text{Mg}_{0.28}\text{Mn}_{0.72}]\text{O}_2$	$\text{Na}_{0.7}\text{Zn}_{0.15}\text{Mn}_{0.75}\text{O}_2$	
Cathode	Nominal Voltage (V)	2.79	3.10	2.61	2.61	2.66	2.56	
	specific capacity (mAh/g)	168.00	200.00	160.00	150.00	180.00	158.00	
	Capacity (Ah)	358.42	322.58	383.14	383.14	375.94	378.79	
	mass (g)	2133.47	1612.90	2394.64	2554.28	2088.55	2228.16	
	estimated commercial unit price (\$/kg)	0.44	0.62	0.64	0.73	0.92	1.11	
	cost (\$)	0.93	1.00	1.53	1.85	1.91	2.47	
Anode	specific capacity (mAh/g)	280.00	280.00	280.00	280.00	280.00	280.00	
	mass (g)	1408.09	1267.28	1505.20	1505.20	1476.91	1488.10	
	commercial unit price (\$/kg)	5.00	5.00	5.00	5.00	5.00	5.00	
	cost (\$)	7.04	6.34	7.53	7.53	7.38	7.44	
Electrolyte	volume (L)	1.08	0.97	1.15	1.15	1.13	1.14	
	commercial unit price (\$/L)	4.00	4.00	4.00	4.00	4.00	4.00	
	cost (\$)	4.30	3.87	4.60	4.60	4.51	4.55	
Conductive Agent	mass(g)	196.75	160.01	216.66	225.53	198.08	206.46	
	commercial unit price (\$/kg)	5.00	5.00	5.00	5.00	5.00	5.00	
	cost (\$)	0.98	0.80	1.08	1.13	0.99	1.03	
Binder	mass(g)	196.75	160.01	216.66	225.53	198.08	206.46	
	commercial unit price (\$/kg)	15.00	15.00	15.00	15.00	15.00	15.00	
	cost (\$)	2.95	2.40	3.25	3.38	2.97	3.10	
Cathode current collector	mass (g)	284.46	215.05	319.28	340.57	278.47	297.09	
	commercial unit price (\$/kg)	1.50	1.50	1.50	1.50	1.50	1.50	
	cost (\$)	0.43	0.32	0.48	0.51	0.42	0.45	
Anode current collector	mass (g)	426.69	322.58	478.93	510.86	417.71	445.63	
	commercial unit price (\$/kg)	1.50	1.50	1.50	1.50	1.50	1.50	
	cost (\$)	0.64	0.48	0.72	0.77	0.63	0.67	
Separator	area (m ²)	14.22	10.75	15.96	17.03	13.92	14.85	
	commercial unit price (\$/m ²)	1.20	1.20	1.20	1.20	1.20	1.20	
	cost (\$)	17.07	12.90	19.16	20.43	16.71	17.83	
Packaging	cost (\$)	8.00	8.00	8.00	8.00	8.00	8.00	
	Total energy (kWh)	1.00	1.00	1.00	1.00	1.00	1.00	
Other Assumptions	Cathode loading (mg/cm ²)	30.00	30.00	30.00	30.00	30.00	30.00	
	Anode type	Hard carbon	Hard carbon	Hard carbon	Hard carbon	Hard carbon	Hard carbon	
	Cathode current collector	Al	Al	Al	Al	Al	Al	
	Anode current collector	Al	Al	Al	Al	Al	Al	
	N/P ratio	1.10	1.10	1.10	1.10	1.10	1.10	
	lean electrolyte usage (g/Ah)	3.00	3.00	3.00	3.00	3.00	3.00	
	carbon ratio (%)	5.00	5.00	5.00	5.00	5.00	5.00	
	binder ratio (%)	5.00	5.00	5.00	5.00	5.00	5.00	
	Total cost	cost (\$)	42.34	36.11	46.34	48.20	43.53	48.75

Continued Table A.5: Cost analysis for NIB full cells at 1KWh level constructed with different cathodes. The unit price for the cathode materials are from the calculation in Figure A.3, and the price of other cell components are sourced from prevailing commercial prices.

Materials	$\text{Na}_{2.9}\text{Ni}_{1.3}\text{Mn}_{2.4}\text{O}_2$	$\text{Na}_{2.0}\text{Ni}_{2.0}\text{Mg}_{1.0}\text{Mn}_{2.0}\text{O}_2$	$\text{Na}_{0.8}[\text{Li}_{0.12}\text{Ni}_{0.22}\text{Mn}_{0.66}]\text{O}_2$	$\text{NaNi}_{1.0}\text{Co}_{1.0}\text{Mn}_{1.0}\text{O}_2$	$\text{Na}_{0.64}\text{Co}_{0.5}\text{O}_2$	LiCoO_2	
Cathode	Nominal Voltage (V)	3.47	3.29	3.03	3.01	3.21	3.80
	specific capacity (mAh/g)	150.00	117.00	116.00	142.00	160.00	150.00
	Capacity (Ah)	288.18	303.95	330.03	332.23	311.53	263.16
	mass (g)	1921.23	2597.87	2845.11	2339.62	1947.04	1754.39
	estimated commercial unit price (\$/kg)	2.44	2.02	2.67	15.96	21.15	30.00
	cost (\$)	4.68	5.24	7.60	37.35	41.18	52.63
Anode	specific capacity (mAh/g)	280.00	280.00	280.00	280.00	280.00	330.00
	mass (g)	1132.15	1194.09	1296.56	1305.17	1223.85	877.19
	commercial unit price (\$/kg)	5.00	5.00	5.00	5.00	5.00	15.00
	cost (\$)	5.66	5.97	6.48	6.53	6.12	13.16
	volume (L)	0.86	0.91	0.99	1.00	0.93	0.79
Electrolyte	commercial unit price (\$/L)	4.00	4.00	4.00	4.00	4.00	7.50
	cost (\$)	3.46	3.65	3.96	3.99	3.74	5.92
Conductive Agent	mass(g)	169.63	210.66	230.09	202.49	176.16	146.20
	commercial unit price (\$/kg)	5.00	5.00	5.00	5.00	5.00	5.00
	cost (\$)	0.85	1.05	1.15	1.01	0.88	0.73
Binder	mass(g)	169.63	210.66	230.09	202.49	176.16	146.20
	commercial unit price (\$/kg)	15.00	15.00	15.00	15.00	15.00	15.00
	cost (\$)	2.54	3.16	3.45	3.04	2.64	2.19
Cathode current collector	mass (g)	256.16	346.38	379.35	311.95	259.61	233.92
	commercial unit price (\$/kg)	1.50	1.50	1.50	1.50	1.50	1.50
	cost (\$)	0.38	0.52	0.57	0.47	0.39	0.35
Anode current collector	mass (g)	384.25	519.57	569.02	467.92	389.41	350.88
	commercial unit price (\$/kg)	1.50	1.50	1.50	1.50	1.50	5.00
	cost (\$)	0.58	0.78	0.85	0.70	0.58	1.75
Separator	area (m ²)	12.81	17.32	18.97	15.60	12.98	11.70
	commercial unit price (\$/m ²)	1.20	1.20	1.20	1.20	1.20	1.20
Packaging	cost (\$)	15.37	20.78	22.76	18.72	15.58	14.04
	cost (\$)	8.00	8.00	8.00	8.00	8.00	8.00
Other Assumptions	Total energy (kWh)	1.00	1.00	1.00	1.00	1.00	1.00
	Cathode loading (mg/cm ²)	30.00	30.00	30.00	30.00	30.00	30.00
	Anode type	Hard carbon	Hard carbon	Hard carbon	Hard carbon	Hard carbon	Graphite
	Cathode current collector	Al	Al	Al	Al	Al	Al
	Anode current collector	Al	Al	Al	Al	Al	Cu
	N/P ratio	1.10	1.10	1.10	1.10	1.10	1.10
	lean electrolyte usage (g/Ah)	3.00	3.00	3.00	3.00	3.00	3.00
	carbon ratio (%)	5.00	5.00	5.00	5.00	5.00	5.00
	binder ratio (%)	5.00	5.00	5.00	5.00	5.00	5.00
	Total cost	cost (\$)	41.52	49.15	54.83	79.80	79.11

Appendix B Supporting Information for Chapter 3

The modified co-precipitation method for pure phase meso-structure controlled NFMO begins with synthesizing a spherical pure TM carbonate precursor. Pure TM carbonate precursor, without hydroxide or other impurities, making it possible to specify the desired molar ratio of TM to Na in the final product. The pH value of the co-precipitation reaction must be controlled to obtain a pure phase TM carbonate precursor. If the pH value is too acidic, residual TM ions will be in the solution, and if the pH value is too basic, hydroxide impurities will form. The optimal pH range for the co-precipitation reaction was experimentally determined by testing the TM sulfates separately with different concentrations of sodium carbonate. The residual concentration of Fe and Mn were determined after the reaction using ICP-OES with the lowest residual TM concentrations at a pH range of 7.8-9.0 shown in **Figure B.1** and **Table B.1**.

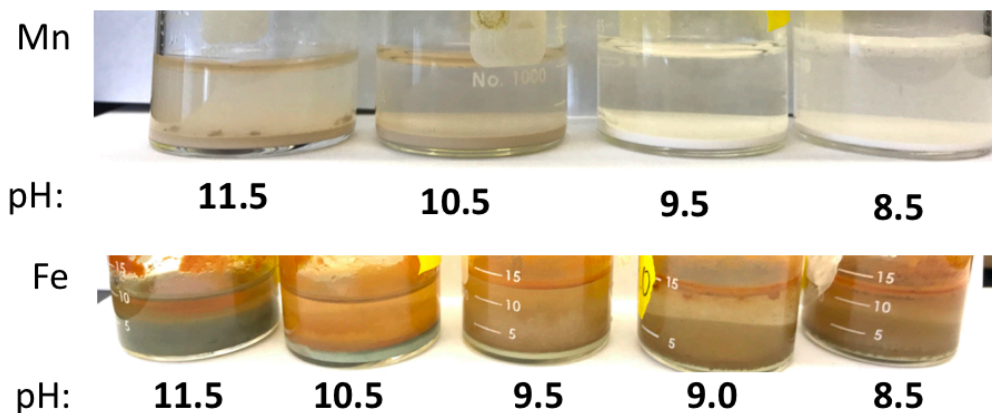


Figure B.1: $\text{Mn}(\text{SO}_4)$ (top) and $\text{Fe}(\text{SO}_4)$ (bottom) aqueous solutions mixed with Na_2CO_3 at different pH values.

Table B.1: Residual TM in solutions shown in SI Figure 1. The optimized pH values are highlighted for Mn and Fe.

Mn			Fe		
initial pH	final pH	residual conc.	initial pH	final pH	residual conc.
11.85	10.68	0	11.69	10.8	0.000417
10.55	9.88	0	10.5	10.03	5.386 E-05
10.06	9.6	0.000110	9.58	8.8	0
9.58	7.69	0	9.01	8.36	0.001305
8.4	6.25	0.079366	8.53	6.22	0.000344

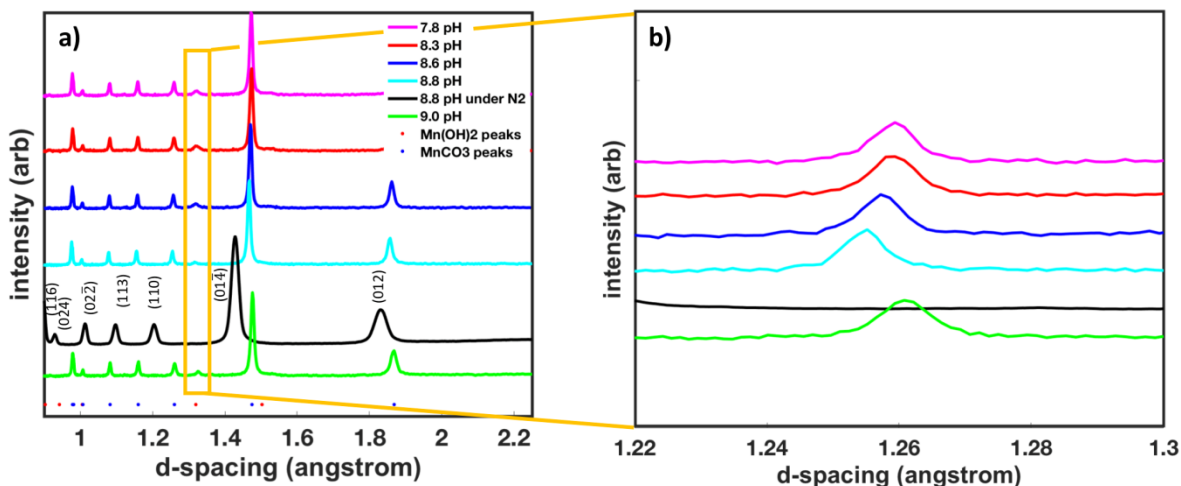


Figure B.2: (a) XRD spectra of iron manganese precipitates synthesized at different pH and atmospheres with enhanced view (b) of the hydroxide impurity peak at 1.26 Å.

The co-precipitation reaction was initially tested in an air atmosphere for the synthesis of $\text{Fe}_{1/4}\text{Mn}_{3/4}\text{CO}_3$ using pH values of 7.8, 8.3, 8.6, 8.8, and 9. The precursors synthesized under air were determined to contain an impurity, identified by a small peak found in the XRD data at 1.26 Å shown in **Figure B.2**. This hydroxide impurity is formed by a TM reaction with oxygen in the solution. A common method to reduce oxygen gas in aqueous solutions is to bubble N_2 gas through the reaction vessel. Through this method, a pure phase of $\text{Fe}_{1/4}\text{Mn}_{3/4}\text{CO}_3$ was obtained as confirmed by XRD result. The refined XRD data of $\text{Fe}_{1/4}\text{Mn}_{3/4}\text{CO}_3$ and SEM images of the particles are shown in SI Figure 3. The $\text{Fe}_{1/4}\text{Mn}_{3/4}\text{CO}_3$ particles were spherical in shape and between 0.6-3.0 μm in diameter.

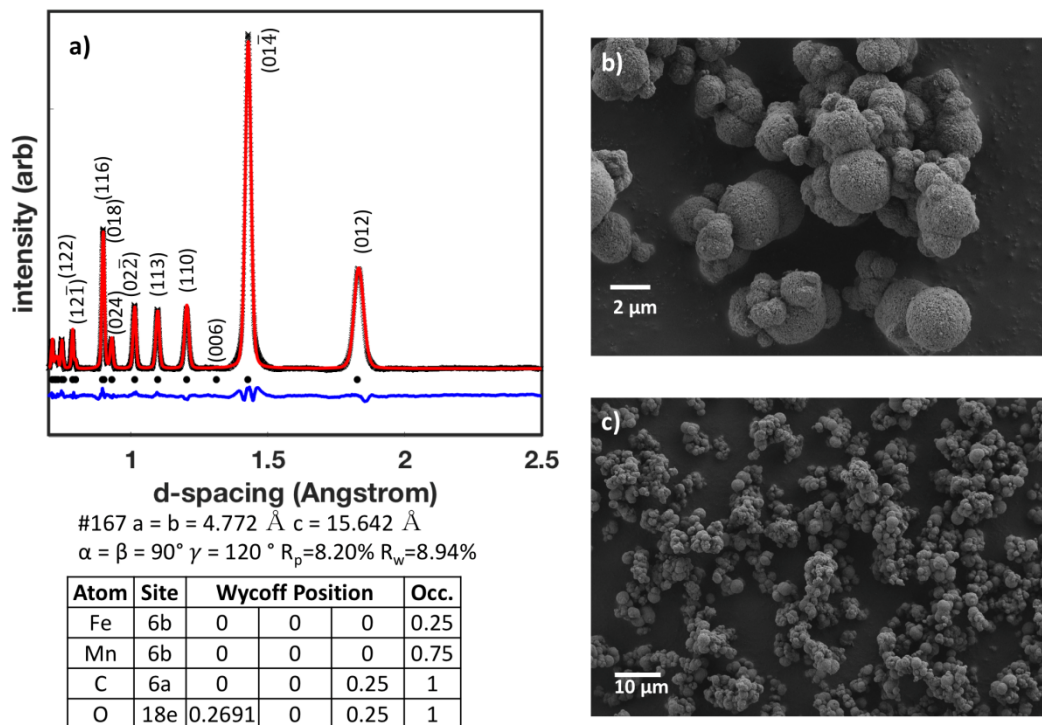


Figure B.3: (a) XRD spectra and Rietveld refinement of $\text{Fe}_{1/4}\text{Mn}_{3/4}\text{CO}_3$ synthesized by co-precipitation and with the refined atomic positions and lattice parameters in the table and (b, c) SEM images showing the spherical morphology.

To synthesize phase pure meso-structure controlled particles using spherical carbonate precursors, the following parameters were sequentially optimized: calcination atmosphere, calcination time, calcination temperature, molar ratio of Na_2CO_3 , and cooling time. First, we compared synthesizing a pure phase of NFMO in an argon atmosphere versus an air atmosphere. The result was that NFMO calcinated in air had a higher fraction of P2 phase than NFMO calcinated in an argon atmosphere. Second, calcination time was tested. NFMO calcinated in air for 15 hours contained a higher fraction of P2 phase than NFMO calcinated for 12 hours. Third, the calcination temperature for NFMO was set at 850°C , 900°C , and 950°C . The sample prepared at 900°C was determined to contain the smallest quantity of impurities. Fourth, the sodium content of $\text{Na}_x\text{Fe}_{1/4}\text{Mn}_{3/4}\text{O}_2$, was adjusted and tested with $x=0.61$, 0.67 , and 0.75 shown in **Figure B.4**. The

result of testing these combinations indicated that a pure phase of P2- $\text{Na}_x\text{Fe}_{1/4}\text{Mn}_{3/4}\text{O}_2$ was synthesized with $x=0.67$ and a calcination of 900°C for 15 h under air.

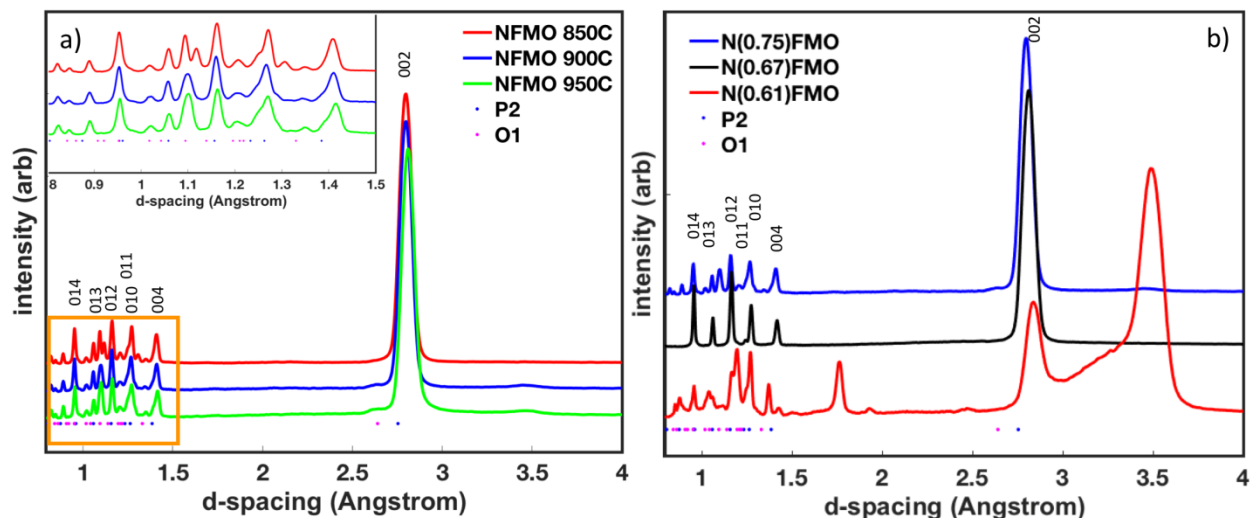


Figure B.4: (a) XRD spectra of NFMO calcinated at different temperatures and (b) NFMO with different sodium content.

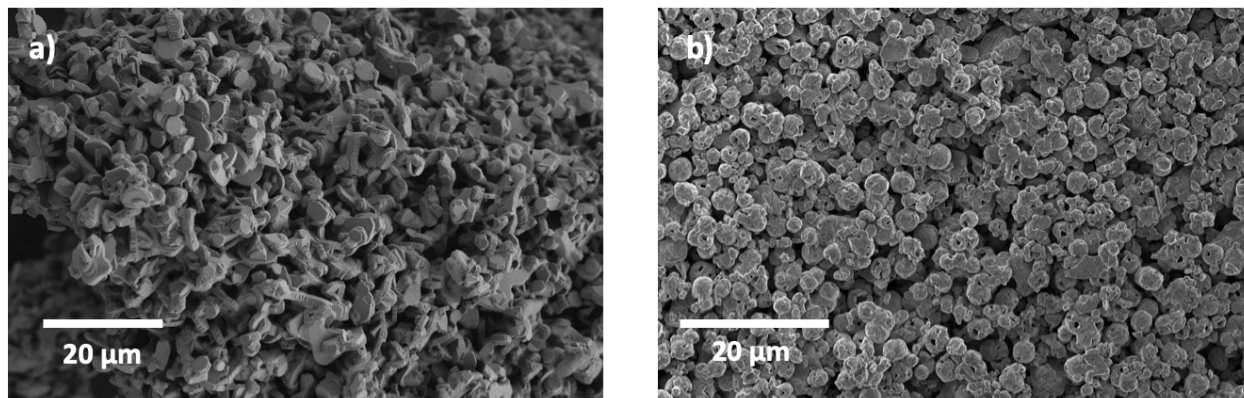


Figure B.5: SEM images of (a) quenched and (b) slow-cooled NFMO.

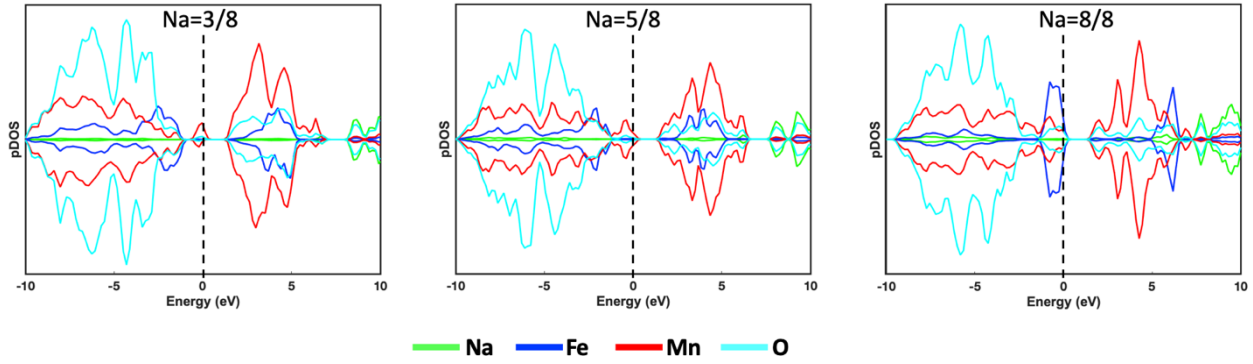


Figure B.6: Partial density of states for $\text{Na}_x\text{Fe}_{0.25}\text{Mn}_{0.75}\text{O}_2$ when $x=3/8, 5/8,$ and $8/8$.

Table B.2: XRD Refinement parameters for slow cooled and quenched NFMO.

Slow cool

#194 $a = b = 2.915\text{\AA}$ $c = 11.255\text{\AA}$

$\alpha = \beta = 90^\circ$ $\gamma = 120^\circ$

$R_p=9.07\%$ $R_w=9.45\%$

Atom	Site	Wyckoff Position			Occ.
Fe1	2a	0	0	0	0.25
Mn1	2a	0	0	0	0.75
O1	4f	1/3	2/3	0.0891	2
Na1	2b	0	0	0.25	0.199
Na2	2d	2/3	1/3	0.25	0.431

Quench

#194 $a = b = 2.916\text{\AA}$ $c = 11.286\text{\AA}$

$\alpha = \beta = 90^\circ$ $\gamma = 120^\circ$

$R_p=11.1\%$ $R_w=11.9\%$

Atom	Site	Wyckoff Position			Occ.
Fe1	2a	0	0	0	0.25
Mn1	2a	0	0	0	0.75
O1	4f	1/3	2/3	0.0891	2
Na1	2b	0	0	0.25	0.209
Na2	2d	2/3	1/3	0.25	0.343

Tables B.3 (a,b): Surface contamination concentration determined by titration of Na₂CO₃ with HCl

a) Calibration

mass of Na ₂ CO ₃ (g)	start pH	end pH	volume of 0.05 M HCl solution (mL)	calculated mass of Na ₂ CO ₃ (g)
0.0011	10.4	7.79	0.2	0.00105
0.0102	11.15	7.86	1.3	0.00688
0.0498	11.46	8.07	6.4	0.03391
0.1002	11.58	8.03	11.9	0.06306

b) Test

material	mass of initial material (g)	start pH	end pH	volume of 0.05 M HCl solution (mL)	adjusted mass (g) (according to calibration)	% surface contamination
NFMO quench	1.0004	12.75	7.45	8.6	0.0710	7.10
NFMO slow cool	1.0002	11.67	8.02	5.3	0.0432	4.32

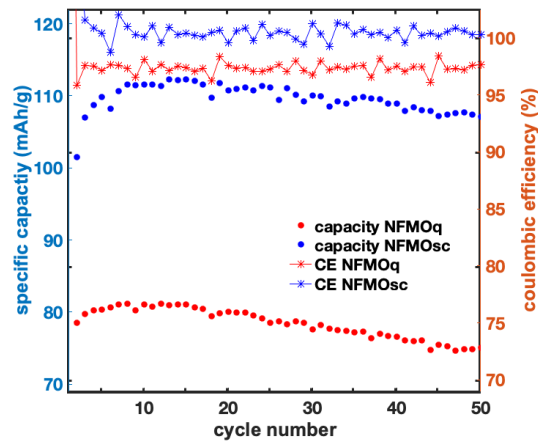


Figure B.7: Specific discharge capacity versus cycle number at a rate of C/10 and coulombic efficiency as a function of cycle number.

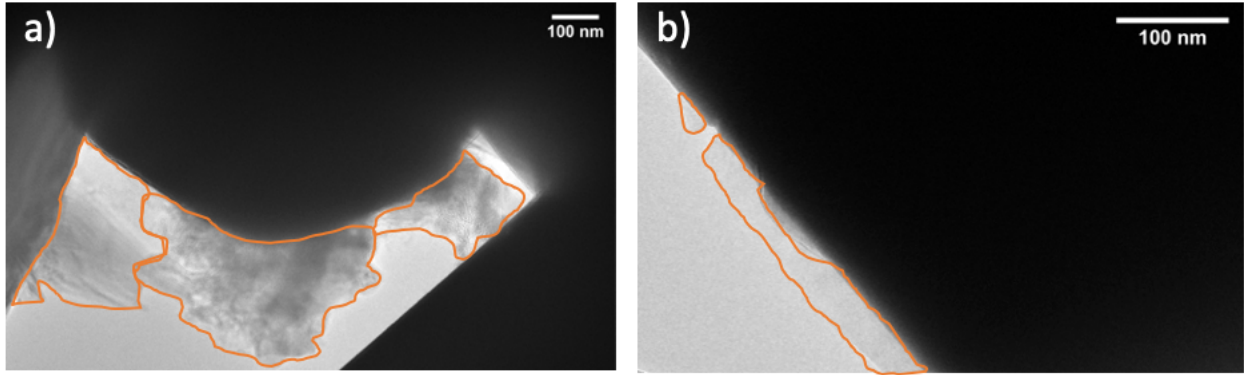


Figure B.8: TEM images of (a) quenched and (b) slow cooled NFMO with the surface contamination outlined in orange.

Appendix C Supporting Information for Chapter 4

Table C.1: NIB cathodes with first discharge energy density greater than 450 Wh/kg made from abundant TM from literature.

Compound	1st dis. energy density (Wh/kg)	C-rate	# cycles	retention (%)	low V	high V	phase	DOI
Na ₂ /3Fe ₁ /2Mn ₁ /2O ₂	619	0.1	10	93	1.5	4.2	P2	10.1016/j.matlet.2017.05.084
Na _{0.67} Mn _{0.5} Fe _{0.5} O ₂	600	0.05	50	64	1.5	4.3	P2	10.1021/acs.chemmater.5b00097
Na ₂ /3Mg ₁ /3Ti ₁ /6Mn ₁ /2O ₂	561	0.2	50	69.5	1.5	4.5	P2	10.1016/j.chempr.2019.08.003
Na ₂ /3Fe ₁ /2Mn ₁ /2O ₂	555	0.1	50	41.9	1.5	4.3	P2	10.1149/2.0911802jes
Na ₂ /3Fe ₁ /2Mn ₁ /2O ₂	520	0.05	30	79	1.5	4.2	P2	10.1038/NMAT3309
NaMnO ₂	519.2	0.05	100	65.8	2	4.2	Pmnm	10.1021/ja509704t
Na _{0.67} Mn _{0.6} Fe _{0.4} O ₂	501	0.1	100	77.7	1.5	4.3	P2	10.1007/s11581-018-2442-5
Na _{0.653} Mn _{0.929} O ₂	491.1	0.1	60	86.7	1.5	4.3	O3	10.1016/j.ensm.2018.10.025
Na _{0.67} Fe _{0.5} Mn _{0.5} O ₂	491	0.1	20	76	1.5	4.3	P2	10.1038/ncomms10308
Na _{0.67} Mn _{0.66} Fe _{0.20} Cu _{0.14} O ₂	490	0.05	100	52	1.5	4.3	P2	10.1021/acs.chemmater.7b01146
Na _{0.67} Mn _{0.6} Fe _{0.3} Zn _{0.1} O ₂	489	0.1	100	88.3	1.5	4.3	P2	10.1007/s11581-018-2442-5
Na ₂ /3Mn ₇ /9Zn ₂ /9O ₂	481	0.1	50	60	1.5	4.2	P2	10.1002/aenm.201802379
Na _{0.67} Mn _{0.702} Fe _{0.198} Ti _{0.102}	479.8	0.1	200	86	1.5	4.3	P'2	10.1002/adfm.201901912
Na ₂ /3Fe ₁ /3Mn ₂ /3O ₂	470	0.05	40	79	1.5	4.3	P2	10.1016/j.jpowsour.2014.04.048
Na _{0.5} Fe _{0.5} Mn _{0.5} O ₂	455	0.1	20	85	1.5	4.25	O3	10.1149/2.058302jes

Table C.2: Selected refinement parameters for XRD of NFMO13, NFMO12, and NFMO11.

	A (Å)	C (Å)	O Z-POSITION	WR (%)
NFMO13	2.8894	11.198	0.0870	3.67
NFMO12	2.8925	11.198	0.0913	2.61
NFMO11	2.9103	11.230	0.0791	4.31

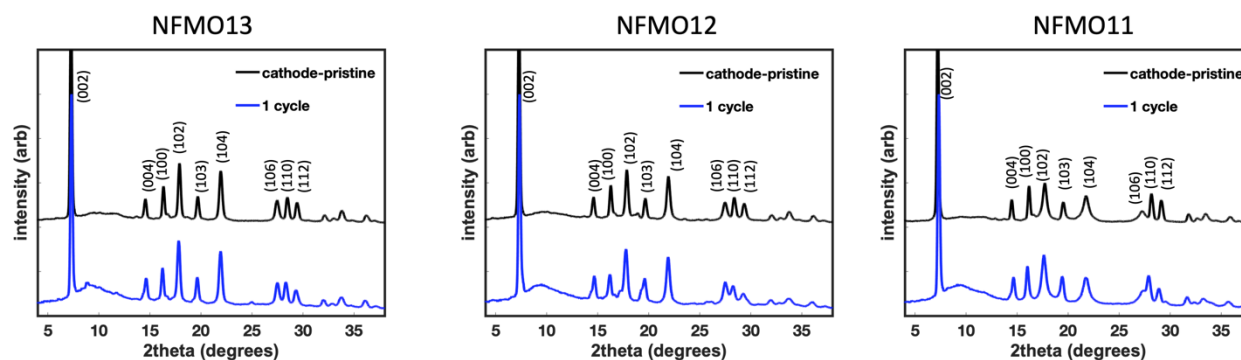


Figure C.1: XRD data of the pristine cathode and cathode after 1 cycle for NFMO13, NFMO12, and NFMO11.

Table C.3: 1st cycle CE and % (discharge) capacity retention after 50 cycles for NFMO13, NFMO12, and NFMO11, corresponding to Figure 4.3.

	1 st cycle CE (%)	% retention (50 cycles)
NFMO13	165	105
NFMO12	191	84.5
NFMO11	158	75.4

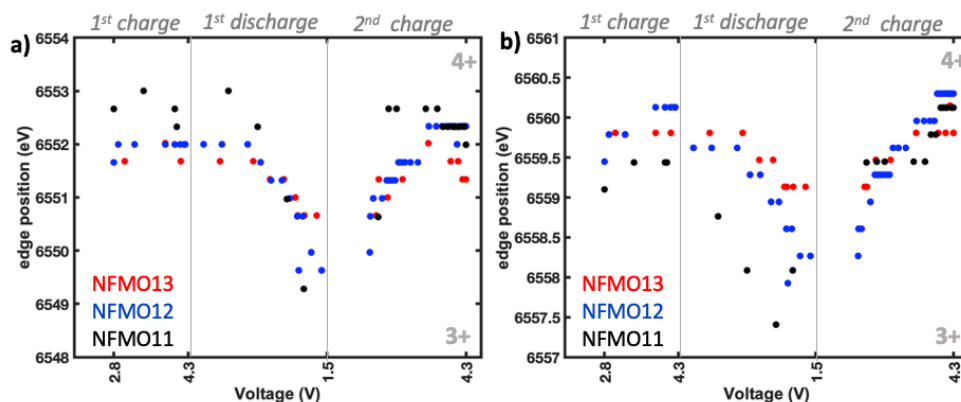


Figure C.2: The Mn K-edge position as analyzed us the (a) half-height method and (b) edge-crest method.

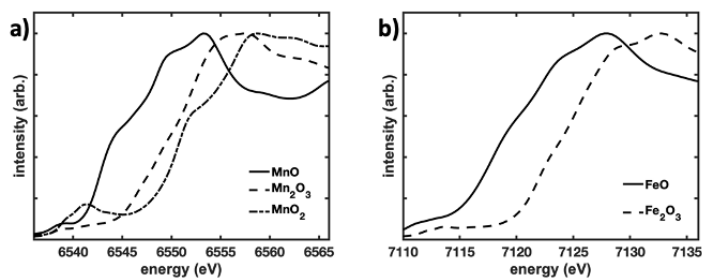


Figure C.3: XANES spectra of the Mn K-edge for (a) MnO, Mn₂O₃, and MnO₂ and the Fe K-edge for (b) FeO and Fe₂O₃.

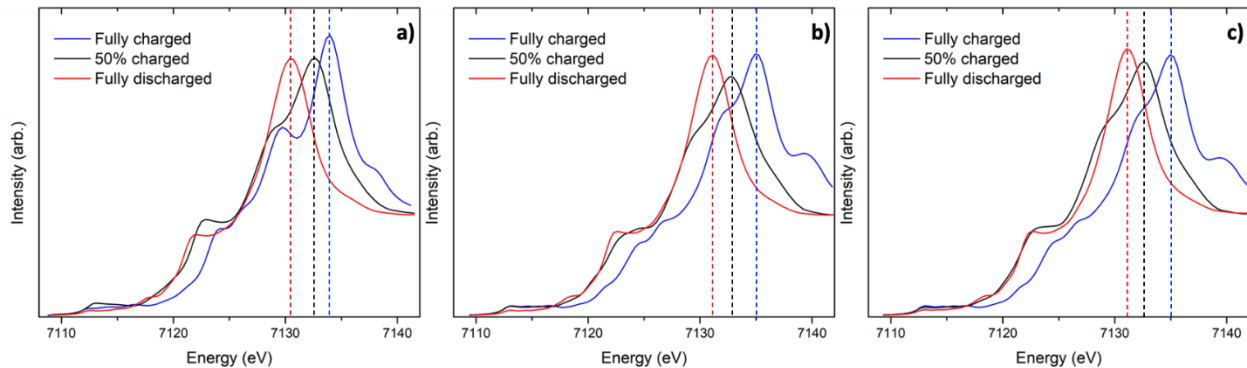


Figure C.4: FEFF9 simulations of the Fe K-edge for a) NFM013, b) NFM012, and c) NFM011 at different states of charge.

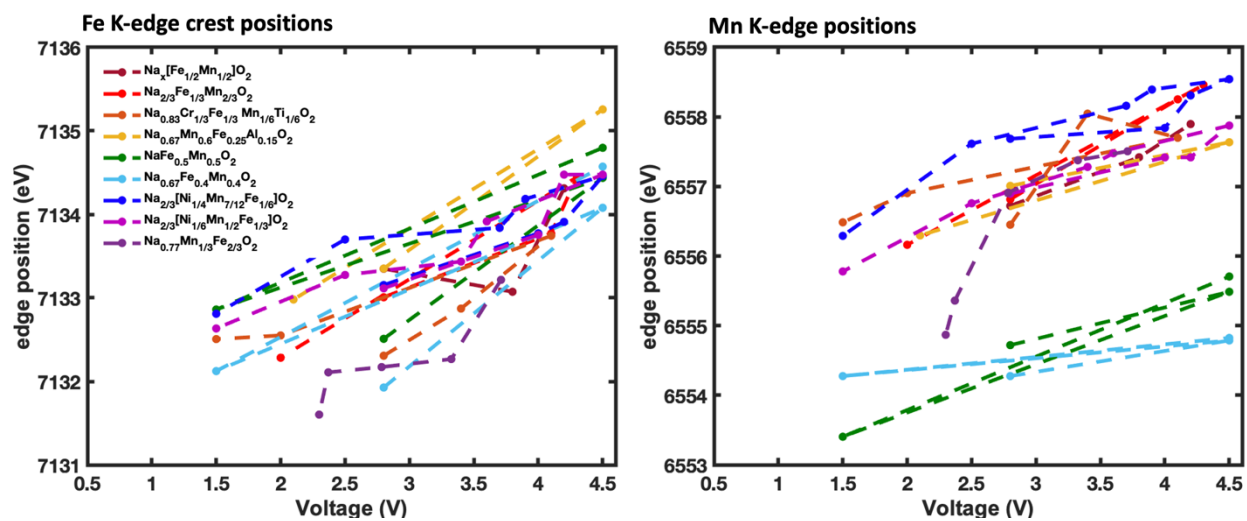


Figure C.5: Extracted Fe K-edge edge-crest positions and Mn K-edge inflection points for NaTMO₂ in literature.

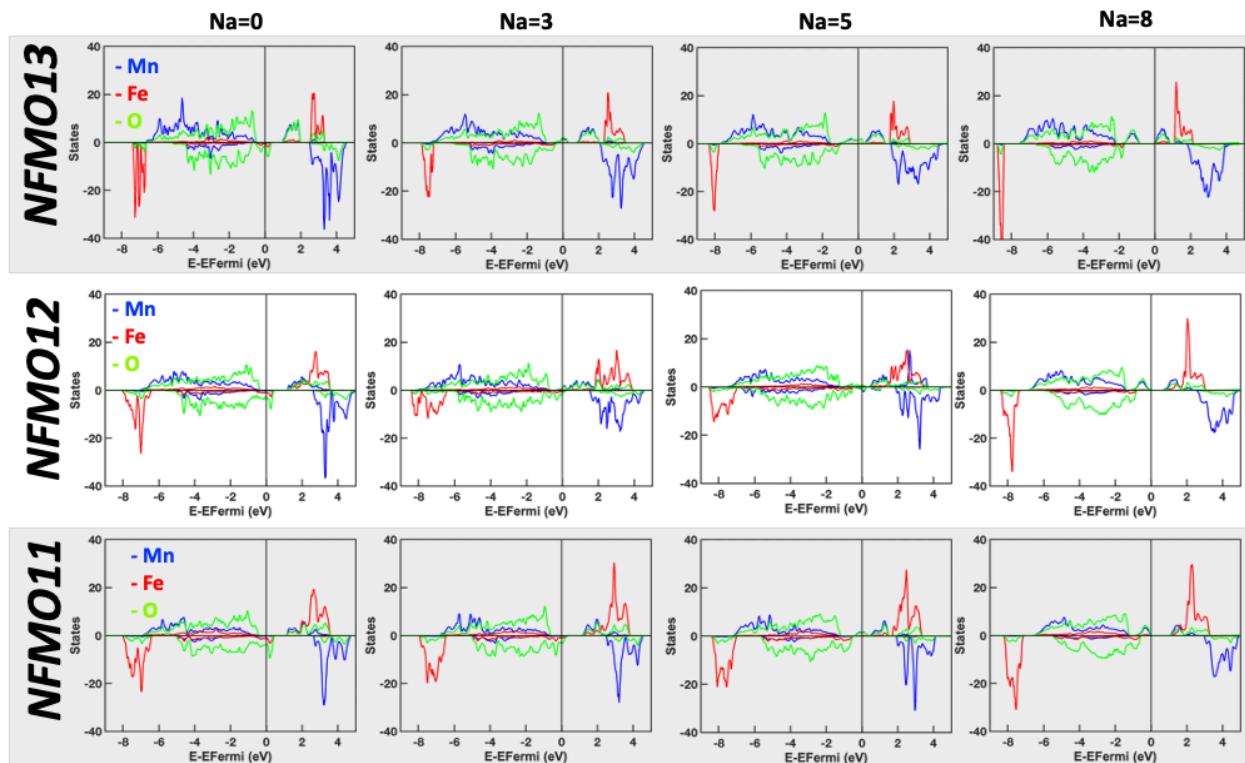


Figure C.6: Calculated DOS of NFM013, NFM012, and NFM011 at different states of charge (Na= 0, 3, 5, and 8 out of 8 possible Na atoms) with blue representing Mn DOS, red representing Fe DOS, and green representing O DOS. DOS sign refers to spin state.

Appendix D Supporting Information for Chapter 5

Table D.1: NIB cathodes with oxygen redox. Compounds containing Ni are highlighted in blue.

Compound	Ni cont.	Phase	claim ox. redox reversibility	1st char. cap. (mAh/g)	1st CE	1st volt. hysteresis	char. ret. at 10 th cycle	rate	Volt. range	Ref. #	Comments
$\text{Na}_{2.3}\text{Ni}_{1.3}\text{Mn}_{2.3}\text{O}_2$	0.33	P2	N	160	0.75	0.17	0.69	0.1	2.6-4.3	[247]	
$\text{Na}_{2.3}\text{Ni}_{1.3}\text{Mn}_{2.3}\text{O}_2$	0.33	P2	N	160	0.98	0.41	0.70	0.1	2-4.5	[287]	
$\text{Na}_{2.3}\text{Ni}_{0.283}\text{Mg}_{0.05}\text{Mn}_{2.3}\text{O}_2$	0.28	P2	N	150	0.95	0.17	0.86	0.077	2-4.5	[288]	more Mg and less Ni reduces phase transition and has better retention
$\text{NaLi}_{0.07}\text{Ni}_{0.26}\text{Mn}_{0.4}\text{Co}_{0.26}\text{O}_2$	0.26	O3	N	181	0.81	1.01	0.80	0.17	1.5-4.5	[289]	
$\text{Na}_{0.78}\text{Ni}_{0.23}\text{Mn}_{0.69}\text{O}_2$	0.23	P2	N	180	0.75	0.54	0.73	0.1	2-4.5	[230]	
$\text{Na}_{2.3}\text{Fe}_{2.9}\text{Ni}_{2.9}\text{Mn}_{5.9}\text{O}_2$	0.22	P2	Y	145	0.94	0.2	0.94	0.1	2.6-4.3	[247]	iron hybridizes with O
$\text{Na}_{0.6}\text{Li}_{0.2}\text{Mn}_{0.8}\text{O}_2$	0	P2	Y	165	0.98	1.19	1	0.067	2-4.6	[290]	reversible but fades
$\text{Na}_{1.3}\text{Nb}_{0.3}\text{Mn}_{0.4}\text{O}_2$	0	disordered rock salt	N	214	0.76	0.94	0.62	0.05	1.0-4.0	[291]	at 50C
$\text{Na}_{2.3}\text{Mg}_{0.28}\text{Mn}_{0.72}\text{O}_2$	0	P2	Y	148	1.10	1.09	1.18	0.067	2-4.5	[42]	
$\text{Na}_{0.7}\text{Li}_{0.3}\text{Mn}_{0.75}\text{O}_2$	0	P2	Y	175	0.85	1.09	0.73	0.1	2-4.4	[292]	
$\text{Na}_{2.3}\text{Mn}_{7.9}\text{Zn}_{2.9}\text{O}_2$	0	P2	Y	195	2.08	0.99	0.86	0.1	1.5-4.2	[179]	
$\text{Na}_{0.72}\text{Li}_{0.24}\text{Mn}_{0.76}\text{O}_2$	0	P2	Y	210	1.29	1.44	1.17	0.05	1.5-4.5	[228]	
$\text{Na}_{2.3}\text{Mg}_{1/3}\text{Ti}_{1/6}\text{Mn}_{1/2}\text{O}_2$	0	P2	Y	175	1.41	1.58	1.19	0.1	1.5-4.5	[76]	
$\text{Na}_{0.6}\text{Li}_{0.35}\text{Fe}_{0.1}\text{Ru}_{0.55}\text{O}_2$	0	P2	Y	126	1.16	0.78	0.99	0.1	1.5-4	[293]	
$\text{Na}_{2.3}\text{Mg}_{0.28}\text{Mn}_{0.72}\text{O}_2$	0	P2	Y	155	1.39	1.37	1.29	0.05	1.5-4.4	[294]	
Na_2RuO_3	0	ordered R-3m	Y	186	0.96	0.4	0.86	0.2	1.5-4	[240]	
$\text{Na}_{2.3}\text{MnO}_{2.33}$	0	P1	Y	78	2.73	1.37	2.17	0.1	1.5-4.5	[295]	poor crystallinity
$\text{Na}_{2.3}\text{Mn}_{0.7}\text{Zn}_{0.3}\text{O}_2$	0	P2	Y	115	1.65	1.9	1.63	0.1	1.5-4.6	[74]	
$\text{Na}_{0.6}\text{Mg}_{0.2}\text{Mn}_{0.6}\text{Co}_{0.2}\text{O}_2$	0	P2	Y	148	1.45	1.27	1.49	0.1	1.5-4.6	[296]	
$\text{Na}_{0.75}\text{Li}_{0.25}\text{Mn}_{0.75}\text{O}_2$	0	honeycomb	Y	163	0.83	0.94	0.84	0.067	2-4.5	[297]	
$\text{Na}_{0.6}\text{Li}_{0.2}\text{Mn}_{0.8}\text{O}_2$	0	ribbon	Y	115	0.90	0.54	0.93	0.067	2-4.5	[297]	
$\text{Na}_{0.67}\text{Cu}_{0.28}\text{Mn}_{0.72}\text{O}_2$	0	P2	Y	110	0.93	0.6	0.94	0.1	2-4.5	[298]	

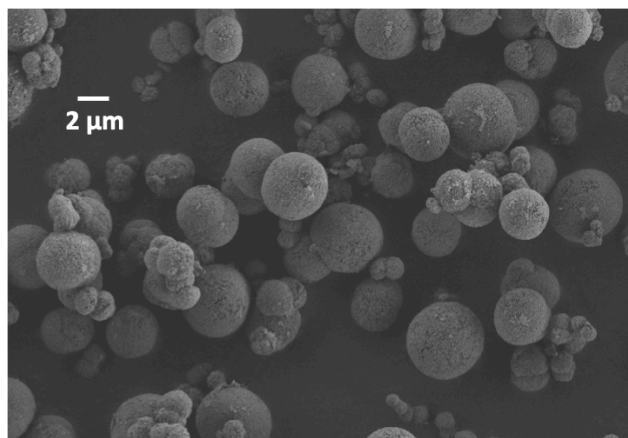


Figure D.1: Spherical $\text{Ni}_{1/4}\text{Mn}_{3/4}\text{CO}_3$ precursors of NLNMO.

Table D.2: Refinement parameters of NLNMO
 #194 $a = b = 2.8933 \text{ \AA}$ $c = 11.0148 \text{ \AA}$

$$\alpha = \beta = 90^\circ \quad \gamma = 120^\circ$$

$$R_p = 2.98\% \quad R_w = 4.60\%$$

Atom	Site	Wyckoff Position			Occ
Ni1	2a	0	0	0	0.259
Mn1	2a	0	0	0	0.649
Li1	2a	0	0	0	0.120
O1	4f	1/3	2/3	0.9224	2.00
Na1	2b	0	0	1/4	0.237
Na2	2d	1/3	2/3	3/4	0.522

ICP results: $\text{Na}_{0.77}\text{Li}_{0.13}\text{Ni}_{0.21}\text{Mn}_{0.66}\text{O}_2$

Table D.3: Refinement parameters of powder NLNMO PDF pattern
 $a = b = 2.8772 \text{ \AA}$, $c = 10.9957 \text{ \AA}$, $\alpha = \beta = 90^\circ$, $\gamma = 120^\circ$

Elem.	x	y	z	U11	U33	U12
Li	0	0	0.5	0.00205	0.00409	0.00102
Li	0	0	0	0.00205	0.00409	0.00102
Ni	0	0	0.5	0.00205	0.00409	0.00102
Ni	0	0	0	0.00205	0.00409	0.00102
Mn	0	0	0.5	0.00205	0.00409	0.00102
Mn	0	0	0	0.00205	0.00409	0.00102
Na	0	0	0.25	0.04	0.04	0.04
Na	0	0	0.75	0.04	0.04	0.04
Na	2/3	1/3	0.25	0.08305	0.01762	0.04152
Na	1/3	2/3	0.35	0.08305	0.01762	0.04152
O	1/3	2/3	0.09	0.00438	0.00252	0.00219
O	2/3	1/3	0.59	0.00438	0.00252	0.00219
O	2/3	1/3	0.91	0.00438	0.00252	0.00219
O	1/3	2/3	0.41	0.00438	0.00252	0.00219

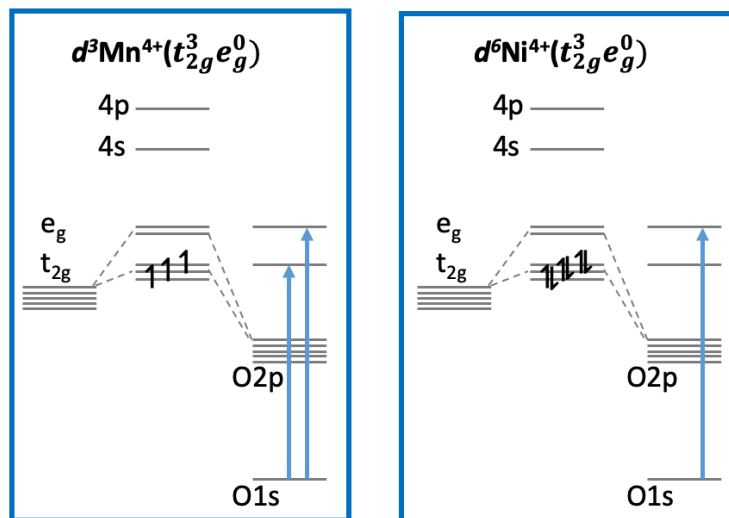


Figure D.2: Schematic diagrams of the O K-edge sXAS electronic transitions from the O1s state to empty states in the transition metals of NLNMO. The diagram is simplified to show one electron energy and does not distinguish between spin-up and spin-down states.

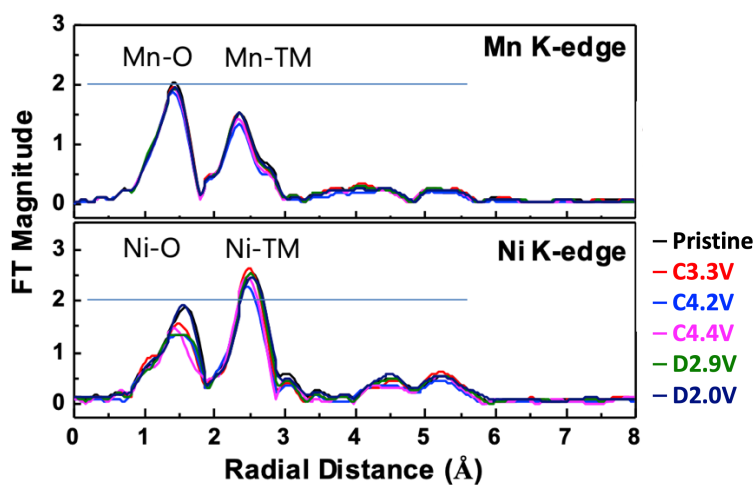


Figure D.3: Fourier transformed EXAFS of NLNMO at the Mn K-edge and Ni K-edge. The blue lines at a FT magnitude of 2 are guides to compare the backscattering ability.

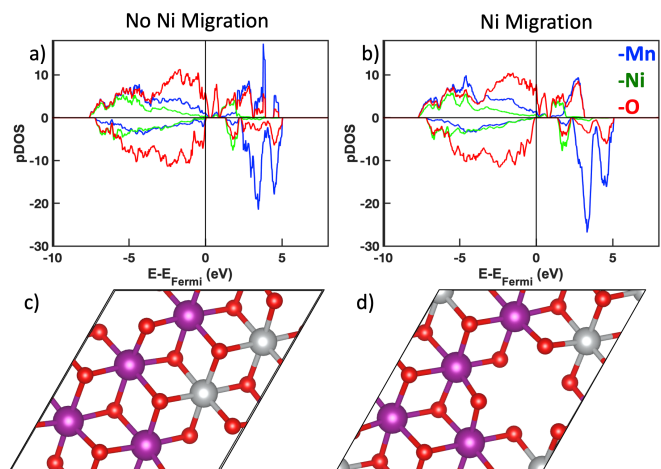


Figure D.4: Calculated DOS for fully charged NLNMO with (a) no Ni migration and (b) with Ni migration with their respective TM layer structures (c, d). Purple represents Mn atoms, silver represents Ni atoms, and red represents oxygen atoms.

Appendix E Supporting Information for Chapter 6

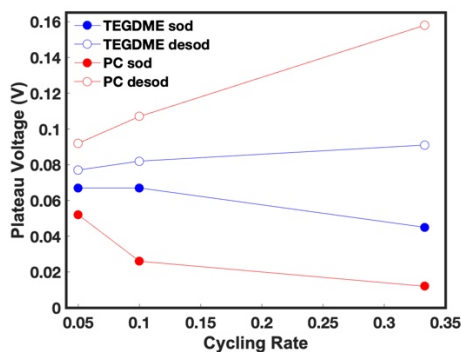


Figure E.1: Plateau voltages of the first cycle of HC in PC or TEGDME electrolyte at different cycling rates.

Table E.1: Percent of plateau capacity during the first cycle of HC in PC or TEGDME electrolyte at different cycling rates.

Rate	TEGDME		PC	
	sod.	desod.	sod.	desod.
0.333	66%	71%	40%	41%
0.1	65%	70%	62%	67%
0.05	65%	70%	62%	68%

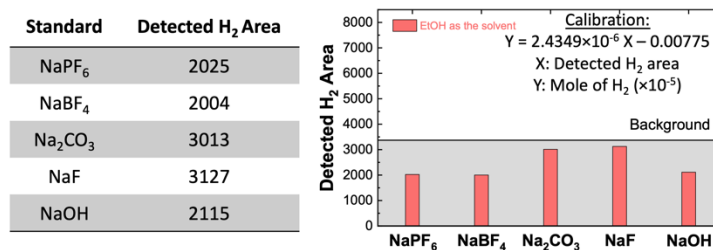


Table and Figure E.2: TGC results of the potential SEI components of HC in PC or TEGDME electrolyte.

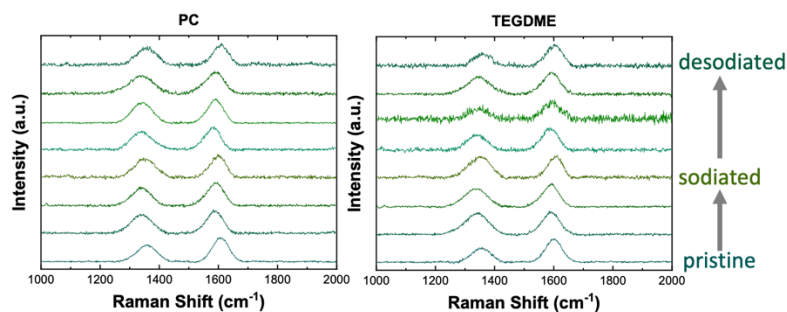


Figure E.3: Raman spectra of HC in PC or TEGDME electrolytes at different states of (de)sodiation.

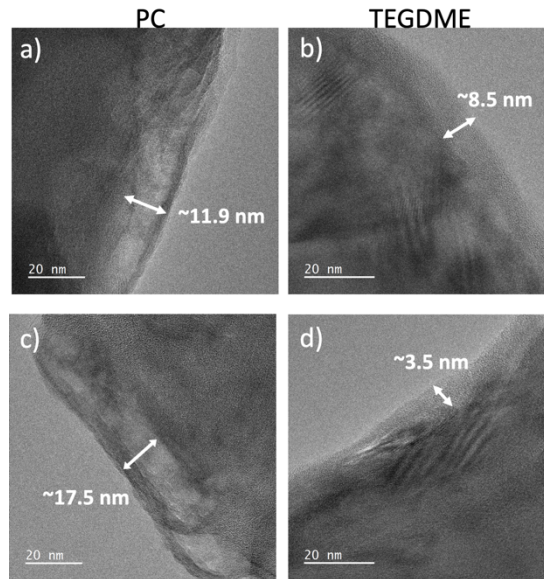


Figure E.4: Cryo-TEM images of HC after 1 cycle at a rate of C/3 in (a,c) PC and (b,d) TEGDME electrolyte. The thickness of the SEI at various location is measured and labeled in the images.

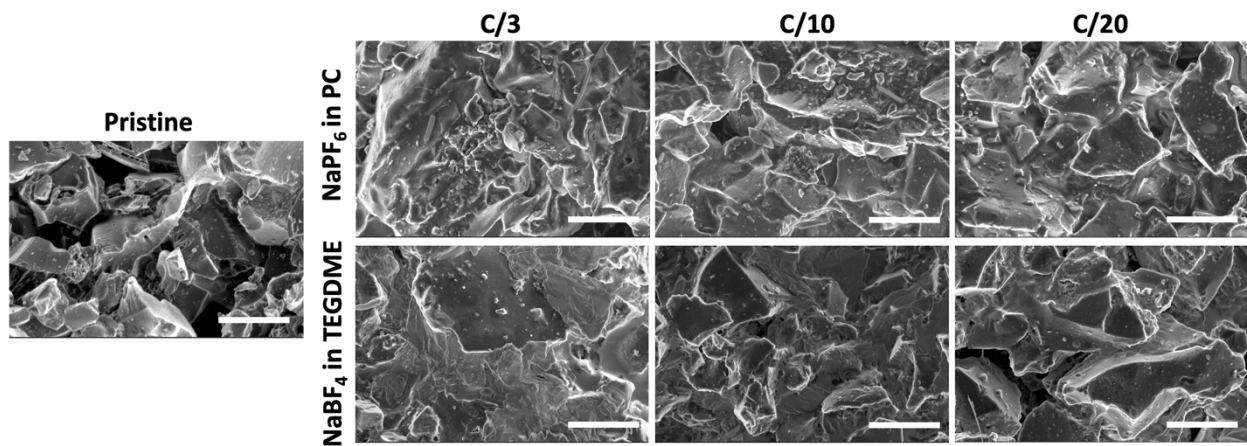


Figure E.5: SEM images of pristine HC, HC after 1 cycle at a rate of C/3, C/10, and C/20 with PC (top row) or TEGDME (bottom row) as the electrolyte. The scale bar represents 5 μm .

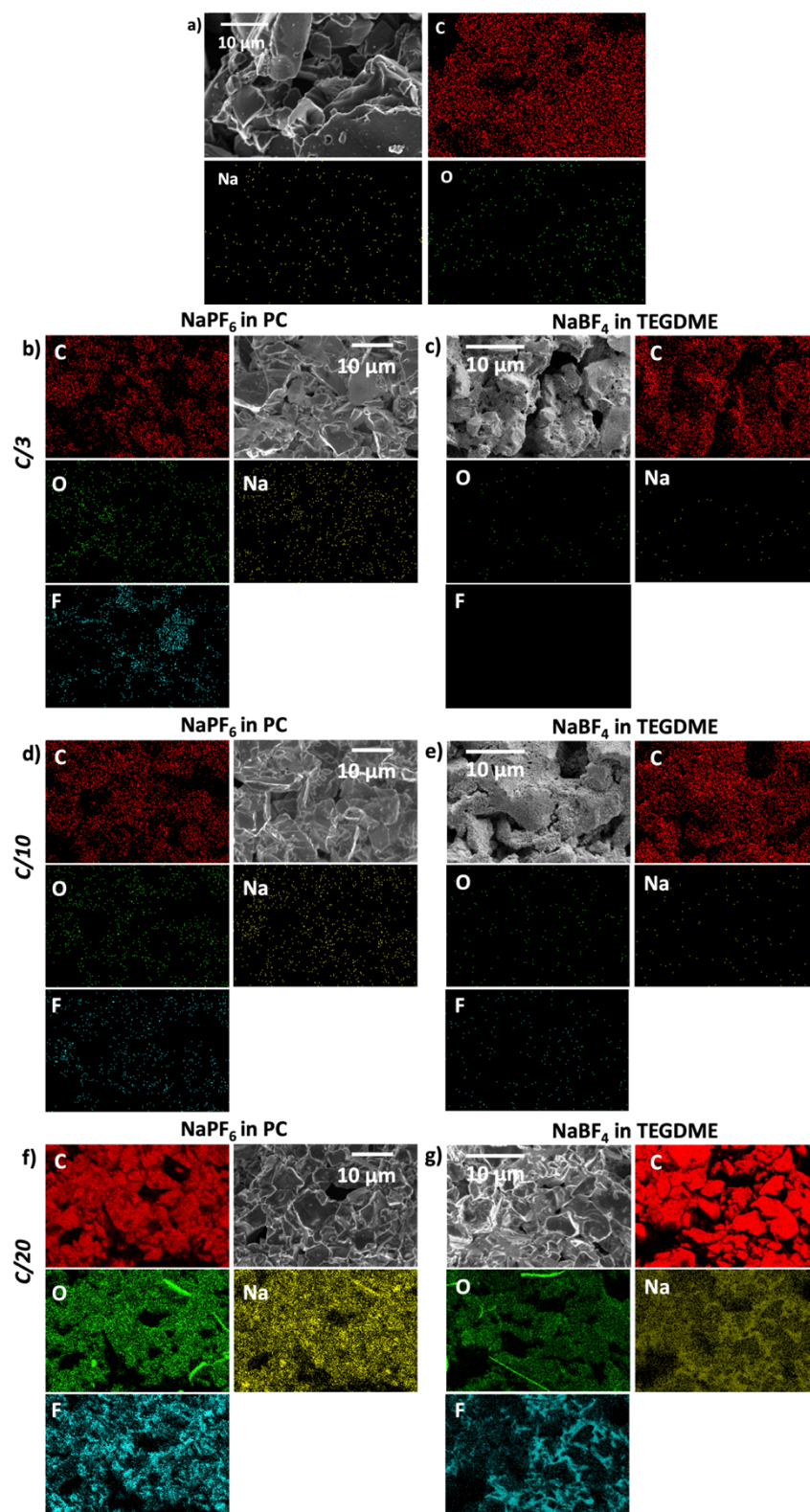


Figure E.6: EDS mapping of (a) pristine HC, (b,c) HC after 1 cycle at a rate of C/3, (d,e) C/10, and (f,g) C/20 with PC or TEGDME electrolytes.

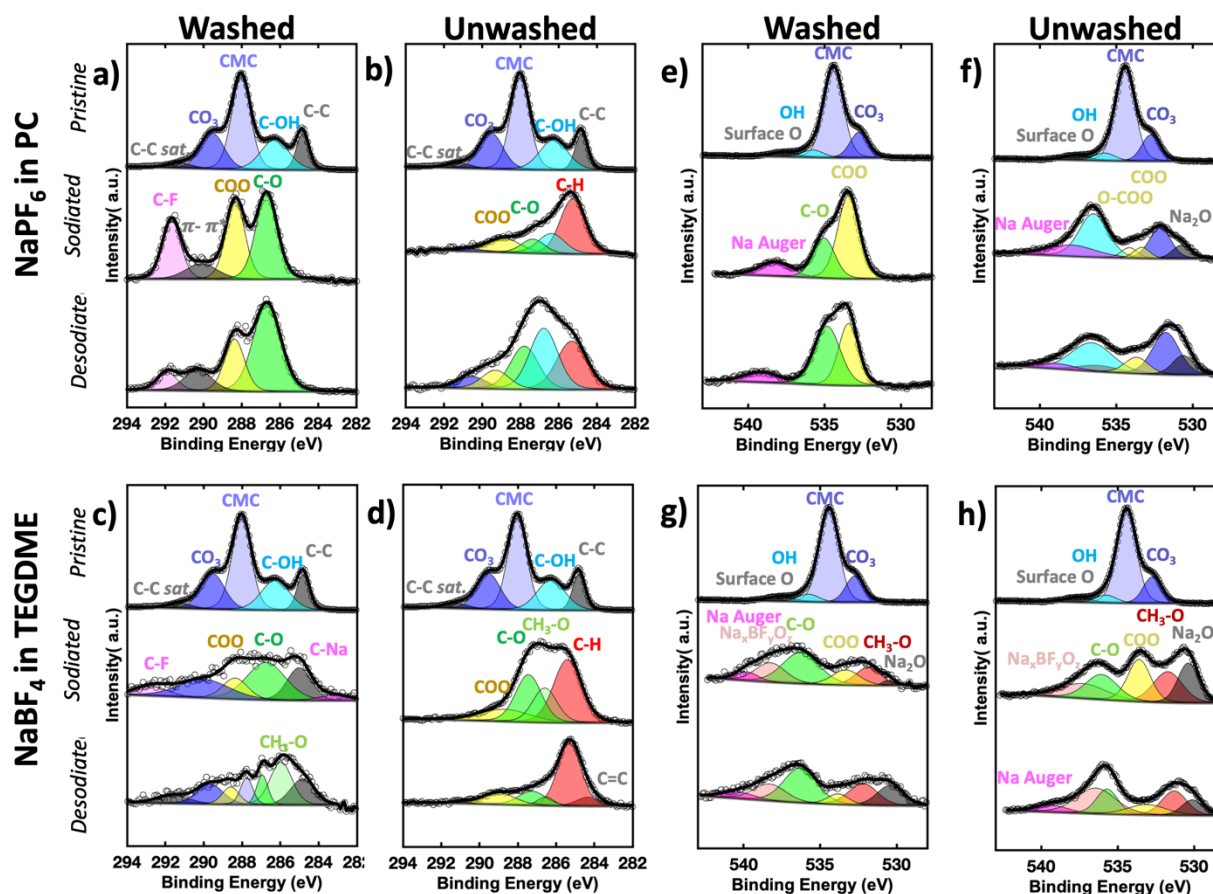


Figure E.7: XPS C 1s regions of washed (left) and unwashed (right) samples of HC at different states of charge with (a,b) PC or (c,d) TEGDME as the electrolyte. XPS O 1s regions of washed (left) and unwashed (right) samples of HC at different states of charge with (e,f) PC or (g,h) TEGDME as the electrolyte.

E.1 XPS sample preparation discussion

There are two key observations of the differences between the washed and unwashed XPS samples. 1) There are components in the unwashed samples that are not identified in the washed samples. This implies that these SEI components are susceptible to being removed by washing. For PC, the washed samples are missing the C-H, C-OH, CO₃, and Na₂O bonding species. These bonding species could either be dissolved in PC or physically removed during the washing process. In fact, -OH species are partially soluble in PC and likely removed by excess PC during washing.[299] Additionally, organic carbonates tend to form on the part of the SEI farthest from

the HC surface. Hydroxyl and carbonate species tend to form a loosely packed SEI which could aid in their removal, as well as any chemical species attached to them, like sodium oxide.[300] For TEGDME there are less differences between the washed and unwashed samples, with only the C-H peak not visible in the washed sample. Hydrocarbons have been reported to form on the top layer of the SEI and the C-H peak is missing for both washed electrodes implying that the outer layer of the SEI is removed by washing for both PC and TEGDME.[283] However, the reduced differences of the washed and unwashed TEGDME samples, when compared to the PC samples, suggest that the SEI formed in the TEGDME electrolyte is more stable chemically and/or mechanically than the SEI formed in the PC electrolyte. 2) There are components in the washed samples that are not identified in the unwashed samples. This implies that either the SEI components are depth dependent and/or washing the sample promotes new chemical reactions. However, it is more probable that the SEI has a multilayered structure as previously reported in literature. [301,302] Specially, C-F bonding is only visible on the washed samples for both SEI formed in the PC and TEGDME electrolytes. This bonding is likely caused by the reaction of the salt anions with either the HC surface or with solvent decomposition products on the HC surface.

It is also important to note that the salt species do not overwhelm the signals for the unwashed samples (**Figure E.8**), which repudiates the arguments for washing XPS samples. For these reasons, in order to observe the complex surface species of the SEI, samples were not washed with a solvent. Instead, samples were cycled with limited electrolyte and dried under vacuum to remove the electrolyte solvent. This method of sample preparation enabled observation of a more complete picture of the SEI and was used throughout this study.

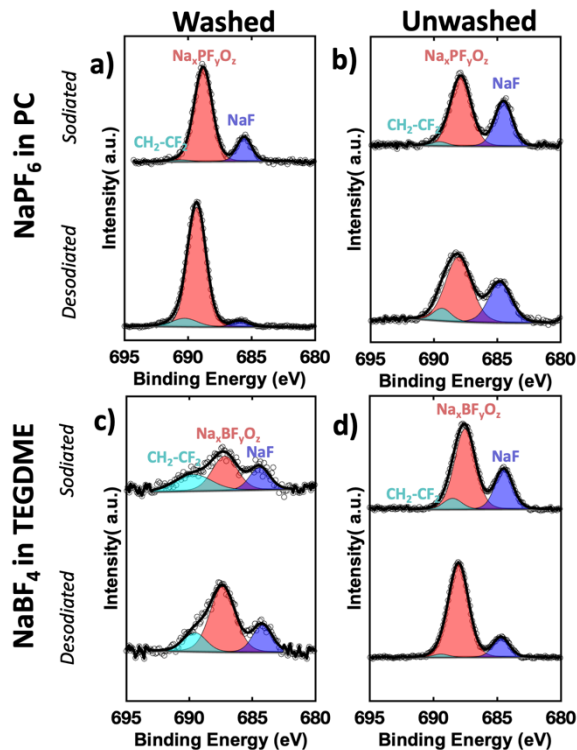


Figure E.8: XPS F 1s regions of washed (left) and unwashed (right) samples of HC at different states of charge with (a,b) PC or (c,d) TEGDME electrolyte.

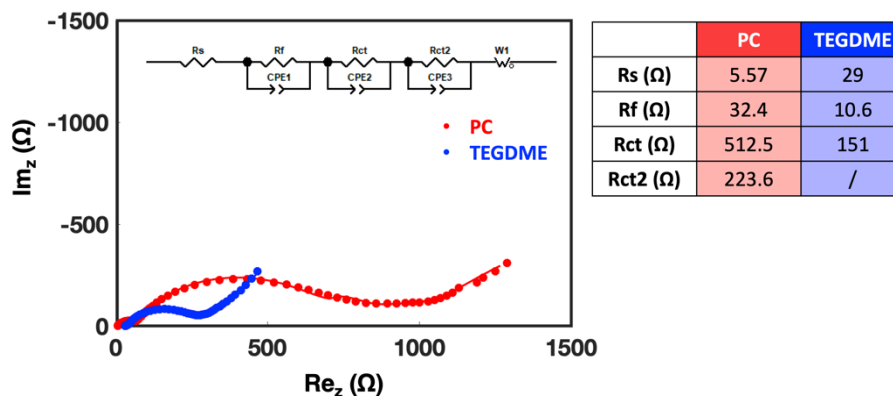


Figure E.9: Nyquist plots of HC in PC (red) or TEGDME (blue) electrolyte after 1 cycle at a rate of C/3. The fit of the data is based on the circuit (inset). The table contains the values from the impedance data fit.

The circuit model in **Figure E.9** accounts for the ohmic resistance of the electrolyte (R_s), the resistance due to Na⁺ diffusion through the SEI on HC (R_f), the double layer capacitance of the electrode/electrolyte interface (CPE_1), the charge transfer resistance (R_{ct} , R_{ct2}), the double layer

capacitance (CPE_2 , CPE_3), and the Warburg impedance (W_o) known as the impedance of solid-state diffusion of Na^+ through the bulk of HC.

References

- [1] R. Fu, T. Remo, R. Margolis, R. Fu, T. Remo, R. Margolis, 2018 U . S . Utility-Scale Photovoltaics- Plus-Energy Storage System Costs Benchmark, Natl. Renew. Energy Lab. (2018) 32. <https://www.nrel.gov/docs/fy19osti/71714.pdf>.%0Ahttps://www.nrel.gov/docs/fy19osti/71714.pdf.
- [2] M. Winter, R.J. Brodd, What Are Batteries , Fuel Cells , and Supercapacitors ? What Are Batteries , Fuel Cells , and Supercapacitors ?, 104 (2004) 4245–4270. doi:10.1021/cr020730k.
- [3] Y. Li, Y. Lu, C. Zhao, Y.S. Hu, M.M. Titirici, H. Li, X. Huang, L. Chen, Recent advances of electrode materials for low-cost sodium-ion batteries towards practical application for grid energy storage, Energy Storage Mater. 7 (2017) 130–151. doi:10.1016/j.ensm.2017.01.002.
- [4] N. Yabuuchi, K. Kubota, M. Dahbi, S. Komaba, Research development on sodium-ion batteries., Chem. Rev. 114 (2014) 11636–11682. doi:10.1021/cr500192f.
- [5] C.S. Rustomji, Y. Yang, T.K. Kim, J. Mac, Y.J. Kim, E. Caldwell, H. Chung, Y.S. Meng, Liquefied gas electrolytes for electrochemical energy storage devices, Science (80-.). 356 (2017). doi:10.1126/science.aal4263.
- [6] L.B. Mccusker, R.B. Von Dreele, D.E. Cox, D. Louër, P. Scardi, Rietveld refinement guidelines, J. Appl. Crystallogr. 32 (1999) 36–50. doi:10.1107/S0021889898009856.
- [7] O.J. Borkiewicz, B. Shyam, K.M. Wiaderek, C. Kurtz, P.J. Chupas, K.W. Chapman, The AMPIX electrochemical cell: A versatile apparatus for in situ X-ray scattering and spectroscopic measurements, J. Appl. Crystallogr. 45 (2012) 1261–1269. doi:10.1107/S0021889812042720.
- [8] F.M.F. De Groot, X-ray absorption and dichroism of transition metals and their compounds, J. Electron Spectros. Relat. Phenomena. 67 (1994) 529–622. doi:10.1016/0368-2048(93)02041-J.
- [9] S.J.L. Billinge, The rise of the X-ray atomic pair distribution function method: A series of fortunate events, Philos. Trans. R. Soc. A Math. Phys. Eng. Sci. 377 (2019). doi:10.1098/rsta.018.0413.
- [10] C.S. Fadley, X-ray photoelectron spectroscopy: Progress and perspectives, J. Electron Spectros. Relat. Phenomena. 178–179 (2010) 2–32. doi:10.1016/j.elspec.2010.01.006.
- [11] K.D. Parry V, Scanning Electron Microscopy : An introduction, III-Vs Rev. 13 (2000) 40–44. doi:10.1016/S0961-1290(00)80006-X.
- [12] R. Fu, D. Feldman, R. Margolis, M. Woodhouse, K. Ardani, R. Fu, D. Feldman, R. Margolis, M. Woodhouse, K. Ardani, U . S . Solar Photovoltaic System Cost Benchmark :

- Q1 2017 U . S . Solar Photovoltaic System Cost Benchmark : Q1 2017, Natl. Renew. Energy Lab. (2017) 1–59. <https://www.nrel.gov/docs/fy17osti/68925.pdf>.
- [13] W. Cole, A.W. Frazier, W. Cole, A.W. Frazier, Cost Projections for Utility- Scale Battery Storage Cost Projections for Utility- Scale Battery Storage, Nrel. (2019).
- [14] B. Dunn, H. Kamath, J.-M. Tarascon, Electrical Energy Storage for the Grid: A Battery of Choices, *Science* (80-.). 334 (2011) 928–935. doi:10.1126/science.1212741.
- [15] J. Alvarado, C. Ma, S. Wang, K. Nguyen, M. Kodur, Y.S. Meng, Improvement of the Cathode Electrolyte Interphase on P2-Na $\frac{2}{3}$ Ni $\frac{1}{3}$ Mn $\frac{2}{3}$ O $\frac{2}{3}$ by Atomic Layer Deposition, *ACS Appl. Mater. Interfaces*. 9 (2017) 26518–26530. doi:10.1021/acsami.7b05326.
- [16] H. Wang, X.-Z. Liao, Y. Yang, X. Yan, Y.-S. He, Z.-F. Ma, Large-Scale Synthesis of NaNi $\frac{1}{3}$ Fe $\frac{1}{3}$ Mn $\frac{1}{3}$ O $\frac{2}{3}$ as High Performance Cathode Materials for Sodium Ion Batteries, *J. Electrochem. Soc.* 163 (2016) A565–A570. doi:10.1149/2.0011605jes.
- [17] M. Schimpe, M. Naumann, N. Truong, H.C. Hesse, S. Santhanagopalan, A. Saxon, A. Jossen, Energy efficiency evaluation of a stationary lithium-ion battery container storage system via electro-thermal modeling and detailed component analysis, *Appl. Energy*. 210 (2018) 211–229. doi:10.1016/j.apenergy.2017.10.129.
- [18] L. Munuera, H. Fukui, Tracking Energy Integration, 2019. <https://www.iea.org/reports/tracking-energy-integration/demand-response>.
- [19] D.M. Kammen, D.A. Sunter, City-integrated renewable energy for urban sustainability, *Science* (80-.). 352 (2016) 922–928. doi:10.1126/science.aad9302.
- [20] A.T.D. Perera, S. Coccolo, J.L. Scartezzini, The influence of urban form on the grid integration of renewable energy technologies and distributed energy systems, *Sci. Rep.* 9 (2019) 1–14. doi:10.1038/s41598-019-53653-w.
- [21] B. Dunn, B. Dunn, H. Kamath, J. Tarascon, Electrical energy storage for the gridfor the Grid : A Battery of choices, *Sci. Mag.* 334 (2011) 928–936. doi:10.1126/science.1212741.
- [22] Q. Huang, Q. Wang, Next-generation, high-energy-density redox flow batteries, *Chempluschem*. 80 (2015) 312–322. doi:10.1002/cplu.201402099.
- [23] M.D. Bhatt, C. O’Dwyer, Recent progress in theoretical and computational investigations of Li-ion battery materials and electrolytes, *Phys. Chem. Chem. Phys.* 17 (2015) 4799–4844. doi:10.1039/c4cp05552g.
- [24] T.M. Letcher, Storing Energy: With Special Reference to Renewable Energy Sources, 2016. doi:10.1515/ci-2016-0627.
- [25] G. Li, Z. Chen, J. Lu, Lithium-Sulfur Batteries for Commercial Applications, *Chem.* 4 (2018) 3–7. doi:10.1016/j.chempr.2017.12.012.

- [26] T. Placke, R. Kloepsch, S. Dühnen, M. Winter, Lithium ion, lithium metal, and alternative rechargeable battery technologies: the odyssey for high energy density, *J. Solid State Electrochem.* 21 (2017) 1939–1964. doi:10.1007/s10008-017-3610-7.
- [27] M. Agostini, Y. Aihara, T. Yamada, B. Scrosati, J. Hassoun, A lithium-sulfur battery using a solid, glass-type P2S 5-Li2S electrolyte, *Solid State Ionics.* 244 (2013) 48–51. doi:10.1016/j.ssi.2013.04.024.
- [28] Y.G. Lee, S. Fujiki, C. Jung, N. Suzuki, N. Yashiro, R. Omoda, D.S. Ko, T. Shiratsuchi, T. Sugimoto, S. Ryu, J.H. Ku, T. Watanabe, Y. Park, Y. Aihara, D. Im, I.T. Han, High-energy long-cycling all-solid-state lithium metal batteries enabled by silver-carbon composite anodes, *Nat. Energy.* 5 (2020) 299–308. doi:10.1038/s41560-020-0575-z.
- [29] A. Manthiram, Y. Fu, S. Chung, C. Zu, Y. Su, Rechargeable Lithium – Sulfur Batteries, *Chem. Rev.* 114 (2014) 11751–11787.
- [30] W. Zhang, J. Nie, F. Li, Z.L. Wang, C. Sun, A durable and safe solid-state lithium battery with a hybrid electrolyte membrane, *Nano Energy.* 45 (2018) 413–419. doi:10.1016/j.nanoen.2018.01.028.
- [31] Y. Wang, W.D. Richards, S.P. Ong, L.J. Miara, J.C. Kim, Y. Mo, G. Ceder, Design principles for solid-state lithium superionic conductors, *Nat. Mater.* 14 (2015) 1026–1031. doi:10.1038/nmat4369.
- [32] Y.-S. Hu, Batteries: Getting solid, *Nat. Energy.* 1 (2016). doi:10.1038/nenergy.2016.42.
- [33] J. Wen, Y. Yu, C. Chen, A review on lithium-ion batteries safety issues: Existing problems and possible solutions, *Mater. Express.* 2 (2012) 197–212. doi:10.1166/mex.2012.1075.
- [34] Y. Wang, W.H. Zhong, Development of electrolytes towards achieving safe and high-performance energy-storage devices: A review, *ChemElectroChem.* 2 (2015) 22–36. doi:10.1002/celec.201402277.
- [35] D. Gleisberg, MINERAL COMMODITY SUMMARIES, 2019. doi:10.1007/978-3-540-47108-0_4.
- [36] M. Garside, Average Lithium Carbonate Price from 2010 to 2018, Statista. (2019). <https://www.statista.com/statistics/606350/battery-grade-lithium-carbonate-price/>.
- [37] C. Werber, Global lithium prices, Th Atlas. (2016).
- [38] Taylor S.R, Abundance of chemical elements in the continental crust: a new table, *Geochim. Cosmochim. Acta.* 28 (1964) 1273–1285.
- [39] F. Culkin, R.A. Cox, Sodium, potassium, magnesium, calcium and strontium in sea water, *Deep. Res. Oceanogr. Abstr.* 13 (1966) 789–804. doi:10.1016/0011-7471(76)90905-0.
- [40] M. Chen, W. Hua, J. Xiao, D. Cortie, W. Chen, E. Wang, Z. Hu, Q. Gu, X. Wang, S. Indris,

- S.L. Chou, S.X. Dou, NASICON-type air-stable and all-climate cathode for sodium-ion batteries with low cost and high-power density, *Nat. Commun.* 10 (2019) 1–11. doi:10.1038/s41467-019-09170-5.
- [41] K. Saravanan, C.W. Mason, A. Rudola, K.H. Wong, P. Balaya, The first report on excellent cycling stability and superior rate capability of $\text{Na}_3\text{V}_2(\text{PO}_4)_3$ for sodium ion batteries, *Adv. Energy Mater.* 3 (2013) 444–450. doi:10.1002/aenm.201200803.
- [42] U. Maitra, R.A. House, J.W. Somerville, N. Tapia-Ruiz, J.G. Lozano, N. Guerrini, R. Hao, K. Luo, L. Jin, M.A. Pérez-Osorio, F. Massel, D.M. Pickup, S. Ramos, X. Lu, D.E. McNally, A. V. Chadwick, F. Giustino, T. Schmitt, L.C. Duda, M.R. Roberts, P.G. Bruce, Oxygen redox chemistry without excess alkali-metal ions in $\text{Na}_{2/3}[\text{Mg}_{0.28}\text{Mn}_{0.72}]\text{O}_2$, *Nat. Chem.* 10 (2018) 288–295. doi:10.1038/nchem.2923.
- [43] Y. Li, X. Wang, Y. Gao, Q. Zhang, G. Tan, Q. Kong, S. Bak, G. Lu, X.Q. Yang, L. Gu, J. Lu, K. Amine, Z. Wang, L. Chen, Native Vacancy Enhanced Oxygen Redox Reversibility and Structural Robustness, *Adv. Energy Mater.* 9 (2019) 1–9. doi:10.1002/aenm.201803087.
- [44] E. Zhao, M. Zhang, X. Wang, E. Hu, J. Liu, X. Yu, M. Olguin, T.A. Wynn, Y.S. Meng, K. Page, F. Wang, H. Li, X.Q. Yang, X. Huang, L. Chen, Local structure adaptability through multi cations for oxygen redox accommodation in Li-Rich layered oxides, *Energy Storage Mater.* (2019). doi:10.1016/j.ensm.2019.07.032.
- [45] K.M. Mogare, K. Friese, W. Klein, M. Jansen, Syntheses and crystal structures of two sodium ruthenates: Na_2RuO_4 and Na_2RuO_3 , *Zeitschrift Fur Anorg. Und Allg. Chemie.* 630 (2004) 547–552. doi:10.1002/zaac.200400012.
- [46] W. Zhou, L. Xue, X. Lü, H. Gao, Y. Li, S. Xin, G. Fu, Z. Cui, Y. Zhu, J.B. Goodenough, $\text{Na}_x\text{MV}(\text{PO}_4)_3$ (M = Mn, Fe, Ni) Structure and Properties for Sodium Extraction, *Nano Lett.* 16 (2016) 7836–7841. doi:10.1021/acs.nanolett.6b04044.
- [47] M. Law, V. Ramar, P. Balaya, $\text{Na}_2\text{MnSiO}_4$ as an attractive high capacity cathode material for sodium-ion battery, *J. Power Sources.* 359 (2017) 277–284. doi:10.1016/j.jpowsour.2017.05.069.
- [48] Y. You, X.L. Wu, Y.X. Yin, Y.G. Guo, High-quality Prussian blue crystals as superior cathode materials for room-temperature sodium-ion batteries, *Energy Environ. Sci.* 7 (2014) 1643–1647. doi:10.1039/c3ee44004d.
- [49] R. Chen, Y. Huang, M. Xie, Z. Wang, Y. Ye, L. Li, F. Wu, Chemical inhibition method to synthesize highly crystalline prussian blue analogs for sodium-ion battery cathodes, *ACS Appl. Mater. Interfaces.* 8 (2016) 31669–31676. doi:10.1021/acsami.6b10884.
- [50] Y. You, X.L. Wu, Y.X. Yin, Y.G. Guo, A zero-strain insertion cathode material of nickel ferricyanide for sodium-ion batteries, *J. Mater. Chem. A.* 1 (2013) 14061–14065. doi:10.1039/c3ta13223d.

- [51] H. Lee, Y. Il Kim, J.K. Park, J.W. Choi, Sodium zinc hexacyanoferrate with a well-defined open framework as a positive electrode for sodium ion batteries, *Chem. Commun.* 48 (2012) 8416–8418. doi:10.1039/c2cc33771a.
- [52] C. Zhao, Q. Wang, Y. Lu, Y.S. Hu, B. Li, L. Chen, Review on anionic redox for high-capacity lithium- and sodium-ion batteries, *J. Phys. D. Appl. Phys.* 50 (2017). doi:10.1088/1361-6463/aa646d.
- [53] X. Rong, J. Liu, E. Hu, Y. Liu, Y. Wang, J. Wu, X. Yu, K. Page, Y.S. Hu, W. Yang, H. Li, X.Q. Yang, L. Chen, X. Huang, Structure-Induced Reversible Anionic Redox Activity in Na Layered Oxide Cathode, *Joule*. 2 (2018) 125–140. doi:10.1016/j.joule.2017.10.008.
- [54] B. Zhang, R. Dugas, G. Rousse, P. Rozier, A.M. Abakumov, J.-M. Tarascon, Insertion compounds and composites made by ball milling for advanced sodium-ion batteries, *Nat. Commun.* 7 (2016) 10308. doi:10.1038/ncomms10308.
- [55] V. Duffort, E. Talaie, R. Black, L.F. Nazar, Uptake of CO₂ in Layered P2-Na_{0.67}Mn_{0.5}Fe_{0.5}O₂: Insertion of Carbonate Anions, *Chem. Mater.* 27 (2015) 2515–2524. doi:10.1021/acs.chemmater.5b00097.
- [56] M.H. Han, B. Acebedo, E. Gonzalo, P.S. Fontecoba, S. Clarke, D. Saurel, T. Rojo, Synthesis and Electrochemistry Study of P2- and O3-phase Na_{2/3}Fe_{1/2}Mn_{1/2}O₂, *Electrochim. Acta.* 182 (2015) 1029–1036. doi:10.1016/j.electacta.2015.10.003.
- [57] D. Buchholz, C. Vaalma, L.G. Chagas, S. Passerini, Mg-doping for improved long-term cyclability of layered Na-ion cathode materials - The example of P2-type Na_xMg_{0.11}Mn_{0.89}O₂, *J. Power Sources*. 282 (2015) 581–585. doi:10.1016/j.jpowsour.2015.02.069.
- [58] R. Viswanatha, B. Kishore, U. Bharath, N. Munichandraiah, Communication—Electrochemical Investigation of Plate-Like Na_{2/3}Fe_{1/2}Mn_{1/2}O₂ for Sodium Ion Cathode, *J. Electrochem. Soc.* 165 (2018) A263–A265. doi:10.1149/2.0911802jes.
- [59] H. Xu, J. Zong, X. Liu, With High-Capacity for Sodium-Ion Battery, (2018) 1939–1946.
- [60] J. Billaud, R.J. Clément, A.R. Armstrong, J. Canales-Vázquez, P. Rozier, C.P. Grey, P.G. Bruce, β-NaMnO₂: A high-performance cathode for sodium-ion batteries, *J. Am. Chem. Soc.* 136 (2014) 17243–17248. doi:10.1021/ja509704t.
- [61] X. Ma, H. Chen, G. Ceder, Electrochemical Properties of Monoclinic NaMnO₂, *J. Electrochem. Soc.* 158 (2011) A1307. doi:10.1149/2.035112jes.
- [62] T.-R. Chen, T. Sheng, Z.-G. Wu, J.-T. Li, E.-H. Wang, C.-J. Wu, H.-T. Li, X.-D. Guo, B.-H. Zhong, L. Huang, S.-G. Sun, Cu²⁺ Dual-Doped Layer-Tunnel Hybrid Na_{0.6}Mn_{1-x}Cu_xO₂ as a Cathode of Sodium-Ion Battery with Enhanced Structure Stability, Electrochemical Property, and Air Stability, *ACS Appl. Mater. Interfaces*. (2018) acsami.8b00614. doi:10.1021/acsami.8b00614.

- [63] H. Wang, R. Gao, Z. Li, L. Sun, Z. Hu, X. Liu, Different Effects of Al Substitution for Mn or Fe on the Structure and Electrochemical Properties of $\text{Na}_{0.67}\text{Mn}_{0.5}\text{Fe}_{0.5}\text{O}_2$ as a Sodium Ion Battery Cathode Material, *Inorg. Chem.* (2018) 2–10. doi:10.1021/acs.inorgchem.8b00284.
- [64] J. Billaud, G. Singh, A.R. Armstrong, E. Gonzalo, V. Roddatis, M. Armand, T. Rojo, P.G. Bruce, $\text{Na}_{0.67}\text{Mn}_{1-x}\text{Mg}_x\text{O}_2$ ($0 \leq x \leq 0.2$): a high capacity cathode for sodium-ion batteries, *Energy Environ. Sci.* 7 (2014) 1387–1391. doi:10.1039/C4EE00465E.
- [65] B. Mortemard De Boisse, J.H. Cheng, D. Carlier, M. Guignard, C.J. Pan, S. Bordère, D. Filimonov, C. Drathen, E. Suard, B.J. Hwang, A. Wattiaux, C. Delmas, $\text{O}_3\text{-Na}_x\text{Mn}_{1/3}\text{Fe}_{2/3}\text{O}_2$ as a positive electrode material for Na-ion batteries: Structural evolutions and redox mechanisms upon Na^+ (de)intercalation, *J. Mater. Chem. A.* 3 (2015) 10976–10989. doi:10.1039/c4ta06688j.
- [66] L. Mu, S. Xu, Y. Li, Y.S. Hu, H. Li, L. Chen, X. Huang, Prototype Sodium-Ion Batteries Using an Air-Stable and Co/Ni-Free O_3 -Layered Metal Oxide Cathode, *Adv. Mater.* 27 (2015) 6928–6933. doi:10.1002/adma.201502449.
- [67] J.S. Thorne, R.A. Dunlap, M.N. Obrovac, Structure and Electrochemistry of $\text{Na}_x\text{Fe}_x\text{Mn}_{1-x}\text{O}_2$ ($1.0 \leq x \leq 0.5$) for Na-Ion Battery Positive Electrodes, *J. Electrochem. Soc.* 160 (2012) A361–A367. doi:10.1149/2.058302jes.
- [68] P.K. Nayak, L. Yang, K. Pollok, F. Langenhorst, L. Wondraczek, P. Adelhelm, Electrochemical performance and ageing mechanisms of sol-gel synthesized $\text{Na}_{2/3}[\text{Mn}_{3/5}\text{Fe}_{2/5}]\text{O}_2$ for Na-ion batteries, *Batter. Supercaps.* (2018). doi:10.1002/batt.201800034.
- [69] M. Sathiya, Q. Jacquet, M.L. Doublet, O.M. Karakulina, J. Hadermann, J.M. Tarascon, A Chemical Approach to Raise Cell Voltage and Suppress Phase Transition in O_3 Sodium Layered Oxide Electrodes, *Adv. Energy Mater.* 8 (2018) 1–10. doi:10.1002/aenm.201702599.
- [70] M. Cao, Z. Shadik, Y. Zhou, Z. Fu, Sodium-deficient O_3 -type $\text{Na}_{0.83}\text{Cr}_{1/3}\text{Fe}_{1/3}\text{Mn}_{1/6}\text{Ti}_{1/6}\text{O}_2$ as a new cathode material for Na-ion batteries, *Electrochim. Acta.* 295 (2019) 918–925. doi:10.1016/j.electacta.2018.11.137.
- [71] E. Marelli, C. Villevieille, S. Park, N. Hérault, C. Marino, Co-Free $\text{P}_2\text{-Na}_{0.67}\text{Mn}_{0.6}\text{Fe}_{0.25}\text{Al}_{0.15}\text{O}_2$ as Promising Cathode Material for Sodium-Ion Batteries, *ACS Appl. Energy Mater.* 1 (2018) 5960–5967. doi:10.1021/acsaem.8b01015.
- [72] C. Zhao, Q. Wang, Y. Lu, L. Jiang, L. Liu, X. Yu, L. Chen, B. Li, Y.S. Hu, Decreasing transition metal triggered oxygen redox activity in Na-deficient oxides, *Energy Storage Mater.* (2018) 1–6. doi:10.1016/j.ensm.2018.10.025.
- [73] D. Zhou, W. Huang, F. Zhao, X. Lv, The effect of Na content on the electrochemical performance of the O_3 -type $\text{Na}_x\text{Fe}_{0.5}\text{Mn}_{0.5}\text{O}_2$ for sodium-ion batteries, *J. Mater. Sci.* 54 (2019) 7156–7164. doi:10.1007/s10853-018-03277-8.

- [74] A. Konarov, J.H. Jo, J.U. Choi, Z. Bakenov, H. Yashiro, J. Kim, S.T. Myung, Exceptionally highly stable cycling performance and facile oxygen-redox of manganese-based cathode materials for rechargeable sodium batteries, *Nano Energy*. 59 (2019) 197–206. doi:10.1016/j.nanoen.2019.02.042.
- [75] J. Li, J. Wang, X. He, L. Zhang, A. Senyshyn, B. Yan, M. Muehlbauer, X. Cao, B. Vortmann-Westhoven, V. Kraft, H. Liu, C. Luerenbaum, G. Schumacher, E. Paillard, M. Winter, J. Li, P2 – Type $\text{Na}_{0.67}\text{Mn}_{0.8}\text{Cu}_{0.1}\text{Mg}_{0.1}\text{O}_2$ as a new cathode material for sodium-ion batteries: Insights of the synergetic effects of multi-metal substitution and electrolyte optimization, *J. Power Sources*. 416 (2019) 184–192. doi:10.1016/j.jpowsour.2019.01.086.
- [76] C. Zhao, Z. Yao, J. Wang, Y. Lu, X. Bai, A. Aspuru-Guzik, L. Chen, Y.S. Hu, Ti Substitution Facilitating Oxygen Oxidation in $\text{Na}_{2/3}\text{Mg}_{1/3}\text{Ti}_{1/6}\text{Mn}_{1/2}\text{O}_2$ Cathode, *Chem*. 5 (2019) 2913–2925. doi:10.1016/j.chempr.2019.08.003.
- [77] E. Talaie, S.Y. Kim, N. Chen, L.F. Nazar, Structural Evolution and Redox Processes Involved in the Electrochemical Cycling of $\text{P2-Na}_{0.67}[\text{Mn}_{0.66}\text{Fe}_{0.20}\text{Cu}_{0.14}]\text{O}_2$, *Chem. Mater*. 29 (2017) 6684–6697. doi:10.1021/acs.chemmater.7b01146.
- [78] Z. Yan, L. Tang, Y. Huang, W. Hua, Y. Wang, R. Liu, Q. Gu, S. Indris, S.L. Chou, Y. Huang, M. Wu, S.X. Dou, A Hydrostable Cathode Material Based on the Layered P2@P3 Composite that Shows Redox Behavior for Copper in High-Rate and Long-Cycling Sodium-Ion Batteries, *Angew. Chemie - Int. Ed.* 58 (2019) 1412–1416. doi:10.1002/anie.201811882.
- [79] Y. Li, Z.Y. Li, K. Sun, Y.T. Liu, D.F. Chen, S.B. Han, L.F. He, M.J. Li, X.L. Liu, M.M. Wu, Layered Co/Ni-free Mn-rich oxide $\text{P2-Na}_{2/3}\text{Mn}_{0.8}\text{Fe}_{0.1}\text{Mg}_{0.1}\text{O}_2$ as high-performance cathode material for sodium-ion batteries, *Ionics (Kiel)*. 26 (2020) 735–743. doi:10.1007/s11581-019-03208-w.
- [80] J. Zhang, G. Liu, H. Yu, X. Wang, Synthesis and electrochemical properties of $\text{P2-Na}_{0.7}\text{Zn}_{0.15}\text{Mn}_{0.75}\text{O}_2$, *Ionics (Kiel)*. 173 (2018) 550–555. doi:10.1007/s11581-018-2681-5.
- [81] Y.J. Park, J.U. Choi, J.H. Jo, C.H. Jo, J. Kim, S.T. Myung, A New Strategy to Build a High-Performance P2-Type Cathode Material through Titanium Doping for Sodium-Ion Batteries, *Adv. Funct. Mater.* 29 (2019) 1–10. doi:10.1002/adfm.201901912.
- [82] H. Hirsh, M. Olguin, H. Chung, Y. Li, S. Bai, D. Feng, D. Wang, M. Zhang, Y.S. Meng, Meso-Structure Controlled Synthesis of Sodium Iron-Manganese Oxides Cathode for Low-Cost Na-Ion Batteries, *J. Electrochem. Soc.* 166 (2019) A2528–A2535. doi:10.1149/2.0701912jes.
- [83] B. Acebedo, T. Rojo, J.M. López del Amo, N. Ortiz-Vitoriano, F.J. Bonilla, N.E. Drewett, E. Gonzalo, P2 manganese rich sodium layered oxides: Rational stoichiometries for enhanced performance, *J. Power Sources*. 401 (2018) 117–125. doi:10.1016/j.jpowsour.2018.08.068.

- [84] J. Chen, S. Zhong, X. Zhang, J. Liu, S. Shi, Y. Hu, L. Wu, High performance of hexagonal plates P2-Na₂/3Fe₁/2Mn₁/2O₂ cathode material synthesized by an improved solid-state method, *Mater. Lett.* 202 (2017) 21–24. doi:10.1016/j.matlet.2017.05.084.
- [85] J. Zhao, J. Xu, D.H. Lee, N. Dimov, Y.S. Meng, S. Okada, Electrochemical and thermal properties of P2-type Na₂/3Fe₁/3Mn₂/3O₂ for Na-ion batteries, *J. Power Sources.* 264 (2014) 235–239. doi:10.1016/j.jpowsour.2014.04.048.
- [86] Z. Fu, M.-H. Cao, Y. Wang, Z. Shadike, J. Yue, E. Hu, S.-M. Bak, Y.-N. Zhou, X.-Q. Yang, Suppressing Chromium Disproportion Reaction in O3-type Layered Cathode Material for High Capacity Sodium-ion Batteries, *J. Mater. Chem. A.* 5 (2017) 5442–5448. doi:10.1039/C6TA10818K.
- [87] N. Yabuuchi, M. Kajiyama, J. Iwatate, H. Nishikawa, S. Hitomi, R. Okuyama, R. Usui, Y. Yamada, S. Komaba, P2-type Na_x[Fe₁/2Mn₁/2]O₂ made from earth-abundant elements for rechargeable Na batteries, *Nat. Mater.* 11 (2012) 512–517. doi:10.1038/nmat3309.
- [88] Z.-Y. Li, H. Wang, W. Yang, J. Yang, L. Zheng, D. Chen, K. Sun, S. Han, X. Liu, Modulating the Electrochemical Performances of Layered Cathode Materials for Sodium Ion Batteries through Tuning Coulombic Repulsion between Negatively Charged TMO 2 Slabs, *ACS Appl. Mater. Interfaces.* 10 (2018) 1707–1718. doi:10.1021/acsami.7b15590.
- [89] J. Xu, D.H. Lee, R.J. Clément, X. Yu, M. Leskes, A.J. Pell, G. Pintacuda, X.Q. Yang, C.P. Grey, Y.S. Meng, Identifying the critical role of Li substitution in P2-Na_x[Li_yNi_zMn_{1-y-z}]O₂ (0 < x, y, z < 1) intercalation cathode materials for high-energy Na-ion batteries, *Chem. Mater.* 26 (2014) 1260–1269. doi:10.1021/cm403855t.
- [90] X. Qi, L. Liu, N. Song, F. Gao, K. Yang, Y. Lu, H. Yang, Y. Hu, Z. Cheng, L. Chen, Design and Comparative Study of O3 / P2 Hybrid Structures for Room Temperature Sodium-Ion Batteries, *ACS Appl. Mater. Interfaces.* 9 (2017) 40215–40223. doi:10.1021/acsami.7b11282.
- [91] K. Kaliyappan, J. Liu, B. Xiao, A. Lushington, R. Li, T.K. Sham, X. Sun, Enhanced Performance of P2-Na_{0.66}(Mn_{0.54}Co_{0.13}Ni_{0.13})O₂ Cathode for Sodium-Ion Batteries by Ultrathin Metal Oxide Coatings via Atomic Layer Deposition, *Adv. Funct. Mater.* 27 (2017) 13–16. doi:10.1002/adfm.201701870.
- [92] H. Yoshida, N. Yabuuchi, S. Komaba, NaFe_{0.5}Co_{0.5}O₂ as high energy and power positive electrode for Na-ion batteries, *Electrochem. Commun.* 34 (2013) 60–63. doi:10.1016/j.elecom.2013.05.012.
- [93] J.-Y. Hwang, S.-T. Myung, J.U. Choi, C.S. Yoon, H. Yashiro, Y.-K. Sun, Resolving the degradation pathways on O3-type layered oxides cathode surface through the nano-scale aluminum oxide coating for high-energy density sodium-ion batteries, *J. Mater. Chem. A.* (2017). doi:10.1039/C7TA08443A.
- [94] Y. Liu, X. Fang, A. Zhang, C. Shen, Q. Liu, H.A. Enaya, C. Zhou, Layered P2-Na₂/3[Ni₁/3Mn₂/3]O₂ as high-voltage cathode for sodium-ion batteries: The capacity

- decay mechanism and Al₂O₃ surface modification, *Nano Energy*. 27 (2016) 27–34. doi:10.1016/j.nanoen.2016.06.026.
- [95] L. Wang, Y.-G. Sun, L.-L. Hu, J.-Y. Piao, J. Guo, A. Manthiram, J. Ma, A.-M. Cao, Copper-Substituted Na_{0.67}Ni_{0.3-x}Cu_xMn_{0.7}O₂ Cathode Materials for Sodium-Ion Batteries with Suppressed P2-O2 Phase Transition, *J. Mater. Chem. A*. (2017). doi:10.1039/C7TA00880E.
- [96] W. Zhao, H. Kirie, A. Tanaka, M. Unno, S. Yamamoto, H. Noguchi, Synthesis of metal ion substituted P2-Na_{2/3}Ni_{1/3}Mn_{2/3}O₂ cathode material with enhanced performance for Na ion batteries, *Mater. Lett.* 135 (2014) 131–134. doi:10.1016/j.matlet.2014.07.153.
- [97] L. Yang, X. Li, X. Ma, S. Xiong, P. Liu, Y. Tang, S. Cheng, Y.Y. Hu, M. Liu, H. Chen, Design of high-performance cathode materials with single-phase pathway for sodium ion batteries: A study on P2-Na_x(Li_yMn_{1-y})O₂ compounds, *J. Power Sources*. 381 (2018) 171–180. doi:10.1016/j.jpowsour.2017.12.072.
- [98] J. Qian, C. Wu, Y. Cao, Z. Ma, Y. Huang, X. Ai, H. Yang, Prussian Blue Cathode Materials for Sodium-Ion Batteries and Other Ion Batteries, *Adv. Energy Mater.* 8 (2018) 1–24. doi:10.1002/aenm.201702619.
- [99] Q. Liu, Z. Hu, M. Chen, C. Zou, H. Jin, S. Wang, S.-L. Chou, Y. Liu, S.-X. Dou, The Cathode Choice for Commercialization of Sodium-Ion Batteries: Layered Transition Metal Oxides versus Prussian Blue Analogs, *Adv. Funct. Mater.* 1909530 (2020) 1–15. doi:10.1002/adfm.201909530.
- [100] C. Delmas, Sodium and Sodium-Ion Batteries: 50 Years of Research, *Adv. Energy Mater.* 1703137 (2018) 1703137. doi:10.1002/aenm.201703137.
- [101] Y. Kim, K.H. Ha, S.M. Oh, K.T. Lee, High-capacity anode materials for sodium-ion batteries, *Chem. - A Eur. J.* 20 (2014) 11980–11992. doi:10.1002/chem.201402511.
- [102] C. Vaalma, D. Buchholz, M. Weil, S. Passerini, A cost and resource analysis of sodium-ion batteries, *Nat. Rev. Mater.* 3 (2018). doi:10.1038/natrevmats.2018.13.
- [103] C. Niu, H. Lee, S. Chen, Q. Li, J. Du, W. Xu, J.G. Zhang, M.S. Whittingham, J. Xiao, J. Liu, High-energy lithium metal pouch cells with limited anode swelling and long stable cycles, *Nat. Energy*. 4 (2019). doi:10.1038/s41560-019-0390-6.
- [104] M.H. Han, N. Sharma, E. Gonzalo, J.C. Pramudita, H.E.A. Brand, J.M. López Del Amo, T. Rojo, Moisture exposed layered oxide electrodes as Na-ion battery cathodes, *J. Mater. Chem. A*. 4 (2016) 18963–18975. doi:10.1039/C6TA07950D.
- [105] L. Zheng, L. Li, R. Shunmugasundaram, M.N. Obrovac, Effect of Controlled-Atmosphere Storage and Ethanol Rinsing on NaNi_{0.5}Mn_{0.5}O₂ for Sodium-Ion Batteries, *ACS Appl. Mater. Interfaces*. 10 (2018) 38246–38254. doi:10.1021/acsami.8b14209.
- [106] J. Martinez De Ilarduya, L. Otaegui, J.M. López del Amo, M. Armand, G. Singh, Na₃ addition, a strategy to overcome the problem of sodium deficiency in P2-

- Na_{0.67}[Fe_{0.5}Mn_{0.5}]O₂ cathode for sodium-ion battery, *J. Power Sources*. 337 (2017) 197–203. doi:10.1016/j.jpowsour.2016.10.084.
- [107] C.-H. Jo, J.U. Choi, H. Yashiro, S.-T. Myung, Controllable charge capacity using a black additive for high-energy-density sodium-ion batteries, *J. Mater. Chem. A*. (2019) 3903–3909. doi:10.1039/c8ta09833f.
- [108] J.H. Jo, J.U. Choi, Y.J. Park, J. Zhu, H. Yashiro, S.-T.T. Myung, J.H. Jo, J. Zhu, Y.J. Park, J.U. Choi, S.-T.T. Myung, New Insight into Ethylenediaminetetraacetic Acid Tetrasodium Salt as a Sacrificing Sodium Ion Source for Sodium-Deficient Cathode Materials for Full Cells, *ACS Appl. Mater. Interfaces*. 11 (2019) 5957–5965. doi:10.1021/acsami.8b18488.
- [109] S. Mariyappan, Q. Wang, J.M. Tarascon, Will Sodium Layered Oxides Ever Be Competitive for Sodium Ion Battery Applications?, *J. Electrochem. Soc.* 165 (2018) A3714–A3722. doi:10.1149/2.0201816jes.
- [110] M. Zarrabeitia, L. Gomes Chagas, M. Kuenzel, E. Gonzalo, T. Rojo, S. Passerini, M.Á. Muñoz-Márquez, Toward Stable Electrode/Electrolyte Interface of P2-Layered Oxide for Rechargeable Na-Ion Batteries, *ACS Appl. Mater. Interfaces*. 11 (2019) 28885–28893. doi:10.1021/acsami.9b07963.
- [111] E.A. Wu, C.S. Kompella, Z. Zhu, J.Z. Lee, S.C. Lee, I.H. Chu, H. Nguyen, S.P. Ong, A. Banerjee, Y.S. Meng, New Insights into the Interphase between the Na Metal Anode and Sulfide Solid-State Electrolytes: A Joint Experimental and Computational Study, *ACS Appl. Mater. Interfaces*. 10 (2018) 10076–10086. doi:10.1021/acsami.7b19037.
- [112] D.A. Stevens, J.R. Dahn, High Capacity Anode Materials for Rechargeable Sodium-Ion Batteries, *J. Electrochem. Soc.* 147 (2000) 1271. doi:10.1149/1.1393348.
- [113] Q. Zhang, J. Luo, Y. Qiu, J. Han, C. Fang, K. Wang, J. Peng, Y. Huang, Y. Jin, S. Sun, Low-Cost and High-Performance Hard Carbon Anode Materials for Sodium-Ion Batteries, *ACS Omega*. 2 (2017) 1687–1695. doi:10.1021/acsomega.7b00259.
- [114] A. Ponrouch, A.R. Goñi, M.R. Palacín, High capacity hard carbon anodes for sodium ion batteries in additive free electrolyte, *Electrochem. Commun.* 27 (2013) 85–88. doi:10.1016/j.elecom.2012.10.038.
- [115] Y.S. Wu, Q.Q. Shi, Y.H. Li, Z.C. Lai, H. Yu, H.J. Wang, F. Peng, Nitrogen-doped graphene-supported cobalt carbonitride@oxide core-shell nanoparticles as a non-noble metal electrocatalyst for an oxygen reduction reaction, *J. Mater. Chem. A*. 3 (2015) 1142–1151. doi:10.1039/c4ta03850a.
- [116] K.L. Hong, L. Qie, R. Zeng, Z.Q. Yi, W. Zhang, D. Wang, W. Yin, C. Wu, Q.J. Fan, W.X. Zhang, Y.H. Huang, Biomass derived hard carbon used as a high performance anode material for sodium ion batteries, *J. Mater. Chem. A*. 2 (2014) 12733–12738. doi:10.1039/c4ta02068e.
- [117] N. Sun, H. Liu, B. Xu, Facile synthesis of high performance hard carbon anode materials

- for sodium ion batteries, *J. Mater. Chem. A.* 3 (2015) 20560–20566. doi:10.1039/c5ta05118e.
- [118] W. Lv, F. Wen, J. Xiang, J. Zhao, L. Li, L. Wang, Z. Liu, Y. Tian, Peanut shell derived hard carbon as ultralong cycling anodes for lithium and sodium batteries, *Electrochim. Acta.* 176 (2015) 533–541. doi:10.1016/j.electacta.2015.07.059.
- [119] V. Simone, A. Boulineau, A. de Geyer, D. Rouchon, L. Simonin, S. Martinet, Hard carbon derived from cellulose as anode for sodium ion batteries: Dependence of electrochemical properties on structure, *J. Energy Chem.* 25 (2016) 761–768. doi:10.1016/j.jechem.2016.04.016.
- [120] P. Liu, Y. Li, Y.S. Hu, H. Li, L. Chen, X. Huang, A waste biomass derived hard carbon as a high-performance anode material for sodium-ion batteries, *J. Mater. Chem. A.* 4 (2016) 13046–13052. doi:10.1039/c6ta04877c.
- [121] Y. Li, Y.S. Hu, M.M. Titirici, L. Chen, X. Huang, Hard Carbon Microtubes Made from Renewable Cotton as High-Performance Anode Material for Sodium-Ion Batteries, *Adv. Energy Mater.* 6 (2016) 1–9. doi:10.1002/aenm.201600659.
- [122] Y. Zheng, Y. Wang, Y. Lu, Y.S. Hu, J. Li, A high-performance sodium-ion battery enhanced by macadamia shell derived hard carbon anode, *Nano Energy.* 39 (2017) 489–498. doi:10.1016/j.nanoen.2017.07.018.
- [123] Y. Lu, L. Mu, Q. Ma, Y. Wang, X. Qi, Y. Zheng, J. Li, Y.S. Hu, Y. Li, Y. Lu, X. Qi, Y. Wang, L. Mu, Y. Li, Q. Ma, J. Li, Y.S. Hu, Superior electrochemical performance of sodium-ion full-cell using poplar wood derived hard carbon anode, *Energy Storage Mater.* 18 (2018) 269–279. doi:10.1016/j.ensm.2018.09.002.
- [124] J. Tang, D.K. Kye, V.G. Pol, Ultrasound-assisted synthesis of sodium powder as electrode additive to improve cycling performance of sodium-ion batteries, *J. Power Sources.* 396 (2018) 476–482. doi:10.1016/j.jpowsour.2018.06.067.
- [125] Z. Li, C. Bommier, Z. Sen Chong, Z. Jian, T.W. Surta, X. Wang, Z. Xing, J.C. Neufeind, W.F. Stickle, M. Dolgos, P.A. Greaney, X. Ji, Mechanism of Na-Ion Storage in Hard Carbon Anodes Revealed by Heteroatom Doping, *Adv. Energy Mater.* 7 (2017) 1–10. doi:10.1002/aenm.201602894.
- [126] K. Gotoh, T. Ishikawa, S. Shimadzu, N. Yabuuchi, S. Komaba, K. Takeda, A. Goto, K. Deguchi, S. Ohki, K. Hashi, T. Shimizu, H. Ishida, NMR study for electrochemically inserted Na in hard carbon electrode of sodium ion battery, *J. Power Sources.* 225 (2013) 137–140. doi:10.1016/j.jpowsour.2012.10.025.
- [127] Z. Li, J. Ding, D. Mitlin, Tin and Tin Compounds for Sodium Ion Battery Anodes: Phase Transformations and Performance, *Acc. Chem. Res.* 48 (2015) 1657–1665. doi:10.1021/acs.accounts.5b00114.
- [128] X. Zheng, C. Bommier, W. Luo, L. Jiang, Y. Hao, Y. Huang, Sodium Metal Anodes for

- Room-Temperature Sodium-Ion Batteries: Applications, Challenges and Solutions, *Energy Storage Mater.* 16 (2018) 6–23. doi:10.1016/j.ensm.2018.04.014.
- [129] S. Komaba, W. Murata, T. Ishikawa, N. Yabuuchi, T. Ozeki, T. Nakayama, A. Ogata, K. Gotoh, K. Fujiwara, Electrochemical Na Insertion and Solid Electrolyte Interphase for Hard-Carbon Electrodes and Application to Na-Ion Batteries, *Adv. Funct. Mater.* 21 (2011) 3859–3867. doi:10.1002/adfm.201100854.
- [130] M. Dahbi, T. Nakano, N. Yabuuchi, T. Ishikawa, K. Kubota, M. Fukunishi, S. Shibahara, J.Y. Son, Y.T. Cui, H. Oji, S. Komaba, Sodium carboxymethyl cellulose as a potential binder for hard-carbon negative electrodes in sodium-ion batteries, *Electrochem. Commun.* 44 (2014) 66–69. doi:10.1016/j.elecom.2014.04.014.
- [131] K. Lu, S. Gao, G. Li, J. Kaelin, Z. Zhang, Y. Cheng, Regulating Interfacial Na-Ion Flux via Artificial Layers with Fast Ionic Conductivity for Stable and High-Rate Na Metal Batteries, *ACS Mater. Lett.* 1 (2019) 303–309. doi:10.1021/acsmaterialslett.9b00257.
- [132] R.-S. Xie, J.-T. Li, L. Huang, Y.-C. Zhang, S.-G. Sun, K. Wang, Y.-R. Pei, Q. Liu, Y.-Y. Zhang, S.-J. Zhang, Improvement of electrochemical properties of P2-type $\text{Na}_{2/3}\text{Mn}_{2/3}\text{Ni}_{1/3}\text{O}_2$ sodium ion battery cathode material by water-soluble binders, *Electrochim. Acta.* 298 (2018) 496–504. doi:10.1016/j.electacta.2018.12.089.
- [133] J. Zhao, L. Zhao, K. Chihara, S. Okada, J.I. Yamaki, S. Matsumoto, S. Kuze, K. Nakane, Electrochemical and thermal properties of hard carbon-type anodes for Na-ion batteries, *J. Power Sources.* 244 (2013) 752–757. doi:10.1016/j.jpowsour.2013.06.109.
- [134] D.H.S. Tan, A. Banerjee, Z. Chen, Y.S. Meng, From nanoscale interface characterization to sustainable energy storage using all-solid-state batteries, *Nat. Nanotechnol.* 15 (2020) 1–11. doi:10.1038/s41565-020-0657-x.
- [135] E. Gies, Recycling: Lazarus batteries, *Nature.* 526 (2015) S100–S101. doi:10.1038/526S100a.
- [136] X. Zhang, Q. Xue, L. Li, E. Fan, F. Wu, R. Chen, Sustainable Recycling and Regeneration of Cathode Scraps from Industrial Production of Lithium-Ion Batteries, *ACS Sustain. Chem. Eng.* 4 (2016) 7041–7049. doi:10.1021/acssuschemeng.6b01948.
- [137] T. Liu, Y. Zhang, C. Chen, Z. Lin, S. Zhang, J. Lu, Sustainability-inspired cell design for a fully recyclable sodium ion battery, *Nat. Commun.* 10 (2019) 1–7. doi:10.1038/s41467-019-09933-0.
- [138] Y. Jiang, Z. Yang, W. Li, L. Zeng, F. Pan, M. Wang, X. Wei, G. Hu, L. Gu, Y. Yu, Nanoconfined carbon-coated $\text{Na}_3\text{V}_2(\text{PO}_4)_3$ particles in mesoporous carbon enabling ultralong cycle life for sodium-ion batteries, *Adv. Energy Mater.* 5 (2015) 1–8. doi:10.1002/aenm.201402104.
- [139] J.Z. Guo, X.L. Wu, F. Wan, J. Wang, X.H. Zhang, R.S. Wang, A Superior $\text{Na}_3\text{V}_2(\text{PO}_4)_3$ -

- Based Nanocomposite Enhanced by Both N-Doped Coating Carbon and Graphene as the Cathode for Sodium-Ion Batteries, *Chem. - A Eur. J.* 21 (2015) 17371–17378. doi:10.1002/chem.201502583.
- [140] J. Song, L. Wang, Y. Lu, J. Liu, B. Guo, P. Xiao, J.J. Lee, X.Q. Yang, G. Henkelman, J.B. Goodenough, Removal of interstitial H₂O in hexacyanometallates for a superior cathode of a sodium-ion battery, *J. Am. Chem. Soc.* 137 (2015) 2658–2664. doi:10.1021/ja512383b.
- [141] F. Wan, X.L. Wu, J.Z. Guo, J.Y. Li, J.P. Zhang, L. Niu, R.S. Wang, Nanoeffects promote the electrochemical properties of organic Na₂C₈H₄O₄ as anode material for sodium-ion batteries, *Nano Energy*. 13 (2015) 450–457. doi:10.1016/j.nanoen.2015.03.017.
- [142] A.K. Padhi, K.S. Nanjundaswamy, J.B. Goodenough, Phospho-olivines as Positive-Electrode Materials for Rechargeable Lithium Batteries, *J. Electrochem. Soc.* 144 (1997) 1–7.
- [143] N. Ortiz Vitoriano, N. Drewett, E. Gonzalo, T. Rojo, High Performance Manganese-based Layered Oxide Cathodes: Overcoming the Challenges of Sodium Ion Batteries, *Energy Environ. Sci.* (2017). doi:10.1039/C7EE00566K.
- [144] X. Li, Y. Wang, D. Wu, L. Liu, S.H. Bo, G. Ceder, Jahn-Teller assisted Na diffusion for high performance Na ion batteries, *Chem. Mater.* 28 (2016) 6575–6583. doi:10.1021/acs.chemmater.6b02440.
- [145] M. Zhang, H. Liu, Z. Liu, C. Fang, Y.S. Meng, Modified Coprecipitation Synthesis of Mesostructure-Controlled Li-Rich Layered Oxides for Minimizing Voltage Degradation, *ACS Appl. Energy Mater.* 1 (2018) 3369–3376. doi:10.1021/acsaem.8b00545.
- [146] Y. Zhuo, J. Yan, X. Chen, T. Chen, K. Liu, J. Zhang, H. Hu, R. Cai, P. Liu, W. Liu, Nanoparticles Assembled Microspheres as a High-Rate Cathode Material for Sodium Ion Batteries, *J. Electrochem. Soc.* 166 (2019) A10–A14. doi:10.1149/2.0251902jes.
- [147] X. He, J. Li, Y. Cai, Y. Wang, J. Ying, C. Jiang, C. Wan, Preparation of co-doped spherical spinel LiMn₂O₄ cathode materials for Li-ion batteries, *J. Power Sources*. 150 (2005) 216–222. doi:10.1016/j.jpowsour.2005.02.029.
- [148] M.A. Martin, C.-F. Chen, P.P. Mukherjee, S. Pannala, J.-F. Dietiker, J.A. Turner, D. Ranjan, Morphological Influence in Lithium-Ion Battery 3D Electrode Architectures, *J. Electrochem. Soc.* 162 (2015) A991–A1002. doi:10.1149/2.0631506jes.
- [149] K.S. Lee, S.T. Myung, H.J. Bang, S. Chung, Y.K. Sun, Co-precipitation synthesis of spherical Li_{1.05}M_{0.05}Mn_{1.90}O₄ (M = Ni, Mg, Al) spinel and its application for lithium secondary battery cathode, *Electrochim. Acta.* 52 (2007) 5201–5206. doi:10.1016/j.electacta.2007.02.029.
- [150] L. Mu, M.M. Rahman, Y. Zhang, X. Feng, X. Du, D. Nordlund, F. Lin, Surface transformation by a “cocktail” solvent enables stable cathode materials for sodium ion

- batteries, *J. Mater. Chem. A*. 00 (2018) 1–9. doi:10.1039/C7TA08410B.
- [151] B. Tiwari, I. Bhattacharya, Layered P2- type novel $\text{Na}_{0.7}\text{Ni}_{0.3}\text{Mn}_{0.59}\text{Co}_{0.1}\text{Cu}_{0.01}\text{O}_2$ cathode material for high-capacity & stable rechargeable sodium ion battery, *Electrochim. Acta*. 270 (2018) 363–368. doi:10.1016/j.electacta.2018.03.058.
- [152] T.-Y. Yu, J.-Y. Hwang, D. Aurbach, Y.-K. Sun, Microsphere $\text{Na}_{0.65}[\text{Ni}_{0.17}\text{Co}_{0.11}\text{Mn}_{0.72}]\text{O}_2$ Cathode Material for High-Performance Sodium-Ion Batteries, *ACS Appl. Mater. Interfaces*. 9 (2017) 4534–44541. doi:10.1021/acsami.7b15267.
- [153] M. Islam, M.G. Jeong, J.Y. Hwang, I.H. Oh, Y.K. Sun, H.G. Jung, Self-assembled nickel-cobalt oxide microspheres from rods with enhanced electrochemical performance for sodium ion battery, *Electrochim. Acta*. 258 (2017) 220–227. doi:10.1016/j.electacta.2017.10.114.
- [154] M.-H. Lee, Y.-J. Kang, S.-T. Myung, Y.-K. Sun, Synthetic optimization of $\text{Li}[\text{Ni}_{1/3}\text{Co}_{1/3}\text{Mn}_{1/3}]\text{O}_2$ via co-precipitation, *Electrochim. Acta*. 50 (2004) 939–948. doi:10.1016/j.electacta.2004.07.038.
- [155] S.H. Park, S.H. Kang, I. Belharouak, Y.K. Sun, K. Amine, Physical and electrochemical properties of spherical $\text{Li}_{1+x}(\text{Ni}_{1/3}\text{Co}_{1/3}\text{Mn}_{1/3})_{1-x}\text{O}_2$ cathode materials, *J. Power Sources*. 177 (2008) 177–183. doi:10.1016/j.jpowsour.2007.10.062.
- [156] D.K. Lee, S.H. Park, K. Amine, H.J. Bang, J. Parakash, Y.K. Sun, High capacity $\text{Li}[\text{Li}_{0.2}\text{Ni}_{0.2}\text{Mn}_{0.6}]\text{O}_2$ cathode materials via a carbonate co-precipitation method, *J. Power Sources*. 162 (2006) 1346–1350. doi:10.1016/j.jpowsour.2006.07.064.
- [157] S. Chu, S. Wei, Y. Chen, R. Cai, K. Liao, W. Zhou, Z. Shao, Optimal synthesis and new understanding of P2-type $\text{Na}_{2/3}\text{Mn}_{1/2}\text{Fe}_{1/4}\text{Co}_{1/4}\text{O}_2$ as an advanced cathode material in sodium-ion batteries with improved cycle stability, *Ceram. Int*. 44 (2018) 5184–5192. doi:10.1016/j.ceramint.2017.12.124.
- [158] H. Xu, J. Zong, X. Liu, P2-type $\text{Na}_{0.67}\text{Mn}_{0.6}\text{Fe}_{0.4-x-y}\text{Zn}_x\text{Ni}_y\text{O}_2$ cathode material with high-capacity for sodium-ion battery, *Ionics (Kiel)*. 24 (2018) 1939–1946. doi:10.1007/s11581-018-2442-5.
- [159] D. Nayak, T. Sarkar, N.V.P. Chaudhary, M.D. Bharadwaj, S. Ghosh, V. Adyam, Electrochemical properties and first-principle analysis of $\text{Na}_x[\text{M}_y\text{Mn}_{1-y}]\text{O}_2$ (M = Fe, Ni) cathode, *J. Solid State Electrochem*. 4 (2017) 133–137. doi:10.1007/s10008-017-3850-6.
- [160] J. Park, G. Park, H.H. Kwak, S.-T. Hong, J. Lee, Enhanced Rate Capability and Cycle Performance of Titanium-Substituted P2-Type $\text{Na}_{0.67}\text{Fe}_{0.5}\text{Mn}_{0.5}\text{O}_2$ as a Cathode for Sodium-Ion Batteries, *ACS Omega*. 3 (2018) 361–368. doi:10.1021/acsomega.7b01481.
- [161] Y. Kee, N. Dimov, S. Champet, D.H. Gregory, S. Okada, Investigation of Al-doping effects on the $\text{NaFe}_{0.5}\text{Mn}_{0.5}\text{O}_2$ cathode for Na-ion batteries, *Ionics (Kiel)*. 22 (2016) 2245–2248.

doi:10.1007/s11581-016-1839-2.

- [162] P. Vassilaras, A.J. Toumar, G. Ceder, Electrochemical properties of $\text{NaNi}_{1/3}\text{Co}_{1/3}\text{Fe}_{1/3}\text{O}_2$ as a cathode material for Na-ion batteries, *Electrochem. Commun.* 38 (2014) 79–81. doi:10.1016/j.elecom.2013.11.015.
- [163] B.M. De Boisse, D. Carlier, M. Guignard, C. Delmas, Structural and electrochemical characterizations of P2 and New $\text{O}_3\text{-Na}_x\text{Mn}_{1-y}\text{Fe}_y\text{O}_2$ phases prepared by auto-combustion synthesis for na-ion batteries, *J. Electrochem. Soc.* 160 (2013) 569–574. doi:10.1149/2.032304jes.
- [164] J.Y. Hwang, S.T. Myung, D. Aurbach, Y.K. Sun, Effect of nickel and iron on structural and electrochemical properties of O_3 type layer cathode materials for sodium-ion batteries, *J. Power Sources.* 324 (2016) 106–112. doi:10.1016/j.jpowsour.2016.05.064.
- [165] D. Kim, E. Lee, M. Slater, W. Lu, S. Rood, C.S. Johnson, Layered $\text{Na}[\text{Ni}_{1/3}\text{Fe}_{1/3}\text{Mn}_{1/3}]\text{O}_2$ cathodes for Na-ion battery application, *Electrochem. Commun.* 18 (2012) 66–69. doi:10.1016/j.elecom.2012.02.020.
- [166] C. Delmas, J.-J. Braconnier, C. Fouassier, P. Hagenmuller, ELECTROCHEMICAL INTERCALATION OF SODIUM IN Na_xCoO_2 BRONZES, *Solid State Ionics.* 3–4 (1981) 165–169. doi:10.1016/0167-2738(81)90076-X.
- [167] G.K. Wertheim, S. Hüfner, H.J. Guggenheim, Systematics of core-electron exchange splitting in 3d-group transition-metal compounds, *Phys. Rev. B.* 7 (1973) 556–558. doi:10.1103/PhysRevB.7.556.
- [168] M. Descostes, F. Mercier, N. Thromat, C. Beaucaire, M. Gautier-Soyer, Use of XPS in the determination of chemical environment and oxidation state of iron and sulfur samples: Constitution of a data basis in binding energies for Fe and S reference compounds and applications to the evidence of surface species of an oxidized py, *Appl. Surf. Sci.* 165 (2000) 288–302. doi:10.1016/S0169-4332(00)00443-8.
- [169] A.P. Grosvenor, B.A. Kobe, M.C. Biesinger, N.S. McIntyre, Investigation of multiplet splitting of Fe 2p XPS spectra and bonding in iron compounds, *Surf. Interface Anal.* 36 (2004) 1564–1574. doi:10.1002/sia.1984.
- [170] I. Hasa, D. Buchholz, S. Passerini, B. Scrosati, J. Hassoun, High Performance $\text{Na}_{0.5}[\text{Ni}_{0.23}\text{Fe}_{0.13}\text{Mn}_{0.63}]\text{O}_2$ Cathode for Sodium-Ion Batteries, *Adv. Energy Mater.* 4 (2014) 1400083. doi:10.1002/aenm.201400083.
- [171] D.W. Shin, C.A. Bridges, A. Huq, M.P. Paranthaman, A. Manthiram, Role of Cation Ordering and Surface Segregation in High-Voltage Spinel $\text{LiMn}_{1.5}\text{Ni}_{0.5-x}\text{M}_x\text{O}_4$ ($\text{M} = \text{Cr, Fe, and Ga}$) Cathodes for Lithium-Ion Batteries, *Chem. Mater.* 24 (2012) 3720–3731. doi:10.1021/cm301844w.
- [172] Y. Cao, L. Xiao, W. Wang, D. Choi, Z. Nie, J. Yu, L. V. Saraf, Z. Yang, J. Liu, Reversible sodium ion insertion in single crystalline manganese oxide nanowires with long cycle life,

- Adv. Mater. 23 (2011) 3155–3160. doi:10.1002/adma.201100904.
- [173] B.D. McCloskey, A. Speidel, R. Scheffler, D.C. Miller, V. Viswanathan, J.S. Hummelshøj, J.K. Nørskov, A.C. Luntz, Twin problems of interfacial carbonate formation in nonaqueous Li-O₂ batteries, *J. Phys. Chem. Lett.* 3 (2012) 997–1001. doi:10.1021/jz300243r.
- [174] G. V. Zhuang, G. Chen, J. Shim, X. Song, P.N. Ross, T.J. Richardson, Li₂CO₃ in LiNi_{0.8}Co_{0.15}Al_{0.05}O₂ cathodes and its effects on capacity and power, *J. Power Sources.* 134 (2004) 293–297. doi:10.1016/j.jpowsour.2004.02.030.
- [175] L. Zhang, W. Borong, L. Ning, W. Feng, Hierarchically porous micro-rod lithium-rich cathode material Li_{1.2}Ni_{0.13}Mn_{0.54}Co_{0.13}O₂ for high performance lithium-ion batteries, *Electrochim. Acta.* 118 (2014) 67–74. doi:10.1016/j.electacta.2013.11.186.
- [176] R. Schmich, R. Wagner, G. Hörpel, T. Placke, M. Winter, Performance and cost of materials for lithium-based rechargeable automotive batteries, *Nat. Energy.* 3 (2018) 267–278. doi:10.1038/s41560-018-0107-2.
- [177] P.C.K. Vesborg, T.F. Jaramillo, Addressing the terawatt challenge: scalability in the supply of chemical elements for renewable energy, *RSC Adv.* 2 (2012) 7933. doi:10.1039/c2ra20839c.
- [178] H.S. Hirsh, Y. Li, D.H.S. Tan, M. Zhang, E. Zhao, Y.S. Meng, Sodium-Ion Batteries Paving the Way for Grid Energy Storage, *Adv. Energy Mater.* 10 (2020) 1–8. doi:10.1002/aenm.202001274.
- [179] X. Bai, M. Sathiya, B. Mendoza-Sánchez, A. Iadecola, J. Vergnet, R. Dedryvère, M. Saubanère, A.M. Abakumov, P. Rozier, J.-M. Tarascon, Anionic Redox Activity in a Newly Zn-Doped Sodium Layered Oxide P₂-Na_{2/3}Mn_{1-y}Zn_yO₂ (0 < y < 0.23), *Adv. Energy Mater.* 2 (2018) 1802379. doi:10.1002/aenm.201802379.
- [180] X. Wang, M. Tamaru, M. Okubo, A. Yamada, Electrode properties of P₂-Na_{2/3}Mn_yCo_{1-y}O₂ as cathode materials for sodium-ion batteries, *J. Phys. Chem. C.* 117 (2013) 15545–15551. doi:10.1021/jp406433z.
- [181] a. Caballero, L. Hernán, J. Morales, L. Sánchez, J. Santos Peña, M. a. G. Aranda, Synthesis and characterization of high-temperature hexagonal P₂-Na_{0.6}MnO₂ and its electrochemical behaviour as cathode in sodium cells, *J. Mater. Chem.* 12 (2002) 1142–1147. doi:10.1039/b108830k.
- [182] B. Silván, E. Gonzalo, L. Djuandhi, N. Sharma, F. Fauth, D. Saurel, On the dynamics of transition metal migration and its impact on the performance in layered oxides for sodium-ion batteries: NaFeO₂ as a case study., *J. Mater. Chem. A.* (2018) 15132–15146. doi:10.1039/C8TA02473A.
- [183] E. Lee, D.E. Brown, E.E. Alp, Y. Ren, J. Lu, J.J. Woo, C.S. Johnson, New Insights into the Performance Degradation of Fe-Based Layered Oxides in Sodium-Ion Batteries: Instability of Fe³⁺/Fe⁴⁺ Redox in α -NaFeO₂, *Chem. Mater.* 27 (2015) 6755–6764.

doi:10.1021/acs.chemmater.5b02918.

- [184] J. Xu, Z. Han, K. Jiang, P. Bai, Y. Liang, X. Zhang, P. Wang, S. Guo, H. Zhou, Suppressing Cation Migration and Reducing Particle Cracks in a Layered Fe-Based Cathode for Advanced Sodium-Ion Batteries, *Small*. 1904388 (2019) 1–7. doi:10.1002/sml.201904388.
- [185] J.E. Wang, W.H. Han, K.J. Chang, Y.H. Jung, D.K. Kim, New insight into Na intercalation with Li substitution on alkali site and high performance of O3-type layered cathode material for sodium ion batteries, *J. Mater. Chem. A*. 6 (2018) 22731–22740. doi:10.1039/c8ta06159a.
- [186] Y. Li, Y. Gao, X. Wang, X. Shen, Q. Kong, R. Yu, G. Lu, Z. Wang, L. Chen, Iron Migration and Oxygen Oxidation during Sodium Extraction from NaFeO₂, *Nano Energy*. 47 (2018) 519–526. doi:10.1016/j.nanoen.2018.03.007.
- [187] D. Susanto, M.K. Cho, G. Ali, J.Y. Kim, H.J. Chang, H.S. Kim, K.W. Nam, K.Y. Chung, Anionic Redox Activity as a Key Factor in the Performance Degradation of NaFeO₂ Cathodes for Sodium Ion Batteries, *Chem. Mater.* 31 (2019) 3644–3651. doi:10.1021/acs.chemmater.9b00149.
- [188] Y. Takeda, K. Nakahara, M. Nishijima, N. Imanishi, O. Yamamoto, M. Takano, R. Kanno, Sodium deintercalation from sodium iron oxide, *Mater. Res. Bull.* 29 (1994) 659–666. doi:10.1016/0025-5408(94)90122-8.
- [189] X. Zhu, T. Lin, E. Manning, Y. Zhang, M. Yu, B. Zuo, L. Wang, Recent advances on Fe- and Mn-based cathode materials for lithium and sodium ion batteries, *J. Nanoparticle Res.* 20 (2018). doi:10.1007/s11051-018-4235-1.
- [190] M. Hirayama, H. Tomita, K. Kubota, R. Kanno, Structure and electrode reactions of layered rocksalt LiFeO₂ nanoparticles for lithium battery cathode, *J. Power Sources*. 196 (2011) 6809–6814. doi:10.1016/j.jpowsour.2010.10.009.
- [191] J. Wang, D. Zhou, X. He, L. Zhang, X. Cao, D. Ning, B. Yan, X. Qi, J. Li, V. Murzin, E. Paillard, X. Liu, G. Schumacher, M. Winter, J. Li, Insights into P2-Type Layered Positive Electrodes for Sodium Batteries: From Long- to Short-Range Order, *ACS Appl. Mater. Interfaces*. 12 (2020) 5017–5024. doi:10.1021/acsami.9b18109.
- [192] J.W. Somerville, R.A. House, N. Tapia-Ruiz, A. Sobkowiak, S. Ramos, A. V. Chadwick, M.R. Roberts, U. Maitra, P.G. Bruce, Identification and characterisation of high energy density P2-type Na_{2/3} [Ni_{1/3-y/2} Mn_{2/3-y/2} Fe_y]O₂ compounds for Na-ion batteries, *J. Mater. Chem. A*. (2018). doi:10.1039/C7TA09607K.
- [193] S. Xu, J. Wu, E. Hu, Q. Li, J. Zhang, Y. Wang, E. Stavitski, L. Jiang, X. Rong, X. Yu, W. Yang, X.Q. Yang, L. Chen, Y.S. Hu, Suppressing the voltage decay of low-cost P2-type iron-based cathode materials for sodium-ion batteries, *J. Mater. Chem. A*. 6 (2018) 20795–20803. doi:10.1039/C8TA07933A.
- [194] C. Zhang, R. Gao, L. Zheng, Y. Hao, X. Liu, New Insights into the Roles of Mg in

- Improving the Rate Capability and Cycling Stability of $\text{O}_3\text{-NaMn}_{0.48}\text{Ni}_{0.2}\text{Fe}_{0.3}\text{Mg}_{0.02}\text{O}_2$ for Sodium-Ion Batteries, *ACS Appl. Mater. Interfaces*. (2018) acsami.7b18226. doi:10.1021/acsami.7b18226.
- [195] L. Yang, X. Li, J. Liu, S. Xiong, X. Ma, P. Liu, J. Bai, W. Xu, Y. Tang, Y.Y. Hu, M. Liu, H. Chen, Lithium-Doping Stabilized High-Performance $\text{P}_2\text{-Na}_{0.66}\text{Li}_{0.18}\text{Fe}_{0.12}\text{Mn}_{0.7}\text{O}_2$ Cathode for Sodium Ion Batteries, *J. Am. Chem. Soc.* 141 (2019) 6680–6689. doi:10.1021/jacs.9b01855.
- [196] M. Keller, T. Eisenmann, D. Meira, G. Aquilanti, D. Buchholz, D. Bresser, S. Passerini, In Situ Investigation of Layered Oxides with Mixed Structures for Sodium-Ion Batteries, *Small Methods*. 1900239 (2019) 1900239. doi:10.1002/smt.201900239.
- [197] B.H. Toby, R.B. Von Dreele, GSAS-II: The genesis of a modern open-source all purpose crystallography software package, *J. Appl. Crystallogr.* 46 (2013) 544–549. doi:10.1107/S0021889813003531.
- [198] B. Ravel, M. Newville, ATHENA, ARTEMIS, HEPHAESTUS: Data analysis for X-ray absorption spectroscopy using IFEFFIT, *J. Synchrotron Radiat.* 12 (2005) 537–541. doi:10.1107/S0909049505012719.
- [199] D. Joubert, From ultrasoft pseudopotentials to the projector augmented-wave method, *Phys. Rev. B - Condens. Matter Mater. Phys.* 59 (1999) 1758–1775. doi:10.1103/PhysRevB.59.1758.
- [200] G. Kresse, J. Hafner, Ab initio molecular-dynamics simulation of the liquid-metalamorphous- semiconductor transition in germanium, *Phys. Rev. B.* 49 (1994) 14251–14269. doi:10.1103/PhysRevB.49.14251.
- [201] G. Kresse, J. Furthmüller, Efficiency of ab-initio total energy calculations for metals and semiconductors using a plane-wave basis set, *Comput. Mater. Sci.* 6 (1996) 15–50. doi:10.1016/0927-0256(96)00008-0.
- [202] S. Dudarev, G. Botton, Electron-energy-loss spectra and the structural stability of nickel oxide: An LSDA+U study, *Phys. Rev. B - Condens. Matter Mater. Phys.* 57 (1998) 1505–1509. doi:10.1103/PhysRevB.57.1505.
- [203] J.J. Rehr, J.J. Kas, F.D. Vila, M.P. Prange, K. Jorissen, Parameter-free calculations of X-ray spectra with FEFF9, *Phys. Chem. Chem. Phys.* 12 (2010) 5503–5513. doi:10.1039/b926434e.
- [204] E. Bosman, J. Thieme, Modeling of XANES-spectra with the FEFF-program, *J. Phys. Conf. Ser.* 186 (2009) 2–5. doi:10.1088/1742-6596/186/1/012004.
- [205] R.D. Shannon, Revised effective ionic radii and systematic studies of interatomic distances in halides and chalcogenides, *Acta Crystallogr. Sect. A.* 32 (1976) 751–767. doi:10.1107/S0567739476001551.

- [206] B. Mortemard De Boisse, D. Carlier, M. Guignard, E. Guerin, M. Duttine, A. Wattiaux, C. Delmas, Influence of Mn/Fe Ratio on Electrochemical and Structural Properties of P2-NaxMn1-yFeyO2 Phases as Positive Electrode Material for Na-Ion Batteries, *Chem. Mater.* 30 (2018) 7672–7681. doi:10.1021/acs.chemmater.8b02953.
- [207] G.A. Waychunas, M.J. Apter, G.E. Brown, X-ray K-edge absorption spectra of Fe minerals and model compounds: Near-edge structure, *Phys. Chem. Miner.* 10 (1983) 1–9. doi:10.1007/BF01204319.
- [208] R. Rajagopalan, B. Chen, Z. Zhang, X.L. Wu, Y. Du, Y. Huang, B. Li, Y. Zong, J. Wang, G.H. Nam, M. Sindoro, S.X. Dou, H.K. Liu, H. Zhang, Improved Reversibility of Fe³⁺/Fe⁴⁺ Redox Couple in Sodium Super Ion Conductor Type Na₃Fe₂(PO₄)₃ for Sodium-Ion Batteries, *Adv. Mater.* 29 (2017). doi:10.1002/adma.201605694.
- [209] A.E. Bocquet, A. Fujimori, T. Mizokawa, T. Saitoh, H. Namatame, S. Suga, N. Kimizuka, Y. Takeda, M. Takano, Electronic structure of SrFe⁴⁺O₃ and related Fe perovskite oxides, *Phys. Rev. B.* 45 (1992) 1561–1570. doi:10.1103/PhysRevB.45.1561.
- [210] Y. Nanba, T. Iwao, B.M. De Boisse, W. Zhao, E. Hosono, D. Asakura, H. Niwa, H. Kiuchi, J. Miyawaki, Y. Harada, M. Okubo, A. Yamada, Redox Potential Paradox in NaxMO₂ for Sodium-Ion Battery Cathodes, *Chem. Mater.* 28 (2016) 1058–1065. doi:10.1021/acs.chemmater.5b04289.
- [211] D.H. Seo, J. Lee, A. Urban, R. Malik, S. Kang, G. Ceder, The structural and chemical origin of the oxygen redox activity in layered and cation-disordered Li-excess cathode materials, *Nat. Chem.* 8 (2016) 692–697. doi:10.1038/nchem.2524.
- [212] M. Ben Yahia, J. Vergnet, M. Saubanère, M.L. Doublet, Unified picture of anionic redox in Li/Na-ion batteries, *Nat. Mater.* 18 (2019) 496–502. doi:10.1038/s41563-019-0318-3.
- [213] X. Cao, H. Li, Y. Qiao, X. Li, M. Jia, J. Cabana, H. Zhou, Stabilizing Reversible Oxygen Redox Chemistry in Layered Oxides for Sodium-Ion Batteries, *Adv. Energy Mater.* 1903785 (2020) 1903785. doi:10.1002/aenm.201903785.
- [214] W.E. Gent, K. Lim, Y. Liang, Q. Li, T. Barnes, S. Ahn, K.H. Stone, M. McIntire, J. Hong, J.H. Song, Y. Li, A. Mehta, S. Ermon, T. Tylliszczak, D. Kilcoyne, D. Vine, J. Park, S. Doo, M.F. Toney, W. Yang, D. Prendergast, W.C. Chueh, Strong Coupling Between Bulk Oxygen Redox and Cation Migration Explains Unusual Electrochemistry in 3 d Li-Rich Layered Oxides, *Nat. Commun.* (2017) 1–27. doi:10.1038/s41467-017-02041-x.
- [215] Y. Sun, S. Guo, H. Zhou, Exploration of Advanced Electrode Materials for Rechargeable Sodium-Ion Batteries, *Adv. Energy Mater.* 1800212 (2018) 1–18. doi:10.1002/aenm.201800212.
- [216] N.A. Katcho, J. Carrasco, D. Saurel, E. Gonzalo, M. Han, F. Aguesse, T. Rojo, Origins of Bistability and Na Ion Mobility Difference in P2- and O3-Na_{2/3}Fe_{2/3}Mn_{1/3}O₂ Cathode Polymorphs, *Adv. Energy Mater.* 7 (2017) 1–9. doi:10.1002/aenm.201601477.

- [217] Y. Guo, J. Zhang, J.-Z. Guo, W. Pang, X. Wu, Q. Yang, P. Wang, Z. Chen, K. Huang, Advanced P2-Na 2/3 Ni 1/3 Mn 7/12 Fe 1/12 O 2 Cathode Material with Suppressed P2–O2 Phase Transition toward High-Performance Sodium-Ion Battery, *ACS Appl. Mater. Interfaces*. 10 (2018) 34272–34282. doi:10.1021/acsami.8b12204.
- [218] P. He, H. Yu, D. Li, H. Zhou, Layered lithium transition metal oxide cathodes towards high energy lithium-ion batteries, *J. Mater. Chem.* 22 (2012) 3680–3695. doi:10.1039/c2jm14305d.
- [219] K. Luo, M.R. Roberts, R. Hao, N. Guerrini, D.M. Pickup, Y.-S. Liu, K. Edström, J. Guo, A. V. Chadwick, L.C. Duda, P.G. Bruce, Charge-compensation in 3d-transition-metal-oxide intercalation cathodes through the generation of localized electron holes on oxygen, *Nat. Chem.* 8 (2016) 684–691. doi:10.1038/nchem.2471.
- [220] A.J. Perez, Q. Jacquet, D. Batuk, A. Iadecola, M. Saubanère, G. Rousse, D. Larcher, H. Vezin, M.-L. Doublet, J.-M. Tarascon, Approaching the limits of cationic and anionic electrochemical activity with the Li-rich layered rocksalt Li3IrO4, *Nat. Energy*. 2 (2017). doi:10.1038/s41560-017-0042-7.
- [221] G. Assat, J.M. Tarascon, Fundamental understanding and practical challenges of anionic redox activity in Li-ion batteries, *Nat. Energy*. 3 (2018) 373–386. doi:10.1038/s41560-018-0097-0.
- [222] N. Yabuuchi, Solid-state Redox Reaction of Oxide Ions for Rechargeable Batteries, *Chem. Lett.* 46 (2017) 412–422. doi:10.1246/cl.161044.
- [223] J. Hong, H.D. Lim, M. Lee, S.W. Kim, H. Kim, S.T. Oh, G.C. Chung, K. Kang, Critical role of oxygen evolved from layered Li-Excess metal oxides in lithium rechargeable batteries, *Chem. Mater.* 24 (2012) 2692–2697. doi:10.1021/cm3005634.
- [224] E. McCalla, A.M. Abakumov, M. Saubanere, D. Foix, E.J. Berg, G. Rousse, M.-L. Doublet, D. Gonbeau, P. Novak, G. Van Tendeloo, R. Dominko, J.-M. Tarascon, Visualization of O-O peroxo-like dimers in high-capacity layered oxides for Li-ion batteries, *Science* (80-.). 350 (2015) 1516–1521. doi:10.1126/science.aac8260.
- [225] M. Okubo, A. Yamada, Molecular Orbital Principles of Oxygen-Redox Battery Electrodes, *ACS Appl. Mater. Interfaces*. 9 (2017) 36463–36472. doi:10.1021/acsami.7b09835.
- [226] K. Luo, M.R. Roberts, N. Guerrini, N. Tapia-Ruiz, R. Hao, F. Massel, D.M. Pickup, S. Ramos, Y.S. Liu, J. Guo, A. V. Chadwick, L.C. Duda, P.G. Bruce, Anion Redox Chemistry in the Cobalt Free 3d Transition Metal Oxide Intercalation Electrode Li[Li0.2Ni0.2Mn0.6]O2, *J. Am. Chem. Soc.* 138 (2016) 11211–11218. doi:10.1021/jacs.6b05111.
- [227] B. Li, D. Xia, Anionic Redox in Rechargeable Lithium Batteries, *Adv. Mater.* 29 (2017) 1–28. doi:10.1002/adma.201701054.
- [228] F. Meng, L. Chen, E. Hu, Y. Lu, H. Li, X. Huang, X. Yu, C. Delmas, L. Gu, Y.-S. Hu, X.-

- Q. Yang, C. Zhao, X. Rong, Q. Zhang, X. Wang, Anionic Redox Reaction-Induced High-Capacity and Low-Strain Cathode with Suppressed Phase Transition, *Joule*. (2018) 1–15. doi:10.1016/j.joule.2018.10.022.
- [229] P.F. Wang, Y. Xiao, N. Piao, Q.C. Wang, X. Ji, T. Jin, Y.J. Guo, S. Liu, T. Deng, C. Cui, L. Chen, Y.G. Guo, X.Q. Yang, C. Wang, Both cationic and anionic redox chemistry in a P2-type sodium layered oxide, *Nano Energy*. 69 (2020) 104474. doi:10.1016/j.nanoen.2020.104474.
- [230] C. Ma, J. Alvarado, J. Xu, R.J. Clement, M. Kodur, W. Tong, C.P. Grey, Y.S. Meng, Exploring Oxygen Activity in the High Energy P2-Type Na_{0.78}Ni_{0.23}Mn_{0.69}O₂ Cathode Material for Na-Ion Batteries, *J. Am. Chem. Soc.* 139 (2017) 4835–4845. doi:10.1021/jacs.7b00164.
- [231] Q. Jacquet, A. Iadecola, M. Saubanère, H. Li, E.J. Berg, G. Rousse, J. Cabana, M.L. Doublet, J.M. Tarascon, Charge Transfer Band Gap as an Indicator of Hysteresis in Li-Disordered Rock Salt Cathodes for Li-Ion Batteries, *J. Am. Chem. Soc.* 141 (2019) 11452–11464. doi:10.1021/jacs.8b11413.
- [232] W.E. Gent, K. Lim, Y. Liang, Q. Li, T. Barnes, S.J. Ahn, K.H. Stone, M. McIntire, J. Hong, J.H. Song, Y. Li, A. Mehta, S. Ermon, T. Tyliczszak, D. Kilcoyne, D. Vine, J.H. Park, S.K. Doo, M.F. Toney, W. Yang, D. Prendergast, W.C. Chueh, Coupling between oxygen redox and cation migration explains unusual electrochemistry in lithium-rich layered oxides, *Nat. Commun.* (2017). doi:10.1038/s41467-017-02041-x.
- [233] Y. Li, M.J. Zuba, S. Bai, Z.W. Lebens-Higgins, B. Qiu, S. Park, Z. Liu, M. Zhang, L.F.J. Piper, Y.S. Meng, Regeneration of degraded Li-rich layered oxide materials through heat treatment-induced transition metal reordering, *Energy Storage Mater.* 35 (2021) 99–107. doi:10.1016/j.ensm.2020.11.013.
- [234] C.L. Farrow, P. Juhas, J.W. Liu, D. Bryndin, E.S. Boin, J. Bloch, T. Proffen, S.J.L. Billinge, PDFfit2 and PDFgui: Computer programs for studying nanostructure in crystals, *J. Phys. Condens. Matter*. 19 (2007). doi:10.1088/0953-8984/19/33/335219.
- [235] J.P. Perdew, K. Burke, M. Ernzerhof, Generalized gradient approximation made simple, *Phys. Rev. Lett.* 77 (1996) 3865–3868. doi:10.1103/PhysRevLett.77.3865.
- [236] A. Jain, S.P. Ong, G. Hautier, W. Chen, W.D. Richards, S. Dacek, S. Cholia, D. Gunter, D. Skinner, G. Ceder, K.A. Persson, Commentary: The materials project: A materials genome approach to accelerating materials innovation, *APL Mater.* 1 (2013). doi:10.1063/1.4812323.
- [237] R.A. House, U. Maitra, L. Jin, J.G. Lozano, J.W. Somerville, N.H. Rees, A.J. Naylor, L.C. Duda, F. Massel, A. V. Chadwick, S. Ramos, D.M. Pickup, D.E. McNally, X. Lu, T. Schmitt, M.R. Roberts, P.G. Bruce, What Triggers Oxygen Loss in Oxygen Redox Cathode Materials?, *Chem. Mater.* 31 (2019) 3293–3300. doi:10.1021/acs.chemmater.9b00227.
- [238] a R. Armstrong, M. Holzapfel, P. Novk, S. Christopher, S. Kang, M.M. Thackeray, P.G.

- Bruce, L. Ni, L. Mn, P. Nova, C.S. Johnson, Demonstrating Oxygen Loss and Associated Structural Reorganization in the Lithium Battery Cathode Li [Ni Li Mn] O, *Jacs.* (2006) 8694–8698. doi:10.1021/ja062027.
- [239] Y. Wang, R. Xiao, Y.S. Hu, M. Avdeev, L. Chen, $\text{P2-Na}_{0.6}[\text{Cr}_{0.6}\text{Ti}_{0.4}]\text{O}_2$ cation-disordered electrode for high-rate symmetric rechargeable sodium-ion batteries, *Nat. Commun.* 6 (2015) 1–9. doi:10.1038/ncomms7954.
- [240] B. Mortemard de Boisse, G. Liu, J. Ma, S. Nishimura, S.-C. Chung, H. Kiuchi, Y. Harada, J. Kikkawa, Y. Kobayashi, M. Okubo, A. Yamada, Intermediate honeycomb ordering to trigger oxygen redox chemistry in layered battery electrode, *Nat. Commun.* 7 (2016) 11397. doi:10.1038/ncomms11397.
- [241] F.M.E. DeGroot, M. Grioni, J.C. Fuggle, J. Ghijsen, G.A. Sawatzky, Oxygen 1s XAS edges of TM oxides.pdf, *Phys. Rev. B.* 40 (1989) 5715–5723. doi:10.1103/PhysRevB.40.5715.
- [242] T. Kroll, M. Knupfer, J. Geck, C. Hess, T. Schwieger, G. Krabbes, C. Sekar, D.R. Batchelor, H. Berger, B. Büchner, X-ray absorption spectroscopy of $\text{Na}_x\text{Co}_2\text{O}$ layered cobaltates, *Phys. Rev. B.* 74 (2006) 115123. doi:10.1103/PhysRevB.74.115123.
- [243] Z. Lu, L.Y. Beaulieu, R.A. Donaberger, C.L. Thomas, J.R. Dahn, Synthesis, Structure, and Electrochemical Behavior of $\text{Li}[\text{Ni}_x\text{Li}_{1/3-2x/3}\text{Mn}_{2/3-x/3}]\text{O}_2$, *J. Electrochem. Soc.* 149 (2002) A778. doi:10.1149/1.1471541.
- [244] E. de la Llave, P.K. Nayak, E. Levi, T.R. Penki, S. Bublil, P. Hartmann, F.-F. Chesneau, M. Greenstein, L.F. Nazar, D. Aurbach, Electrochemical performance of $\text{Na}_{0.6}[\text{Li}_{0.2}\text{Ni}_{0.2}\text{Mn}_{0.6}]\text{O}_2$ cathodes with high-working average voltage for Na-ion batteries, *J. Mater. Chem. A.* 5 (2017) 5858–5864. doi:10.1039/C6TA10577G.
- [245] D. Kim, S.H. Kang, M. Slater, S. Rood, J.T. Vaughey, N. Karan, M. Balasubramanian, C.S. Johnson, Enabling sodium batteries using lithium-substituted sodium layered transition metal oxide cathodes, *Adv. Energy Mater.* 1 (2011) 333–336. doi:10.1002/aenm.201000061.
- [246] J. Bréger, N. Dupré, P.J. Chupas, P.L. Lee, T. Proffen, J.B. Parise, C.P. Grey, Short- and long-range order in the positive electrode material, $\text{Li}(\text{NiMn})_{0.5}\text{O}_2$: A joint X-ray and neutron diffraction, pair distribution function analysis and NMR study, *J. Am. Chem. Soc.* 127 (2005) 7529–7537. doi:10.1021/ja050697u.
- [247] Y. Zhang, M. Wu, J. Ma, G. Wei, Y. Ling, R. Zhang, Y. Huang, Revisiting the $\text{Na}_{2/3}\text{Ni}_{1/3}\text{Mn}_{2/3}\text{O}_2$ Cathode: Oxygen Redox Chemistry and Oxygen Release Suppression, *ACS Cent. Sci.* (2020). doi:10.1021/acscentsci.9b01166.
- [248] B. Jache, J.O. Binder, T. Abe, P. Adelhelm, A comparative study on the impact of different glymes and their derivatives as electrolyte solvents for graphite co-intercalation electrodes

- in lithium-ion and sodium-ion batteries, *Phys. Chem. Chem. Phys.* 18 (2016) 14299–14316. doi:10.1039/c6cp00651e.
- [249] B. Jache, P. Adelhelm, Use of graphite as a highly reversible electrode with superior cycle life for sodium-ion batteries by making use of co-intercalation phenomena, *Angew. Chemie - Int. Ed.* 53 (2014) 10169–10173. doi:10.1002/anie.201403734.
- [250] C. Bao, B. Wang, P. Liu, H. Wu, Y. Zhou, D. Wang, H. Liu, S. Dou, Solid Electrolyte Interphases on Sodium Metal Anodes, *Adv. Funct. Mater.* 2004891 (2020) 1–27. doi:10.1002/adfm.202004891.
- [251] V.S.A. Piriya, R.C. Shende, G.M. Seshadhri, D. Ravindar, S. Biswas, S. Loganathan, T.S. Balasubramanian, K. Rambabu, M. Kamaraj, S. Ramaprabhu, Synergistic Role of Electrolyte and Binder for Enhanced Electrochemical Storage for Sodium-Ion Battery, *ACS Omega.* 3 (2018) 9945–9955. doi:10.1021/acsomega.8b01407.
- [252] L. Ling, Y. Bai, Z. Wang, Q. Ni, G. Chen, Z. Zhou, C. Wu, Remarkable Effect of Sodium Alginate Aqueous Binder on Anatase TiO₂ as High-Performance Anode in Sodium Ion Batteries, *ACS Appl. Mater. Interfaces.* 10 (2018) 5560–5568. doi:10.1021/acsami.7b17659.
- [253] W. Luo, Z. Jian, Z. Xing, W. Wang, C. Bommier, M.M. Lerner, X. Ji, Electrochemically expandable soft carbon as anodes for Na-ion batteries, *ACS Cent. Sci.* 1 (2015) 516–522. doi:10.1021/acscentsci.5b00329.
- [254] J. Zhao, Y.Z. Zhang, F. Zhang, H. Liang, F. Ming, H.N. Alshareef, Z. Gao, Partially Reduced Holey Graphene Oxide as High Performance Anode for Sodium-Ion Batteries, *Adv. Energy Mater.* 1803215 (2018). doi:10.1002/aenm.201803215.
- [255] E.M. Lotfabad, J. Ding, K. Cui, A. Kohandehghan, W.P. Kalisvaart, M. Hazelton, D. Mitlin, High-density sodium and lithium ion battery anodes from banana peels, *ACS Nano.* 8 (2014) 7115–7129. doi:10.1021/nn502045y.
- [256] Y. Bai, Z. Wang, C. Wu, R. Xu, F. Wu, Y. Liu, H. Li, Y. Li, J. Lu, K. Amine, Hard carbon originated from polyvinyl chloride nanofibers as high-performance anode material for Na-ion battery, *ACS Appl. Mater. Interfaces.* 7 (2015) 5598–5604. doi:10.1021/acsami.5b00861.
- [257] Y. Cao, L. Xiao, M.L. Sushko, W. Wang, B. Schwenzer, J. Xiao, Z. Nie, L. V. Saraf, Z. Yang, J. Liu, Sodium ion insertion in hollow carbon nanowires for battery applications, *Nano Lett.* 12 (2012) 3783–3787. doi:10.1021/nl3016957.
- [258] X. Dou, I. Hasa, D. Saurel, C. Vaalma, L. Wu, D. Buchholz, D. Bresser, S. Komaba, S. Passerini, Hard carbons for sodium-ion batteries: Structure, analysis, sustainability, and electrochemistry, *Mater. Today.* 23 (2019) 87–104. doi:10.1016/j.mattod.2018.12.040.
- [259] K. Kubota, S. Shimadzu, N. Yabuuchi, S. Tominaka, S. Shiraishi, M. Abreu-Sepulveda, A. Manivannan, K. Gotoh, M. Fukunishi, M. Dahbi, S. Komaba, Structural Analysis of

- Sucrose-Derived Hard Carbon and Correlation with the Electrochemical Properties for Lithium, Sodium, and Potassium Insertion, *Chem. Mater.* 32 (2020) 2961–2977. doi:10.1021/acs.chemmater.9b05235.
- [260] A. Ponrouch, E. Marchante, M. Courty, J.M. Tarascon, M.R. Palacín, In search of an optimized electrolyte for Na-ion batteries, *Energy Environ. Sci.* 5 (2012) 8572–8583. doi:10.1039/c2ee22258b.
- [261] M. Liu, J. Zhang, S. Guo, B. Wang, Y. Shen, X. Ai, H. Yang, J. Qian, Chemically Presodiated Hard Carbon Anodes with Enhanced Initial Coulombic Efficiencies for High-Energy Sodium Ion Batteries, *ACS Appl. Mater. Interfaces.* 12 (2020) 17620–17627. doi:10.1021/acsami.0c02230.
- [262] D.M. Davies, M.G. Verde, O. Mnyshenko, Y.R. Chen, R. Rajeev, Y.S. Meng, G. Elliott, Combined economic and technological evaluation of battery energy storage for grid applications, *Nat. Energy.* 4 (2019) 42–50. doi:10.1038/s41560-018-0290-1.
- [263] K. Kubota, S. Komaba, Review—Practical Issues and Future Perspective for Na-Ion Batteries, *J. Electrochem. Soc.* 162 (2015) A2538–A2550. doi:10.1149/2.0151514jes.
- [264] K. Du, C. Wang, L.U. Subasinghe, S.R. Gajella, M. Law, A. Rudola, P. Balaya, A comprehensive study on the electrolyte, anode and cathode for developing commercial type non-flammable sodium-ion battery, *Energy Storage Mater.* 29 (2020) 287–299. doi:10.1016/j.ensm.2020.04.021.
- [265] R. Mogensen, S. Colbin, A.S. Menon, E. Björklund, R. Younesi, Sodium Bis(oxalato)borate in Trimethyl Phosphate: A Fire-Extinguishing, Fluorine-Free, and Low-Cost Electrolyte for Full-Cell Sodium-Ion Batteries, *ACS Appl. Energy Mater.* 3 (2020) 4974–4982. doi:10.1021/acsaem.0c00522.
- [266] P. Bai, Y. He, P. Xiong, X. Zhao, K. Xu, Y. Xu, Long cycle life and high rate sodium-ion chemistry for hard carbon anodes, *Energy Storage Mater.* 13 (2018) 274–282. doi:10.1016/j.ensm.2018.02.002.
- [267] C. Fang, J. Li, M. Zhang, Y. Zhang, F. Yang, J.Z. Lee, M.-H. Lee, J. Alvarado, M.A. Schroeder, Y. Yang, B. Lu, N. Williams, M. Ceja, L. Yang, M. Cai, J. Gu, K. Xu, X. Wang, Y.S. Meng, Quantifying inactive lithium in lithium metal batteries, *Nature.* 572 (2019) 511–515. doi:10.1038/s41586-019-1481-z.
- [268] A. Ponrouch, R. Dedryvère, D. Monti, A.E. Demet, J.M. Ateba Mba, L. Croguennec, C. Masquelier, P. Johansson, M.R. Palacín, Towards high energy density sodium ion batteries through electrolyte optimization, *Energy Environ. Sci.* 6 (2013) 2361–2369. doi:10.1039/c3ee41379a.
- [269] G.G. Eshetu, T. Diemant, M. Hekmatfar, S. Grugeon, R.J. Behm, S. Laruelle, M. Armand, S. Passerini, Impact of the electrolyte salt anion on the solid electrolyte interphase formation in sodium ion batteries, *Nano Energy.* 55 (2019) 327–340. doi:10.1016/j.nanoen.2018.10.040.

- [270] J. Patra, H.T. Huang, W. Xue, C. Wang, A.S. Helal, J. Li, J.K. Chang, Moderately concentrated electrolyte improves solid–electrolyte interphase and sodium storage performance of hard carbon, *Energy Storage Mater.* 16 (2019) 146–154. doi:10.1016/j.ensm.2018.04.022.
- [271] S. Komaba, T. Ishikawa, N. Yabuuchi, W. Murata, A. Ito, Y. Ohsawa, Fluorinated ethylene carbonate as electrolyte additive for rechargeable Na batteries, *ACS Appl. Mater. Interfaces.* 3 (2011) 4165–4168. doi:10.1021/am200973k.
- [272] E.J. McShane, E.J. McShane, A.M. Colclasure, D.E. Brown, D.E. Brown, Z.M. Konz, Z.M. Konz, K. Smith, B.D. McCloskey, B.D. McCloskey, Quantification of Inactive Lithium and Solid-Electrolyte Interphase Species on Graphite Electrodes after Fast Charging, *ACS Energy Lett.* 5 (2020) 2045–2051. doi:10.1021/acsenerylett.0c00859.
- [273] J. Petrovic, G. Thomas, *Reaction of Aluminum with Water to Produce Hydrogen*, 2010.
- [274] C. Bommier, W. Luo, W.Y. Gao, A. Greaney, S. Ma, X. Ji, Predicting capacity of hard carbon anodes in sodium-ion batteries using porosity measurements, *Carbon N. Y.* 76 (2014) 165–174. doi:10.1016/j.carbon.2014.04.064.
- [275] C. Matei Ghimbeu, J. Górká, V. Simone, L. Simonin, S. Martinet, C. Vix-Guterl, Insights on the Na⁺ion storage mechanism in hard carbon: Discrimination between the porosity, surface functional groups and defects, *Nano Energy.* 44 (2018) 327–335. doi:10.1016/j.nanoen.2017.12.013.
- [276] M. Inaba, H. Yoshida, Z. Ogumi, In situ Raman Study of Electrochemical Lithium Insertion into Mesocarbon Microbeads Heat-Treated at Various Temperatures, *J. Electrochem. Soc.* 143 (1996) 2572–2578. doi:10.1149/1.1837049.
- [277] A. Raj K, M.R. Panda, D.P. Dutta, S. Mitra, Bio-derived mesoporous disordered carbon: An excellent anode in sodium-ion battery and full-cell lab prototype, *Carbon N. Y.* 143 (2019) 402–412. doi:10.1016/j.carbon.2018.11.038.
- [278] S. Maruyama, T. Fukutsuka, K. Miyazaki, T. Abe, In situ Raman spectroscopic analysis of solvent co-intercalation behavior into a solid electrolyte interphase-covered graphite electrode, *J. Appl. Electrochem.* 49 (2019) 639–646. doi:10.1007/s10800-019-01312-3.
- [279] C. Sole, N.E. Drewett, L.J. Hardwick, In situ Raman study of lithium-ion intercalation into microcrystalline graphite, *Faraday Discuss.* 172 (2014) 223–237. doi:10.1039/c4fd00079j.
- [280] C.T. Chan, K.M. Ho, W.A. Kamitakahara, Zone-center phonon frequencies for graphite and graphite intercalation compounds: Charge-transfer and intercalate-coupling effects, *Phys. Rev. B.* 36 (1987) 3499–3502. doi:10.1103/PhysRevB.36.3499.
- [281] M. Anji Reddy, M. Helen, A. Groß, M. Fichtner, H. Euchner, Insight into Sodium Insertion and the Storage Mechanism in Hard Carbon, *ACS Energy Lett.* 3 (2018) 2851–2857. doi:10.1021/acsenerylett.8b01761.

- [282] K. Pan, H. Lu, F. Zhong, X. Ai, H. Yang, Y. Cao, Understanding the Electrochemical Compatibility and Reaction Mechanism on Na Metal and Hard Carbon Anodes of PC-Based Electrolytes for Sodium-Ion Batteries, *ACS Appl. Mater. Interfaces*. 10 (2018) 39651–39660. doi:10.1021/acsami.8b13236.
- [283] J. Huang, X. Guo, X. Du, X. Lin, J.-Q. Huang, H. Tan, Y. Zhu, B. Zhang, Nanostructures of solid electrolyte interphases and their consequences for microsized Sn anodes in sodium ion batteries, *Energy Environ. Sci.* 12 (2019) 1550–1557. doi:10.1039/c8ee03632b.
- [284] B. Zhang, G. Rousse, D. Foix, R. Dugas, D.A.D. Corte, J.M. Tarascon, Microsized Sn as Advanced Anodes in Glyme-Based Electrolyte for Na-Ion Batteries, *Adv. Mater.* 28 (2016) 9824–9830. doi:10.1002/adma.201603212.
- [285] C. Wang, L. Wang, F. Li, F. Cheng, J. Chen, Bulk Bismuth as a High-Capacity and Ultralong Cycle-Life Anode for Sodium-Ion Batteries by Coupling with Glyme-Based Electrolytes, *Adv. Mater.* 29 (2017) 1–7. doi:10.1002/adma.201702212.
- [286] J. Zhang, D.W. Wang, W. Lv, S. Zhang, Q. Liang, D. Zheng, F. Kang, Q.H. Yang, Achieving superb sodium storage performance on carbon anodes through an ether-derived solid electrolyte interphase, *Energy Environ. Sci.* 10 (2017) 370–376. doi:10.1039/c6ee03367a.
- [287] C. Cheng, S. Li, T. Liu, Y. Xia, L.Y. Chang, Y. Yan, M. Ding, Y. Hu, J. Wu, J. Guo, L. Zhang, Elucidation of Anionic and Cationic Redox Reactions in a Prototype Sodium-Layered Oxide Cathode, *ACS Appl. Mater. Interfaces*. 11 (2019) 41304–41312. doi:10.1021/acsami.9b13013.
- [288] N. Tapia-Ruiz, W.M. Dose, N. Sharma, H. Chen, J. Heath, J. Somerville, U. Maitra, S. Islam, P.G. Bruce, High voltage structural evolution and enhanced Na-ion diffusion in $\text{P2-Na}_{2/3}\text{Ni}_{1/3-x}\text{Mg}_x\text{Mn}_{2/3}\text{O}_2$ ($0 < x < 0.20$) cathodes from diffraction, electrochemical and ab-initio studies, *Energy Environ. Sci.* 2 (2018). doi:10.1039/C7EE02995K.
- [289] J. Xu, H. Liu, Y.S. Meng, Exploring Li substituted O3-structured layered oxides $\text{NaLi}_x\text{Ni}_{1/3-x}\text{Mn}_{1/3} + x\text{Co}_{1/3-x}\text{O}_2$ ($x=0.07, 0.13, \text{ and } 0.2$) as promising cathode materials for rechargeable Na batteries, *Electrochem. Commun.* 60 (2015) 13–16. doi:10.1016/j.elecom.2015.07.023.
- [290] E. De La Llave, E. Talaie, E. Levi, P.K. Nayak, M. Dixit, P.T. Rao, P. Hartmann, F. Chesneau, D.T. Major, M. Greenstein, D. Aurbach, L.F. Nazar, Improving Energy Density and Structural Stability of Manganese Oxide Cathodes for Na-Ion Batteries by Structural Lithium Substitution, *Chem. Mater.* 28 (2016) 9064–9076. doi:10.1021/acs.chemmater.6b04078.
- [291] K. Sato, M. Nakayama, A.M. Glushenkov, T. Mukai, Y. Hashimoto, K. Yamanaka, M. Yoshimura, T. Ohta, N. Yabuuchi, Na-Excess Cation-Disordered Rocksalt Oxide: $\text{Na}_{1.3}\text{Nb}_{0.3}\text{Mn}_{0.4}\text{O}_2$, *Chem. Mater.* 29 (2017) 5043–5047. doi:10.1021/acs.chemmater.7b00172.

- [292] H. Yu, G. Liu, G. Li, J. Zhang, Q. Shun, G. Chen, L. Wen, Study on enhancing electrochemical properties of Li in layered compound $\text{Na}_{0.7}\text{Li}_{0.3}\text{Mn}_{0.75}\text{O}_2$, *Electrochim. Acta.* (2017). doi:10.1016/j.electacta.2017.12.177.
- [293] M. Jia, Y. Qiao, X. Li, F. Qiu, X. Cao, P. He, H. Zhou, Identifying Anionic Redox Activity within the Related O3- and P2-Type Cathodes for Sodium-Ion Battery, *ACS Appl. Mater. Interfaces.* 12 (2020) 851–857. doi:10.1021/acsami.9b18493.
- [294] N. Yabuuchi, R. Hara, K. Kubota, J. Paulsen, S. Kumakura, S. Komaba, A new electrode material for rechargeable sodium batteries: P2-type $\text{Na}_{2/3}[\text{Mg}_{0.28}\text{Mn}_{0.72}]\text{O}_2$ with anomalously high reversible capacity, *J. Mater. Chem. A.* 2 (2014) 16851–16855. doi:10.1039/C4TA04351K.
- [295] Q. Wang, W. Yang, F. Kang, B. Li, $\text{Na}_2\text{Mn}_3+0.3\text{Mn}_4+2.7\text{O}_6.85$: A cathode with simultaneous cationic and anionic redox in Na-ion battery, *Energy Storage Mater.* 14 (2018) 361–366. doi:10.1016/j.ensm.2018.06.003.
- [296] H.J. Kim, A. Konarov, J.H. Jo, J.U. Choi, K. Ihm, H.K. Lee, J. Kim, S.T. Myung, Controlled Oxygen Redox for Excellent Power Capability in Layered Sodium-Based Compounds, *Adv. Energy Mater.* 9 (2019) 1–9. doi:10.1002/aenm.201901181.
- [297] R.A. House, U. Maitra, M.A. Pérez-Osorio, J.G. Lozano, L. Jin, J.W. Somerville, L.C. Duda, A. Nag, A. Walters, K.J. Zhou, M.R. Roberts, P.G. Bruce, Superstructure control of first-cycle voltage hysteresis in oxygen-redox cathodes, *Nature.* 577 (2020) 502–508. doi:10.1038/s41586-019-1854-3.
- [298] W. Zheng, Q. Liu, Z. Wang, Z. Wu, S. Gu, L. Cao, K. Zhang, J. Fransaer, Z. Lu, Oxygen redox activity with small voltage hysteresis in $\text{Na}_{0.67}\text{Cu}_{0.28}\text{Mn}_{0.72}\text{O}_2$ for sodium-ion batteries, *Energy Storage Mater.* 28 (2020) 300–306. doi:10.1016/j.ensm.2020.03.016.
- [299] M. Moshkovich, Y. Gofer, D. Aurbach, Investigation of the Electrochemical Windows of Aprotic Alkali Metal (Li, Na, K) Salt Solutions, *J. Electrochem. Soc.* 148 (2001) E155. doi:10.1149/1.1357316.
- [300] L. Gao, J. Chen, Y. Liu, Y. Yamauchi, Z. Huang, X. Kong, Revealing the chemistry of an anode-passivating electrolyte salt for high rate and stable sodium metal batteries, *J. Mater. Chem. A.* (2018) 12012–12017. doi:10.1039/C8TA03436B.
- [301] D. Aurbach, Review of selected electrode–solution interactions which determine the performance of Li and Li ion batteries, *J. Power Sources.* (2000) 206–218. doi:https://doi.org/10.1016/S0378-7753(00)00431-6.
- [302] B. Philippe, M. Valvo, F. Lindgren, H. Rensmo, K. Edström, Investigation of the electrode/electrolyte interface of Fe_2O_3 composite electrodes: Li vs Na batteries, *Chem. Mater.* 26 (2014) 5028–5041. doi:10.1021/cm5021367.